The Dynamic Breakup of Soft Glassy Material

Thesis submitted to the University of Nottingham for the degree of **Doctor of Philosophy**, March 2022.

M.J. Hayes

4315922

School of Physics and Astronomy

Supervised by

Dr. M.I. Smith

Dr. D. Snoswell

Contents

Acknowledgements

I would like to thank everybody who supported me during this undertaking. I thank Dr Mike Smith for all of his, patience and assistance. His guidance in this work has been instrumental and I could not have asked for a better supervisor. I am also grateful to Dr David Snoswell, Dr Andrew Clarke and the research staff at Schlumberger, Cambridge for their input in this work. Dr Snoswell gave me a real insight into the world of industrial research and the facilities provided by the company were extremely useful.

I would also like to thank my parents for their support over the last few years as well as our cats, Perry, Jasper, Robbie and Coco who provided a lot of cuddles when I was stressed. Lastly I would like to thank my friends and loved ones in Portland, Oregon who provided me with so much support over the last four years. Thank you, Jay, Nabia, Zeke, Taylor, Katie, Chris, Gary, Nova, Juniper and Fev, I could not have done it without you all.

Abstract

The work contained within this thesis is focused on the rheology of soft glassy materials, namely yield stress fluids and how the breakup of these fluids is affected by physical properties such as adhesion, slip and thixotropy. These fluids are of particular interest to several industries, including the oil and gas industry, where their adhesive properties can hamper the drilling process. Questions concerning the adhesive character of yield stress fluids are also of interest in academia where there is still some debate as to the mechanism by which these types of fluids adhere to surfaces.

The two most significant sets of experiments in this work made use of a shear rheometer to carry out adhesion tests on samples of kaolin and also laponite clays. In each case the behaviour during the adhesion test was related to the measured shear properties of the samples. The study using kaolin focussed on the role of slip, whilst the study using laponite investigated the role of aging. Additional experiments were also performed with a centrifuge to understand the compaction of kaolin clay under compressive stress. The flow of water / changes in solid volume fraction over time were also followed using x-ray shadowgraphy.

This work showed several interesting behaviours that affect adhesion measurements. In the adhesion study on kaolin clay it was shown that despite the breakup being strongly influenced by the concentration of the clay, the start-up behaviour of these experiments is greatly affected by the slip of the experiment. The slip behaviour exhibits a crossover between wall slip and shear-localisation which can be significant enough to influence the final break-up behaviour. Through careful manipulation of the sample history we also showed that the lubrication conditions at the interface can be altered through compaction, modifying the peak adhesion force and the strain at which this occurs. Investigating this compaction further using centrifugation we counterintuitively found that a defined stress does not result in a unique final value of the suspension density. Rather a dense suspension will form a denser final sediment than a less dense suspension when subjected to the same stress. In the adhesion tests on laponite gels we showed that the sample break-up becomes increasingly brittle as the samples age. This can be observed visually, but we also demonstrated that by taking measurements of the sample midpoint and contact angles at the plate surfaces, key rheological properties, such as the yield strain, can be quantified and compared for different samples.

Nomenclature

Main Equations

Herschel-Bulkely	$\sigma = \sigma y + K\dot{\gamma}n$
Hencky Strain	$\varepsilon = \ln {}^{l}/_{l_o}$
Beer's Law	$A = log_{10}\left({}^{I_o}/_{I}\right)$
Laplace Pressure	$\Delta P = \gamma\left(\frac{1}{R_{r\theta}} - \frac{1}{R_{rz}}\right)$

Acronyms

LAOS	Large Amplitude Oscillatory Shear, an oscillatory experiment where the sample is strained further than the linear regime and the sample is broken down.
PDMS	Polydimethylsiloxane, a common reference viscoelastic material used in rheology calibration.
RCP	Random Close Packing, the maximum volume fraction of solid particles when they are packed randomly (0.64).
RLP	Random Loose Packing, the maximum attained in a loose, gently oscillated system (0.55).
RCF	Relative Centrifugal Force, the amount of acceleration exerted on a sample during rotation in a centrifuge
SAOS	Small Amplitude Oscillatory Shear, an oscillatory experiment where a linear response is obtained, sample remains in the elastic regime.
YSF	Yield Stress Fluid, a fluid that behaves like a solid when at rest but will flow when a high enough stress is applied.

Symbols

$\boldsymbol{\sigma}$	the stress, force per unit area applied to an object to cause a deformation (Pa).
$\boldsymbol{\sigma_y}$	the yield stress, the stress at which a fluid transitions from solid to liquid like behaviour (Pa).
$\boldsymbol{\gamma}$	the strain, the change in object length as a function of its original length.
$\boldsymbol{\varepsilon}$	the Hencky strain, also called the true strain, is a logarithmic measure of strain in an elongation
$\boldsymbol{\dot{\gamma}}$	the shear rate, a measure of the deformation as a function of time (s^{-1}).
$\boldsymbol{\dot{\gamma}_{global}}$	the global shear rate, defined as the shear rate applied by a rheometer to a sample (Pa)
h	the height of a sample before and during an experiment (mm).
h_o	the initial height of the sample at t_0 (mm)
h_c	the critical height of the sample, typically where breakup occurs (mm)
η	the viscosity, a measure of the resistance to flow. Calculated as the ratio of stress over strain (Pa s).
$\boldsymbol{\varphi}$	the volume fraction, the volume of a constituent component in a system, typically a measure of the solid components.
K	the consistency index, gives a measure of the viscosity of a fluid. Is defined by the ratio of Attenburg limits. Typically between 1 and 0.
n	the flow index, indicates the degree of non-Newtonian characteristics of a fluid. A Newtonian fluid is represented by 1, as a fluid shows more non-Newtonian behaviour n will decrease to 0.
$\boldsymbol{\omega}$	the frequency of an oscillation (s^{-1})
G'	the elastic modulus, also known as the storage modulus. Is a measure of the solid like behaviour of a fluid or how well it can store energy (Pa)
G"	the viscous modulus, also known as the loss modulus, Is a measure of the liquid like behaviour of a fluid or how well it can dissipate energy (Pa).
$\boldsymbol{W_{Adh}}$	the work of adhesion, the energy required to pull two plates separated by a layer of fluid defined as the ratio of force over distance (J).
D	the diameter of a sample, measured as the thinnest diameter in a sample during an experiment (mm)
$\boldsymbol{D_0}$	the original diameter of the sample, defined as the thinnest diameter in the sample at rest (t = 0 seconds)

V	the radial velocity of the fluid as it is pulled inwards during an extensional experiment (mm s^{-1}).
A	the absorbance of light, a measure of the amount of light that does not reach the detector when light passes through an object.
T	the transmittance of light, the amount of light that passes through an object and is measured by a detector.
$\mathbf{I_0}$	the incident light, this is the light shone into an object for analysis (W m^{-2}).
I	the light transmitted through an object, some of the light is deflected or absorbed by the object resulting in less light reaching the detector (W m^{-2}).
$\mathbf{P^p}$	the pore pressure, the pressure of a fluid in the pore space of a rock. Under external stress can result in a resistance to compaction (Pa).

Chapter 1. Literature Review

1.1 Newtonian and non-Newtonian Fluids

One is used to thinking of the world in terms of three states of matter with distinct physical properties: solids, liquids and gases. To deform an elastic solid requires a finite stress (σ, the force per unit area,). The deformation is characterised by the strain (γ, the ratio of ΔL/h, see figure 1). The energy required for deformation is stored elastically within the structure, with the consequence that when the force is removed the object will return to its original shape. However, when a liquid is deformed, the energy is dissipated (often as heat). As a result, when the stress is removed, it will not return to its original shape [1].

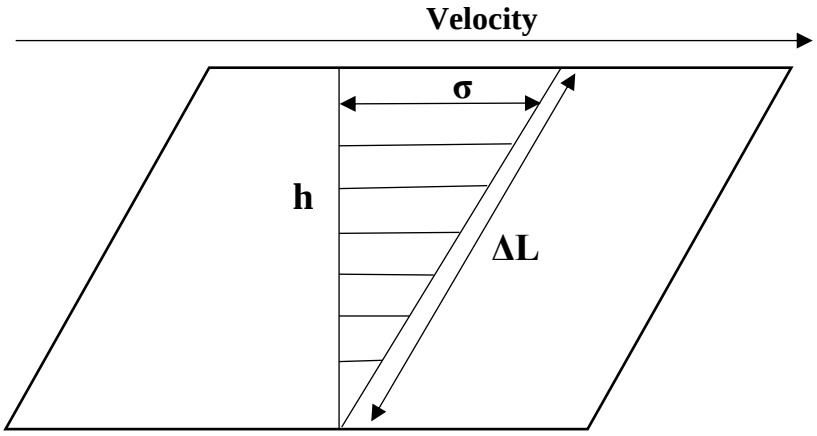

Figure 1: Schematic of an object under shear.

If a sample is sheared as a function of time at a known rate, $\dot{\gamma}$, the measured stress response can be used to obtain material properties that will help to characterise its behaviour. The ratio of measured stress to applied shear-rate is the viscosity (η). The viscosity of a fluid describes how easily it will flow e.g. water flows freely while syrup is more resistant to spreading across a surface. Water and syrup are both examples of Newtonian fluids which are characterised by a constant ratio of stress over strain-rate which is independent of the applied strain rate ($\eta = \sigma/\dot{\gamma}$ = constant). However, this behaviour is not generally true for all fluids.

Non-Newtonian fluids show nonlinear stress/strain-rate relationships, with viscosities that can increase or decrease with shear-rate. A classic example of this class of fluids is a suspension of corn starch. When sheared by a small stress it flows easily but, under a large stress it will behave like a solid that can fracture [2]. The viscosity of non-Newtonian fluids can also be time dependent. For example, condiments such as ketchup and mustard flow more easily after shaking but when left at rest they gradually increase in viscosity [3]. These factors make it impossible to define a single value of the viscosity for a non-Newtonian fluid. Other common examples of non-Newtonian fluids include cosmetics, blood, lava, and paints [4]. Non-Newtonian fluids can also be sub-divided into smaller groups according to some of their properties, such as viscoelasticity, yield stress, thixotropy or rheopecty.

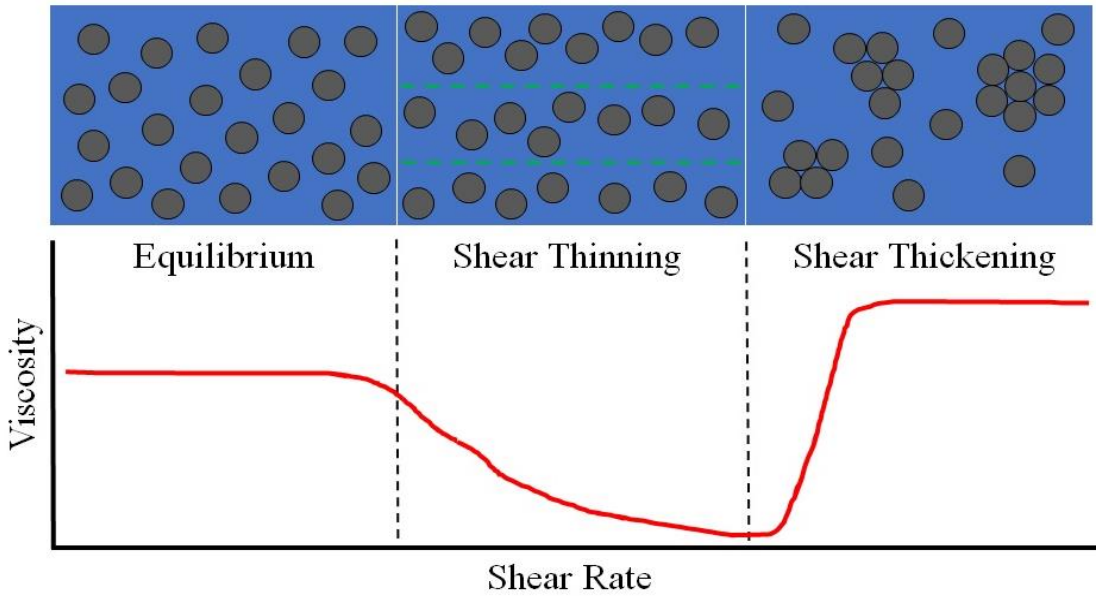

Figure 2: Flow curve showing how the viscosity of a fluid changes if it has shear thinning and thickening behaviour. This example is of a fluid that shows both behaviours depending on the shear rate applied. This Figure has been reproduced from [5].

Some non-Newtonian fluids also show *shear thickening* or *thinning* behaviour, meaning that their viscosity changes as a function of $\dot{\gamma}$ (see figure 2). Shear thinning behaviour is very useful for many applications such as shampoos and detergents as it helps them to be spread more easily [5]. Many fluids such as clays and gels [6] show a mixture of the two behaviours [7]. In some cases, shear thinning is initially observed over a finite $\dot{\gamma}$ range as the particles rearrange to allow for easier flow. However, as the shear rate increases, the particles are brought together by hydrodynamic forces. This results in particle clusters that increase the viscosity of the system (see figure 2). Larger granular particles may also result in shear thinning/thickening, though in these systems

the thickening often arises due to the frictional interactions which result in jammed networks of grains that resist the applied stress [8]. It is important to note that this model is only appropriate in systems where the particles can move freely. In highly concentrated systems where particles are caged rearrangment is less likely to occur.

1.2 Yield Stress Fluids

When a Newtonian fluid is poured onto a surface it will spread under gravity to form a thin layer. However, some non-Newtonian fluids do not show this behaviour, e.g. shaving cream will not run off your hand or face spontaneously. This suggests that a finite amount of stress is required to cause some fluids to flow e.g. when you spread the shaving cream across your skin.

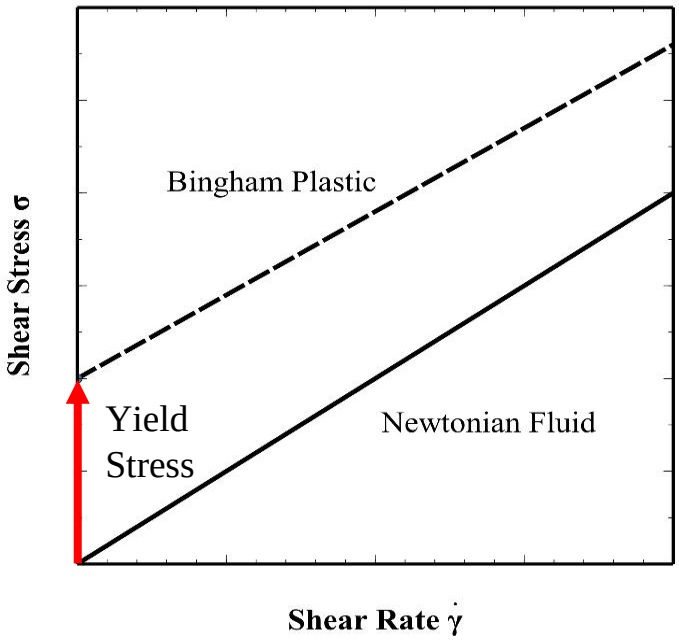

Figure 3: Schematic showing the difference between a Newtonian Fluid and a Bingham Plastic.

The earliest illustration of this behaviour was published by Bingham almost one hundred years ago [9]. His model implied that at low stresses, σ, the fluid behaves like a solid and will not flow. However, above a "yield stress" (σ_y, denoted by the red arrow in fig. 3) the fluid behaves like a Newtonian fluid, and the stress is linearly related to the shear rate (see figure 3), i.e,

$$\sigma < \sigma_y \, , \dot{\gamma} = 0 \, , \tag{1}$$

$$\dot{\gamma} = (\sigma - \sigma_y)/\eta \, , \tag{2}$$

where the η is the slope of the curve in the fluid region. Yield stress behaviour occurs when an interconnected network exists within the fluid that can resist flow. Many examples of this behaviour exist such as colloidal gels, foams, and pastes [10]. Generally, a paste will behave like a yield stress fluid above a critical volume fraction of solid, φ_c, as the particles impede the flow by caging neighbouring particles [11]. However, colloidal suspensions can also form gels with a yield stress at a significantly lower volume fraction (φ_{solid}), as the attractive interparticle forces (i.e. Van der Waals forces) are able to form a weak network to resist flow.

A more commonly used phenomenological model for yield stress fluids is the Herschel-Bulkley model. It is often found to provide a good fit to experimental data for sam41ples such as gels, foams, and emulsions [12,13]. In this model, the shear stress is related to the shear rate by the following equation:

$$\sigma = \sigma_y + K\dot{\gamma}^{n}, \tag{3}$$

where K is the consistency index and n is the flow index (often quoted as simply "material parameters" in the literature).

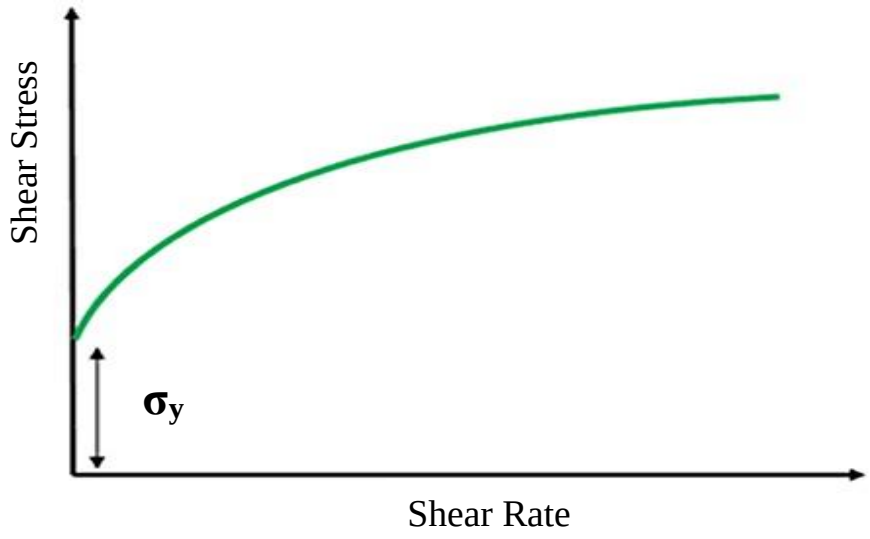

Figure 4: Flow curve of a fluid that obeys the Herschel-Bulkley model. Reproduced from [14].

An example of a yield stress fluid (YSF) that follows this behaviour closely is Carbopol, a polymer gel used extensively within the literature [15-17]. Carbopol suspensions in water are an example of a "*simple* yield stress fluid". The "*simple"* refers to the fact that the properties of these fluids are weakly dependent of their shear history. As a result, they show very reproducible flow behaviour, which makes them

reliable as model fluids for rheological studies. Implicitly, the Herschel-Bulkley model uses the assumption that σ_y is a material constant, but this is not the case for all yield stress fluids.

Despite the Herschel-Bulkley model being used widely in the field of rheology it is only applicable for a limited number of YSFs when $\sigma > \sigma_y$ under a steady external force and authors have seen a departure during the solid/liquid transition [18]. It has been observed that materials do not yield at a given σ_y but instead finite interval of stresses. To overcome this departure models have been proposed which describe the temporal evolution of a microstructural parameter, ā(t) as a function of stress and kinetic parameters.

$$\frac{d\bar{a}(t)}{dt} = F[\bar{a}(t), \sigma(t), C_1, C_2, \dots, C_m] , \qquad (4)$$

The parameters necessary for this model (C_1, …, C_m) are obtainable from macroscopic rheological tests such as flow ramps, SAOS/LAOS, creep/relaxation tests. As the applied stress is increased ā(t) varies smoothly from 1 (the volume is entirely in a solid state) to 0 (the sample volume has transitioned to a liquid state) [19]. This model is useful to a rheologist as with very little adjustment of parameters several types of test can be modelled with relative practical ease.

There has been some debate within the literature concerning whether the "yield stress" is a genuine material property. The 1985 paper "The Yield Stress Myth?" by Barnes and Walters argued that although the concept of a "yield stress" is useful it is an idealization. They performed a series of measurements concluding that no yield stress exists and instead that there exists an, albeit very large, viscosity [20]. They showed using PVA and Carbopol gels that the resultant flow curves fitted those of a "Cross fluid" (a Newtonian fluid whose viscosity depends on shear rate) and that no yield stress was required to explain the flow behaviour.

This behaviour was investigated further by authors such as Møller et al. [21] who performed similar experiments. They were able to recreate the results that Barnes and Walters observed, however they concluded that this low stress viscosity response is the result of artefacts in the shear experiment and what is observed instead is a transient shear band. They argue that below the yield stress, steady state flow is not possible. They also found that even when sheared below the yield stress for periods

exceeding 10^4 seconds the apparent viscosity would increase with no sign of reaching a constant value, providing further evidence that it is in a solid-like phase below the yield stress. Despite the debate, many examples of fluids reported in the literature appear to show a yield stress in practise. The yield stress therefore remains a useful property for practical characterisation of fluids.

1.3 Measuring the Yield stress

As the debate above shows, measurements of the yield stress can be challenging. In fact, there are a number of different definitions of the yield stress which use different measurement techniques; it has been observed that the method used can affect the measured value of the yield stress [22]. Perhaps the simplest definition of the yield stress ("the dynamic yield stress" relies on extrapolation of the Herschel-Bulkley model, fitted to data over a large range, to zero shear-rate [23]). However, this assumes a good fit to the data and is not practical for all types of yield stress fluid (eg thixotropic yield stress fluids, see section 1.4). Many methods have been employed by authors in order to determine the yield stress. This can include incline tests where the fluid is placed on a surface which is then inclined to a known angle; at a critical angle it will flow down the incline [24]. Despite this however rheologists treat the yield stress as a material constant that is "difficult to measure".

When shear rheology data are collected to determine the yield stress there are generally two accepted definitions of the yield stress: the static or dynamic yield stress. The static yield stress is observed as a stress overshoot that is seen in many real-world systems at low strains. It is understood to be the stress above which a fluid will transition from a solid to liquid state [22]. The overshoot is observed as a "bump" in the stress vs strain curve that initially rises but then falls back down. At higher strains there is a plateau: within this region the measured shear stress is the dynamic yield stress. The yield stress does not change with increase in shear strain between y_0 and y_c, as seen in figure 5. The dynamic yield is defined as the stress below which the fluid will change from a liquid to solid-like phase [22].

Divoux et al. posit that this overshoot is the result of an initially elastic like response to the increased strain. Eventually as the strain is increased further to the stress maximum the system shows elastic recoil and the stress decreases to a steady state fluid-like flow [25].

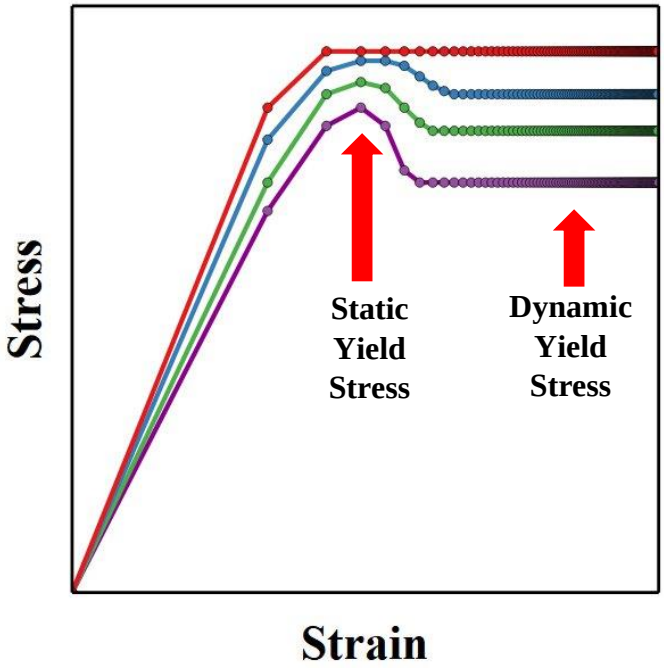

Figure 5: Schematic figure showing the effect of changing the shear rate on the stress overshoot. As we can see the shear rate has a significant effect on the stress overshoot. Recreated from [24]

1.4 Thixotropic Yield Stress Fluids

The stress at which a simple yield stress fluid starts to flow is a constant. This is the case for fluids like whipped cream or Carbopol. However, there are also a plethora of fluids like ketchup that show a strong dependence on their shear history, known as “thixotropic” yield stress fluids. This means that how these fluids are handled before experiments can affect their measured properties (such as σ_y). They exhibit a variety of phenomena such as stress plateaus, shear banding and viscosity bifurcation [1,11,26-30]. The flow curves of many thixotropic fluids show that at low shear rates the measured shear stress does not increase as expected by the Bingham or H-B models. Instead, what is observed is that the stress remains the same over a wide range of shear-rates, as seen in figure 6.

Consider a bottle of ketchup, a commonly experienced problem is that it is hard to get the ketchup to flow out of the bottle. Instinctively the solution to this problem is to apply a strong force to the bottle by shaking it. The ketchup viscosity decreases to allow a flow to occur. Often this results in too much ketchup landing on the plate as the viscosity has significantly decreased and it flows more easily than we anticipated. However, if the bottle of ketchup is then left to stand for a significant period of time it regains its former high viscosity; ketchup is a good example of a thixotropic fluid.

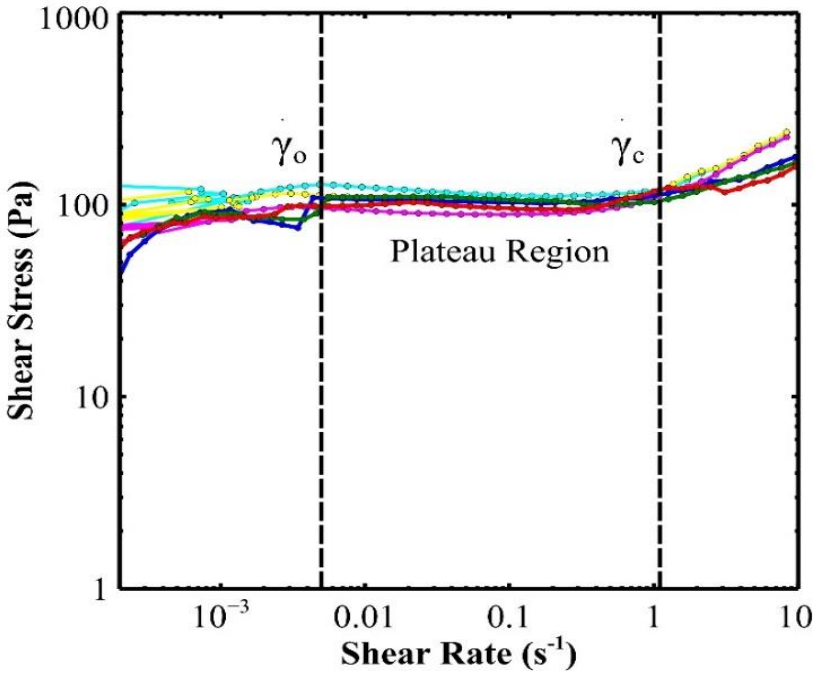

Figure 6: Shear ramp data recorded using a 55 wt% kaolin clay. Unlike carbopol a plateau is observed over two decades of shear rates. This behaviour is dependent on the material and is observed for many fluids over a multitude of shear rates. Shear ramps performed over 5 minutes, one minute per decade. Data was recorded as part of this work.

The stress observed in this plateau is useful in measuring the "apparent" yield stress, σ_y [1] but the magnitude of the plateau can be history dependent, meaning that the yield stress is a dynamic property for thixotropic fluids. This plateau region exists between two shear rates ($\dot{\gamma}_o$ and $\dot{\gamma}_c$). Above $\dot{\gamma}_c$, the fluid begins to show homogenous flow and behaviour similar to the H-B model is observed [26]. However, below $\dot{\gamma}_c$ the flow is inhomogenous, with different regions of the fluid experiencing different shear-rates, those that visibly flow with local shear rate ($\dot{\gamma}_c$), and regions where the shear is much lower or non-existent. This phenomenon is known as shear banding (see figure 7). At very low $\dot{\gamma}$ we observe a very thin liquid region, referred to as shear localisation. Typically this region is of the order of between 5 to 10 grain sizes in length, much smaller than observed for true shear bands [12,31]. It is also observed that there is a gradient that decreases to zero at the interface [32].

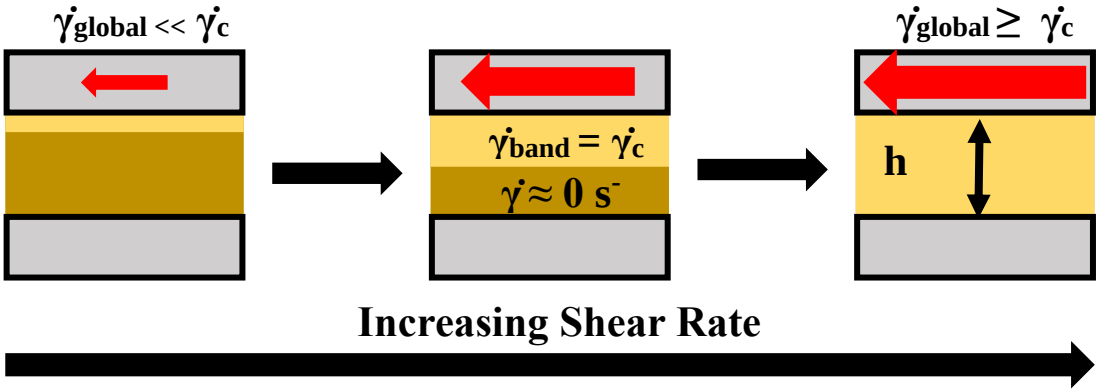

Figure 7: Schematic diagram of shear banding in complex fluids. At $\dot{\gamma}$ below $\dot{\gamma}_c$ flow, is restricted to a small region adjacent to the moving plate (the beige region) while the bulk of the sample remains stationary. As the global shear rate is increased the sheared region grows until it encompasses the sample bulk.

Thixotropy results from changes in the fluid microstructure induced by the flow which then recovers over time. When a significant force is applied to a thixotropic fluid it results in a breakdown of the particle microstructure. This allows the particles to move, relative to each other, more easily and so the viscosity decreases. Fluids in this state are often described as being "rejuvenated". The viscosity of these fluids is time dependent and when left to rest the microstructure may re-organise back into its initial state ("aging") and the viscosity increases [33]. Aging occurs because the particles move in order to find locations associated with a lower energy configuration [11]. When a thixotropic fluid is sheared its behaviour depends on a balance between these two competing processes. At low shear rates the aging process dominates, and the stress will increase with constant $\dot{\gamma}$ while at high shear rate ($\dot{\gamma} > \dot{\gamma}_c$) rejuvenation dominates and the stress decreases over time.

While the rate of breakup is controlled by the shear rate, the rate of restructuring is dependent on factors such as: material properties, volume fraction and temperature [1,11,34]. In the past authors have reported that if a sample is sheared for a sufficiently long time at fixed stress; what results is the evolution of the fluid either to complete stoppage or steady state flow as a function of the stress applied to the fluid when it is sheared. This behaviour has been demonstrated by Bonn et al using "avalanche" experiments [28,35]: a fluid is loaded onto a surface which is then inclined to angles that would cause shear deformation. The authors found that at small stresses the viscosity would increase until the material stops flowing. However, at larger stresses the viscosity would continuously decrease, and the flow would accelerate. Known as "viscosity bifurcation" [28] as the behaviour can drastically change

depending on whether the stress is just above or below the critical stress. They proposed a simple model to demonstrate the evolution [35]:

$$\frac{d\lambda}{dt} = \frac{1}{\tau} - \alpha\lambda\dot{\gamma} \tag{5}$$

Where λ is the degree of flocculation, τ the characteristic time of evolution and α is a system dependent constant. However, while the authors suggest that there are two states present in the equation there is only one available state in this model, which could not result in so called viscosity bifurcation. More recently, Younes et al [36] performed experiments which suggest that rheological hysteresis is the result of shear banding. Using micro-rheo-DPIV they concluded that during rheological measurements there are two distinct flow regions present. They concluded by suggesting that hysteresis is the result of several factors such as elasticity, unsteady loading and unloading as well as shear banding [36].

In experiments thixotropy makes reproducibility difficult, since measurements depend on the previous deformations applied to the sample. It is a common practice therefore to perform a "pre-shear" after loading the fluid for measurement. A pre-shear involves applying a very high shear rate (>>$\dot{\gamma}_c$) to the sample for a known period of time. This process strongly rejuvenates the microstructure such that samples possess a shear history that is dependent only on the pre-shear and subsequent experimental measurements [1]. However, one must still take great care in comparing results as small changes in the methodology can cause significant differences e.g. geometries or sample preparation.

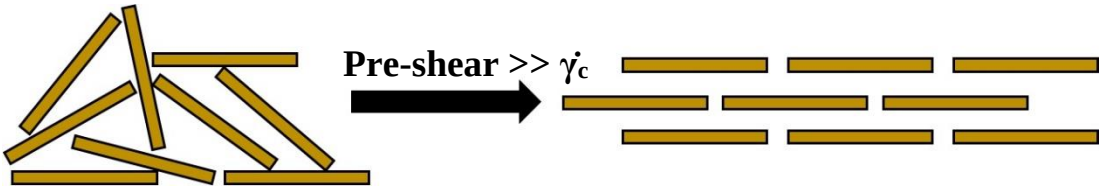

Figure 8: Highly idealised diagram showing the effect of pre-shearing a fluid. Initially the particles are arranged in a random "house of cards" like structure. After applying a strong shear to the fluid, the particles become much more ordered.

1.5 Oscillatory Shear

Viscoelastic materials exhibit both viscous and elastic behaviour. The viscoelastic behaviour of fluids can be measured rheologically through the use of Small Amplitude Oscillatory Shear (SAOS). When an oscillatory shear flow is applied, the strain and strain rate can be described as:

$$\gamma = \gamma_o \sin \omega t \, , \quad \dot{\gamma} = \omega \gamma_o \cos \omega \, t \, , \tag{6}$$

where γ_o is the amplitude and ω is the frequency. If the strain amplitude is kept to a low value a linear stress response is generated which can be written as:

$$\sigma = \sigma_o \sin (\omega t + \delta) \, , \tag{7}$$

where δ is the phase lag of the system [31]. A purely elastic solid would show no phase shift as the spring follows Hookean mechanics. If a material was purely a viscous fluid, i.e. a dashpot, the phase angle would be 90°. When a stress is applied to a system a solid will compress instantaneously. However, a liquid slows down the deformation which causes a phase shift [37]. Viscoelastic fluids show both solid and liquid behaviour and so the phase angle will be between 0 and 90°. Measuring this phase shift can provide information regarding structural properties of the material i.e. if the phase angle was 45° the material is equally as elastic as it is viscous.

In SAOS, material functions are defined to quantify the observed material behaviour. The elastic modulus (G'), also known as the storage modulus, provides information about the solid-like behaviour of a fluid and how effective it is at *storing* energy. The viscous modulus (G") gives information regarding the liquid-like behaviour of the fluid i.e. how effective it is at *losing* energy. G' is obtained from the in-phase stress amplitude while G" is related to the out-of-phase stress.

$$\sigma = G'(\omega) sin\omega t + G"(\omega) cos\omega t \, , \tag{8}$$

G' provides information about the structure of the system: when it is higher than G" the system can be considered elastic. At low strain the measured moduli typically will remain constant, commonly referred to as the linear regime. SAOS is a useful technique when working with thixotropic fluids because at low strains the fluid remains within the linear regime and the microstructure of the fluid is not changed

significantly. This allows one to measure changes to the elastic modulus as a function of waiting time, t_w. [38].

When the strain amplitude is increased to large values non-linear behaviour is observed and the elastic modulus will drastically decrease until eventually it and the viscous modulus cross one another. The assumed sinusoidal stress response breaks down and the moduli lose their straightforward mathematical interpretation as elastic and viscous components [39], as the microstructure is irreversibly altered. This technique is known as Large Amplitude Oscillatory Shear (LAOS) and although destructive this technique can provide useful information regarding the classification of the fluid [40].

Hyun et al proposed four distinct types of behaviour which can be observed in figure 9. Sim et al [41] proposed a network model to explain this behaviour in terms of creation and loss rates. A network is comprised of segments and junctions; segments are part of the microstructure while junctions are the points where interparticle interactions are localised. The creation, f(t), and loss, g(t), terms are expressed in terms of shear stress τ_{12} as follows:

$$f(t) = \exp\left(a|\tau_{12}(t)|\right), \tag{9}$$

$$g(t) = \exp\left(b|\tau_{12}(t)|\right), \tag{10}$$

Here a and b are model parameters defining the creation and loss rates. These model parameters assist in defining each set of behaviour:

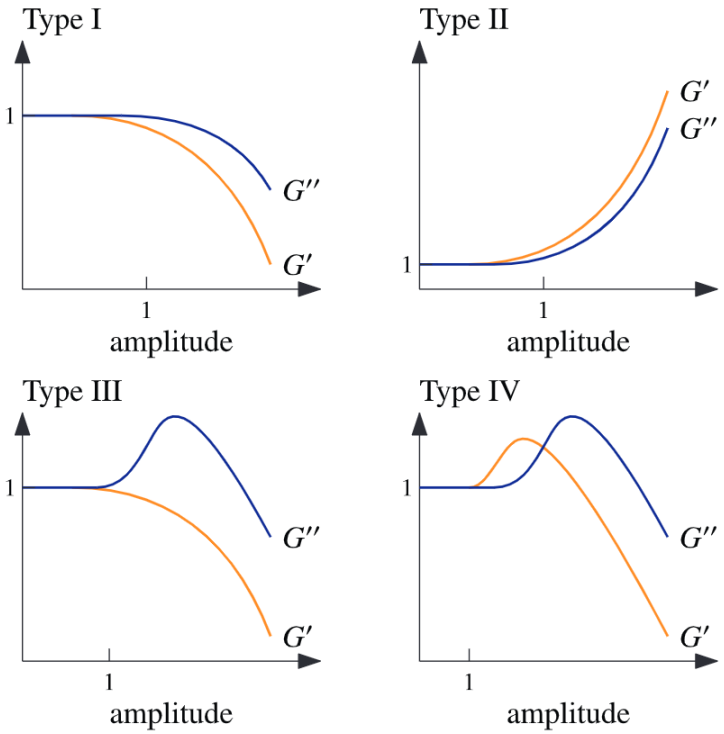

Figure 9: The four types of behaviour of G' and G" (normalised) during a LAOS amplitude sweep in the order Type I, strain thinning; Type II, strain hardening; Type III, weak strain overshoot and Type IV, strong strain overshoot. Obtained from [40].

T*ype I, strain thinning:* like shear thinning, is a very common rheological phenomena that arises as the randomly orientated particles of the microstructure align themselves in the direction of flow and viscosity decreases.

Type II, strain hardening: this could be the result of gelation or a shear induced network provided that there are strong secondary bonding effects. Both increase with strain amplitude suggesting that the creation rate is significantly larger than the loss rate.

Type III, weak strain overshoot: an "overshoot" with increasing amplitude is observed for G" but not for G'. When strain is applied, the structure resists the deformation up to a critical strain. Observed as G" increasing, at this point the structure is destroyed and the fluid flows resulting in G" decreasing. The mechanism here is a combination of the first two types, initially a weak microstructure is generated to resist the applied flow. However, at a critical strain this structure is destroyed. This is commonly observed for soft glassy materials such as emulsions, gels and pastes. Both parameters

are positive but a < b. Sim et al. postulate that this behaviour may come from the equilibrium between formation and destruction of junctions and at high strain this balance is shifted towards destruction.

Type IV, strong strain overshoot: it has been reported in the literature that there are cases where a strain overshoot with increasing amplitude is observed in both G' and G" before they both once again decrease at a critical strain. This results in the material strain hardening before they shear thin.

The linear and nonlinear behaviour of materials is of interest in several fields such as mechanics, electrical and thermal applications. The linear response is important for understanding the basic mechanisms that are responsible for material behaviours. The nonlinear response is important because it provides information that is useful for choosing materials to use in applications [42].

1.6 Rheometry

A common instrument used to measure flow characteristics such as viscosity and the elastic modulus is a rheometer. There are many commercially available models which fall into two categories, shear and extensional. Using a rheometer, the experimentalist will attempt to apply a homogenous strain to a fluid to gain information about its flow behaviour. This is more easily achieved using shear rheometers as there are several challenges to imposing a homogenous elongational shear [43].

A shear rheometer applies a torque, M, to the fluid which is used to calculate the resultant stress, and the resultant shear-rate is measured. For this calculation to be representative of the sample several assumptions need to satisfied [11]:

1. The material remains homogenous
2. Its volume remains constant
3. The sample occupies the geometry as assumed by theory, e.g. a cylinder in between parallel plates
4. The shear is uniform in certain directions (depending on geometry used)

Over the years, as the interests of the field of rheology have changed, several rheometer geometries have been developed to study simple shear of a wide range of fluids.

1.6.1 Rheometer Geometries

The most commonly used geometries are the Couette, parallel plate, and cone and plate geometries. However, there are also more specialist geometries available such as the vane and cup [44] and the annulus geometries [45].

The parallel plate geometry consists of two solid surfaces (a rotating "top" and fixed "bottom" plates) of radius, R, which are separated by a fluid sample of height, H. If the top plate is rotated with an angular velocity of Γ, a point at the sample/rotating plate surface a distance r from the centre will experience a speed equal to Γr [11]. The orientation of the geometry results in a large vertical velocity gradient where the linear speed decreases with distance from the rotating plate. In the absence of slip at the surface of the bottom plate, the speed is zero, see figure 10.

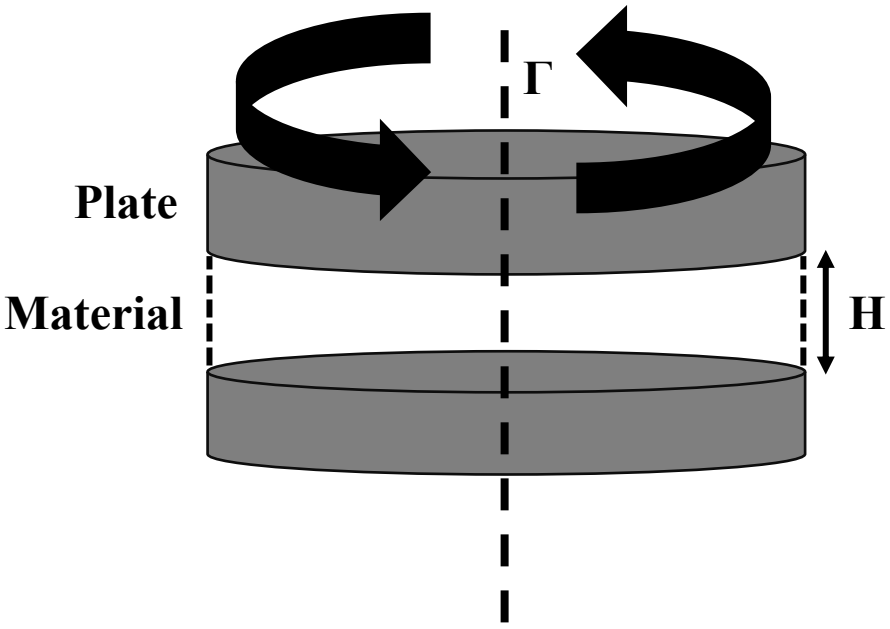

Figure 10: Diagram showing the parallel plate setup, recreated from [9].

There is also a smaller contributing horizontal velocity gradient: material close to the middle of the column remains stationary ($\dot{\gamma} = 0\ s^{-1}$) while the fluid at the edges experiences the maximum deformation rate ($\dot{\gamma} = \Gamma R/H$). As the shear rate is not uniform within the gap the shear stress, σ, is also unevenly distributed. To a first approximation it is assumed that the average shear rate is close to the maximum shear rate obtained at the sample edge [11].

$$\dot{\gamma}_R = \frac{\Gamma R}{H}\ , \tag{11}$$

This assumption implies that the shear stress is constant across the gap in the z direction which can be obtained from the applied torque [9]:

$$\sigma = \frac{3M}{2\pi R^3} \ , \tag{12}$$

To ensure the even distribution of shear stress within the sample we must take the aspect ratio into account. Throughout this thesis we shall define the aspect ratio as being the initial radius R_o, divided by the initial gap height, h_o. It is assumed that if the sample is adequately thin the bulk of the material will undergo a flow that is similar to the global shear rate at every location simultaneously [17]. Parallel plates result in the normal force being evenly distributed over the sample [46]; this makes them ideal for use in adhesion and squeeze flow experiments (see discussion in Section 1.8).

The cone and plate geometry is similar to the parallel plate geometry however the top plate is a cone with a very shallow angle, θ. This conical shape is designed to compensate for the radial dependence of the shear-rate observed in parallel plates. The gap height in these geometries linearly varies with distance ($H = r\theta$) and applying this to equation 7 we obtain a shear rate that is now independent of r, $\dot{\gamma} = \Gamma/\theta$. Cone and plate geometries are also useful for high density fluids and in principle ensure a uniform shear stress throughout the sample [11].

Previously we assumed that the flow between the plates is both uniform and homogenous which is, especially in the case of yield stress fluids, not always the case. Localised strains can result in the geometry used having an effect on the measurements made, meaning that it can be hard to compare measurements taken using different geometries. This effect has been observed in the literature reported as shear stresses that differ by an order of magnitude [27]. Although Rheology is a useful tool which has been well characterised in the case of standard rheometric flows it can still be difficult for laboratory experiments to be compared to real-world observations, such as in the concrete industry [27].

1.7 The Stress Tensor

The stress at any point within a fluid requires nine components to be specified. These components must be defined by both the direction they act as well as the orientation of the surface that it is acting on. If we refer to figure 11 the first index tells us which direction the component acts and the second index shows the orientation of the surface which it is acting upon [47]. Cauchy's Law states that a stress tensor exists that maps the normal force to a surface to a vector, T, on that surface [48].

$$\sigma = [T_1 \ T_2 \ T_3] = \begin{bmatrix} \sigma_{11} & \sigma_{12} & \sigma_{13} \\ \sigma_{21} & \sigma_{22} & \sigma_{23} \\ \sigma_{31} & \sigma_{32} & \sigma_{33} \end{bmatrix}, \tag{13}$$

The σ_{11}, σ_{22} and σ_{33} components correspond to normal stresses acting upon their assigned surfaces. The off-diagonal components (eg σ_{12}, σ_{23}, σ_{13}) characterise the shear stresses.

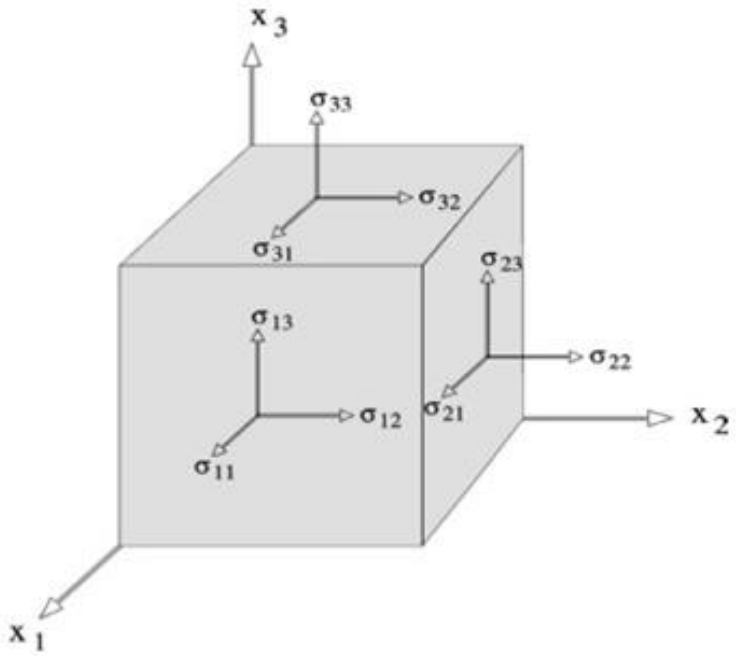

Figure 11: Schematic representation of the stresses that act upon a body. Each much be defined to allow for correct assignment of the overall stress of the system [47].

During a shear flow the symmetry of the system reduces the number of components that must be recorded from nine to five [49].

$$\sigma = \begin{bmatrix} \sigma_{11} & \sigma_{12} & 0 \\ \sigma_{21} & \sigma_{22} & 0 \\ 0 & 0 & \sigma_{33} \end{bmatrix}, \tag{14}$$

This is further reduced from five coordinates to four as $\sigma_{12} = \sigma_{21}$.

During an elongational flow there are only three non-zero values within the matrix. This simplification is the result of symmetry in the system as the sample is strained. There are 180 ^{o} of symmetry around each coordinate axes.

$$\sigma = \begin{bmatrix} \sigma_{11} & 0 & 0 \\ 0 & \sigma_{22} & 0 \\ 0 & 0 & \sigma_{33} \end{bmatrix}, \tag{15}$$

The balance of these components will dictate how the fluid elongates e.g. if the greatest contribution is the σ_{33} then it will compress or elongate in the X_3 direction [50]. Real world flows are neither purely shear or purely extensional: they can be made up of a weighted combination of these two types of deformation.

1.8 The Strain Tensor

Similarly, the strain is a tensor. If a material deforms so that it undergoes a pure stretch, i.e. length changes with no change in angle between them, similar to an ideal extension, then the resultant tensor will take the form:

$$F = \begin{bmatrix} \lambda_1 & 0 & 0 \\ 0 & \lambda_2 & 0 \\ 0 & 0 & \lambda_3 \end{bmatrix}, \tag{16}$$

where F is the deformation gradient and λ is the deformation ($l/l_{initial}$) where l is the length of the material. For any deformation there are always three directions where the material will undergo a pure stretch, these are often referred to as the principal stretches. In general, elements that are off axes will stretch and rotate relative to one another.

A pure shear scenario will present in a similar form to the stress tensor in shear due to symmetry

$$F = \begin{bmatrix} 1 & k & 0 \\ k & 1 & 0 \\ 0 & 0 & 1 \end{bmatrix}, \tag{17}$$

where $k = \tan\theta$. In this situation as the material is deformed the object is stretched by an amount $1 + k$. At the same time along another direction the material will contract by $1 – k$. A deformation that results in both a shear and elongation can be characterised by equation 18.

$$F = \begin{bmatrix} cos\theta & -sin\theta & 0 \\ sin\theta & cos\theta & 0 \\ 0 & 0 & 1 \end{bmatrix} \begin{bmatrix} sec\theta & 0 & 0 \\ 0 & sec\theta & 0 \\ 0 & 0 & 1 \end{bmatrix}, \quad (18)$$

where secθ is $\sqrt{(1 + k^2)}$ [49].

1.9 Extensional Rheometry

Rheometry can also be performed by sandwiching fluid between two parallel plates and then altering the vertical distance between them. This can be done by moving the plates together ("squeeze flow") [51] or moving them apart ("adhesion testing"). Squeeze flow tests are useful for understanding the properties of fluids during industrial scenarios such as hot plate welding [52] and composite material joining [53]. Adhesion tests are often used to test the tensile strength of joints or adhesive layers [54].

1.9.1 Adhesion tests

In an adhesion test a fluid is sandwiched between two parallel plates at a distance h apart. The top plate is then moved upwards (either at constant speed or at an exponential strain rate). Traction forces on the plates deform the fluid, due to the requirement that the fluid has a constant volume. At a critical gap height, h_c, the fluid filament separates into two symmetrical pieces [54].

An adhesion test measures the force, F, required to separate the plates when a fluid is adhered between them. The work of adhesion (W_{Adh}) necessary for complete separation of the plates can be quantified from experimental force-distance curves:

$$W_{Adh} = \int_{h_o}^{h_c} F dh\,, \quad (20)$$

where h_0 is the initial plate separation and h_c is the final plate separation. The work of adhesion is a combination of three major energy contributions: the flow of material leading to either viscous or plastic deformation (W_v), the surface energy due to the change of interfacial area (W_s) and the work due to gravity as the sample moves upwards (W_g) [53]. When the fluid is a simple yield stress fluid Barral et al. [17] showed that in the limit of small velocities $W_{adhesion}$ tends to a constant value which is independent of the plate velocity. Under these conditions, Derks et al [55] have shown

that the force is proportional to the yield stress of the fluid. Integrating the force distance curve was shown to result in a $W_{Adh:}$

$$W_{Adh} \approx \frac{4\pi R_o^3 \sigma_y}{9}, \quad (21)$$

this means that to first order, the W_{Adh} is approximately independent of the initial plate spacing.

1.9.2 Hencky Strain

The strain in a system under tensile stress can be described by the Hencky Strain (ε) which has often been used to describe large strains (>1%). This is sometimes called the logarithmic or "true" strain of a system and can be calculated as:

$$\varepsilon = ln\left(\frac{l}{l_o}\right), \quad (22)$$

where l_0 is the initial dimension of the sample and l is the dimension after application of the strain.

1.9.3 Necking

When materials are subjected to an extensional strain, they can undergo a process known as necking. This has been well studied in metals in which a standard test is to stretch a rod of material. Prior to breakup of the rod the middle begins to narrow accumulating most of the overall strain applied. This section of the rod thins and lengthens dramatically compared to the bulk of the rod. The fracture of materials is often described as being in one of two classes: brittle or ductile. In the brittle case the sample responds elastically with little or no plastic deformation prior to breakup. In ductile systems there is a distinct non-linear regime present before final fracture occurs. Plastic deformation in a ductile system results in necking behaviour [56]. As a result of these differences, brittle materials fail suddenly whilst ductile materials yield smoothly.

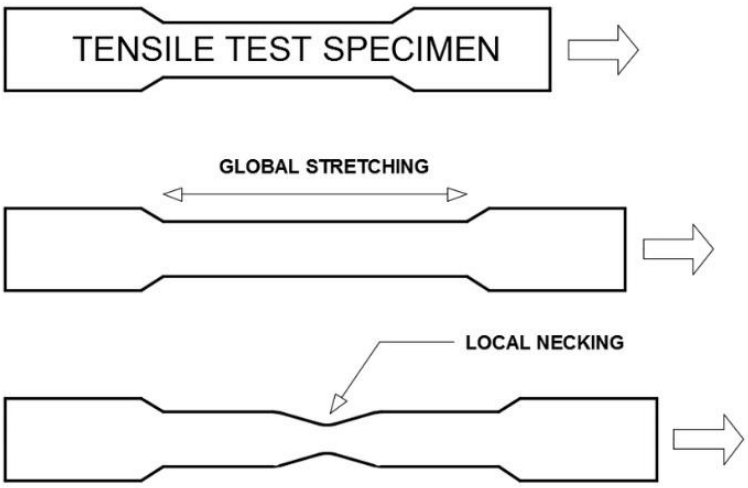

Figure 12: A schematic diagram of what happens when a load, P, is applied to a metal specimen. Initially there may be some elasticity in the sample however, over time localised plastic deformation develops, typically in the centre and most of the deformation occurs in this small region rather than the entire sample, resulting in necking [57].

The problem of necking in materials has been considered for a long time especially in the context of metals. The onset of necking can be related to the Considère Criterion [58]. The criterion describes the process of necking where the strain hardening coefficient, h, drops below the flow stress, σ, at a given strain rate, $\dot{\varepsilon}$, and describes plastic instabilities [59].

$$h \equiv \frac{\delta\sigma}{\delta\varepsilon}\int \dot{\varepsilon} \ , \tag{23}$$

Many glassy materials such as dense colloids, foams and emulsions have also been shown to exhibit both brittle and ductile behaviour [60]. Under small deformations they show solid-like elastic behaviour. Some samples will then fracture in a brittle like manner, however, others exhibit large deformations, yielding plastically much like we see in fig. 12.

A number of theoretical studies have attempted to model the break-up behaviour of glassy fluids in extensional rheometry [61,62]. As samples age they are predicted to display a more brittle break-up behaviour. Brittle break-up behaviour also increases with increasing extensional strain-rate.

1.10 Slip

The preceding discussions have assumed that the velocity of fluid next to the solid surface matches that of the plates (no slip). However, slip is a common feature and problem associated with many rheological measurements, particularly those involving a concentrated suspension of particles. When simple shear is applied to a paste one might expect the particles close to the bottom stationary surface to remain stationary while the particles near the top surface move with the top plate. In between one would observe a linear shear profile as would be observed in a Newtonian liquid. However, experiments carried out by Kaylon on a particle paste showed that the fluid may slip at the boundaries [31] (see figure 13B). The fluid moves along the surface in a "plug-like" fashion. Typically for suspensions "apparent slip" [64] is observed, which occurs due to a particle depletion mechanism at the walls: if particles are homogenously distributed in a liquid, none can be centred at a distance from the wall shorter than their characteristic length [1]. As such the mean concentration diminishes on approach to the wall and there is instead a layer of the interstitial liquid [26] present. When a stress is applied this depletion leads to a decrease in local viscosity and the shear rate increases. This natural migration of particles may also be assisted by flow causing particles to move to locations experiencing a low shear which results in a lubricating layer close to the wall faces that facilitates the slip, ultimately altering the shear behaviour [1].

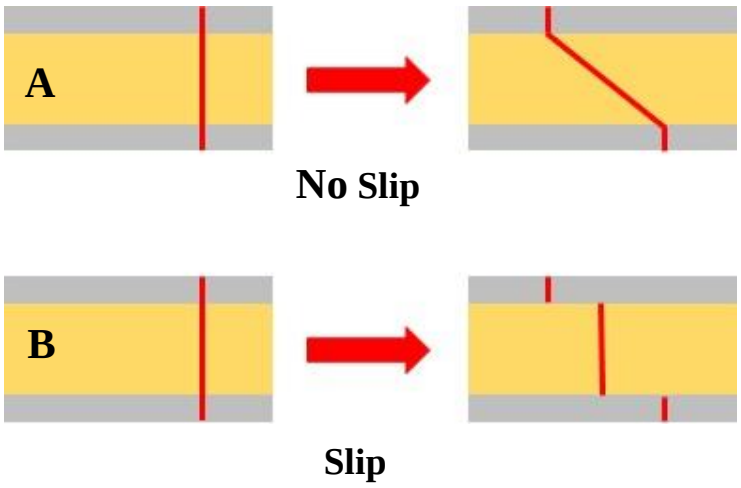

Figure 13: In Kaylon's work a line was drawn on the edge of the fluid before simple shear was applied. If there was no slip then case A would be observed as the fluid is made to flow. However, Kaylon instead observed case B where the fluid moved as a "plug" across the surface of the plate [31].

This slip in a localised region of the paste adjacent to the plates, should not be confused with shear banding. Shear banding is a necessary transition from solid to liquid-like behaviour for thixotropic fluids that results in two regions of the fluid flowing with very different shear-rates. High solid φ dispersions are particularly prone to slip at surfaces which can have a detrimental effect on the measuring of flow properties [63]. Wall slip reduces the adhesion of a fluid to the wall allowing it to move at stresses below that required to cause sample yield.

The most common method of slip mitigation is increasing the roughness of solid surfaces. This can be achieved in several different ways such as sandblasting or the attachment of waterproof sandpaper [63]. The influence of slip is generally considered to be negligible for attractive systems (i.e. those that form aggregates such as clays) when the inclusion size is several orders of magnitude larger than the average size of the elements [1,65]. This is due to the disruption of the lubricating layer, as the topography is no longer flat [63]. Particles are more likely to be in contact with the surface and so when sheared they catch on the ridges and may interlock [66], requiring more force to escape than if a smooth surface was used.

Although slip impacts rheological measurements, there are many real-world examples of its benefits. In natural and biological processes, such as the transport of solid foods; during consumption and waste removal [67] or the movement of gastropods such as slugs and snails [68]. Slip is also useful in civic and industrial engineering in applications such as sewage treatment, paints and pharmaceuticals [63] or the transport of oil and coal [69].

1.11 Clays

The focus of this project is on the rheology of clay. There are many types of clay with different properties e.g bentonite, smectite or chlorite. A clay is defined as being made up of a stack of tetrahedral silicate and octahedral aluminate layers in different ratios [70]. Most of the experimental work carried out in this thesis will focus on the use of two clays: kaolin and laponite. Kaolin particles are made up of a single silicate layer on top of an aluminate layer, whereas laponite particles have a single aluminate layer sandwiched between two silicates. Hydrogen bonding occurs between

the particles, adding some stability to the network [71]. These bonds also play a key role in the absorption of water in between clay particles where they become trapped.

1.11.1 Kaolin

Kaolin (also known as china clay) is a yellowish white mineral that is found all over the world. Kaolin has several industrial uses due to its low conducivity of heat and electricity such as in paint and plastic fillers or paper coatings [72]. It is commonly studied within the literature because it is relatively pure (consisting mainly of kaolinite), is readily available (8.5 million tons were produced in the US alone in 1999) [73], and is non hazardous. These factors as well as the wide range of literature on kaolin were motivators for choosing kaolin for use in this thesis.

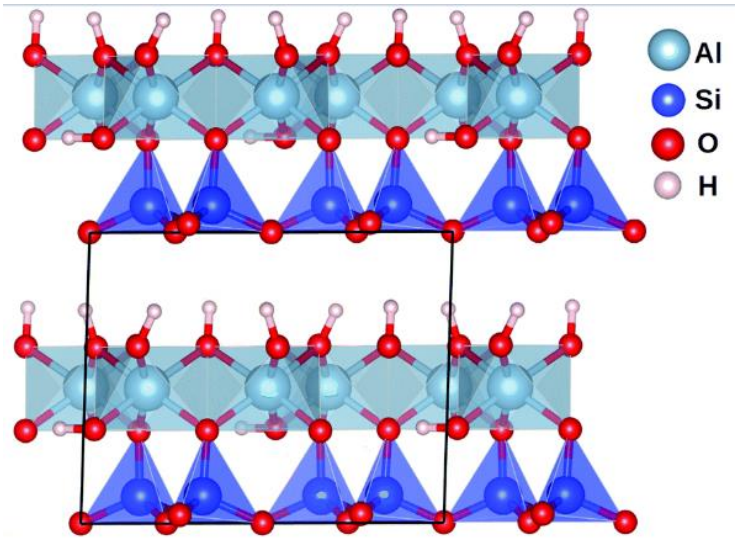

Figure 14: Structure of kaolin particles, the black box indicates the unit cell of the crystal [63]. Hydrogen bonding occurs between the OH group of the aluminate layer and the O atoms of the silicate layer.

Figure 15 shows an SEM image of kaolin. The sample consists of micron scale platelets with an aspect ratio of approximately 10 (face to side) [74]. These platelets have negatively charged faces and positively charged sides [75] and arrange themselves into a “house of cards” type structure. The attraction between surface charges of the platelets can increase the yield stress quite significantly. It is possible to tune the yield stress by changing the pH of the suspension. As the conditions become more alkaline, the yield stress decreases due to screened charges. However, kaolin will remain chemically inert over a wide range of acidic and alkaline conditions [72].

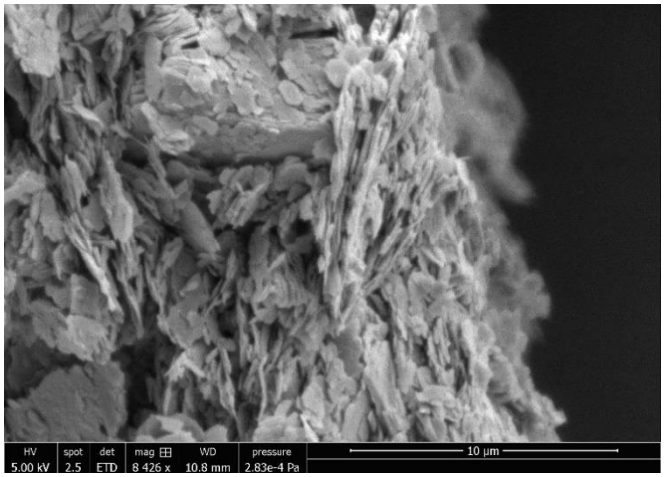

Figure 15: SEM image of an aggregate of kaolin particles in random orientations. Scale bar is 10 µm. Image was taken as part of this work.

1.11.2 Laponite

Unlike most clays, laponite is not a natural formation. It is actually a synthetic clay with a disk-like structure similar to kaolin. Individual particles of laponite are typically much smaller than other clays being approximately 1 nm thick and between 20 and 200 nm wide. These particles have negatively charged faces and positively charged sides [76]. The main advantage of laponite is that monodisperse particles can be produced in extremely pure concentrations, making it an excellent model system for experimentation. Laponite forms a soft, transparent gel at very low solid concentrations (~ 3 wt%) and has many applications such as emulsifying, suspending or plasticizing agents [77].

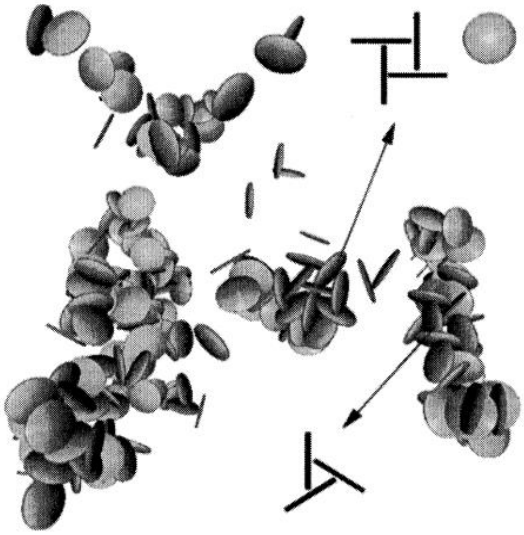

Figure 16: House of Cards configuration of laponite disks arranged into three and four membered rings, obtained from [78].

Due to the anisotropic platelet shape and face to rim interactions, laponite forms complicated structures. It often forms a “house of cards” structure, similar to kaolin (see figure 16), that is held together by so called “T bonds” [78]. These T bonds consist of edge to face interactions that can propagate throughout the structure.

Figure 17: A laponite stock gel that has been perturbed and then left to age. Left image was taken immediately after perturbation while right image was taken 24 hours after perturbation. The left image shows that when initially disturbed the gel can flow much like a liquid, however, when left to stand we observe that the fluid will not flow under the action of gravity alone (right).

Laponite is also noteworthy because of its dramatic thixotropic behaviour. When allowed to rest for a long time the resultant gel will remain rigid and the container can actually be inverted without flow occuring. However, when shaken vigorously the Laponite gel flows easily with no apparent yield stress. The gelation time is dependent on factors such as the initial concentration and pH. In some cases, authors have reported that very low concentration laponite suspensions (<1wt%) can take months to show discernible viscosity changes [78] while a 3.5 wt% suspension can show a three-order increase in viscosity change in approximately 10 minutes [79,80]. This tunable behaviour makes laponite ideal for studying aging dynamics, which will be discussed in Chapter Six.

1.12 The Industrial Problem and Motivations

Measuring the adhesive properties of fluids is of great interest to many commercial sectors such as the oil industry. Particle agglomerations frequently build-up on the drill bit during operation, in a process known as “accretion” [81]. As the drill penetrates the ground under high pressure, a build-up of soil and clay begins to accumulate onto the drill head. This accretion results in the decreased efficiency of drilling until eventually it cannot continue cutting and will slip across the rock. The drill must be brought back up the well (which can be several kilometres) for cleaning

by hand, increasing costs. It has been estimated that the problem of accretion equates to around 20% of total drilling costs [81]. A method of reducing this problem is to pump oil or water-based drilling muds (OBMs and WBMs) down the hole during drilling [83] to lubricate the interface and inhibit surface accretion.

Figure 18: A drill assembly that has been brought back to the surface. As soil and clay becomes adhered to surface it reduces the effectiveness of the drill until it can no longer penetrate the surrounding rock

Due to this and many other industrial problems, there has been a great deal of work done to understand the processes with which soft glassy materials break up using different experimental geometries. The aim of this project was to give insights into the factors affecting adhesion of clays to surfaces. Using kaolin we studied the influence of slip and yield. We aim to characterise the behaviour of this fluid and relate its adhesive properties to simple shear flow observations. We wish to understand what happens to a clay in the initial stages of shear flow and adhesion tests. Slip is an important behaviour that most authors work tirelessly to avoid despite its prevalence in real systems. In our study we used surfaces that allowed limited slip in order to understand how this influences measurements. Whilst kaolin is used for the majority of this thesis, the role of thixotropy is another key property of some clays. We therefore also used Laponite gels to understand its effect on the break-up of clays in an adhesion.

Chapter 2. Method Development and Shear Rheology of Kaolin

2.1 Aims of This Project

The main aims of this chapter were to characterise the rheological properties of Kaolin clays of different concentrations such as the yield stress and shear moduli of the fluids. After these properties were determined we observed the effect of processes such as slip and aging and determine the influences these had on adhesion tests on surfaces of different roughness. In this chapter we outline preliminary investigations to prepare and characterise kaolin clays to better understand their adhesive characters.

2.2 Characterisation of Kaolin Particles

Kaolin clay has been the subject of research for many years due to its properties as a yield stress fluid as well as its many applications such as in building materials, paper coatings and fluid thickeners [83]. It is one of the least reactive clays available and is supplied with high purity, making it ideal as a specimen for use in physical experiments [23]. The powdered kaolin used throughout this manuscript was purchased in bulk from Scarva Pottery Supplies (RM1018 Grolleg).

First, we wished to characterise the kaolin on the scale of individual agglomerates and platelets. An SEM was used to take photographs of dried kaolin powder taken directly from the bulk, see below. As we can see from fig. 19, we have agglomerates of particles that are approximately 50 μm and individual platelets with an average size of 5 μm. We used these measurements to inform how to prepare the Perspex surfaces for shear and extensional rheology experiments.

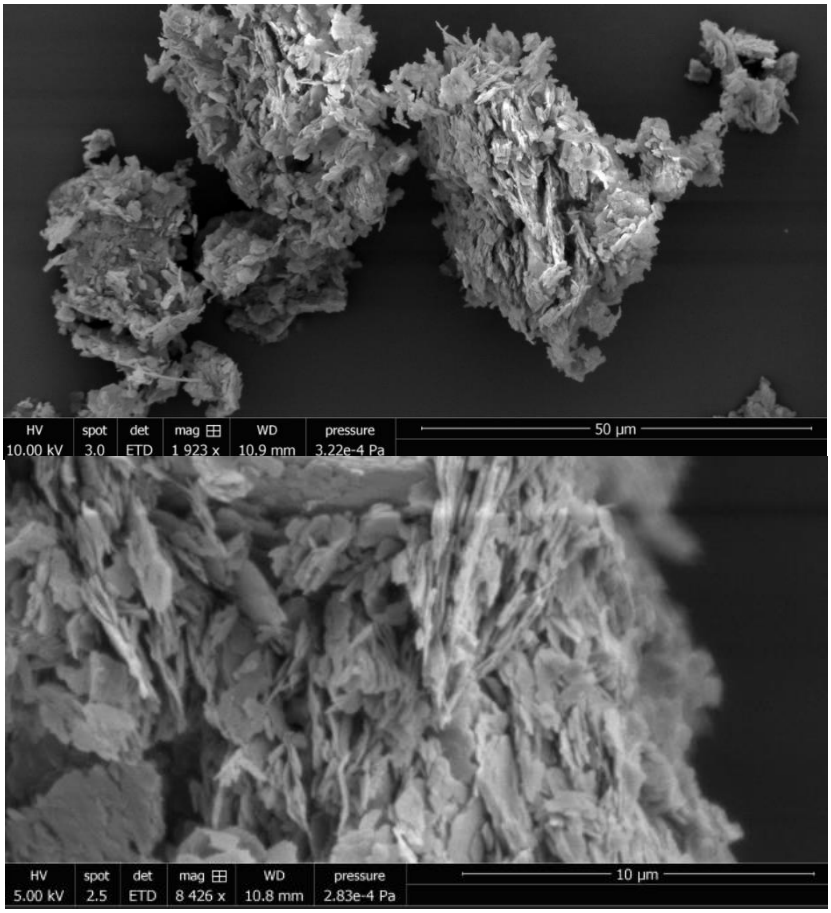

Figure 19: SEM images of the kaolin agglomerates (top). Also visualised are the individual platelets (bottom). From the images we can see the agglomerates are approximately 50 µm wide while individual platelets are approximately 2 µm wide

We also attempted to confirm whether any smaller platelets were present in the kaolin stock using a Zetasizer Dynamic Light Scattering (DLS) instrument, however we found that this was not completely straightforward. A small amount of kaolin powder was suspended in both water and methanol for comparison (methanol does not contain ions, resulting in a smaller double layer). However, we observe only one peak, which is detected between 100 and 600 nm. We do not observe peaks in the micrometre range as measured in the SEM images shown in fig. 19. We found upon inspection of the sample cells that a large proportion of the Kaolin rapidly sediments out (even after re-dispersal) in both solvents. It may be the case that when dispersed at low concentration most particles are too dense to remain suspended. Whilst these measurements do not reflect the full size distribution of the Kaolin we saw little evidence of very small particles below ~ 100nm which should be easily captured by DLS.

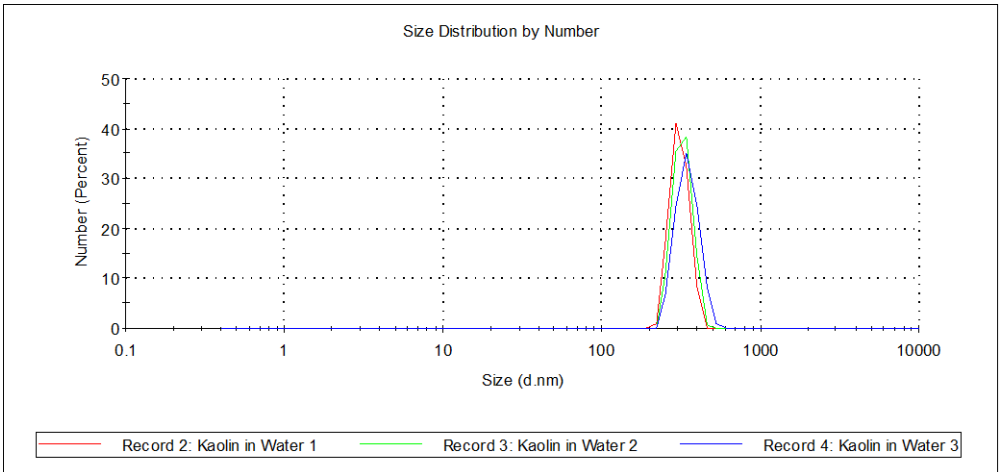

Figure 20: Zetasizer data for the kaolin particles suspended in water.

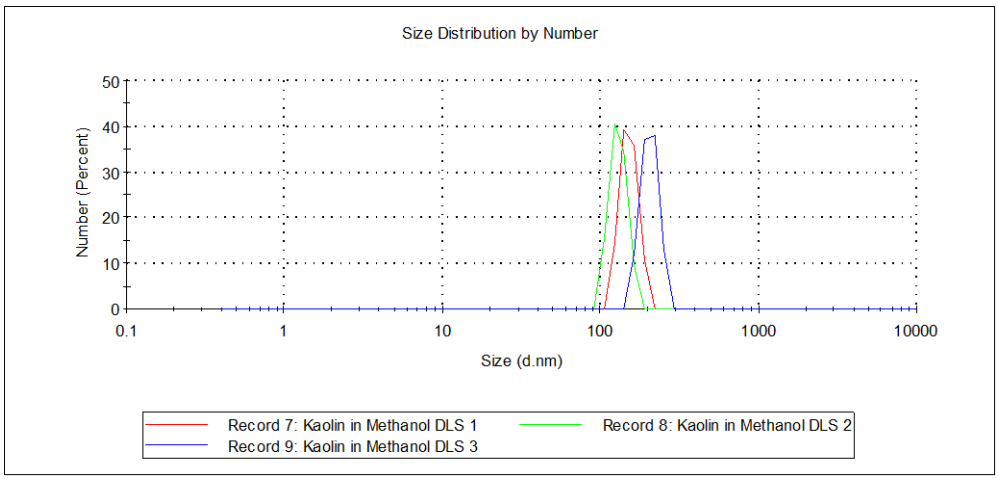

Figure 21: Zetasizer data for the kaolin particles suspended in methanol.

2.3 Method Development

2.3.1 Sample Preparation

Early tests indicated that creating reproducible samples of kaolin at well defined concentration was quite challenging. For this project to be successful it was a priority to develop a consistent method of mixing the clay for use in shear rheology experiments. Clays were prepared with weight percentage between 45 and 65 wt% using masses of powdered kaolin clay (RM1018 Grolleg, Scarva). The concentration range was chosen after undertaking some initial experiments using a large range of concentrations. We found that clays with a solid content below 45 wt% began to separate quickly under gravity. Clays above 65 wt% were found to be too rigid to measure with the Kinexus Pro Rheometer. During compression the instrument would exceed the safe working limit of its internal normal force sensor.

To ensure the correct wt% of clay before preparation the kaolin powder was dried using a vacuum oven overnight at 120^{o}C to remove any residual moisture. The kaolin was allowed to cool under a fume hood before homogenisation. During this time an excess of ELGA high purity deionised water was thermally degassed. Then at room temperature, known masses of kaolin and water were combined in the bowl of an MLITER stand mixer for 5 minutes to make ~1 kg stock samples. After this initial 5 minutes the clay was then gathered in the centre of the bowl to ensure that any remaining powdered kaolin was added to the mixture and then homogenised for an additional minute.

Figure 22: The MLITER stand mixer and MGB 120 meat grinder used throughout the work completed in this manuscript.

This method proved to be effective for making low concentration stocks. However, when making denser fluids it proved to be more difficult to fully homogenise, and regions of unmixed clay became more prevalent. We also observed that some rheology experiments performed using these standard mixed samples were inconsistent. This may suggest that the fluid had not been thoroughly mixed during this process. There may be concentration gradients in the stocks that caused these inconsistencies.

Figure 23: A 50 wt% kaolin clay suspension after being mixed.

To help remedy this problem an MGB 120 electric grinder was introduced to the protocol. The stand mixer was used to perform a “coarse” mixing which was then followed by the grinder to provide the addition of a “fine” mixing the kaolin was ground and extruded through the nozzle via multiple openings into a more consistent paste. This two-stage process of mixing the clay was used when mixing every concentration used in this thesis to ensure that the specimens were all in a similar comparable state. One drawback of this method of making the clay was that as the mixture was transferred from each piece of equipment, particularly the electric grinder, there was a small amount left adhered to its surface. To mitigate this problem a palette knife was used to scrape as much of the remaining residue from the machinery as possible.

After being processed in the grinder the kaolin was transferred to caulking gun tubes for long term storage in a fridge (~a month). An experiment was carried out to observe whether the mass would change over time due to evaporation after extended storage. A tube was filled with a known mass of kaolin and consistently weighed over a period of two months. This experiment showed that there was a negligible loss of water during this period.

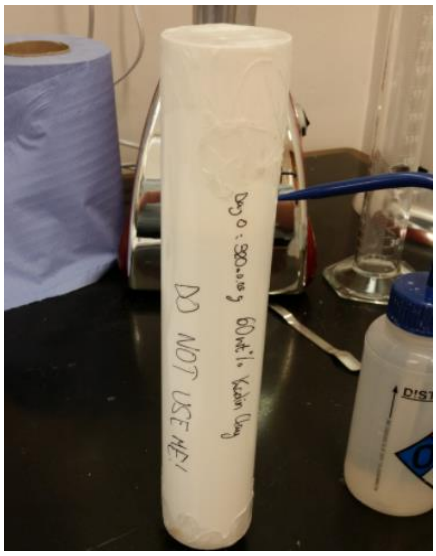

Figure 24: Caulking gun tube used for long term storage of kaolin in the fridge.

There were also concerns that eventually a concentration gradient would become established within a stock tube under gravity. To establish if this was the case a caulking tube was cut into rings and samples taken from different points. These were then dried to constant mass in a vacuum oven overnight (120 ^{o}C). This was completed for examples of each concentration multiple times and showed that while there may be a small change (~0.5 wt%) it remains consistent over the volume of the clay stock in the fridge.

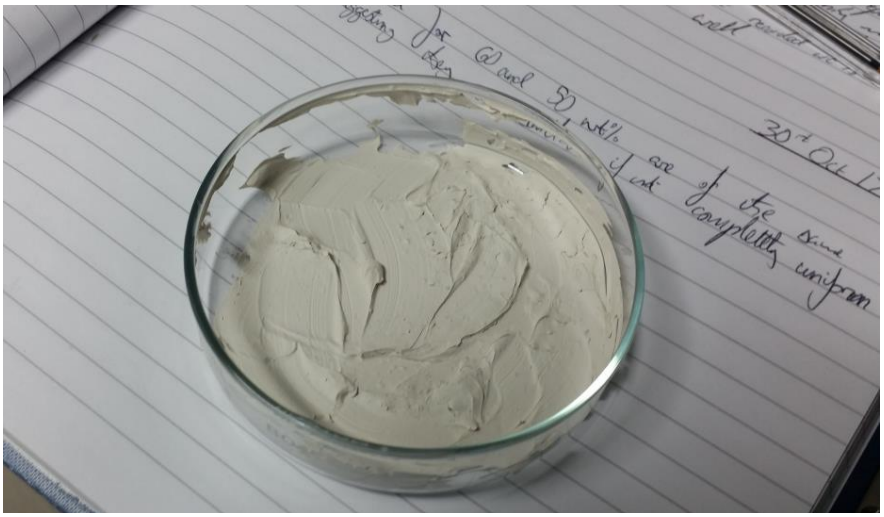

Figure 25: A sample of kaolin clay after it has been dried to continuous mass in the vacuum oven.

When rheology experiments were carried out samples were extruded into 50 ml sample tubes for easier access. A problem arose during this extrusion as air often became entrained within the sample. Air bubbles could modify the rheology of the fluid. An effective method of doing this was found to be the use of a vortex mixer as stated by Rabideau et al [84]. An IKA vortex mixer was set up with a retort stand and left to shake the clay samples overnight before shear rheology experiments were performed.

2.3.2 Controlling the moisture content of samples

The standard experimental covers supplied with the Kinexus rheometer resulted in the clay losing a significant amount of moisture during the timescale of an experiment. This was apparent from the volume of the clay which was observed to shrink. Tests were completed by recording the drying of a sample of kaolin on an analytical balance over the time scale of an experiment (approximately 20 minutes). It was found that the mass loss due to evaporation was as much as 5%.

The solution to this problem was to increase the local humidity under the covers. We needed to ensure that the mass loss of the clay was not significant on the timescale of an experiment. A pair of custom covers were made from Perspex so that we would be able to visualise the clay during pull off experiments from a side view without removing the covers. These covers had water reservoirs machined into them and soaked sponges were also attached to the inside of the covers to support them. This resulted in a stable humidity of ~90%. Experiments with these covers showed that the mass loss over 20 minutes was <0.5%. This showed that the covers were effective at mitigating the moisture loss of the kaolin. During subsequent experiments these covers were only removed during the sample loading and trim steps of the experiments.

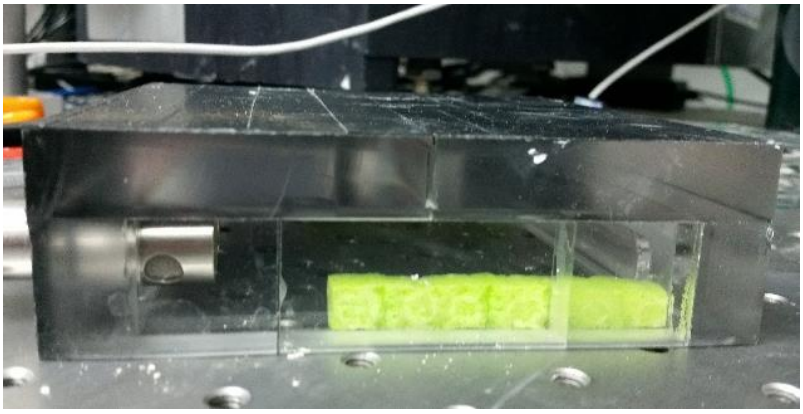

Figure 26: The custom-built covers used throughout this manuscript. The green strip is a sponge that was wet to boost the internal humidity. These covers were also wrapped in black tape to control the amount of light within for video capture.

2.3.3 Camera and Lighting Setup

The rheometer was fitted with a custom cartridge that held a Perspex block. This cartridge was hollow to allow for observation of the sample from below. For the adhesion tests two Point Grey Flea 3 cameras were set up, one viewing from the side, lit using a SOLIS-C LED to give a silhouette, the other from below lit by total internal reflection of LED strips attached to the sides of the plate.

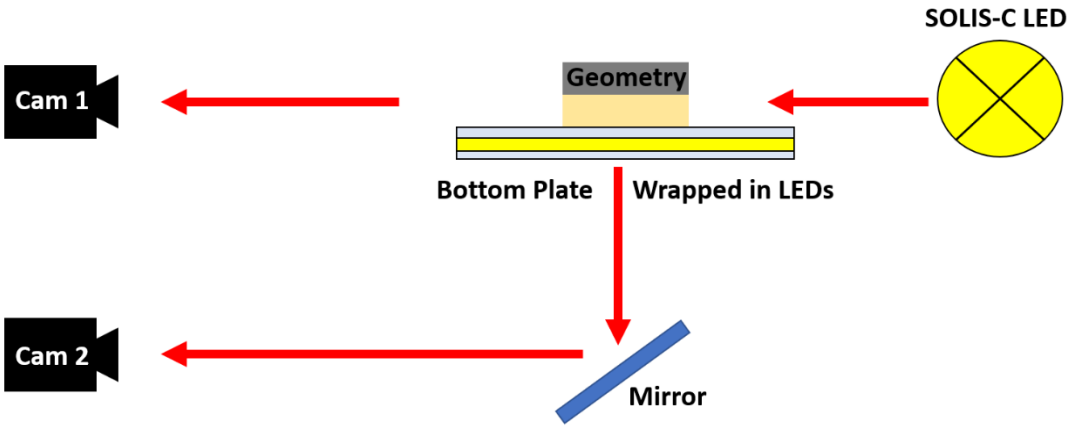

Figure 27: Schematic diagram of the experimental setup.

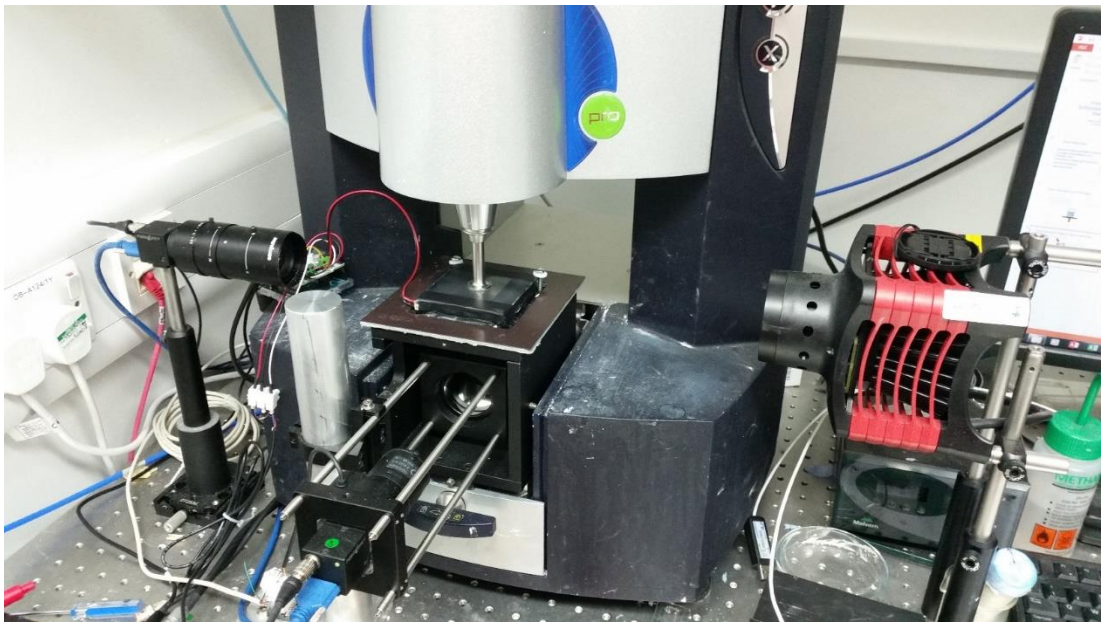

Figure 28: Photograph of the experimental set up showing the positions of the cameras and the LED lighting. Lighting for bottom camera is wrapped around the Perspex block and covered with electrical tape.

This setup presented challenges that also needed to be overcome, namely how to ensure that the lighting setups did not interfere with each other when recording video. If the LEDs were left on constantly they were clearly visible in the other camera which greatly obscured the images recorded from both directions. The solution to this problem was to control both the cameras and the LEDs via a trigger circuit. This trigger was controlled by an Arduino which was programmed and wired to control the two camera setups independently. Each camera was controlled to take a single photo every 5 seconds, with the corresponding LED flashing to provide light. These photographs were then compiled to generate videos such as those included in the supplementary information. The cameras operated out of phase with each other by setting a delay of 2.5 seconds between them and no longer appear in the footage of the other camera.

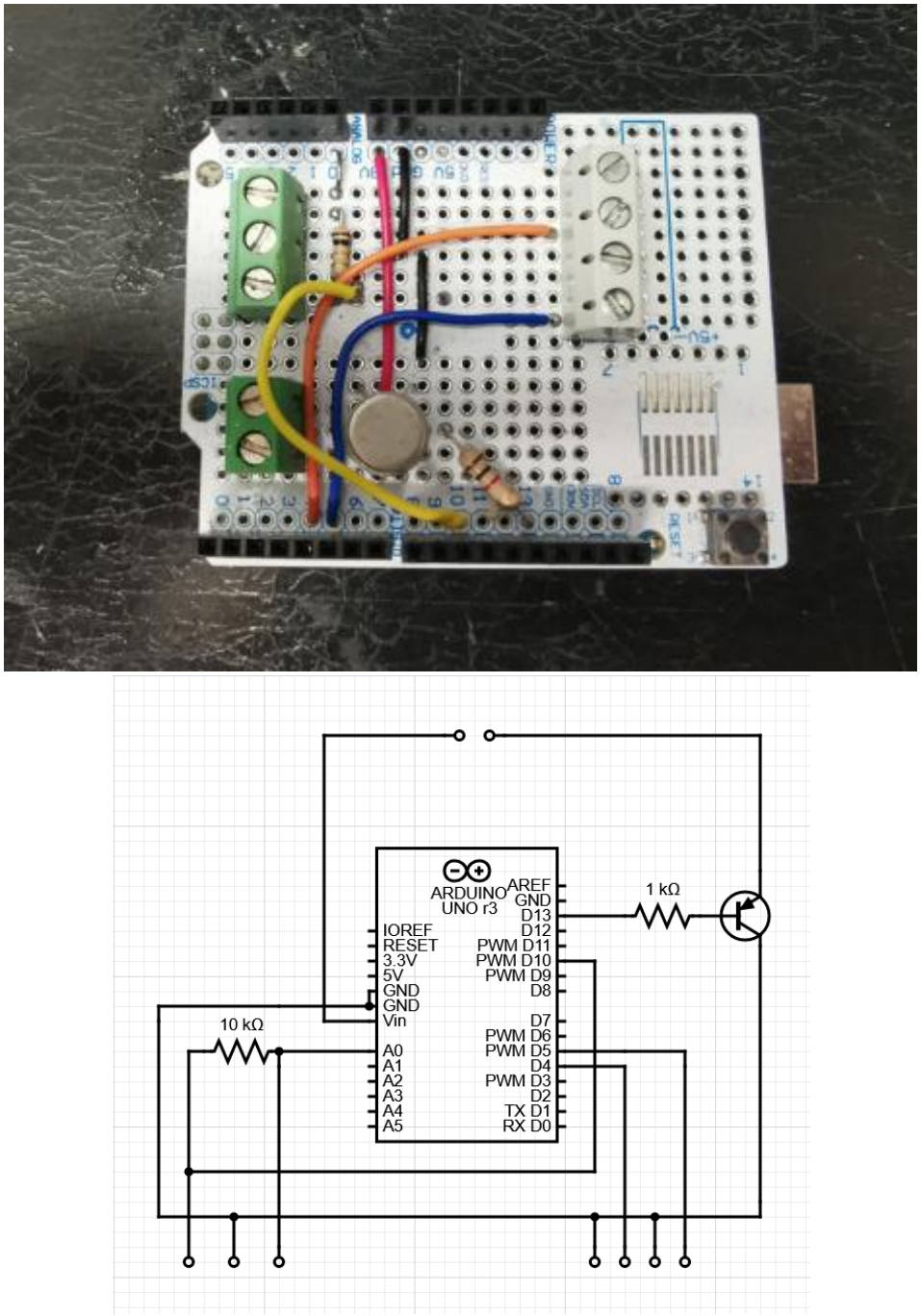

Figure 29: Top) the Arduino circuit that controls the camera setup. The cameras and LEDs are connected to the terminal boxes. Bottom) also shown is a schematic of how the trigger circuit with the bottom terminal boxes (3 and 4 pins) controlling the cameras and the top box (2 pins) controlling an LED panel.

2.3.4 Rheology Method Development

The samples of kaolin that we produced were sometimes inhomogeneous, this resulted in different results being obtained. It was found that the rheology experiments were very sensitive to how the kaolin had been previously handled. Initial tests showed very little consistency between individual experiments despite the same protocol being used for the shear experiments. Differences in the shear stress higher than 100 Pa were observed in some tests when using the same concentration of kaolin clay. This differs markedly from some of the model systems more commonly studied in the literature e.g. Carbopol. For example, it was found early on that if the rate of compression to trim height was not kept equal in each test it would drastically affect the results. We define the trim height as the height at which we take a plastic scraper to remove the excess clay from around the geometries before an experiment is performed. The sample was compressed to the trim height, trimmed, and then compressed to the working height. A standard trim height of 1.05 mm (compressed at 0.01 mm s^{-1}) was chosen since it resulted in a flush interface when the kaolin was compressed to the working height. A working height of 1 mm was also selected for all shear experiments.

Despite maintaining a similar compression history between each experiment we observe that there is a large difference between each experiment using the same concentration. These represented another challenge that needed to be overcome before characterisation of the kaolin could be achieved to a reliable standard.

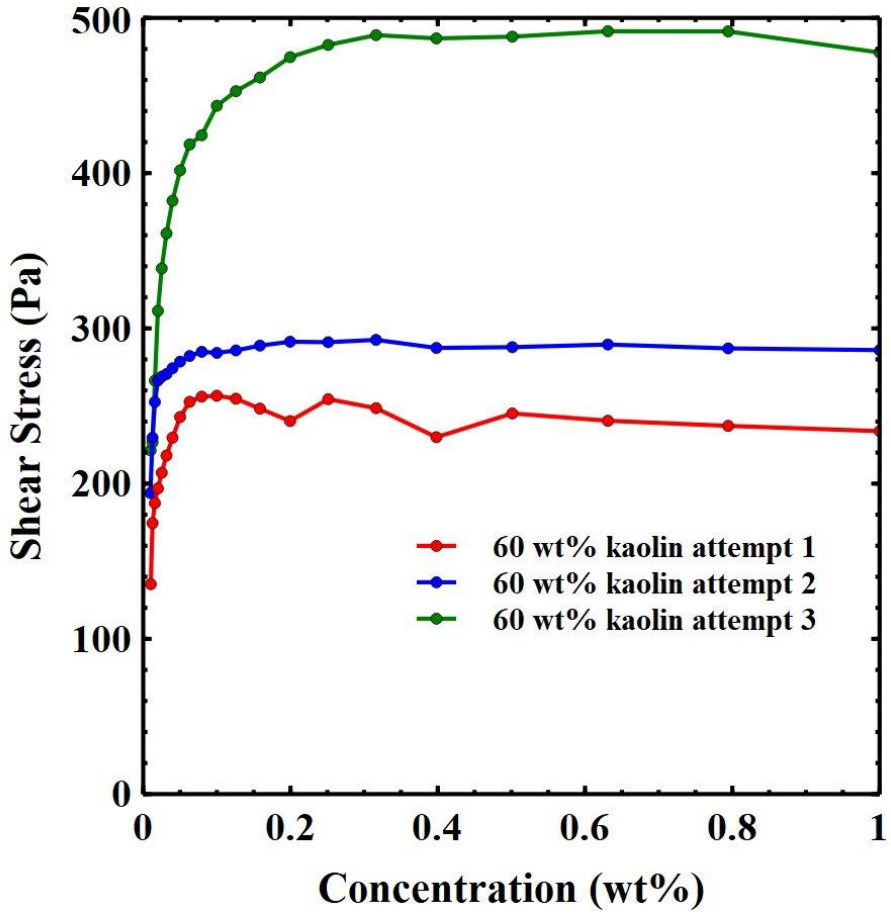

Figure 30: Reproducibility checks for a 60 wt% kaolin clay. Large variations are observed between each experiment despite each experiment being nominally the same. All three experiments use the same concentration.

Many published studies which perform adhesion tests of yield stress fluids simply load the sample and after trimming measure the force with separation of the plates. No other steps are taken to ensure a reproducible initial state [54,55]. In part this is probably helped by the choice of fluid e.g. Carbopol. It is also common that the apparatus does not have the capability to modify the sample in a controlled way prior to plate separation. In contrast our system uses a shear rheometer which allows us to apply rheological deformations prior to the adhesion test. Within the literature a pre-shear step is often used before experiments are carried out in simple shear rheology measurements. The aim of this is to strongly shear the sample so that the previous features of its strain history are overwhelmed and made negligible. At sufficiently high shear rate this process can affect the structural orientation of the particles and relieves any residual stresses in the system. Consequently, this pre-shear must be high enough to cause full fluidisation in the sample.

We found that a compromise shear rate had to be used. The shear rate needed to be high enough to fluidise the sample but also not too high, or the fluid would become dislodged and slip from under the plate. Through testing we found that a pre-shear of 20 s^{-1} satisfied both these conditions. At 50 s^{-1} the sample would start to lose clay from the periphery over time. As discussed later, we also confirmed that the kaolin is fully fluidised during this process. To further reduce the problem of clay becoming dislodged an excess of fluid was also left around the edge during the pre-shear so that during trimming we could ensure that there was the correct volume of clay and ensure a flush interface during shear experiments. For the sake of consistency, this pre-shear procedure was carried out on every sample of kaolin in this chapter and chapter three where rheology experiments have been completed. When we apply a consistent method of compression to 1.05 mm, pre-shear at 20 s^{-1} for 5 minutes and then compression to 1 mm working height we obtain reproducible data as shown in fig. 31.

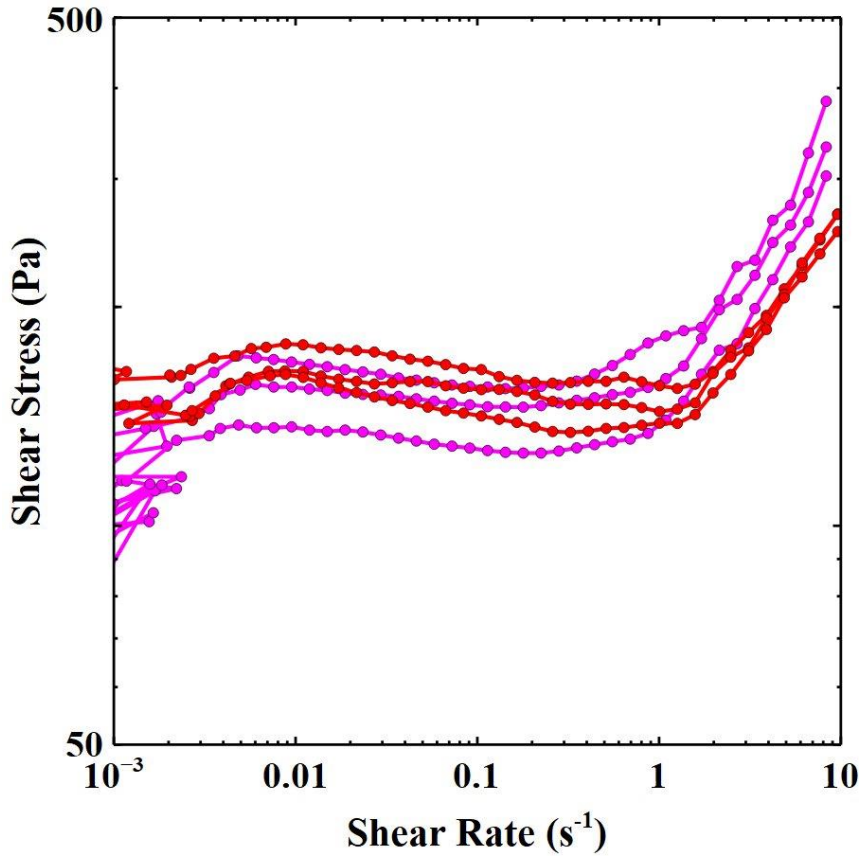

Figure 31: Shear ramp data obtained for the 60 wt% kaolin using the intermediate plates, the red traces are the ascending shear ramp protocol while the magenta traces are the descending shear ramp protocol.

2.4 Results

2.4.1 Rheological Characterisation of Kaolin Clay

To characterise the rheology of the Kaolin clay in the absence of slip, sandpaper of P40 grit was attached to the rheometer geometries. To confirm there was no slip present on these surfaces we performed “red line” experiments. An airbrush was used to spray red acrylic paint through a stencil to draw a line onto the free interface of the kaolin before it was sheared (See figure 32). This technique has been used previously by other authors as a method of visualising the slip of a fluid during shear flow [31,85]. Once the line had been drawn, the samples were sheared at 20 s^{-1} and the deformation of the red line recorded. These experiments confirmed that fluidisation during the pre-shear protocol was immediate, and slip is not observed on the P40 sandpaper.

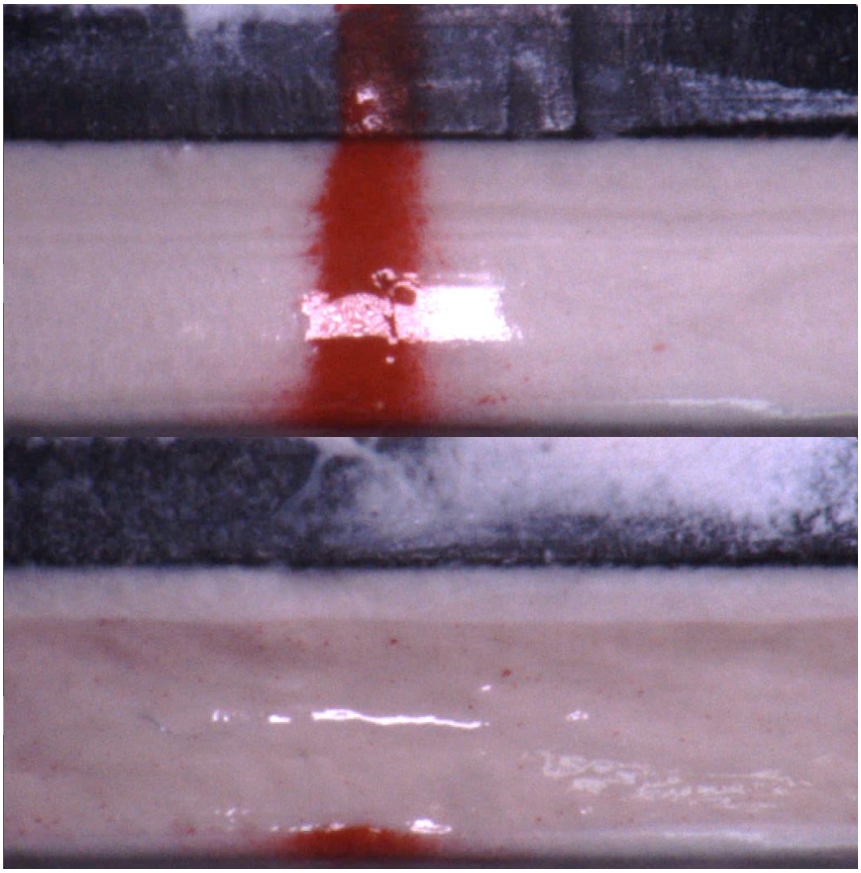

Figure 32: An example of a red line experiment. Top, a stencil is used to spray a line on the kaolin for visualisation of the slip behaviour of the clay at the surfaces. If there is no slip the redline will become completely deformed and then is destroyed as the sample flows as observed in the bottom image.

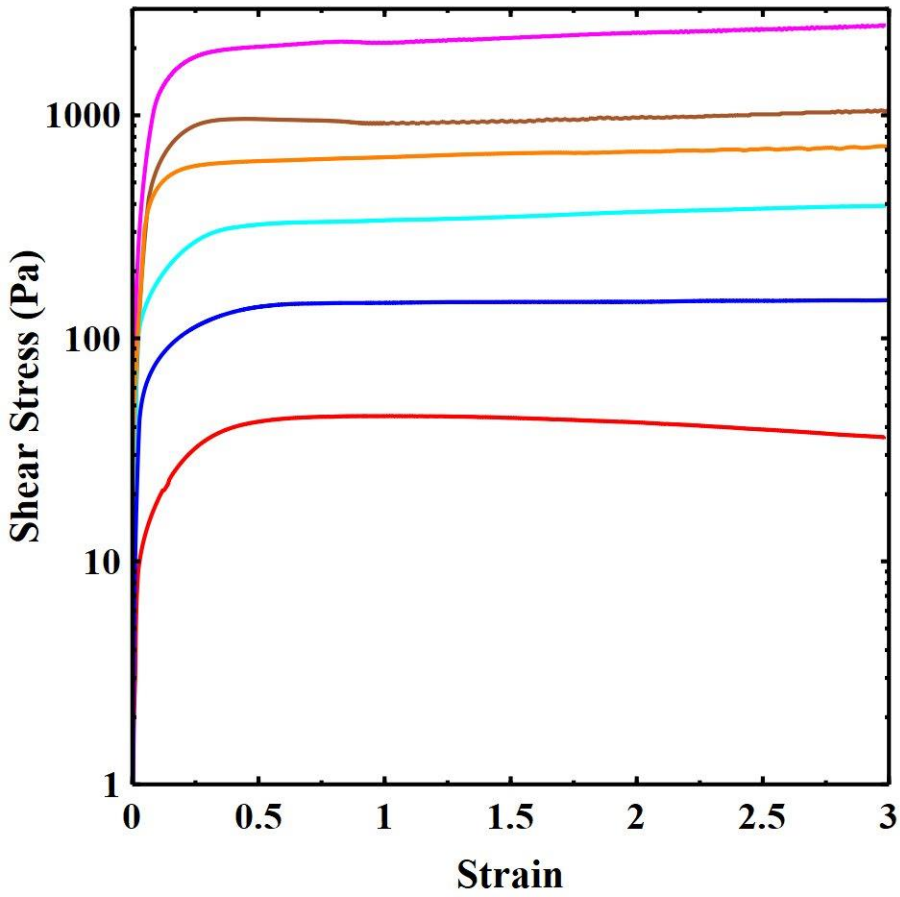

Figure 33: The shear stress vs shear strain data collected for the kaolin concentration range on P40 sandpaper. We observe a small overshoot on each trace before 0.5 strain units are reached. This is used to calculate the static yield stress of the kaolin on these plates. Data presented is the 45 (red), 50 (blue), 55 (cyan), 60 (orange), 62.5 (brown) and 65 wt% (magenta) samples.

The yield stress of the samples was then measured by recording the stress during a start-up experiment using a shear rate of 0.01 s^{-1} for several minutes. We determined the dynamic yield stress of the clays from the plateau values that are obtained when they are strained. As a result of this method the dynamic and static yield stresses are equivalent, as such the samples exhibit almost no stress overshoot, and the resultant plateau is the yield stress of the sample. The results of these experiments are included in fig 34 and table 1.

Concentration (wt%)	Yield Stress (Pa)	US Dept. Shear Strength (Pa)
45	42.5 ± 8	50
50	143 ± 20	122
55	272 ± 32	321
60	621 ± 64	790
62.5	942 ± 110	1270
65	1925 ± 270	2010

Table 1: The static yield stress values of the kaolin clays on P40 Sandpaper. Values obtained from the U.S> Department of Energy are also presented for comparison

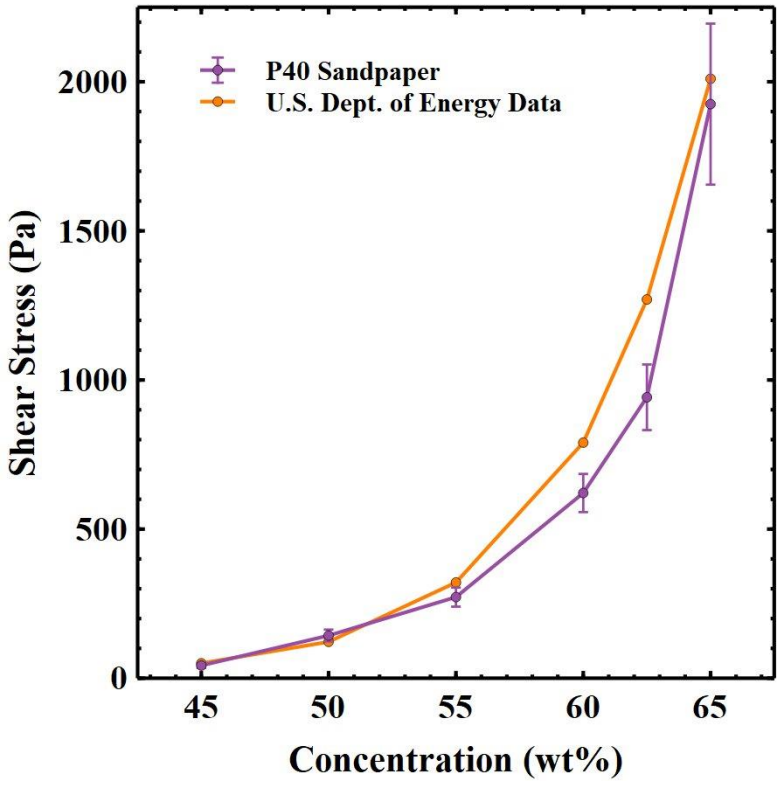

Figure 34: The static yield stress measured for each concentration of kaolin using the P40 sandpaper (purple). Data obtained from the U.S. Department of Energy is displayed in orange

The data presented in table 1 results in very similar values to those published in a review of Kaolin studies [86]. As such the yield stress values recorded using these surfaces are quoted as the true yield stresses of the kaolin clays in chapter three. After accurately defining the yield stress of the samples we wanted to characterise the structural behaviour of the specimens through oscillatory shear.

2.4.2 Oscillatory Shear

To characterise the storage (G') and loss moduli (G") of our kaolin clays we performed a series of SAOS experiments. Firstly, we performed frequency sweeps on samples of 55 wt% using strains of 1 and 10%. We observed a plateau in both frequency sweeps as seen in figure 35 which starts at approximately 0.2 Hz in both cases. However, this plateau begins to show crossover behaviour around 2 Hz when a higher strain is applied. Therefore, we decided to perform all other measurements at 0.4 Hz as a compromise frequency as the strain is increased during the strain sweep experiments.

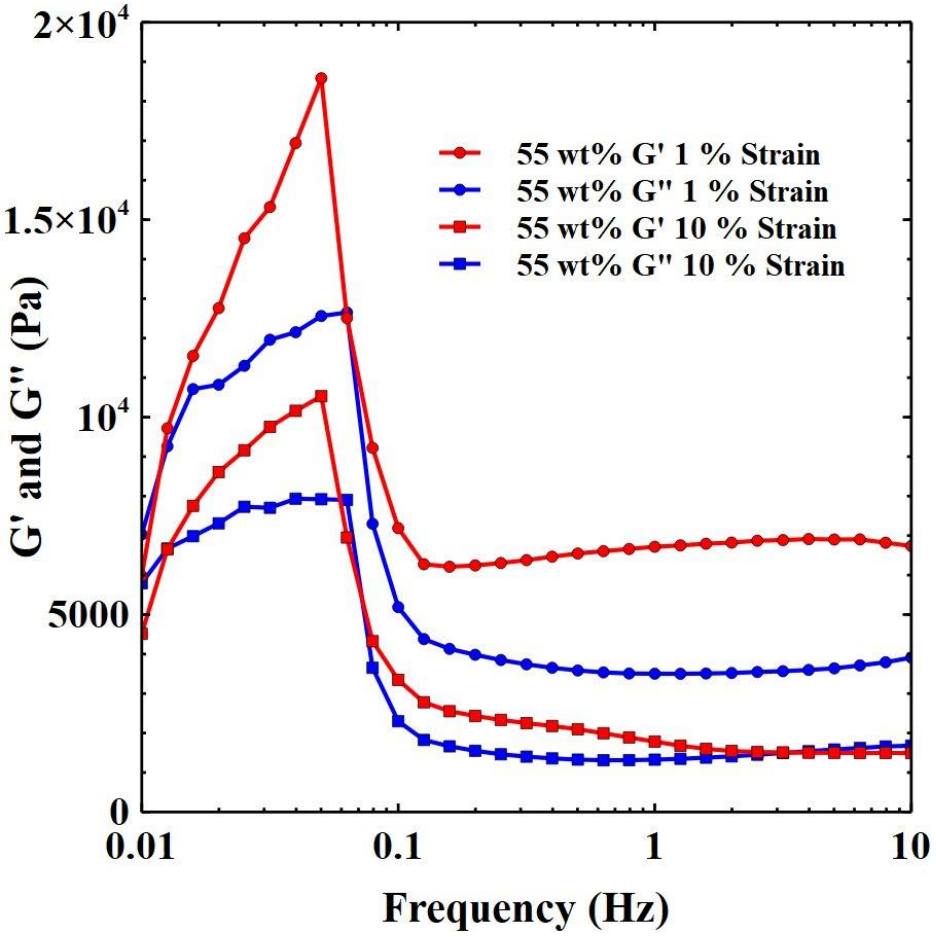

Figure 35: Frequency sweeps of the 55 wt% kaolin clay strained by 1% and 10% strain. We observe that there is no crossover behaviour at low strain while crossover is achieved for the higher strain sample. From this data we selected 0.4 Hz as a compromise frequency to use for the strain sweeps in order to provide stable data over a large proportion of the experiment. Data present is G' and G" strained by 1% (red and blue) and 10% (magenta and cyan).

Often G' is independent of the frequency under some critical shear strain, γ_c. However, usually there is some frequency dependent character: if a fluid shows a more frequency dependent elastic modulus it is a material that shows more fluid-like behaviour [87]. We observe in our data that by increasing the strain in the system, we can induce a dependence on the frequency and with 10% strain we observe crossover behaviour occurring at a frequency of 3 Hz. We do not observe similar behaviour when strained by 1% and the elastic modulus indeed remains independent of the frequency for a much larger range of oscillations between 0.2 and 20 Hz.

We then characterised the behaviour of the clays when subjected to an amplitude sweep. Unlike many gels and yield stress fluids, kaolin clay appears to have relatively small differences between G' and G". This suggests that even at small strains there is a significant plastic contribution to deformations that occur in the structure.

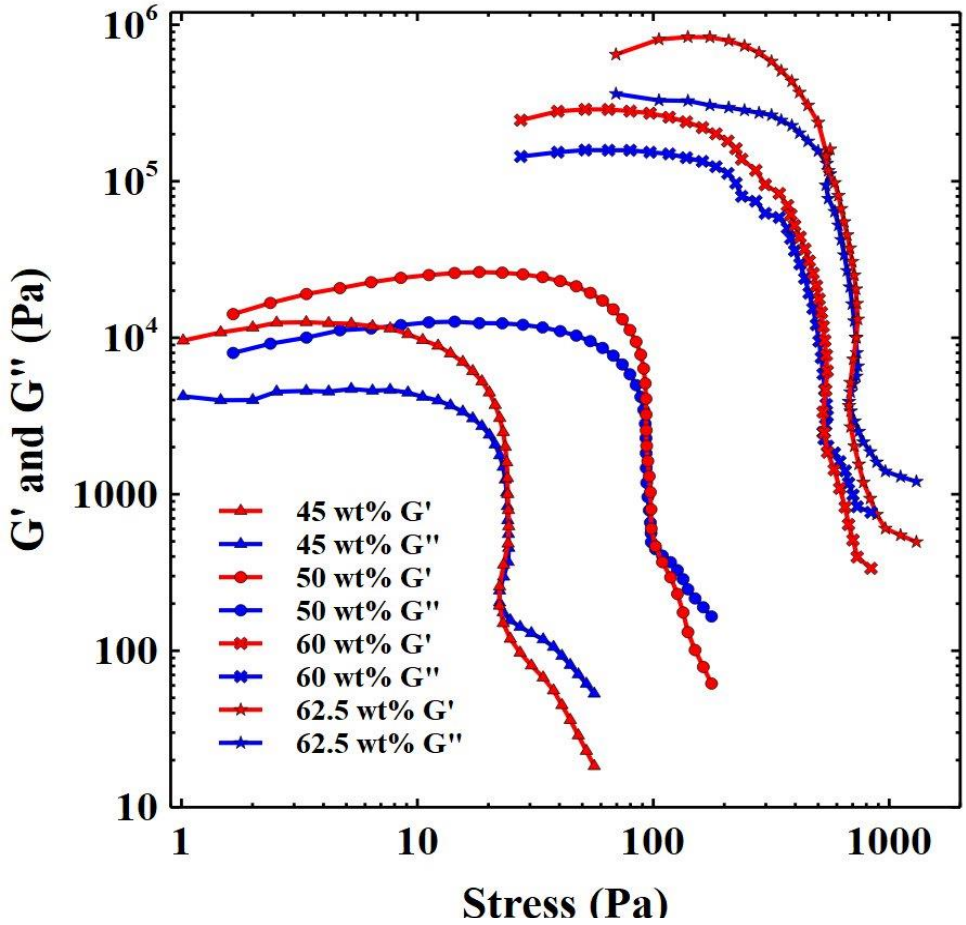

Figure 36: Plot of the elastic and viscous modulus of the 45, 50, 60 and 62.5 wt% Kaolin clays vs the complex shear stress. We observe that the crossover point of each sample is of a similar magnitude to the measured yield stress on the P40 sandpaper.

Using amplitude strain sweeps we measured the dependence of G' and G" on the applied stress. The yield stresses were estimated as the stress at which G' and G" cross / exhibit a large drop. When we plot the elastic and viscous moduli against shear stress, we observe that the transition to liquid-like behaviour is comparable to the measured yield stresses in simple shear. However, the values obtained here are consistently slightly lower, see fig. 36. It is common however to observe that different methods of measuring the yield stress can give different values [24].

We were interested in inducing slip in the samples to observe the effect it would have on their shear rheology. To achieve this, we produced three sets of Perspex plates of differing roughness. We will now analyse the effect of these differing surfaces.

2.4.3 The influence of slip on the Perspex surfaces

Our surfaces were created by taking blocks of Perspex and sandblasting them with abrasives of different grades, these were Honite 13 (grit size 106 – 212 μm with spherical shape) and Saftigrit Brown (80 – 120 μm which has more irregular shape) supplied by Guyson Abrasives. So that both top and bottom surfaces were identical, thin 20 mm plates were prepared in the same way. These plates were attached to the top geometry with a spray adhesive and left to stand for several hours. SEM images were taken of each surface to show their roughness as seen overleaf in fig. 37. We observe a clear difference in the roughness of the resultant surfaces depending on the grade of abrasive used. Measurements taken of the sizes of the resultant inclusions shows that the rough surface has pits with approximate size of 5 μm which is on the same scale as individual kaolin particles. The intermediate surface prepared with Honite shows much larger pits ~50 μm which are of similar size to the kaolin aggregates.

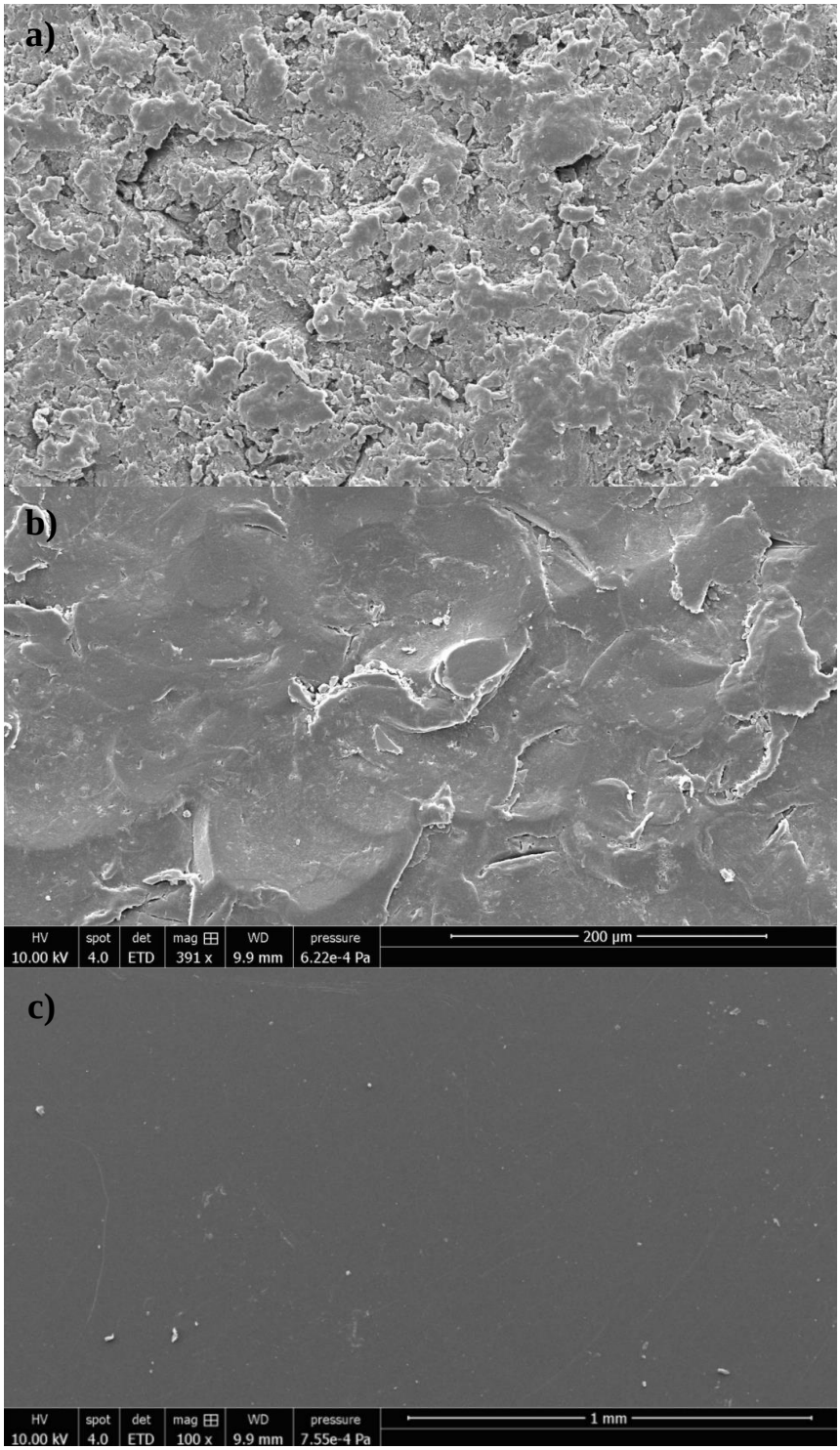

Figure 37: The top image shows a SEM image of the rough Perspex plates (a) sandblasted with Saftigrit Brown; this surface has many small inclusions with an approximate size of 5 µm. The middle image shows the intermediate Perspex plates sandblasted with Honite (b), inclusions on this surface are approximately 50 µm. The bottom image shows the smooth Perspex plates which were left untreated with abrasives (c). This surface was prone to scratches as can be observed in the image. Images of the rough and intermediate plates scale line is 200 µm and the smooth plate image scale line is 1 mm.

In these experiments we induced slip into the samples. Therefore, the shear rheology that is obtained is unlikely to reflect the "true" values that have been previously recorded above. Despite this, we obtained data that showed an effective "yield stress" using the Perspex surfaces much lower than obtained using P40 sandpaper. As the surface roughness increased we observed an increase in "yield stress". Such values for the yield stress are often referred to as the "apparent yield stress", they are the result of slip affecting transmission of strain to the sample.

Shear ramps were carried out between 10^{-4} and 10 s^{-1} in both the ascending and descending directions (ascending: increasing from 10^{-4} to 10 s^{-1}, descending: decreasing from 10 to 10^{-4} s^{-1}). The plateau value from both ascending and descending shear was then averaged to obtain an estimate of the apparent dynamic yield stress.

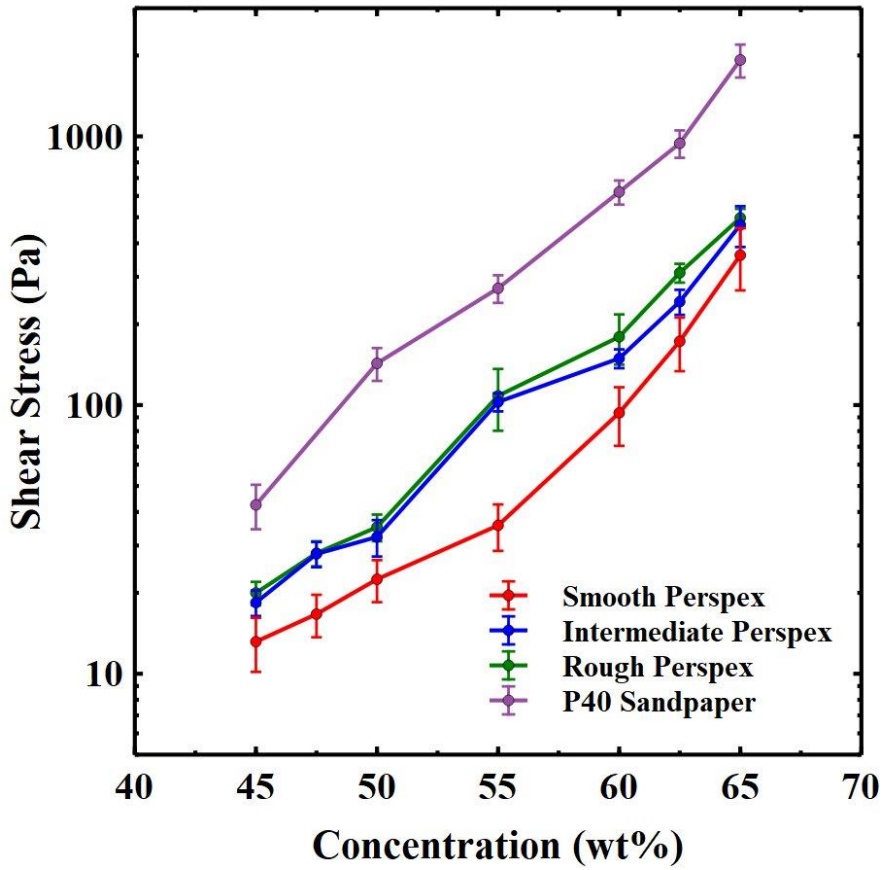

Figure 38: The dynamic yield stress of each concentration calculated from the averages of both the ascending and descending protocols.

Concentration (wt%)	Smooth $\sigma_{y,apparent}$ (Pa)	Intermediate $\sigma_{y,apparent}$ (Pa)	Rough $\sigma_{y,apparent}$ (Pa)
45	13.16 ± 3.39	18.40 ± 1.79	19.98 ± 1.54
47.5	16.67 ± 3.34	27.92 ± 3.07	28.11 ± 2.81
50	22.47 ± 4.23	32.30 ± 4.95	35.13 ± 4.20
55	35.66 ± 6.68	102.70 ± 7.54	108.24 ± 28.28
60	93.50 ± 22.9	149.16 ± 12.21	179.4 ± 37.79
62.5	172.69 ± 38.99	242.52 ± 25.88	310.52 ± 25.48
65	361.19 ± 94.26	468.38 ± 81.49	497.25 ± 40.34

Table 2: Dynamic yield stress values for each concentration of kaolin clay on each Perspex surface.

Figure 38 and table 2 show that there is some similarity in the values of the measured yield stresses on both the intermediate and rough surfaces, particularly at low concentration. However, if we compare the above apparent yield stresses to the values recorded using P40 sandpaper we observe a significant difference. Take the 60 wt% kaolin for example, using the different Perspex surfaces we get a progressive series where the yield stress increases by a small amount with each increase in roughness. However, the yield stress obtained on the P40 sandpaper is significantly greater (621 ± 64 Pa). This suggests that despite having a significantly roughened surface, see SEM images, the rough Perspex surfaces still show a large amount of slip. By roughening the surfaces we are able to reduce the effect of slip on the kaolin clay but our results here suggest that slip has not been eliminated entirely from the experiment.

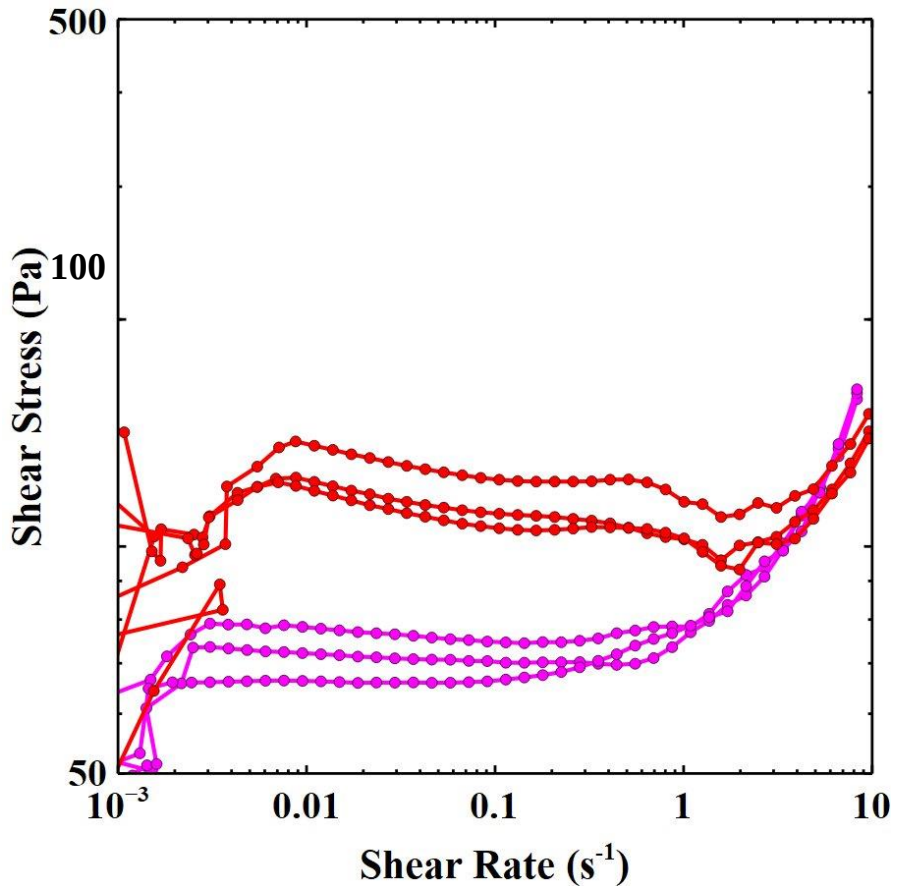

Figure 39: Shear ramp data for the 60 wt% sample measured on the smooth Perspex surfaces. We observe a large gap between the ascending (red) and descending (magenta) traces where the ascending shear ramps appear higher than the descending shear ramp data.

Interestingly we found the relation between the ascending and descending shear ramps were different to one another. We might expect that as the surface roughness increased, the difference in the shear stress diminished until they gave very similar results. However, our data shows that this is not the case. For instance, using the smooth plates the ascending shear stress is greater than that in the descending data, see figure 39. However, when the kaolin is sheared on the rough plates we observe that the descending shear data sits above the ascending shear data, see figure 40.

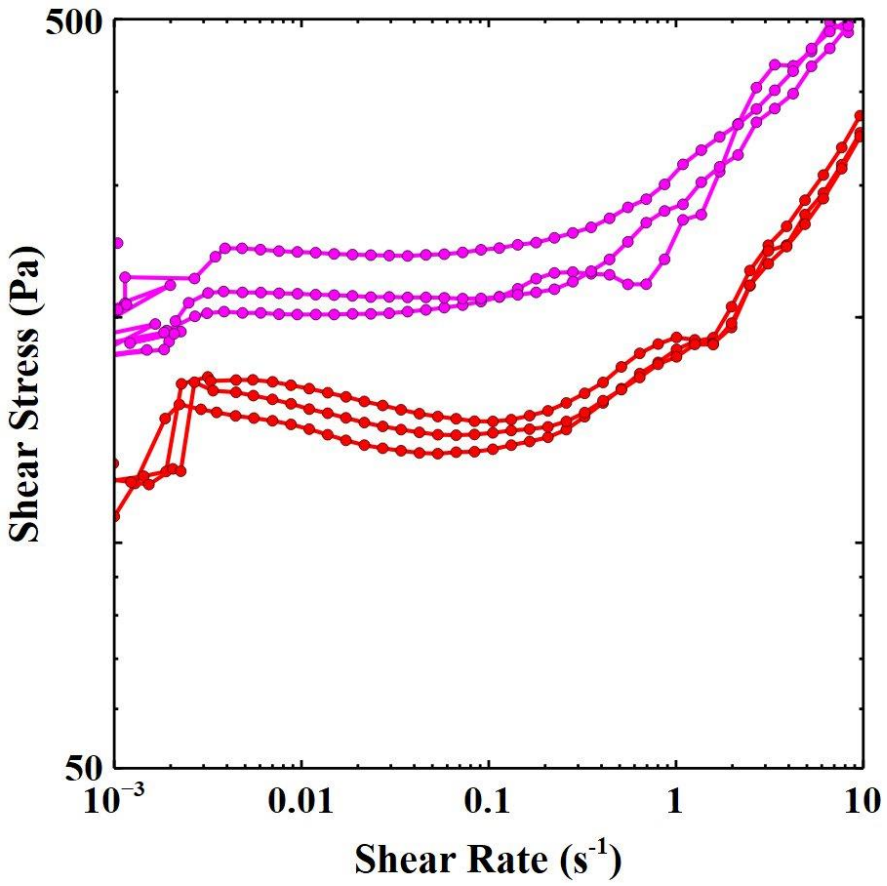

Figure 40: The shear ramp data collected using the 60 wt% kaolin measured on the rough surfaces. In this case we observe that the descending shear ramp data (magenta) appears higher than the ascending shear ramp data (red).

2.4.4 Understanding the Shear Ramp Behaviour

An airbrush was used to spray red acrylic paint through a stencil to draw a line onto the free interface of the kaolin, before it was sheared, on each surface (See first row of figure 41). This technique has been used previously by other authors as a method of visualising the slip behaviour of a fluid during shear rheology [87,88]. Once the line had been applied, the samples were sheared at 20 s^{-1} using the different Perspex surfaces and the deformation of the red lines recorded and compared.

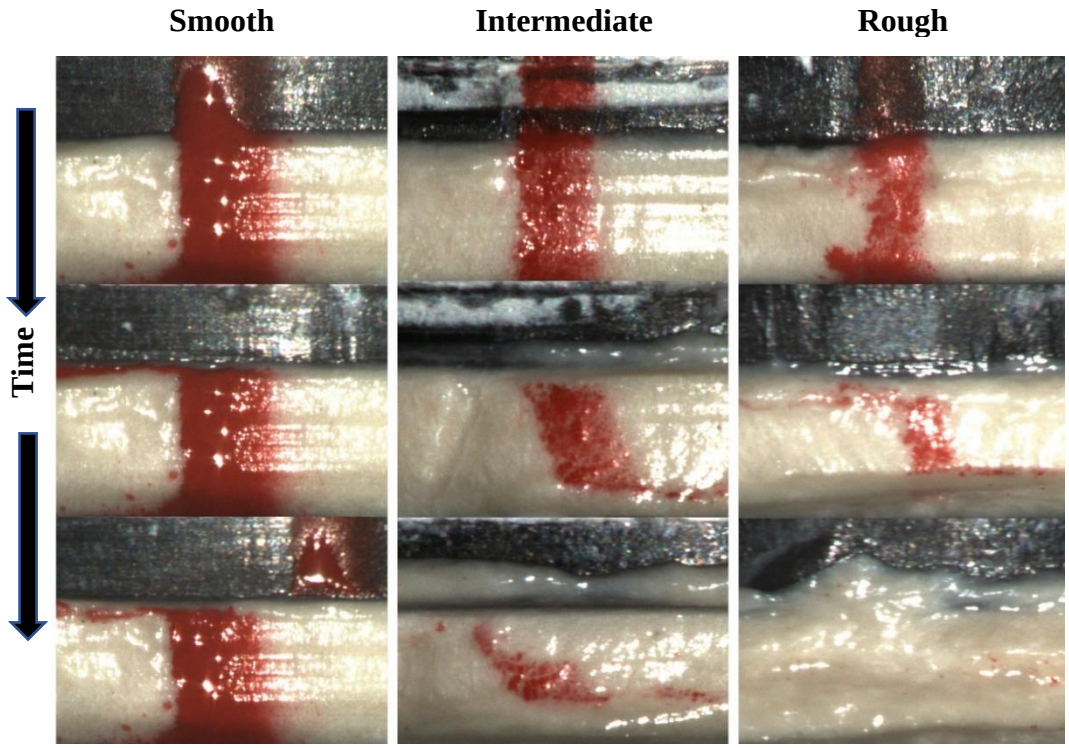

Figure 41: A sample of the 60 wt% kaolin clay sheared on the smooth (left), intermediate (middle) and rough (right) plates within the liquid regime identified in the previous shear ramp experiments.

Figure 41 shows three images for each experiment prior to the start, during the initial stages of the shear and once the flow reached a steady state. The results of the slip experiments obtained with the different surfaces suggest very different fluidisation behaviour at high shear rate. This is an effect of the increasing roughness of the Perspex plates. If we also look at the shear data in figures 39 and 40 we can also see very different behaviour in the liquid regime dependent on the roughness of the surface used. On smooth plates the liquid regimes are equivalent in both directions. Using the rough plates however the descending shear protocol shows a much higher stress than the ascending protocol.

2.4.4.1 Smooth Plates

We observe that the smooth top plate immediately slips which is then followed by the apparent fluidisation of only a small layer adjacent to the top plate. The rest of the clay sample does not deform for the duration of the experiment. If this is the case then a large lubrication layer is present at the plates which will cause a significant amount of slip. A common form of slip that is observed in similar samples is wall depletion [88]. Shear remains localised at the wall, this results in a region approximately 5 to 10 grain sizes thick where the particles migrate away from the plate face and re-enter the bulk, leaving an interface of low solid concentration. As the particles leave this region, slip becomes progressively easier. This behaviour suggests that any water that is squeezed out of the clay is not mixed back into the bulk at high shear rates.

2.4.4.2 Rough Plates

Using the rough plates we observe that initially there is a small amount of slip followed by shear banding at the top and bottom of the sample similarly to the behaviour observed on the intermediate plates. However, these are transient shear bands and over time they merge, fluidisation is observed in the bulk of the sample. The red line is destroyed and all that remains of it are red specks that are observed across the free interface as rotation continues. Any water that is extracted on these plates is likely recirculated relatively quickly and the local concentration at the interfaces is not greater than expected. However, although fluidisation is achieved there is still a significant amount of slip in the system: there is likely still a small lubrication layer present at the interfaces that significantly reduce the yield stresses recorded on these plates. As one may expect the behaviour observed on the intermediate plates resides between these two extremes. Initially there is only lubrication at the plate surfaces, over time these fluidised layers move inwards until a permanent shear band is established. After these experiments it was decided that in experiments concerning slip, work would focus on the rough plates as they showed full fluidisation in the period of this experiment while the other plates did not.

While performing the experiments in this chapter we noticed that volumes of water would be expelled at the plate interfaces. Supplementary video 1 shows a simple video of what happens to the clay as the rheometer plate moves from the trim height to the working height, prior to each experiment.

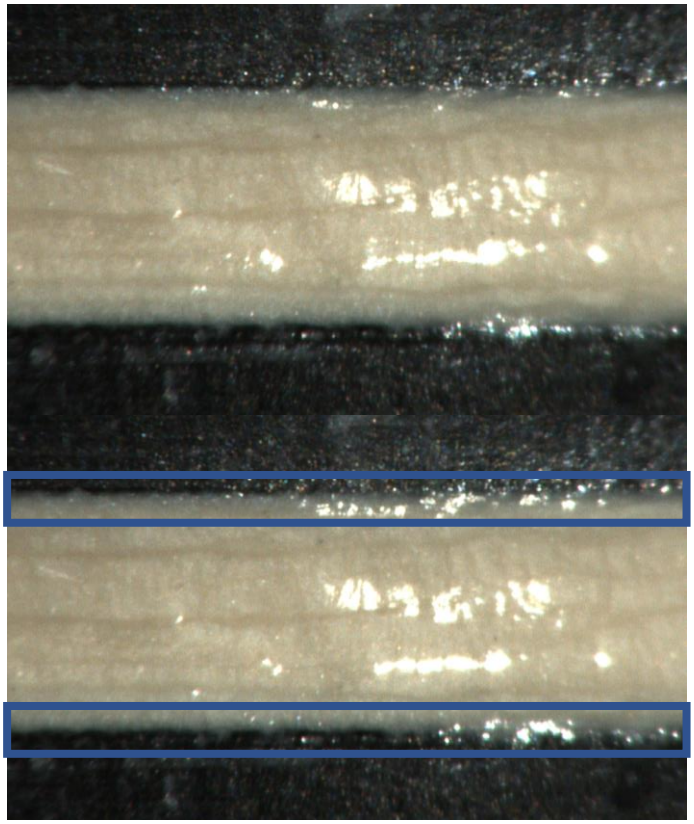

Figure 42: Stills from the supplementary video 1. First still is the initial sample, the second still shows the kaolin during compression where an increase in water can be observed at the plate interfaces.

The observations made in fig. 42, as well as in supplementary video 1, lead to the hypothesis that the lubricating presence of water at the interfaces might be partially responsible for changes in the measured shear rheology. From this observation further experiments were performed to observe the effect of compressing the kaolin from different initial trim heights.

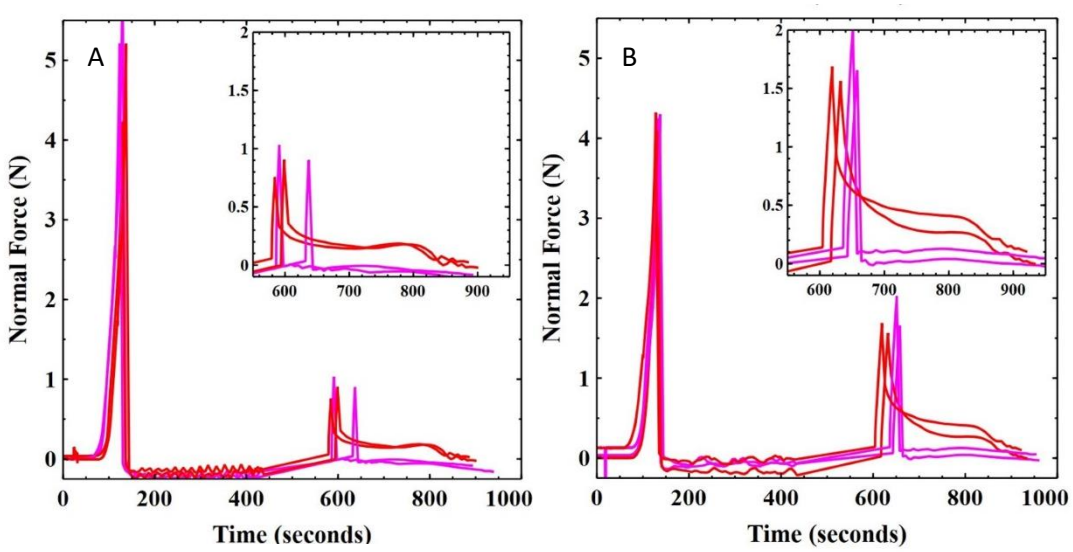

Figure 43: Force profiles of the 60 wt% during a simple shear rheology experiment with increasing initial trim heights of (a) 1.05 and (b) 1.15 mm. Displayed are ascending (red) and descending (pink) shear ramp experiments.

To understand what may occur during the ascending and descending shear ramps we analyse each individually. Figure 43 shows the normal force prior to and during each experiment where a different trim height was used in each case. The initial compression force is then relaxed by the pre-shear protocol, confirming that the process is sufficient to nullify the previous shear history. The second spike in force is due to the compression from trim to working height, the greater the trim height the larger the amount of force is applied in this step. Based on our earlier observations in figure 41, as the force increases a greater amount of water is forced out of the bulk of the clay, lubricating the interface.

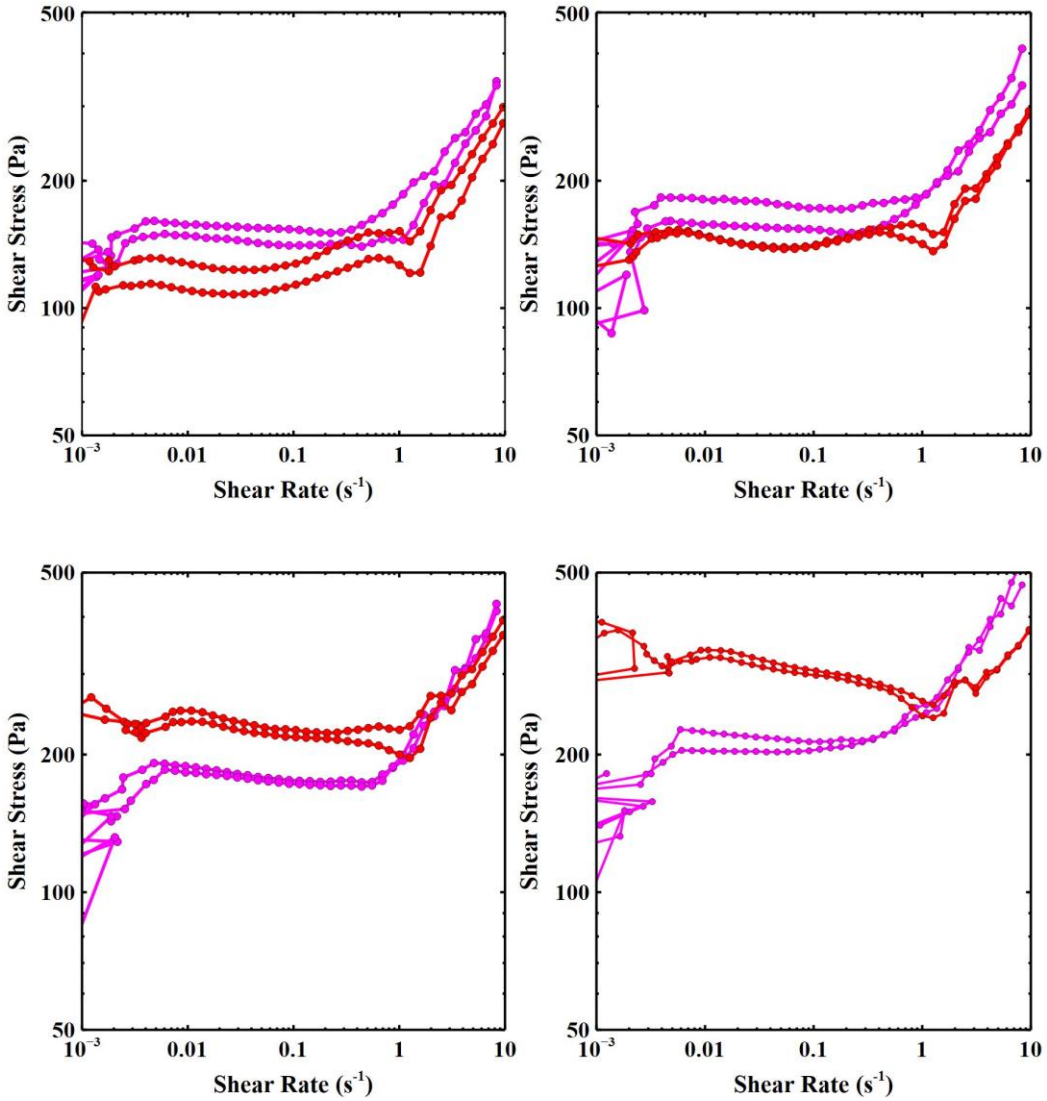

Figure 44: Shear ramp data of the 60 wt% kaolin collected on the rough plates after being compressed from 1.02, 1.05, 1.10 and 1.15 mm respectively. Ascending shear data is presented in red and descending data in pink.

Figure 44 shows the shear ramp data obtained for the 60 wt% kaolin compressed from four increasing trim heights. We observe a small change in the descending shear dynamic yield stress as the force of compression is increased (increasing by about 40 Pa). This suggests that the descending shear protocol is only minimally affected by the initial compression. As the initial strain is high and compressive force is relaxed the structure is broken down and so the shear history is more effectively suppressed.

However, we observe a significant difference in the ascending shear dynamic yield stress. The change is small at low compression but when the kaolin is compressed by 0.10 and 0.15 mm to the working height, we see a much more significant increase in the dynamic yield stress (150 Pa). From fig. 44 we observe that the normal force in the ascending protocol is retained for much longer over the strain process. The shear history of the compression has a much longer lasting effect during the low shear behaviour of the kaolin clay which can greatly affect the rheology of the clay as the shear ramp progresses.

From these observations it seems there are at least two contributing factors to the shear behaviour on the rough surfaces. We have shown that under compression a lubrication layer is expelled from the bulk. The size of this lubrication layer increases with increasing normal force as more water is expelled. The red line experiments show that when strongly sheared this water is redistributed into the bulk as the sample is fluidised. By increasing the normal force the magnitude of the slip hysteresis changes. At low compression the descending shear is greater than the ascending shear however, as the normal force is increased the ascending shear is now higher. This occurs despite a greater amount of water being present at the interfaces. This suggests that there may be another contribution from particle packing. We would expect to see an increase in lubrication but instead the height of the plateau increases.

These observations suggests that for kaolin clay, allowing the system to become fluidised can cause a significant change. This suggests that the beginning of the descending protocol alters the rheology in a way that is not observed in the ascending protocol. Below we will observe what happens to the shear rheology if the clay is not allowed to fluidise.

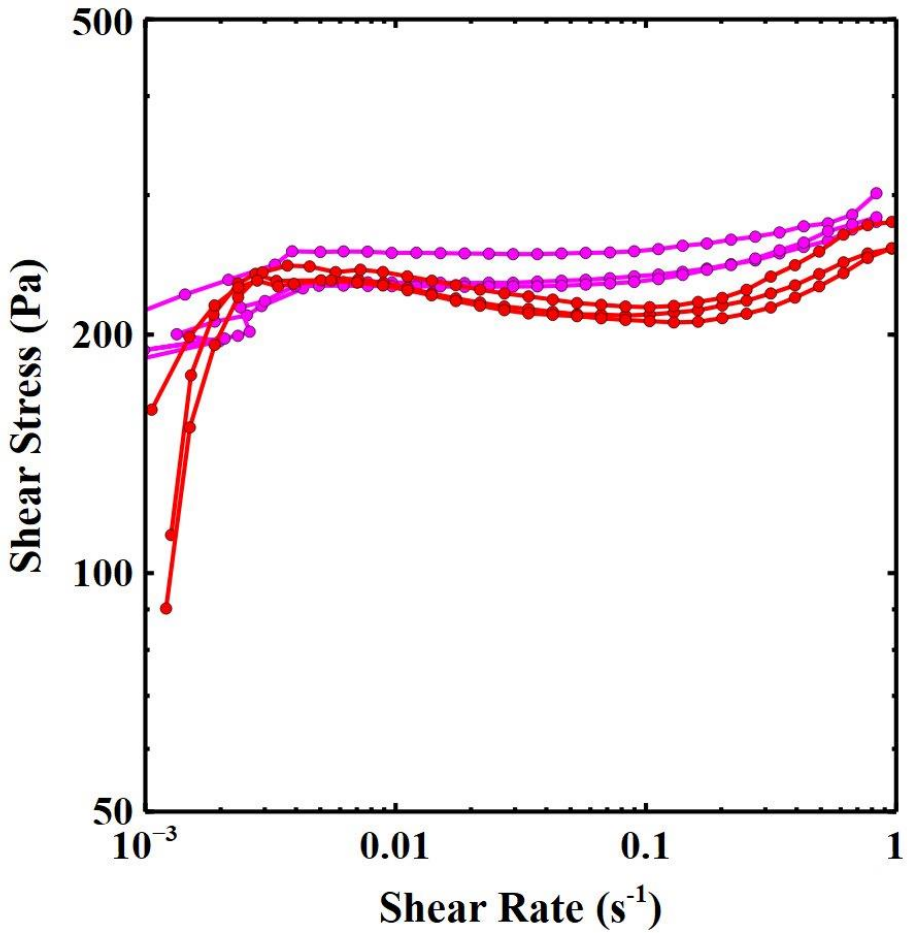

Figure 45: Shear ramp data collected for the 60 wt% kaolin on the rough surfaces. The shear rate range has been reduced by two decades (10^{-3} to 1 s^{-1} instead of 10^{-4} to 10 s^{-1}). We observe that there is a much smaller difference in plateau stress between the ascending and descending shear protocols.

Previously we observed that at high shear rates, using the rough surface, liquid can be recirculated into the bulk of the fluid. At low shear rates this process does not occur and two slip environments evolve. Fig. 45 shows the shear ramp data obtained when the high shear rates (>1 s^{-1}) were removed from the protocol. The above data demonstrates that if the clay is not allowed to enter the fluidising regime the water at the interfaces is unable to recirculate into the bulk. This results in the descending shear data appearing at a lower shear stress plateau that matches data recorded in the

ascending protocol. These results are further evidence in support of our hypothesis of surface lubrication.

2.5 A Hypothesis for our Shear Ramp Data

The results discussed in this chapter suggest that when the clay is initially compressed, a lubrication layer is generated that promotes slip and the kaolin now effectively has a greater solid concentration. At high compression there is a significant amount of water expelled at the interfaces. Consider figure 43, when the kaolin is fluidised immediately at high $\dot{\gamma}$, this layer of water may become recirculated into the bulk. The lubrication layer would be thinner and so on the rough surfaces the descending shear data are greater than the ascending shear. We know that a slip layer is still present in the descending protocol due to the data collected with the P40 sandpaper which are comparable with [88].

In contrast, when sheared at low $\dot{\gamma}$, the amount of strain the sample undergoes is minimal, takes longer to build up, and the lubrication layer remains present at the interfaces. As we compress the kaolin more the effective concentration increases. We would expect that as the lubrication layer gets thicker the amount of slip observed would increase. This would suggest that the plateau of the ascending shear stress would decrease, however this is not the case and it actually increases with greater compression. This suggests that there is a competition between at least two phenomena: slip is promoted by the amount of water at the surfaces but is also reduced by how efficiently the clay packing is compacted. In the descending protocol there is no significant change in the plateau, this is likely due to the clay being fluidised immediately and the packing that has been formed in compression is broken down.

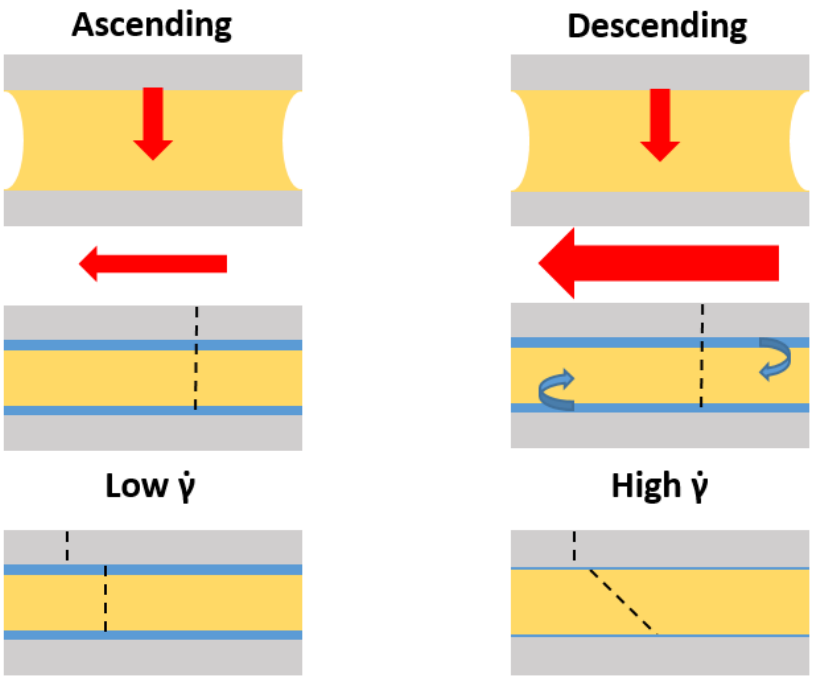

Figure 46: Diagram to show the hypothesis in schematic terms. The compression to working height extrudes some water from the bulk near the plate interfaces, lubricating the surfaces. Depending on which protocol is used, some of this lubricating water may be mixed back into the bulk, reducing the amount of wall slip that is present during shear ramp experiments.

This however does not quite explain the behaviour we observe on the intermediate and smooth plates. Consider, when the water is pushed out during compression to working height rather than sitting as a layer across the entire surface, it is attempting to travel towards the edges of the sample, close to the free interface. However, the success of this process may be related to the surface roughness of the plates. With a higher roughness there is a greater number of locations for the water to become trapped at the plate interface and so water lubricates most of the plate/kaolin interface.

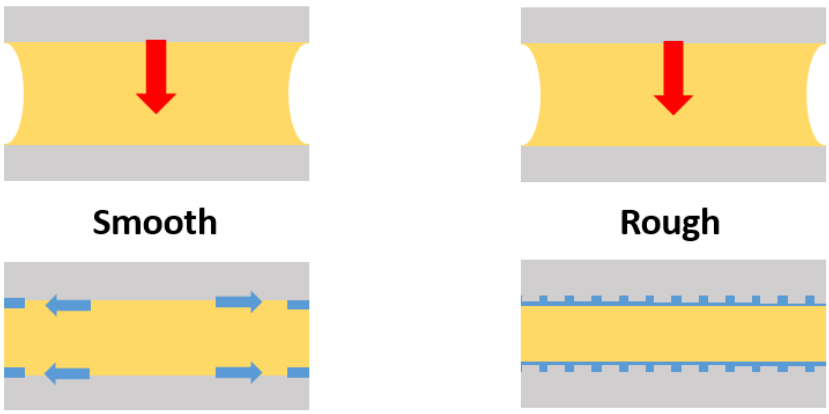

Figure 47: An idealised diagram of our hypothesis on both rough and smooth plates. On the smoother plates the water is pushed outwards to the edges more effectively while on the rough plates some of the water becomes trapped in the inclusions of the surface and so cannot be transported as far. This may result in a drier interface for the smooth ascending protocol causing the ascending shear data to appear above the descending flow data.

A drier local concentration could lead to a relatively stiffer interface that would show shear rheology that has increased shear stress compared to a more liquid rich interface on the same surface. This proposed effective drying does not result in shear stresses that are larger than those observed on more rough plates due to the overall slip characteristics of the smooth surfaces but may provide a framework for why the ascending shear appears higher than the descending shear. The intermediate plates would then show a compromise between these two extremes. However, this is only a hypothesis, and we are unable to visualise the transport of interstitial liquid during the course of an experiment. We are however able to visualise the slip processes that occur in the samples during shear as discussed.

2.6 Stress or Strain Control?

Shear rheology can be performed in one of two ways, shear ramps are either strain or stress controlled. During our method development we decided to perform shear ramps using strain control. We found that the shear ramp data was much more reproducible using strain control rather than stress control.

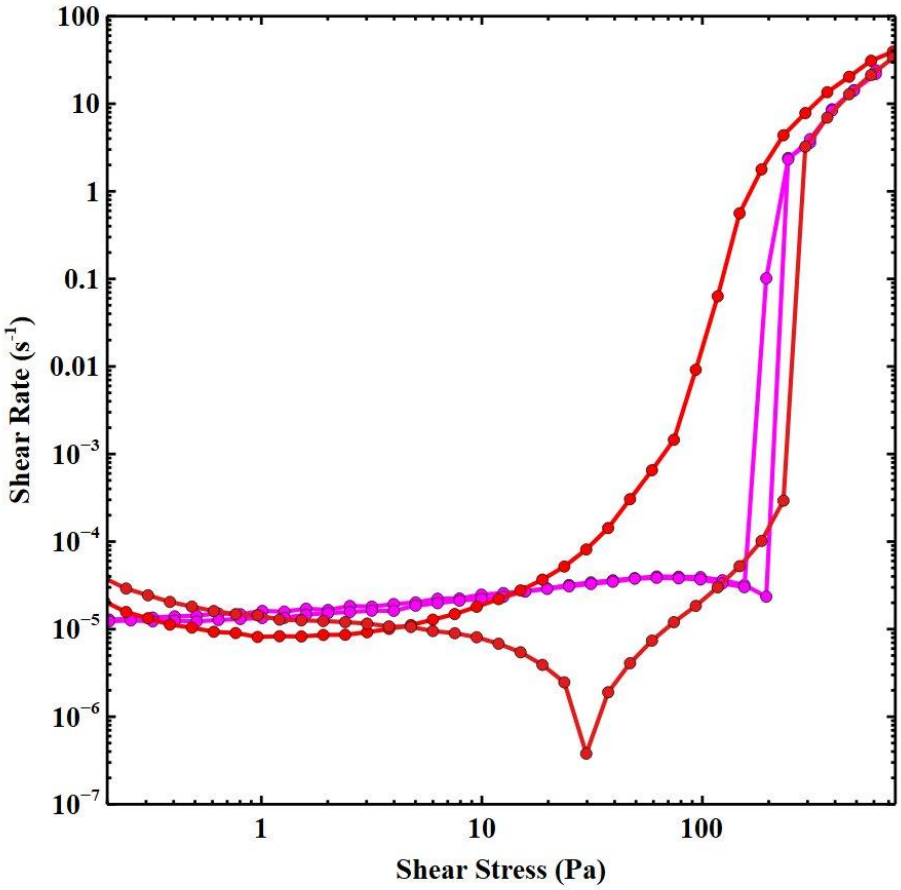

Figure 48: Stress controlled shear ramp data using the 60 wt% kaolin, displayed are the ascending (red) and descending (pink) data.

We observe reproducibility in the descending shear ramps however, in the ascending regime we see artefacts suggesting a large amount of slip. We attempted to acquire more reproducible data using this methodology, but it was unsuccessful. All experiments performed in this chapter were completed using a strain-controlled protocol due to it being easier to obtain reliable results using kaolin.

2.7 Conclusion

Clays can be a difficult system to measure when compared with common model systems such as Carbopol. In this chapter we have developed a reproducible method of preparing samples of kaolin clay for rheological experiments. The properties of the clays such as yield stresses and shear moduli have been successfully measured and are comparable to already agreed upon values suggesting that the samples have been well prepared. Red line experiments showed that the roughened Perspex surfaces were the only surfaces where effective pre-shear could be established. As a result of this observation, in the next chapter we will only use this surface to investigate the effects of slip during adhesion tests.

Chapter 3. The Role of Slip in Adhesion Testing on a Kaolin Clay

3.1 Introduction

Over the years there have been many studies that have focussed on simple shear measurements of yield stress fluids using standard rheological techniques. However, there are many alternative flows frequently used in practical applications. A number of studies have focussed on model systems that approximate these more applied flows such as a flow of liquid down an inclined slope [27], motion of an object through a liquid, [1] coating [89] and capillary flows [90], a rod being drawn from a container [91], squeeze flows [92] and adhesion tests [93]. Interpreting the significance of different features of these flows and understanding how these tests relate to more standard rheological measurements remains a challenge, particularly for yield stress fluids.

In adhesion testing a thin layer (thickness h_0) of fluid is confined between two circular plates of radius R_0 such that the initial aspect ratio, h_0/R_0, is small $<<1$. The normal force on the upper plate is measured as it is slowly moved upwards. A number of studies have focussed on this type of flow which is used extensively in quality control applications of food stuffs e.g. [94] but is also quite similar to the geometry encountered when a flat tool is withdrawn from contact with a fluid, e.g. knife and butter, trowel and mortar [95]. There has been significant research on two main aspects of this problem. Firstly, there has been interest in the deposited patterns left behind on either plate. These patterns can be conical deposits, rough multi-peaked fracture surfaces [96] or viscous-fingering induced tree-like structures [97–100]. Viscous

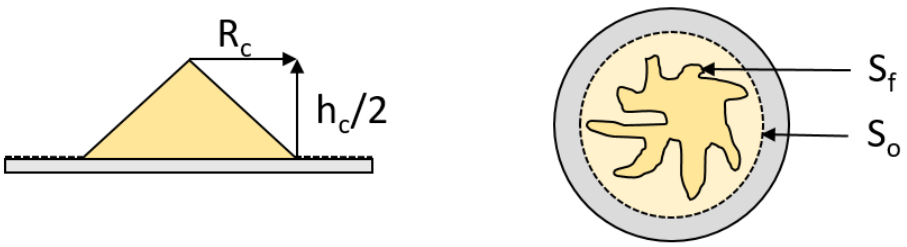

Figure 49: schematic diagrams of a conical deposit and viscous fingering, otherwise known as a Saffman Taylor instability. S_o is the initial surface area and S_f is the final surface area. Recreated from [97]

fingering, while not the focus of this chapter, is caused by the penetration of the fluid being measured by a fluid of significantly lower viscosity, commonly air.

Several studies have focussed on understanding how the measured force (F) scales with plate separation (h) [94,98,102]. This allows one to calculate the total work of adhesion:

$$W_{Adh} = \int_{ho}^{hc} F dh \,, \tag{24}$$

The measured scaling of force (F) with separation of the plates (h) is known to depend strongly on the traction conditions experienced by the fluid at each plate. For a yield stress fluid deformed quasi-statically, resulting in solid-like behaviour, if the surfaces are very rough such that the fluid is pinned then $F \propto h^{-2.5}$, whilst under conditions corresponding to perfect slip, $F \propto h^{-1}$ [101].

In this chapter, we again examine the role of slip in the measured forces. However, our focus is on the transient behaviour during the early stages of the adhesion measurement. This stage is important since it determines the separation of the plates at which the maximum force is measured.

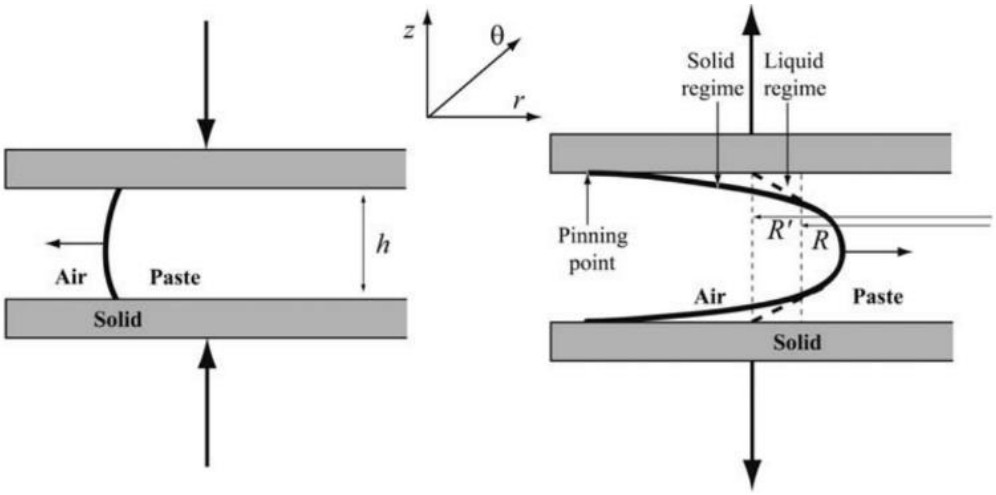

Figure 50: Schematic diagram of an adhesion test at h_o (left). After extension has increased enough to show significant deformation (right) pinning at the plate edges is observed which elongates the surface area of the deposits on both plates, decreasing the inner radius of the filament. Obtained from [21]. R' is the effective radius of the fluid in contact with the solid surface.

During an adhesion test the shape of the sample is dependent on several factors such as the fluid concentration and surface slip as extension occurs. Often simple models assume that until failure the fluid maintains a cylindrical shape due to the large aspect ratio of the setup. However, pinning is known to be important [97] in which the fluid no longer moves across the plate surface and the contact area remains static. As a result pinning has a significant effect on the breakup dynamics of the system [97]. As shown in fig. 49, the region directly next to the pinning point no longer flows and transitions into the solid regime. As the extension continues the liquid region is drawn into a filament and contracts inwards. As the gap increases the solid region will continue to grow while the liquid region shrinks (local $\dot{\gamma}$ decreases) until eventually breakup occurs.

Measurements made during the transient start-up of a rheological measurement in simple shear can exhibit differences from steady state flows. When a yield stress fluid is first subjected to strains below some critical value γ_c ($\sim 0.1{-}0.3$) it typically exhibits a visco-elastic response, whilst above this critical deformation the samples yield, displaying visco-plastic behaviour [1]. In systems where the particles have attractive interactions this can be followed by a second far less obvious yield point at higher strains [102]. Under some conditions the initial stress–strain curve during the transient startup may exhibit a stress overshoot before settling down to a steady-state [103]. The existence of this stress overshoot in some systems has also been strongly linked to the development of wall-slip or transient shear banding which affect the apparent measured properties of yield stress fluids [25].

Slip results in a local velocity that varies over some small but mesoscopic distance from the boundaries. In the case of yield stress fluids composed of soft deformable particles, slip occurs via the creation of elastohydrodynamic lubrication layers [12,63]. In contrast, slip in yield stress fluids of concentrated rigid non-Brownian particles arises from a local depletion of particles, lowering the concentration of the sample near to the wall [12,63,97]. This depletion can result in a thin lubrication layer of the interstitial liquid which lowers both the adhesion and shear induced yield stress. However, the nature of slip can also vary depending on the boundaries and imposed shear rate [104,105].

Under certain conditions the apparent slip is a result of shear banding, with the shear localised to a thin layer near to the boundaries [63]. This results in the fluid being separated into multiple bands that have different shear rates [106] as seen in fig. 51.

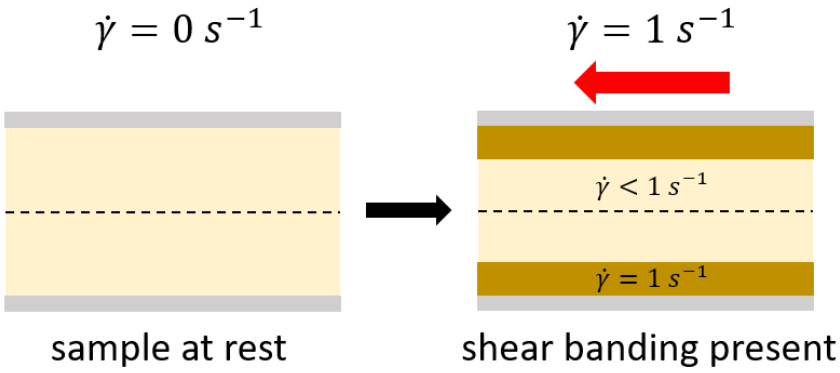

Figure 51: schematic diagram of shear banding. During a shear experiment shear bands can develop as the fluid is strained. These will either grow to encompass the entire sample (transient band) or will remain during an experiment.

The time at which steady-state flow is reached then depends on the applied shear-rate $\dot{\gamma}$. However, permanent shear bands can also be generated as a result of boundary slip. At the microscopic level slip is controlled by the complex interactions of the particles with the rough topography and surface chemistry [107]. Whilst it has been possible to correlate changes in slip with suspension microstructure for certain select cases [65], understanding this complex relationship is still a challenge for most systems.

Traditionally rheological measurements have attempted to avoid or suppress slip of the fluid at boundaries with the use of roughened surfaces as discussed in the previous chapter. However, in many real-world applications, slip can be beneficial (see Chapter One), reducing the stress required to move a sample relative to a boundary [63]. Particularly for the case of high solid dispersions, slip at interfaces controls the sample flow properties and can prove unavoidable [63,108]. Industrially slip is also a very important consideration because it describes how materials can be transported. In the oil and gas sector, slip can be very beneficial.

A major problem in drilling industries is bit balling: large amounts of clay become adhered to the drill and it is no longer able to cut through the sediment. The operators are then forced to bring the assembly, sometimes several kilometres, back up to the surface so that it can be cleaned before drilling can continue. This process

can significantly reduce the efficiency of a site as well as increase its operating costs. Adhesion and slip are both nontrivial behaviours and an understanding of the factors governing the type of slip in an adhesion measurement or its effect on the measured force–distance curves, would have useful consequences for practical applications.

Figure 52: An example of the issue of bit balling. Clay and sediment has adhered to the drill assembly to such a significant degree the operators are using a spade to remove the thick layers built up. Image was taken in Columbia by Schlumberger employees, obtained from [110].

A number of studies have performed adhesion tests on clay [100] or high solid content pastes [95,96,110]. However, the majority of these studies were designed to result in no or very little slip. In this work, we perform adhesion tests using kaolin clay where slip is possible. Focussing on the initial stages of the flow we find that changes in the observed slip of the fluid at the boundaries result in qualitatively different force–distance curves. We show how the nature of the slip during the initial stages varies with clay concentration, boundary roughness, the initial compressive load and deformation rate. We also discuss to what extent these initial differences play a role in the break-up behaviour of the samples.

3.2 Method

Kaolin clay suspensions were prepared as described in chapter two. For comparison, measurements were also performed using a 2 wt%, 10 kDa Carbopol Ultrez 10 suspension, neutralised by dropwise addition of 0.1M NaOH and dispersed using a magnetic stirrer at a spin speed of 200 rpm.

All measurements were made with a Kinexus Pro rheometer (Malvern Panalytical) equipped with a 20 mm diameter parallel plate upper geometry and a Perspex block (10 mm thick) was used as the lower plate. The surface of the top plate was covered with a 20 mm diameter Perspex disc which had been roughened by sandblasting with Saftigrit Brown 100 (Guyson, ~ 125μm). The roughness was chosen to be comparable to the largest particle size in the clay (in monodisperse particle pastes this is believed to provide the optimum conditions to reduce slip [63]). The Perspex block lower plate was also sandblasted to match the surface characteristics of the upper plate. A few experiments were also carried out using rheometer plates covered with P40 and P320 sandpaper (grit size ~ 350μm and 45μm, respectively) for comparison.

Time-lapse images of the samples were recorded with a camera (Point Grey, USB Flea 3) from both the side and from below (through the Perspex block) to observe the sample morphology and dynamics. Using the side view images, the motion of the sample edge was also quantified using image analysis. A binary image of the sample was generated through thresholding (OpenCV, Python). From this the width of the sample at different heights could be calculated in each frame. The width very close to the rheometer plate and the minimum width in each frame, occurring at approximately the midpoint between the plates, were then extracted to quantify the sample slip and break-up behaviour. The gap between the plates was calculated by multiplying the time by the known plate velocity.

The sample moisture content was stabilised throughout the experiment using transparent Perspex covers with in-built moisture reservoirs (humidity ~ 90%) as described in Chapter Two. These were only briefly removed to load and trim the sample. Independent tests were carried out which showed that the mass loss over the timescale of the experiments (~ 20 min) was < 0.5% as described in Chapter Two.

All samples were pre-sheared at 20 s^{-1} for 5 min at a gap height of 1.05 mm, often referred to as the "trim height" (except where specified) before trimming and

lowering to a working height of 1 mm. Several different types of rheological measurements were made on the samples following this initialisation protocol. All the different rheological measurements were performed at least 3 times. Adhesion tests were performed by raising the upper plate at a constant vertical velocity of 10 μms^{-1} (except where specified), whilst measuring the normal force on the upper plate. The velocity was chosen to ensure the estimated shear flow at the sample edge was well below that required for bulk fluidisation.

The bulk properties of the samples were characterised in shear using the 20 mm diameter parallel plate geometry covered with P40 sandpaper. Shear start-up measurements were performed at a constant shear rate of 0.01 s^{-1} (comparable to the extensional rate V_z/h_0). Stress against strain plots were used to extract the measured yield stress from the maximum stress value for all the concentrations used [107]. Selected concentrations were also measured using a decreasing shear ramp (one decade/minute, $\dot{\gamma} \sim 10{-}10^{-3}\,s^{-1}$). Amplitude sweeps in oscillatory shear were also performed at 0.4 Hz to measure the bulk visco-elastic moduli. Estimates of the yield stress with all of these techniques gave comparable values.

Prior to these measurements some samples were sprayed with a vertical line in red acrylic paint using a stencil to confirm there was no slip [31,111]. Similar experiments were also performed with the roughened Perspex to observe the slip behaviour during the initial stages of the flow of 50 and 60 wt% clay. This technique was also used to confirm that the sample was fully fluidised during the pre-shear sample preparation protocol.

Whilst our aim was to study the effects of slip, which is more pronounced on smoother surfaces, initial tests indicated that using Perspex plates sandblasted with a finer grit did not exhibit bulk fluidisation even at high shear rates, see Chapter Two. In contrast, the roughness of the Perspex plates used in this chapter allowed strong bulk fluidisation at high shear rates, ensuring a reproducible initial state. In between each set of experiments both Perspex surfaces were carefully cleaned to remove all clay and then dried with N_2. By default, the normal force sensor on the rheometer uses a low pass frequency filter which is used to smooth the data. Unfortunately, this can result in increasing and decreasing changes in force being smoothed out if the cut off frequency is too low (i.e. the measured peak value is reduced). In order to be confident

of the quantitative forces measured at the peak we switched the frequency filtering off and then after the measurement filtered the raw data using a low pass frequency filter. In doing this we checked carefully that the cut off value did not alter the shape of the measured curves.

3.3 Results and Discussion

3.3.1 Concentration dependence of adhesion tests

Adhesion tests were carried out on kaolin suspensions at a range of concentrations between 45 and 65 wt% ($\varphi \sim 0.31-0.47$). In each measurement the upper plate was slowly raised at a constant velocity of $10\mu ms^{-1}$, the evolution of the samples over the course of breakup was recorded as seen in fig. 53. Examples of these experiments are shown in fig. 54. In low concentration samples the middle of the sample progressively thins in a smooth fashion resulting in the deposition of two conical deposits (Fig. 53a). This is similar to the behaviour observed by a number of authors using the model fluid Carbopol [63,97].

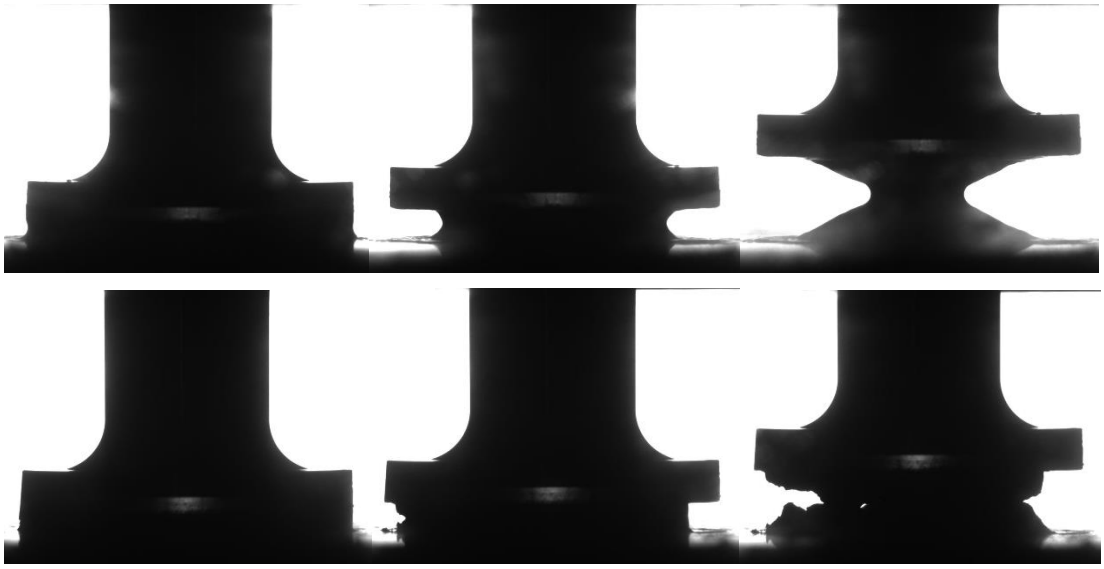

Figure 53: Images of the progression of the breakup dynamics of the 45 (top) and 65 (bottom) wt% kaolin clay samples. We observe that the 45 wt% sample pins on the surface and then the interface becomes a concave as extension increases. Meanwhile, the 65 wt% moves inwards more like a cylinder until it eventually fractures.

However, the break-up behaviour of high concentration samples is very different. These samples do not neck and flow as before but after moving a small distance towards the centre, the fluid breaks up by a solid-like fracture process (Fig. 54c). They appear to break long before a filament can be drawn. These dynamics strongly depend on the clay concentration with a gradual crossover in the behaviour observed at ~ 50-55 wt% (Fig. 53b).

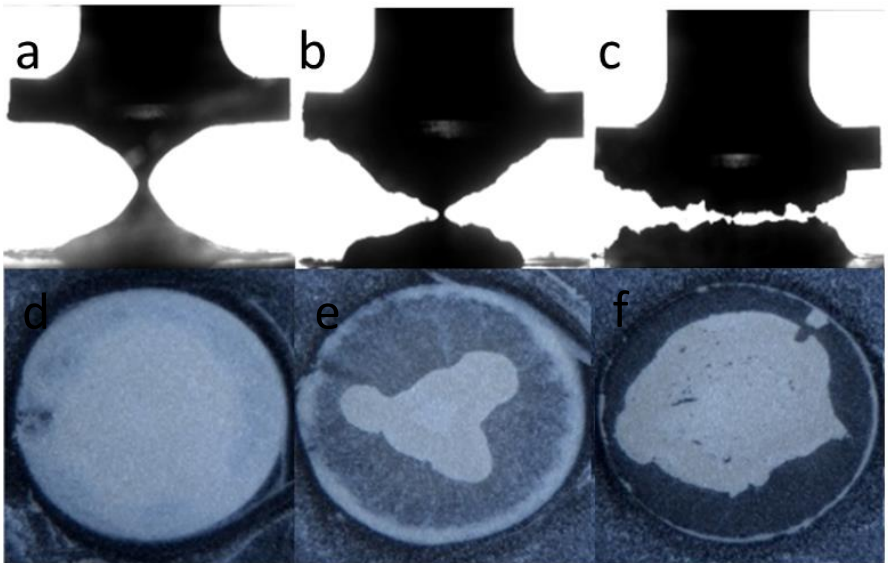

Figure 54: Images taken from the side and from below the kaolin samples during adhesion tests (velocity = 10 µms^{-1}) on the roughened Perspex plates, (a) 45 wt%, (b) 55 wt%, and (c) 65 wt%. The samples show a transition from filament to fracture-like breakup behaviour.

Observation of the adhesion test from below the sample, via the transparent bottom plate, reveals some interesting differences in the deposition behaviour as the concentration of the suspension is increased (see fig. 54 lower panels). Each image shows the final configuration of deposited fluid after breakup. In the middle of each image a white object shows the bulk clay, which is thick enough to be opaque. At the periphery of the sample the highest concentration clay shows a thin white ring of clay. This is wider at intermediate clay concentrations and appears to extend from the edge all the way to the centre for the lowest concentrations. In between the periphery and the central mass of clay we observe that a sparse thin film of clay is left behind on the surface. This region corresponds to the moving contact line of the samples. At low clay concentrations this film is significant and almost thick enough to be opaque. In contrast, at the highest concentration there is almost no clay adhered to the surface in this region. The central region of deposition which is conical and relatively symmetric at low concentrations becomes quite unstable and asymmetric with something

resembling a fracture surface at the highest concentrations [95]; however, we do not observe the fractal-like structures that have been observed in other yield stress fluids [93,97 – 99]. This is perhaps due to the higher yield stress of our paste, a property which can suppress fingering [98]. We include supplementary videos of the 45 and 65 wt% pull-off experiments to demonstrate this behaviour.

A feature that is apparent from the videos of the different concentration experiments is that the initial stages, for both low and high concentrations, look qualitatively different, in each case exhibiting significant slip. These qualitative observations of the dynamics can be confirmed by measuring the width of the sample (viewed from the side) as a function of the plate separation (see pages 75-76). We measured near the rheometer plate and at the narrowest point, which occurs near the middle of the sample, to generate a spatiotemporal diagram from the recordings of the pull off experiments.

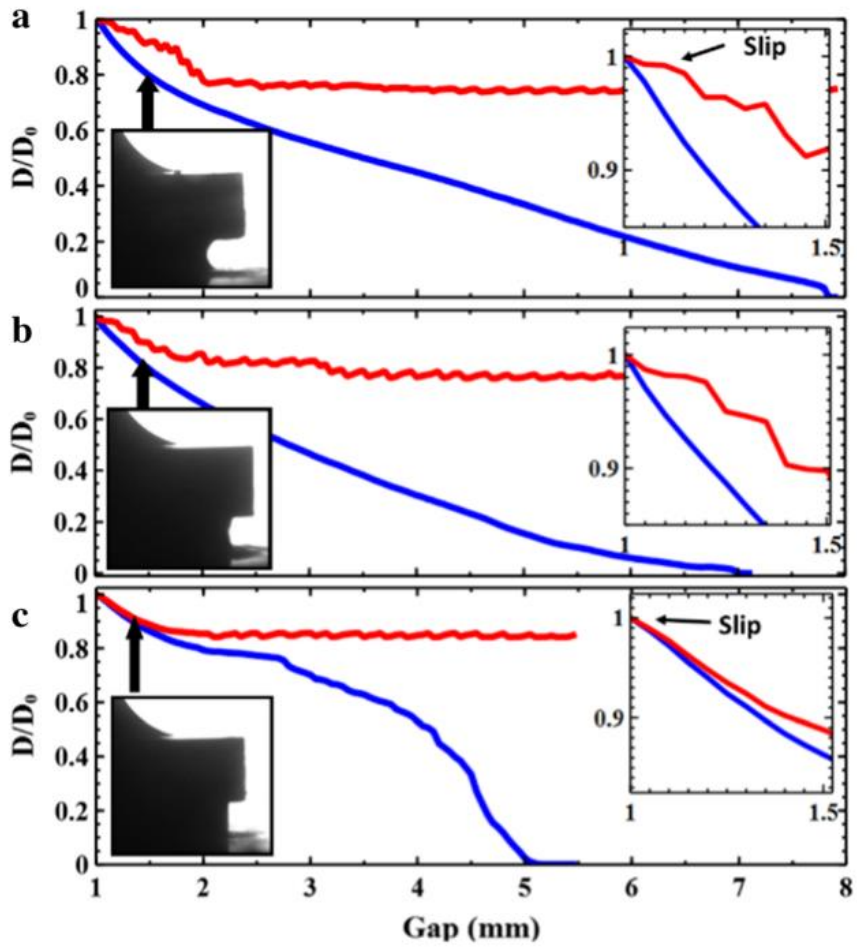

Figure 55: Spatiotemporal diagrams of the 45 (a), 55 (b) and 65 wt% (c) pull off experiments. The red line represents the clay near to the plate surface. The blue lines show the clay at its thinnest point. Arrow in inset is pointing to the initial slip behaviour in each experiment as a function of concentration.

The width measurements in fig. 55 close to the plate (red lines) show some small oscillations. These are an artefact of the image processing due to small variations in lighting and the acute contact angle at the edge of the sample. This can be seen from the fact that they persist even once the contact line remains stationary. Despite this the differences in sample dynamics are clear. Figure 55a shows a 45 wt% sample. From the very first moments of the experiment the width decreases more quickly at the midpoint than near the plate, as a consequence of a pronounced curvature developing at the sample edge. As the plate continues to rise, the contact line undergoes apparent slip. When the contact line has moved approximately a quarter of the way from the edge to the centre it then stops moving. The central region then continues to narrow at a constant rate. Finally, the thin neck between the two halves breaks up, leaving two conical deposits behind.

In contrast to this, the high concentration samples exhibit very different dynamics (see Fig. 55c). At the beginning of the experiment both the mid-point and the region near the plate move together. This corresponds to an initially smooth and approximately vertical contact line slipping along the bottom plate deforming as a block. There then follows a short period in which the sample appears to neck slightly (Gap = 1.5−2mm). However, this is quickly overtaken by a break-up process that resembles fracture, in which the sample does not slip. Although the analysis here helps to clearly delineate the different sample dynamics, it is difficult to reliably extract quantitative information (e.g. contact line velocities) from these plots. As seen in fig. 54d–f the final sample morphologies can be at times quite asymmetric. Consequently, the widths measured would depend on the orientation of the sample relative to the camera.

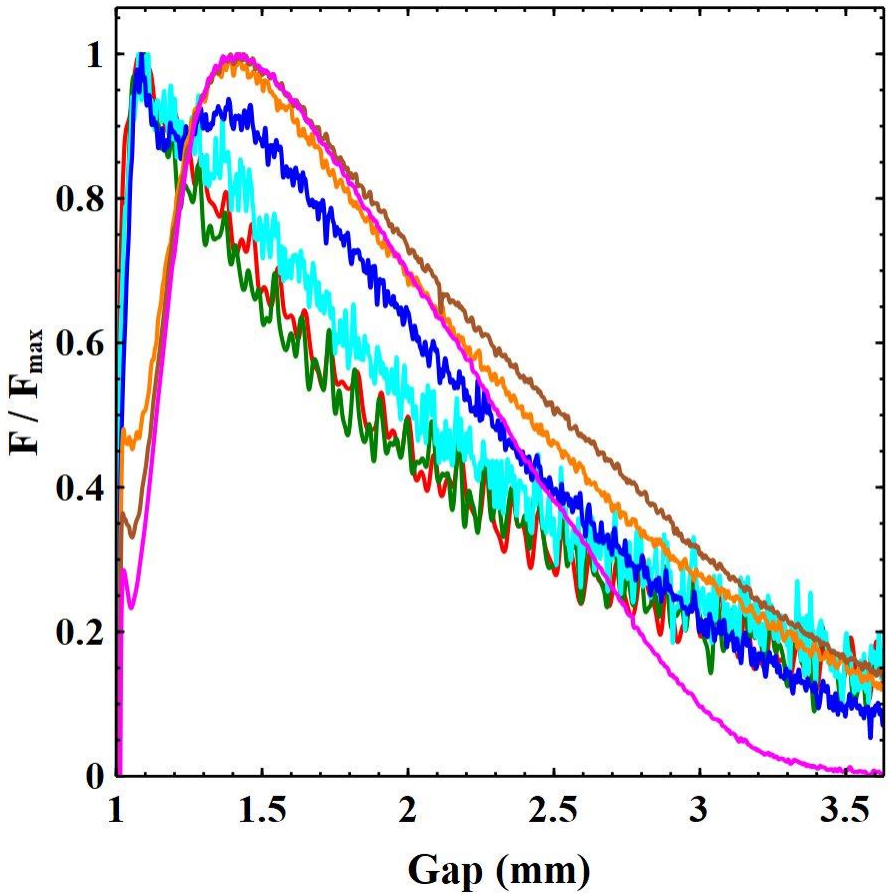

Figure 56: F/Fmax for various concentrations on the Saftigrit roughened plates. 55 (blue). The curves fall into two different qualitative shapes which correlate with the initial slip behaviour at the edge of the sample. The low concentration clays 45 (red), 47.5 (green) 50 (turquoise) show a peak force close to the initial stages of the experiment. The high concentration clays60 (orange), 62.5 (brown) and 65 wt% (pink) show a peak later in the experiment. 55 wt% (blue) shows features of both high and low concentration clays.

The force response of the clays were also recorded. Fig. 56 shows the normal force curves for different clay concentrations; these have been normalised by the maximum measured force (F_{max}). Measurements of the shear yield stress were also obtained using the same parallel plates covered in P40 sandpaper, which prevents slip (see Chapter Two, fig 33). The maximum normal forces measured during the different experimental adhesion tests mirror these large changes in material stiffness spanning two orders of magnitude (see fig. 57). The adhesion test force curves clearly fall into two qualitatively different categories of behaviour. The differences in concentration profoundly affect the shape of the early stages of the measured curves.

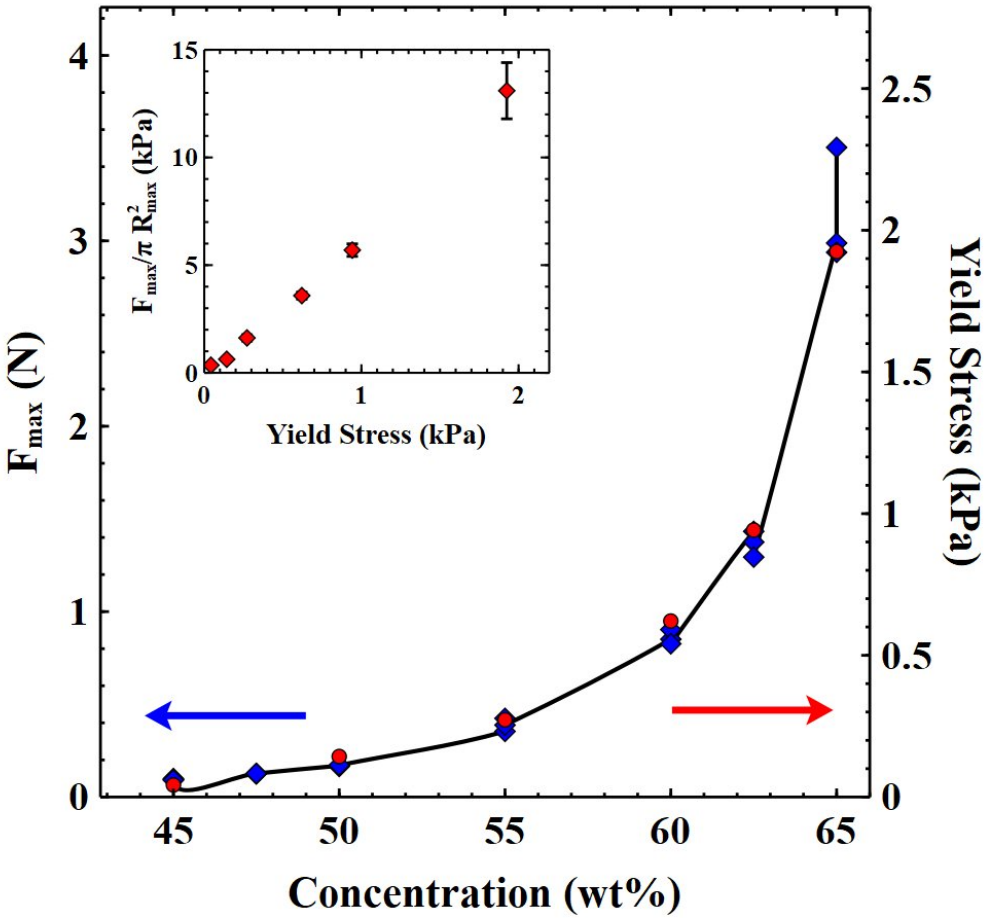

Figure 57: Comparison of the yield stress (red) with the maximum force (blue) of each kaolin concentration. The inset shows the approximately linear relationship between yield stress and the scaled maximum force.

Although the force distance curves have been normalised for easier comparison between the concentrations, the pattern of the evolution of the maximum force fits very well with how the yield stress increases as a function of concentration. The initial rise in the force during an adhesion test has commonly been attributed to some sort of elastic or viscoelastic loading of the sample [1]. All our samples exhibit an initial steep increase in force with separation which is consistent with this.

In the low concentration samples the force curves have a relatively simple form. The force rises to a maximum, after a small movement of the plates ($h/h_0 \approx 1.08$), and then rapidly decays. The slip of the contact line starts at the position shown in the inset of Fig. 55a ($h/h_0 = 1.100 \pm 0.025$). The onset of sample slip and the maximum in the force curve appear to occur together for low concentration samples. An initially pinned contact line, with visco-elastic loading of the bulk sample results in a critical stress that is sufficient to produce yielding of the sample. As the sample contact line begins to move, the deposition of a substantial layer of clay on the surface (see Fig. 54d) seems to indicate that the apparent slip occurs by a kind of shear localisation, resulting in the strong yielding of a thin layer of material near to the plates.

Following this maximum, the measured forces decay as the sample yields and slips concurrently. Figure 58 shows a log–log plot of the force vs separation for the low concentration samples. The scaling of the force with plate separation in an adhesion test is known to depend on the boundary conditions at the interface. Samples undergoing perfect slip exhibit an extensional flow with a force that scales with h^{-1} [101].

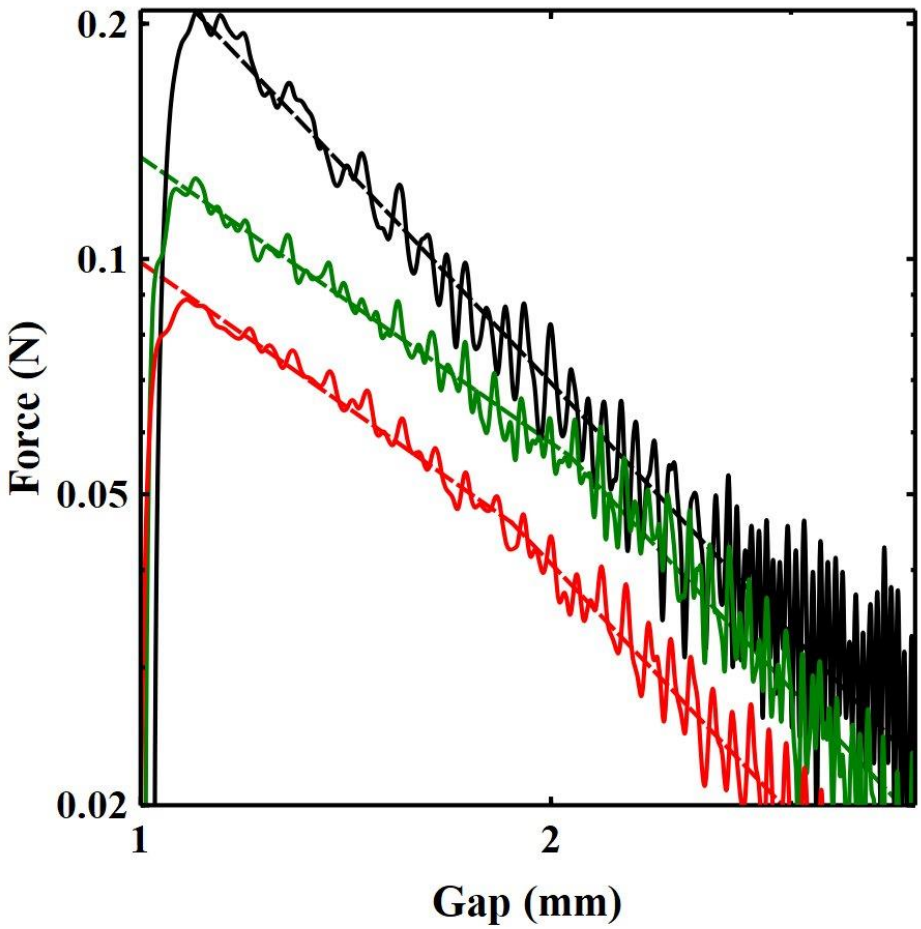

Figure 58: Force distance curves of the Carbopol (black), 47.5 (green) and 45 wt% (red). The Carbopol suspension which does not exhibit slip has a gradient on a log–log plot of −1.9. In contrast, the low concentration kaolin samples, following the maximum in the measured force, slip resulting in a gradient of −1.2. As the plates continue to separate the sample stops slipping which corresponds to a change in the measured gradient to ∼ −1.9.

For comparison we provide a similar measurement obtained in the same way for a 2 wt%, Ultrez U10 Carbopol suspension (Black) which behaves as a model simple yield stress fluid and has been frequently studied with adhesion tests [97,101]. The concentration of Carbopol was chosen to give force measurements of similar magnitude to the low concentration clay samples. Whilst our data covers a limited range and is somewhat noisy it is possible to extract the power law exponents. A fit to the Carbopol data (black), after the peak, results in a power law exponent of ∼ −1.9 for nearly the entire range of the data. Observation of the Carbopol sample reveals very little motion of the contact line/slip. In this and similar measurements by other authors [94,98] the exponent remains constant until the final stages of breakup. In the low concentration clay samples, we however observe that the power law exponent is initially much shallower ∼ −1.2 and then transitions to a gradient of ∼ −1.9

(see Fig. 58). Divoux et al. [99], studying a particle gel, also observed a change in the power law exponent during an adhesion test, to a value ∼ −2. The transition to the second stage occurred at a critical gap at which the final deposit diameter remained constant. The exponent, -2, was found to be related to the necking behaviour of the filament. Figure 58 shows that the transition in our samples occurs at a gap ∼ 2mm. Comparing this with the width measurements in fig. 55a, it seems that this is also the gap at which the contact line is arrested. As the experiment proceeds the aspect ratio of the sample (h/R) grows. The difference in cross-sectional area between the midpoint and the end plates also increases.

The Carbopol suspension which does not exhibit slip has a gradient on a log–log plot of −1.9. In contrast the low concentration kaolin samples, following the maximum in the measured force, slip resulting in a gradient of −1.2. As the plates continue to separate the sample stops slipping which corresponds to a change in the measured gradient to ∼ −1.9. Consequently, the stress is largest at the midpoint and reduces towards the boundaries. Beyond some critical separation, the stress required at the boundary to create slip is no longer exceeded. It seems therefore that the change in exponent reflects the crossover from a force curve that is strongly modified by slip, to one in which the forces reflect solely the necking of the bulk material.

At high clay concentrations we observe a slightly more complicated shape of force curve. The force undergoes an initial steep linear rise (see Fig. 55 main panel and inset c). This initial rise however has a "kink" at very small strain values ($h/h_0 \approx 1.025$, see Fig. 59).

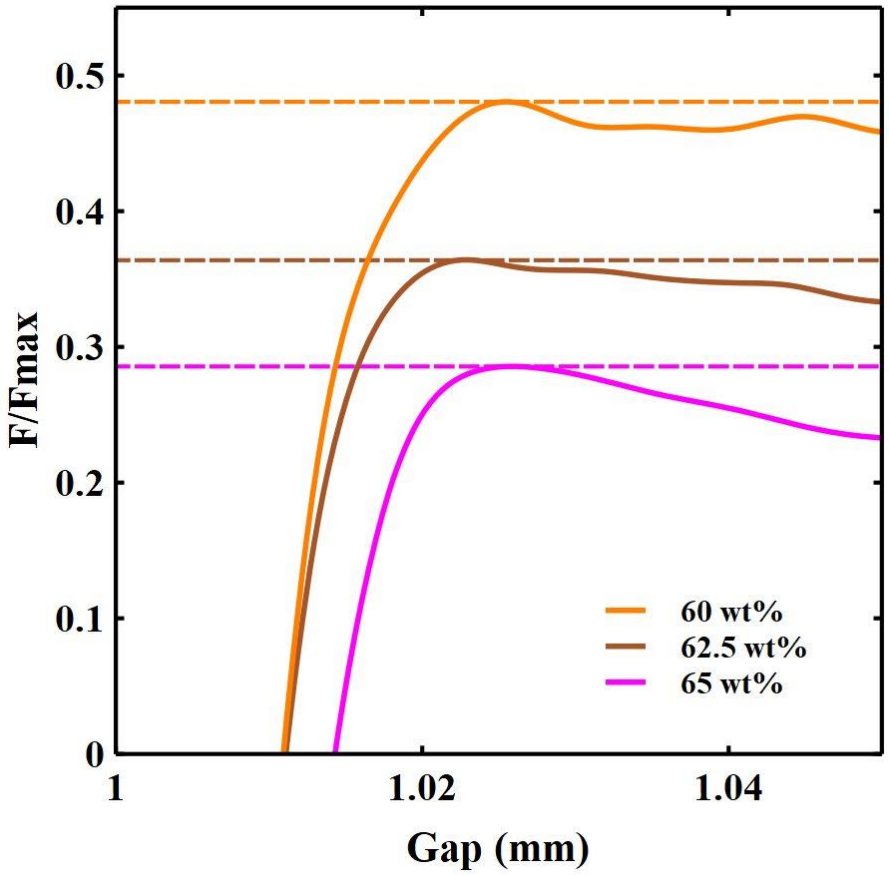

Figure 59: The initial "kinks" in the force data for the high concentration samples which correspond to the onset of slip. The dotted lines indicate the definition of F_{slip}.

Figure 55c shows images of the edge of the 65 wt% sample. This, unlike the low concentration samples, appears to slip almost immediately with a contact angle of close to 90◦. In these stiffer samples, the normal stress for a given extensional strain is larger, exceeding the stress required to induce slip before significant deformation of the exposed interface has begun. The sample therefore begins to slip along the plates, deforming as a cylindrical block, until a plate separation of 1.250 ± 0.025 mm. At this point there is a difference for the first time in the narrowing of the contact line and the sample midpoint. The contact line now gradually slows before becoming completely pinned at $h/h_0 \approx 1.8$. The onset of the "fracture-like" break up begins prior to the cessation of motion of the contact line but after the midpoint has begun to narrow faster than the contact line.

The maximum in the force curve occurs between these two points at $h/h_0 \approx 1.4$, although unlike the low concentration samples it is a broad peak and does not seem to be linked to a specific event, as the onset of slip was for the kink. The influence of the very initial motion of the contact line on the shape of an adhesion test's force–distance curve was commented on previously by Zhang et al. [101] in a slightly different context. They found that with the same sample conditions and experimental parameters there were significant difficulties in reproducing experimentally measured force curves. The curves exhibited two very different shapes and they explained this by the adherence or slip of the contact line in the initial phase. Adherence of the contact line would alter the local shear flow which then evolves as the experiment progresses. They postulate that in their experiments contact line adherence might be affected by drying or imperfections of the solid surface. In addition to using humidity covers (see Chapter Two) to prevent evaporative losses, we confirmed that drying was not responsible for the observed behaviour by performing experiments with a 20 min gap between trimming and the measurement. Adhesion tests performed with and without the wait had the same behaviour, indicating that drying of the sample periphery was not responsible. The roughened surface provides a large number of pinning sites. However, our experiments suggest that different concentration clays interact with this roughness differently, resulting in different slip conditions. The principal idea, that the initial adherence of the contact line plays a role in determining the shape of the measured curves, is however the same.

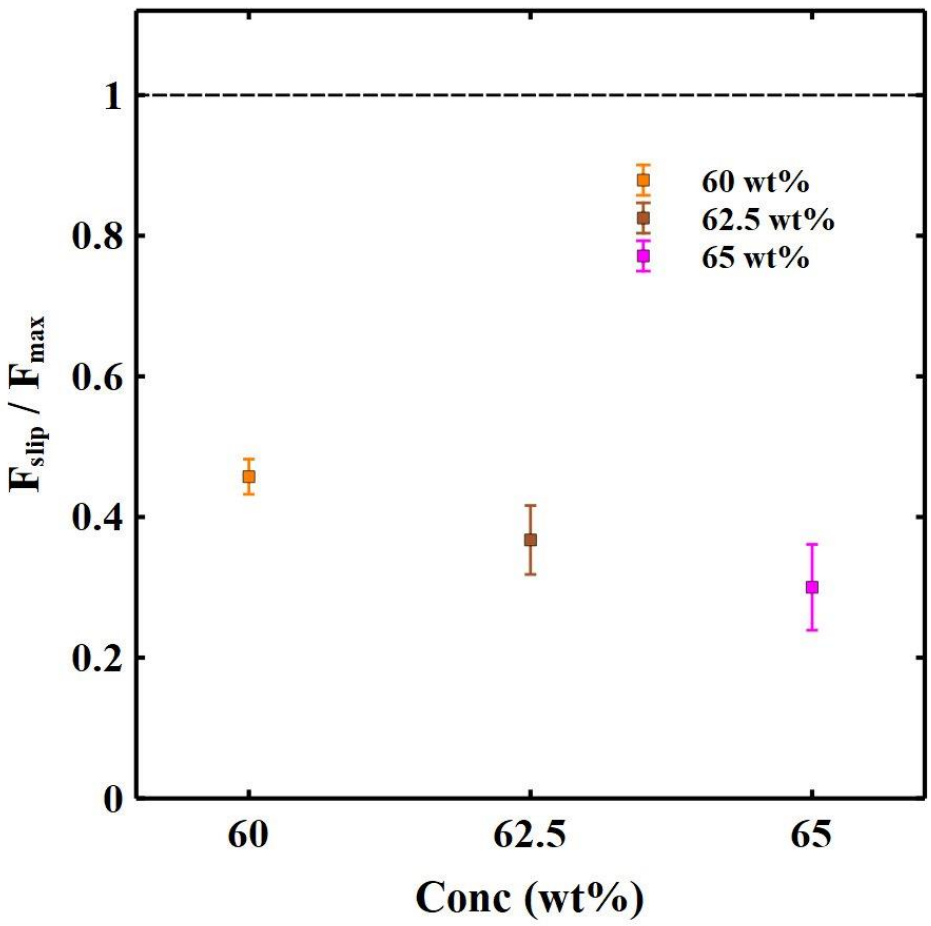

Figure 60: F_{slip}/F_{max} of the 60, 62.5 and 65 wt% kaolin clays. F_{slip} recorded from the "kink" observed at low h/h_o which is displayed as the initial plateau in figure 58.

The measured force at which the high concentration samples begin to slip (F_{slip}) increases monotonically with the clay concentration. Figure 60 shows that the ratio F_{slip}/F_{max} of the higher concentration samples decreases with increasing clay concentration. This indicates that relative to the stress generated by extension of the clay (which is a function of sample stiffness) it becomes easier for these samples to slip with increasing concentration. Our observations in fig. 54 of the deposited clay thickness indicate that as the concentration of clay increases the shear becomes increasingly localised at the boundary. Decreases in slip-layer thickness with increasing concentration of particles have been measured before in capillary flows but with slip-layers a fraction of a particle diameter [63]. The use of roughened surfaces in our experiments would make the development of a particle diameter slip-layer impossible and mean this slip-layer must be thicker. Capillary flow of a concentrated hard sphere suspension comparing flow of smooth and rough surfaces showed a similar increase in the sheared layer thickness [112]. The interaction of the particles with the rough surface topography is complex with effects such as particle layering and

jamming. However, it appears that the thickness of the surface slip layer still decreases with particle concentration and is correlated with an increased propensity for slip prior to strong yielding.

Following the initial rise with increasing gap height, the force (F/F_{max}) in the high concentration samples continues to increase to a maximum. Figure 56 shows that the higher concentration samples have a maximum in the force at a significantly larger plate separation ($h/h_0 \approx 1.4$) than the low concentration samples. This is long after the sample has begun to slip along the wall and seems to correspond to the first signs of the contact line becoming unstable and beginning to pin. An important consequence of the initial slip is therefore to delay the strong yielding of the bulk sample. After this one observes a fracture-like breakup. The crossover from a more ductile to more brittle-like fracture has been observed in similar experiments of both concentrated suspensions and foams and is likely related to the concentration dependent properties of the bulk. [113,114].

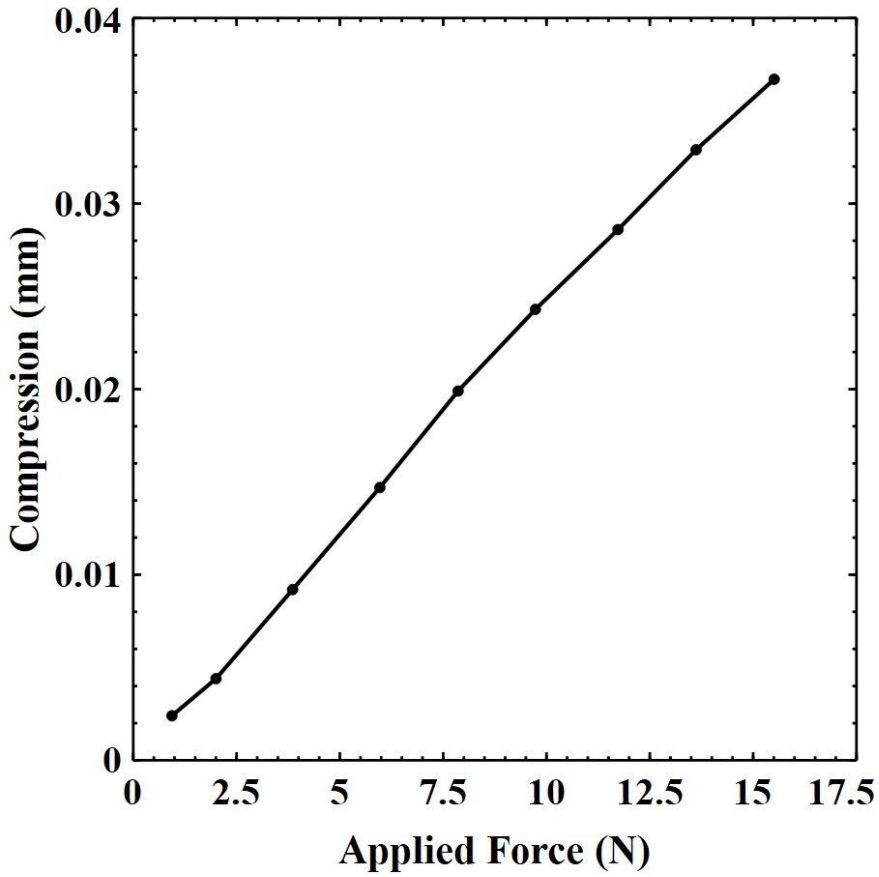

Figure 61: Compliance data recorded for the Kinexus Pro Rheometer

Under some experimental conditions the initial rise in force has also been attributed to the compliance of the rheometer/normal force sensor [93,96]. One can assess the likely impact of this on our experiments by measuring the spring constant of the rheometer load cell. To measure the stiffness of the sensor we placed a steel disc on the rheometer and applied increasing levels of compressive force with the upper plate. Measuring the recorded displacement gives a straight line with gradient 412.3 ± 0.2 kNm^{-1} equal to the effective spring constant of the normal force sensor, see fig. 61. This is an order of magnitude larger than the biggest force gradient measured in this study corresponding to a ~ 2.5 µm gap correction for a 1 N load making this at most a small correction. Furthermore, the motion of the plates is always slow, such that inertia can be neglected. We therefore conclude that the rise in force simply reflects sample properties.

3.3.2 Initial Slip Behaviour and Simple Shear Observations

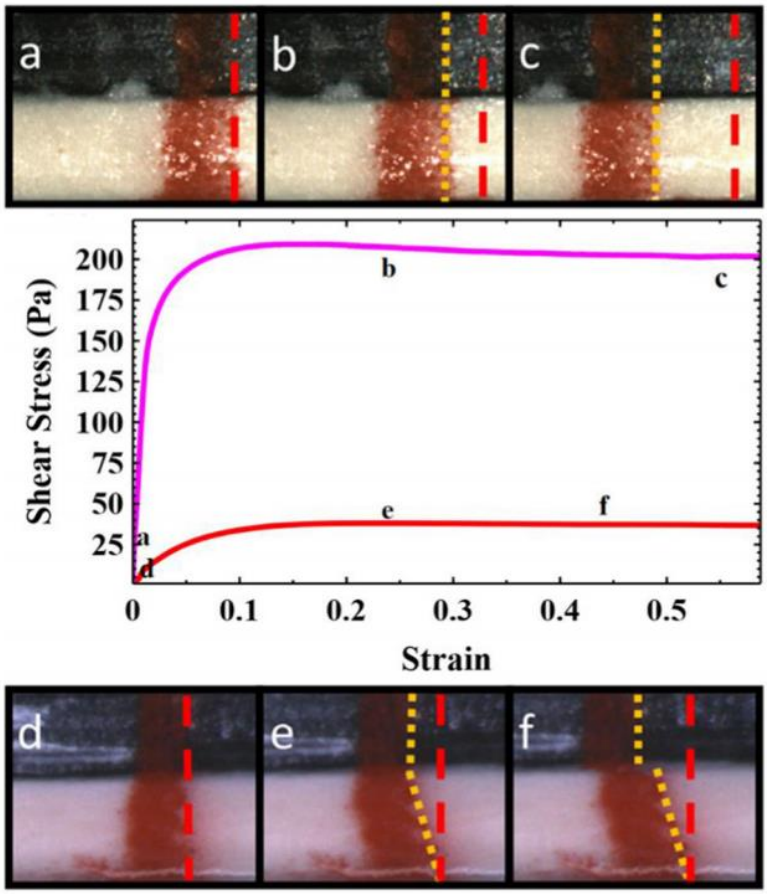

Figure 62: Sample deformation and slip in the startup of simple shear experiments for a 60 wt% (a,b,c, pink) and 50 wt% (d,e,f, red) kaolin clay at a shear rate of 0.01s^{-1}. Before each shear start-up experiment, a red line is sprayed vertically, coating the outside edge of the rheometer plate (black) and the clay (white). The superimposed red line shows the initial position of the right-hand edge of this line. The superimposed yellow line tracks this same edge throughout the experiment.

Using a simple shear measurement at a constant shear rate of 0.01s^{-1} we observed the flow/slip characteristics for the 50 and 60 wt% clay samples on the same roughened Perspex plates. Our aim was to compare the transient behaviour of different concentrations at start-up, since this is similar to the situation encountered during the earliest stages of an adhesion test, where because of the small aspect ratio (h_0/R_0) the flow may exhibit a significant shear component.

A vertical line sprayed on the sample periphery with a stencil enabled us to observe how the clay flows/slips [31,112]. Figure 62 shows example images showing the sample deformation at the appropriate points on the stress– strain curve. The higher concentration sample (top) undergoes no observable deformation, and slips relative to

the bottom plate like a plug almost immediately (b,c). In contrast the lower concentration sample (bottom) initially does not slip and undergoes a shear deformation (e). When the sample reaches a critical strain value ~0.25 the sample then begins to slip relative to the top plate (f), with the bulk undergoing no further deformation. The stress–strain curves in both cases plateau at lower values than those measured with P40 sandpaper in the absence of slip (see Chapter Two, fig. 33). The plateau stress in fig. 62, whilst still related to the sample yield stress, is reduced by the slip.

Prior to reaching steady-state slip, the start-up behaviour of the two concentrations is apparently quite different. For the higher concentration sample the fluid apparently undergoes very little deformation before the sample slips cleanly at one interface. In contrast, for the low concentration samples, we initially observe no slip. A constant velocity gradient results in the line initially rotating with the shear profile. When the shear strain reaches a critical value ~0.25 the sample then begins to slip along the moving plate. This experiment mirrors some of the observations on slip deduced from adhesion tests, supporting our interpretation. There is a change in the slip behaviour that results in slip with very little sample deformation at high concentrations and a strong deformation of the sample prior to slip at lower concentrations.

However, we did also notice some differences between the two types of experiment. In the adhesion test at low concentrations, a thick film of particles is left behind as the clay yields and slips. One might therefore expect an equivalent thin shear band near one of the plates in shear. It is possible that it is too thin to observe, but we estimate this should be within the resolution of our images. Another noticeable feature in the shear experiments is that once the lower concentration sample begins to slip there is no further deformation/yielding of the bulk clay. We can clearly see this by the fact that the red line undergoes no further deformation. This contrasts with the adhesion test where the sample edge deforms up to the point at which slip occurs, thereafter strongly yielding. We believe it is likely that these two observations are related.

In the simple shear experiment the shear stress is constant throughout the thickness of the sample. In contrast the deformation of the interface at the edge of the low concentration adhesion tests results in a narrowing of the central portion of the sample. There is therefore a lower stress at the plate boundaries than at the midpoint. This might suggest that the deposited material is the result of the stress gradient induced by the initial pinning and deformation of the contact line. That we see far less material deposited by higher concentration samples would fit with this interpretation since the vertical contact line ensures a relatively uniform stress.

3.3.3 The Effect of Surface Roughness

Our initial experiments raise some interesting questions as to what extent and in what ways the initial slip characteristics influence the final breakup behaviour and measured force curve? To test this, we performed adhesion tests using P40 and P320 sandpaper (grit sizes ~350μm and ~50μm). In constant shear-rate experiments, using the P40 sandpaper, slip was found to be completely suppressed. In adhesion tests the sample still underwent some slip across the sample surface but it is clear that the slip is significantly reduced. The 60 wt% sample on the Perspex maintains a very straight edge as it slips, only deviating once the plate gap reaches $h \approx 2.5\, h_0$.

In contrast, during an adhesion test on the P40, the clay in contact with the plates initially pins and then lags behind the mid-point of the sample before again pinning and undergoing breakup by a horizontal fracture-like process. Whilst the slip characteristics on the rougher surface are similar to lower concentration samples, the final breakup behaviour still undergoes a fracture-like process consistent with the high concentration clay. Figure 63 shows 3 repeat adhesion test measurements of a 60 wt% Kaolin clay for the roughened Perspex (red) and the much rougher P40 (green). We see a considerable change in the qualitative shape of the measured force curves.

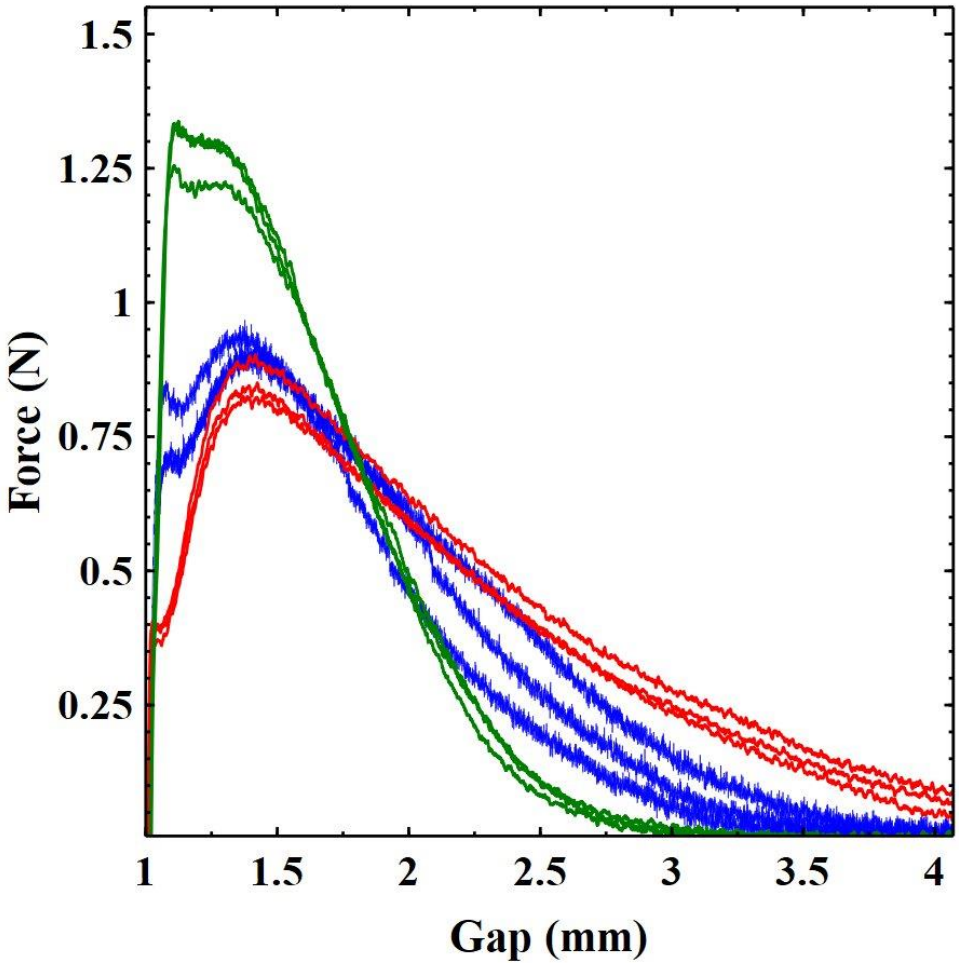

Figure 63: The effect of surface roughness on adhesion tests of a 60 wt% Kaolin paste. Displayed are the roughened Perspex (red), P320 (blue, grit size ~50 μm) and P40 (green, grit size ~350 μm) sandpapers.

To confirm that the physical behaviour measured in fig. 63 was caused by the increase in surface roughness rather than the chemical properties of the surface we also used a finer sandpaper P320 (blue) which more closely matched the roughness of the Perspex than the rougher P40. Comparing the curve shapes with our concentration dependent measurements in fig. 56, the rougher surface appears to have the qualitative shape of a lower concentration sample.

Earlier, we argued that it was harder (relatively speaking) for the low concentration samples to slip. Increasing the roughness of the surface also makes it harder for the samples to slip. Divoux et al. [25] showed, in simple shear start-up experiments on a microgel, that reducing the surface roughness decreased the maximum measured stress and critical strain at which slip began. Our adhesion tests exhibit this same behaviour with smoother surfaces slipping at smaller strains and lower forces. We also invariably observe a small drop in force at the moment slip

begins, before the measured force continues to rise. This relaxation of elastically-stored energy may be akin to the stress overshoot sometimes observed during transient start-up measurements which can be related to slip (see fig. 63) [25,103]. As noted, the final observed breakup behaviour was not so strongly influenced by the change in surface roughness. The fact that this is not obvious from the force curves is due to two factors. Firstly, breakup occurs when $h/h_0 > 3$ by which time the cross-sectional area of the sample and hence measured forces are much lower (cf fig. 55). Secondly, in all cases the sample stops slipping prior to final breakup at which point the breakup behaviour must be solely determined by the sample's bulk properties.

3.3.4 Modifying the initial compressive normal force

Our measurements indicate that the initial development of slip in our experiments can subsequently influence the dynamics and breakup behaviour during an adhesion test. The development of slip during the start of the flow involves the initial interactions of the particles with the confining surfaces and each other. This is presumably modified by factors such as how well the constituent particles pack into the topography of the roughened surface, which generates resistance to slippage [104]. Any changes to this packing not only modify the local volume fraction but also the amount of water, which lubricates particle–particle and particle–surface contacts.

We performed a series of adhesion tests with 60 wt% clay in which we slightly modified the preparation protocol. The pre-shear of the clay was performed at gap heights 1.02, 1.05, 1.10 and 1.15 mm. The normal force was monitored during each stage of the experimental protocol, i.e. the compression to trim height, pre-shear, compression to working height, to monitor how it develops during the experiment. We found that, despite a large build up of force during the compression to trim height, seen in figure 64 as the first spike, the normal force measured is zero at the end of the pre-shear process as it is effectively dissipated. We do however observe that after the sample is trimmed and further compressed to the working height (1 mm) there is a second spike in the measured force. This force increases with increasing Δh as one would expect. We also observe that during simple shear experiments that this built up normal force dissipates as the total strain increases. Of course, this process takes significantly longer than during the pre-shear step owing to the much lower shear strain

rate applied. Despite the normal force also showing a measurable increase it was always shown to dissipate to zero over time. This suggests that an increase in compression force during this step can have a distinct effect on the structure of the sample that will influence how it behaves during rheological tests.

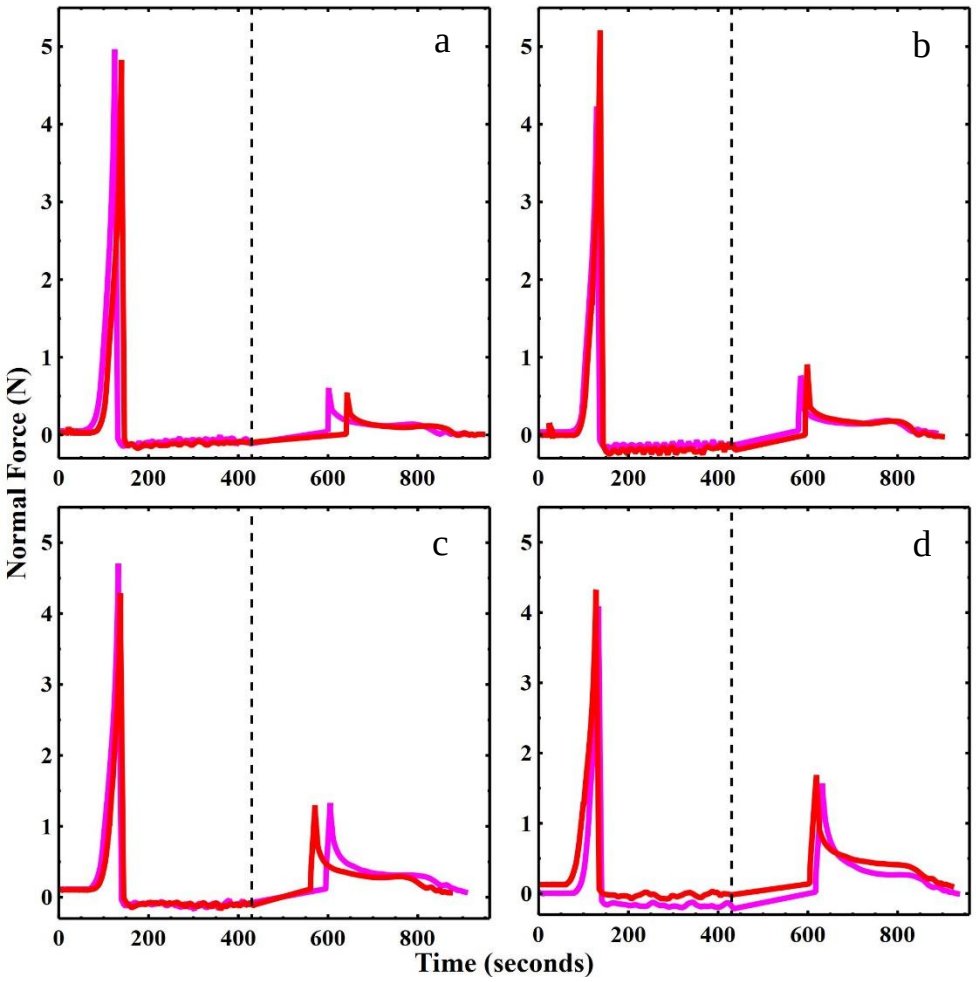

Figure 64: Force profiles of the 60 wt% clay during a simple shear rheology experiment with increasing initial trim heights of 1.02 (a), 1.05 (b), 1.10 (c) and 1.15 mm (d). The initial spike is the result of the initial compression to the trim height and in general decreases as the compression distance decreases. This force is immediately relieved by the pre-shear process (end of the pre-shear step marked by the dotted line). The second spike in force is due to the compression from trim to working height. We observe that for an ascending shear ramp the force from the second spike takes time to dissipate unlike what is observed during the pre-shear step.

Since each sample undergoes a different amount of compression, the sample is subjected to a different final compressive normal force which depends on the clay concentration and the change in gap height prior to the experiment. A particularly interesting observation during this approach to the initial height is that one can observe a small amount of liquid escaping at the periphery of the samples near to the confining

rheometer plates during the larger compression steps. A video of this process, which is included in the supplementary information, shows this process for a 60 wt% clay undergoing the compression step prior to the adhesion test.

To investigate the effect of this difference in preparation history we performed identical adhesion tests after preparation. The samples have the same initial gap height (1 mm) and the upper plate is moved upwards at the same speed (10 μms^{-1}). Figure 65 shows how the forces measured in the early stages depend on the separation of the plates.

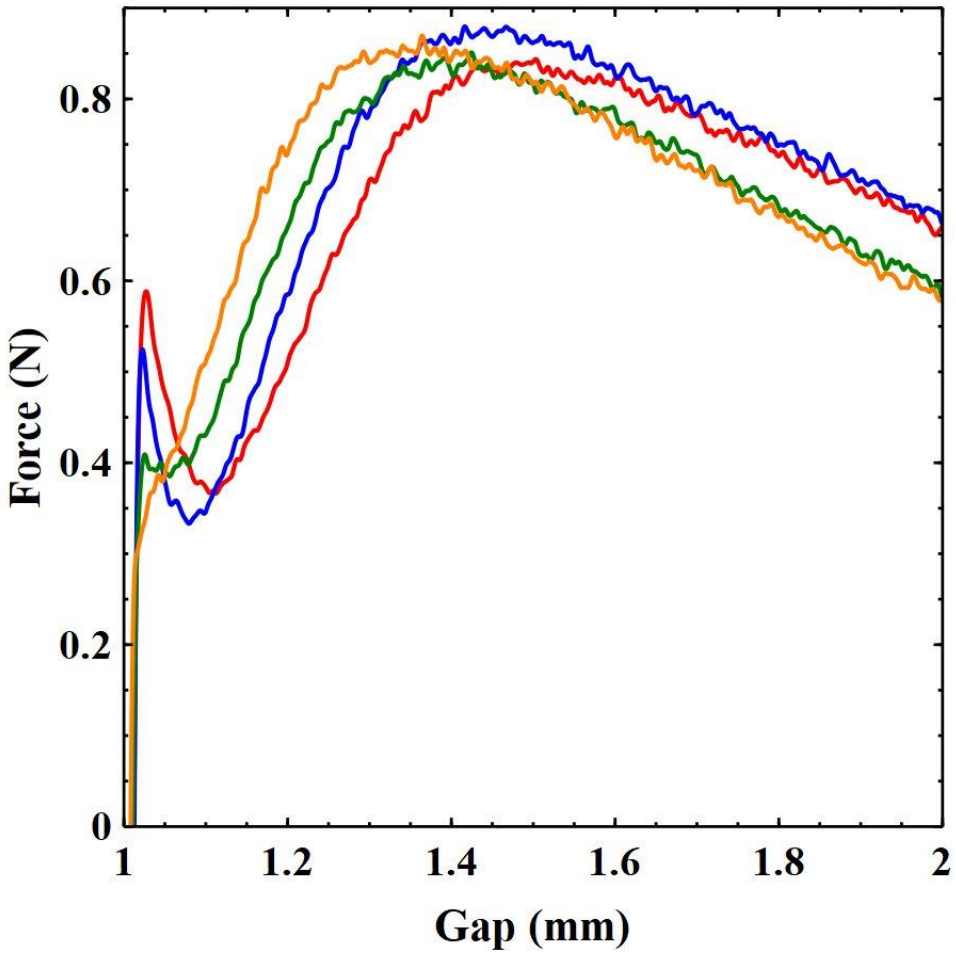

Figure 65: Changes in slip as a function of the sample protocol's compressive load. Samples of 60 wt% kaolin are presheared at slightly different initial gap heights and then trimmed. The gap height is then lowered by Δh (mm) to the working height 1mm. Different compression steps result in a different compressive load. Following this the same adhesion test is performed, moving the plates apart at 10 μms^{-1}. 1.02 (orange), 1.05 (green), 1.10 (blue) and 1.15 mm (red) are displayed.

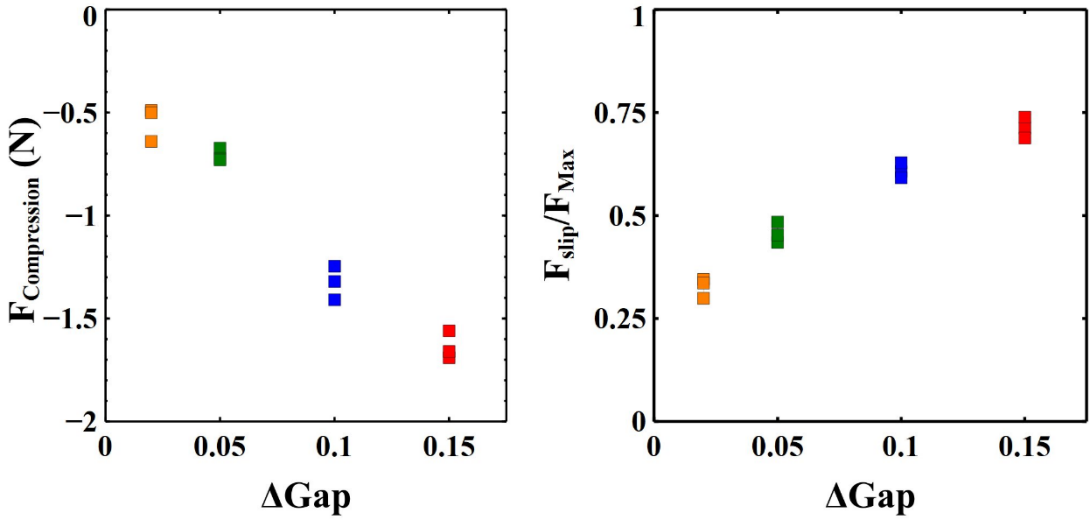

Figure 66: Presented on the left is the dependence of the compressive load on the compression step size. Right shows how the value of F_{slip}/F_{max} is modified by the initial compressive load. It indicates that there is an increased resistance to slip following an increase in initial compressive load during the preparation protocol. The colours in both this figure and fig 64 point to the same changes Δ Gap as indicated.

We observe a significant increase in the value of F_{slip} with increased compression indicating that the initial resistance to slip has significantly increased. However, as soon as slip begins it is obvious (particularly in the more highly compressed samples) that there is a relaxation of the force before it again builds to the maximum. This would seem to indicate that the samples initially undergo visco-elastic loading up to a maximum determined by the force required to induce slip. Slip then releases some of this stored energy before stresses again build up in the sample.

Figures 65 and 66 suggest that the initial slip behaviour of the fluid can be tuned by the compaction force that is applied. Whilst some compaction occurs, one might expect this to make the measured force curves appear more like those of higher concentration samples. Ideally one would like to measure the bulk viscoelastic properties of the samples following each compressive step.

We attempted to perform oscillatory measurements of the moduli; however, due to the slip relative to the rheometer plates, this resulted in very unstable measurements which weren't reproducible. The normal force measurements do however show that F_{max} is independent of the initial compression (Fig. 65). In Fig. 60 the value of F_{max} was shown to be strongly correlated with the bulk yield stress of the sample, providing some evidence that the bulk properties are not significantly altered. In fact, after the initial slip, the shape of the curves looks very similar, though slightly

shifted. In light of this, it is interesting that there is such a dramatic increase in F_{slip} with initial load. Figure 66, right, shows the ratio F_{slip}/F_{max} for these samples. F_{slip}/F_{max} increases with an increase in the initial compression step. Comparing these data with Fig. 65 also indicates that with increasing compression of the sample the slip characteristics are surprisingly more like those of lower concentration samples. This is the opposite of what one might expect if the changes in slip were simply due to compaction of the clay during the compression step. The increase in F_{slip} would however make sense if the clay particles are compressed into a more tightly packed/jammed structure in the rough surface topography. This would also explain why water is seen to emerge preferentially at the surface of the rheometer plates. The increased inter-particle friction and interactions with the surface would make it harder for the sample to generate a slip layer by yielding locally, whilst leaving the bulk properties largely unchanged.

It should be noted that, at the very least, increasing the initial compressive force provides a simple way to modify the initial slip characteristics of a paste without having to alter the sample or surface topography. There are however potential difficulties with these experiments which need to be considered. Firstly, there will be a slight under-/overfilling of the sample edge. Most of the experiments in this chapter were performed using a change in gap height (between trimming and the starting gap height) of 0.05mm. This value was chosen since it resulted in an initially square edge to the sample. Assuming a constant sample volume and that the sample deforms as a cylinder, we estimate that the sample radius would therefore be 0.25 mm (2.5%) overfilled for Δh = 0.1 mm and 0.15 mm (1.5%) underfilled for Δh = 0.02 mm. Secondly, the increased normal force may result in some compaction of the clay, which may or may not be reversible. The escape of water from the sample indicates that there must be some compaction. However, the water appears to be escaping near the plates, and there are no obvious changes to the sample surface at the midpoint which is corroborated by the acrylic paint. The additional volume amounts to just a few percent but it could have an influence on what is measured. For example, the gap at which F_{max} is measured seems to increase with larger compression steps. It would make sense that if there is slightly more clay, that the gap at which different features are observed increases.

3.3.5 The effect of strain-rate on observed slip characteristics

To explore the dependence of strain-rate on slip, we focussed on the intermediate clay concentration of 55 wt%. Figure 67 shows 3 sets of adhesion tests conducted with the 55 wt% clay samples. In these measurements we altered the plate velocity to see whether the shape of the measured force curves indicated changes in slip behaviour. Data are shown for measurements obtained with V_z = 100, 10 and 3.3 μms^{-1}. The lower velocity was chosen so that an experiment could be completed inside 20 min (the timescale for which we previously checked the results were unaffected by drying).

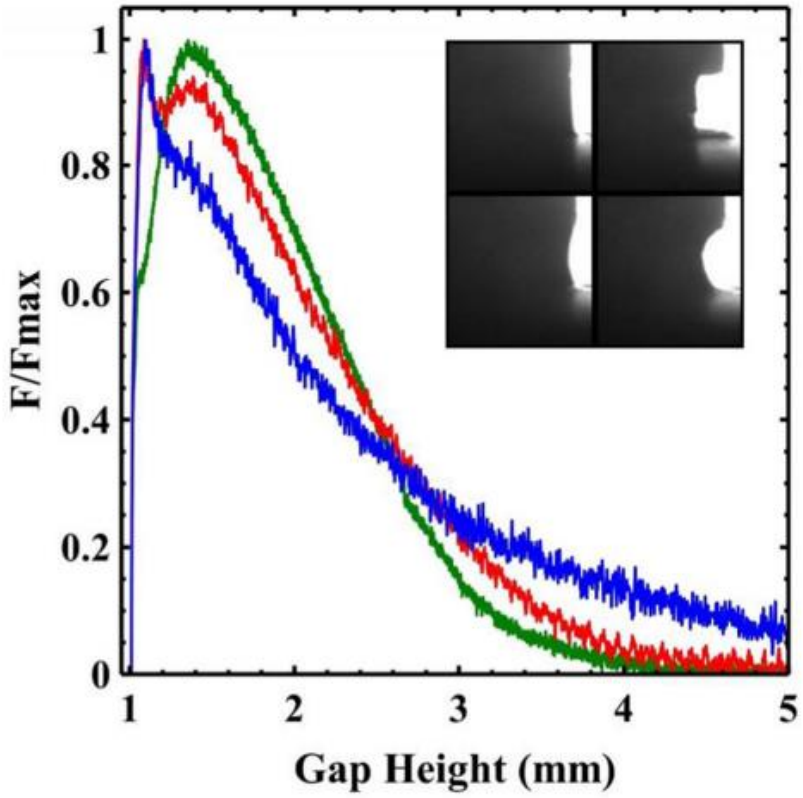

Figure 67: Adhesion test force curves for 55 wt% Kaolin paste. Curves are shown for plate velocities of 100 μms^{-1} (blue), 10 μms^{-1} (red), 3.3 μms^{-1} (green). Inset: images of the sample periphery for the lowest strain-rate (top) and highest strain-rate (bottom).

Shear measurements of the 55 wt% sample showed that the measured stress did not increase significantly above the yield stress at shear rates below 2 s^{-1}. We therefore selected 100 μms^{-1} on the basis that with an aspect ratio h_0/R_0 = 0.1 a crude estimate of the apparent shear-rate induced at the edge of an adhesion test (for a completely pinned sample) would be $2V_{radial}/h_0 \sim 2R_0V_z/h^2_0 = 2\ s^{-1}$. Measurements of

the work of adhesion showed no appreciable change due to rate, indicating that the viscous term associated with the adhesion energy still scales simply with the yield stress [99] as it did for our earlier measurements (Fig. 57). At the lowest plate velocity, one observes that the characteristic shape of the force curves changes to more closely resemble that of the high concentration clays with a single peak at $h/h_0 \approx 1.4$. We see a vertical contact line that slips smoothly across the surface. As the plate velocity is increased the corresponding force curves begin to resemble the lower concentration clays more closely. The force curve at the lowest plate velocity has a marked kink at $F/F_{max} \sim 0.6$ indicating the onset of slip significantly before strong yielding at $h/h_0 = 1.4$.

The force curve for the highest plate velocity does not quite have the same shape as our lowest concentration samples. There is still a significant shoulder at $h \approx 1.3$ mm similar to the one exhibited by the 50 wt% sample as shown in Fig. 55. This indicates that the slip behaviour should be somewhat intermediate between the extremes illustrated in Fig. 55. The sample periphery for the highest rate experiment does appear to have more curvature than the lowest rate, and the slip behaviour is likewise altered in the ways previously outlined. Only a few studies have looked at the rate dependence of slip during transient rheological experiments for yield stress fluids. LAOS experiments on a PDMS yield stress fluid found no dependence on shear-rate [115]. Divoux et al found that shear-rate did modify the measured stress overshoot and slip behaviour of a colloidal gel. However, this dependence appears to relate to the changes in sample elastic modulus with waiting time [25].

In our concentration dependence studies we noted changes to the thickness of deposited clay, thought to be associated with the slip layer. With our strain-rate dependent measurements, the changes to slip were more modest and hence it was difficult to confidently state whether more clay was, or was not being deposited in each case. However, shear rate experiments below a critical value often led to localised shear with a slip-layer thickness that depends on the slip velocity/apparent shear-rate [108]. Given our earlier observations it seems reasonable that there would be some associated change in slip layer thickness. Aral et al. showed that the development of a slip layer to its equilibrium thickness can also require considerable time for a concentrated suspension [117]. One possibility is that the shear-rate dependence results from changes to the magnitude of F_{slip} that arise from the transient development

of the slip-layer in the initial stages. However, more quantitative measurements of the growth of this slip layer during start-up would be required to clarify with confidence the origin of the shear-rate dependence.

3.4 Conclusions

We have shown that whilst the breakup behaviour of a concentrated kaolin clay is controlled by the sample concentration, the initial stages of an adhesion test are very sensitive to slip. Changes in concentration, surface roughness, initial compressive load and extension rate all modify the slip conditions leading to two qualitatively different classes of force-distance curve shape. As the force required for slip relative to the sample yield stress decreases, the plate separation at which the maximum force is measured increases. We observed that features such as a small peak indicating the onset of slip, and the maximum at which large scale yielding of the sample begins can provide useful information about the type of clay being dealt with. The changes in slip appear to originate from differences in the way the layers of clay near the roughened topology of the surface yields compared to that in the bulk. We also showed that the lubrication conditions near to the interface may be changed during the initial sample loading, potentially altering the subsequent slip behaviour.

Chapter 4 Work with ICASE Industrial Partners

4.1 Introduction

The work carried out in this thesis was funded by the EPSRC and the oil and gas services company Schlumberger. As part of the ICASE programme a three-month industrial placement at the Schlumberger Cambridge Research Centre was undertaken towards the end of my second year.

The aim of this project was to develop a method of utilising x-ray shadowgraphy to capture the internal flow behaviour of kaolin clay under shear in real time. A further goal was also to attempt to record any concentration changes within the clay during the process. Rheology is a very useful technique for measuring the overall shear behaviour of fluids. However, it can be difficult to infer changes in the internal macrostructure from it, particularly for opaque fluids like kaolin clay. Could simple shear affect the local concentrations? Are there other processes hidden by the surface? In Chapters Two and Three we demonstrated that under compression there can be a significant release of water, particularly near the fluid/plate interface. This behaviour implies that there is a local concentration gradient which will influence the rheological behaviour one observes as postulated in fig. 68.

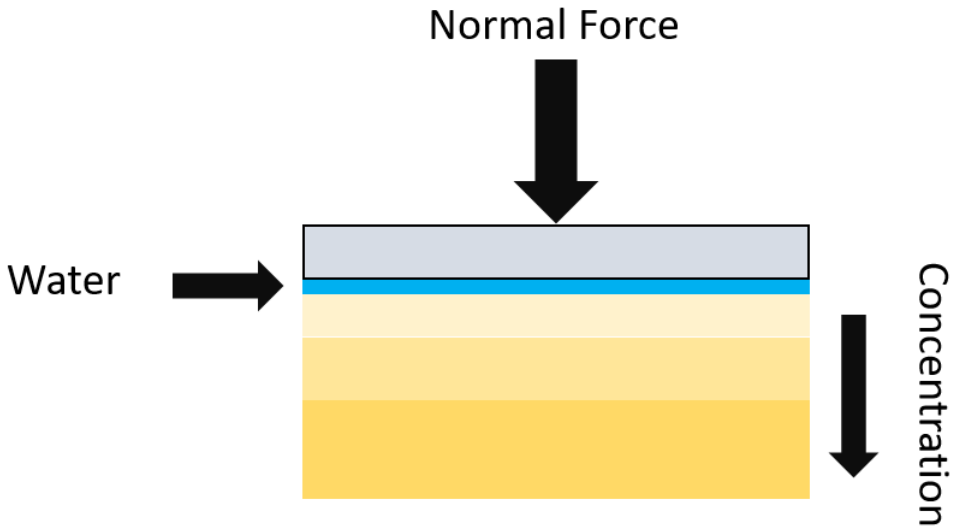

Figure 68: Schematic of a possible concentration gradient that is established in the kaolin when it is compressed by an external normal force.

The inspiration for this project was a commonly used industrial technique called the “Rolling Bar” test [64]. In this technique a length of metal pipe is placed within a chamber with drilling fluid and soil cuttings. The chamber is rolled to simulate conditions within the borehole (at atmospheric pressure). Afterwards the metal bar is removed and dried to measure the solid mass of soil that has adhered to its surface.

Figure 69: Left is an image of a rolling bar test cell, the images on the right are taken after the experiment has been carried out and the clay has adhered to the surface of the bar. Obtained from [118].

Industrial drilling muds have two key functions: they reduce the friction to the assembly head, reducing heat and increasing the lifetime of the cutters. They also provide a coating to the metal surface that discourages the broken-down rock and soils (cuttings) from adhering to its surface. If the build-up of material is too high the drill can no longer penetrate the surrounding rock and excavation ceases. The “Rolling Bar” experiment is used to indicate the effectiveness of drilling fluids at mitigating soil accretion to the surface of the drill. A drawback of this experiment is that it does not provide information about the mechanism of how soil becomes adhered to the drill surface.

In an attempt to provide this information, the rolling bar apparatus was adapted into a horizontal, Couette-like, prototype geometry that shall be referred to here as an "Annular Geometry". The purpose of this rig was to simulate the behaviour of a rotating drill as it travels through the soil to observe the flow dynamics of the mud. This was achieved by x-raying the clay doped with steel balls which appear black under x-ray emission. A very early desktop model was also constructed using sand, steel filling and oil to demonstrate the concept of the instrument. The video of this has been included in supplementary video 2.

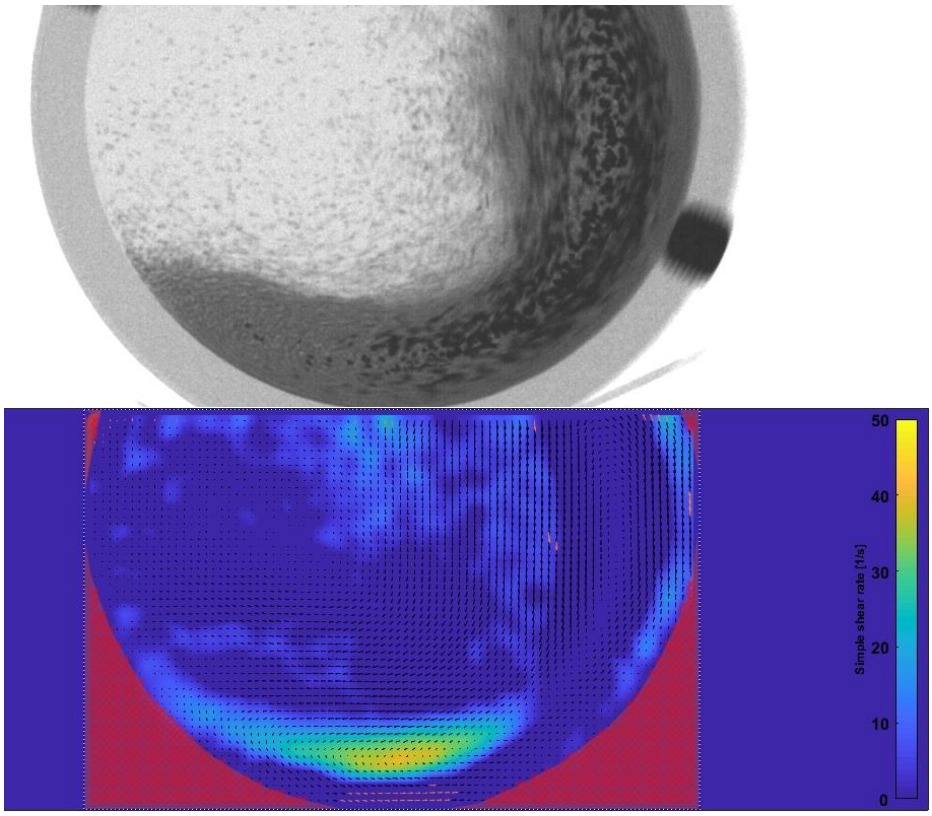

Figure 70: X-ray shadowgraph image of the benchtop model during operation. The colour map shows the average shear rate of the system during the entire process. This setup uses sand under oil to model the granular flow with steel shavings being used as a way of tracking the flow (shown in black).

4.2 Rig Design and Operation

The final rig is based on the desktop model in fig. 70 but consists of two 3D printed cylinders. The aim of the rig was to simulate the adhesive behaviour of clay in a drilling scenario. To achieve this the inner cylinder can rotate to simulate the movement of the drill through soil. The rig was placed in an x-ray chamber to visualise the motion of metal tracer particles. The cylinders were fitted with roughened Perspex strips as described in Chapters Two and Three (Saftigrit) to maintain similar conditions but in a different setup. The outer cylinder was also capable of rotation but we did not focus on this during the experiments performed

The equipment was designed in its entirety by Yousuf Faizi, an Engineering student from the University of Sheffield during his 12 month industrial placement at the research centre. Both he and Gary Oddie (former employee of Schlumberger) built the rig while I was present at the centre. The cylinders are placed within the frame on their side for easier visualisation of the sample during shear experiments, see fig. 71. The main advantage of this setup is that it allows the operator to load and shear large masses of a viscous fluid such as kaolin clay. This is not normally achievable using most rheometer geometries, especially not a traditional Couette geometry which is used to measure the rheology of low concentration fluids like gels or foams. Fig. 71 shows that there are 24 pins separated out evenly every 15 ^{o} to track the rotation of the inner cylinder (radius 89.5 mm). We can use these pins to determine the rotation speed of the cylinder which is 0.175 rad s^{-1}.

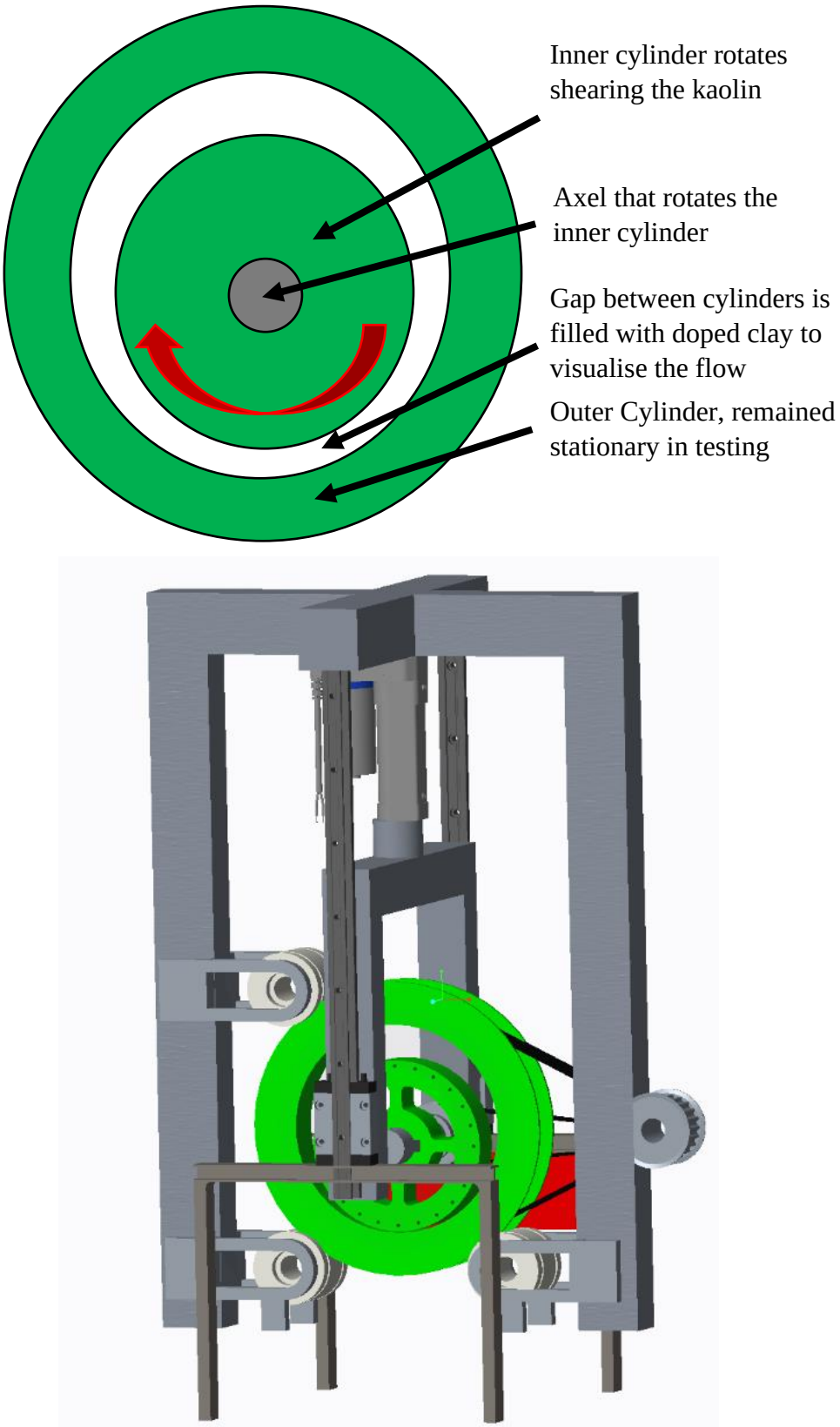

Figure 71: Top, A schematic diagram of the test rig, each cylinder is capable of rotating independently however in most tests one cylinder remains stationary. Bottom, CAD design of the rig made by Yousuf Faizi while at Schlumberger. Two cylinders act as the solid surfaces as the clay is sheared between them.

The cylinders of the rig were suspended within the outer frame pictured in fig 71 and 72. The inner cylinder is held in place by a metal axel which controls the speed that it rotates with as shown in the schematic. The gap between the cylinders was sealed by two Perspex sheets with a flexible rubber boot on either side to maintain moisture content, see fig. 72. By maintaining the moisture content of the kaolin we ensured that the concentration of the clay does not change during the experiment. Measurement of the mass loss showed that after three days within the rig the clay lost 1% of its total mass.

Each cylinder was connected to a motor by a belt to allow independent rotation. The speed of either cylinder could also be varied via two power supplies to provide a wide range of shear speeds. However, these speeds were estimated as it was still an early prototype at this time. This apparatus was put into an x-ray chamber to capture shadowgraphs of the kaolin during shear experiments.

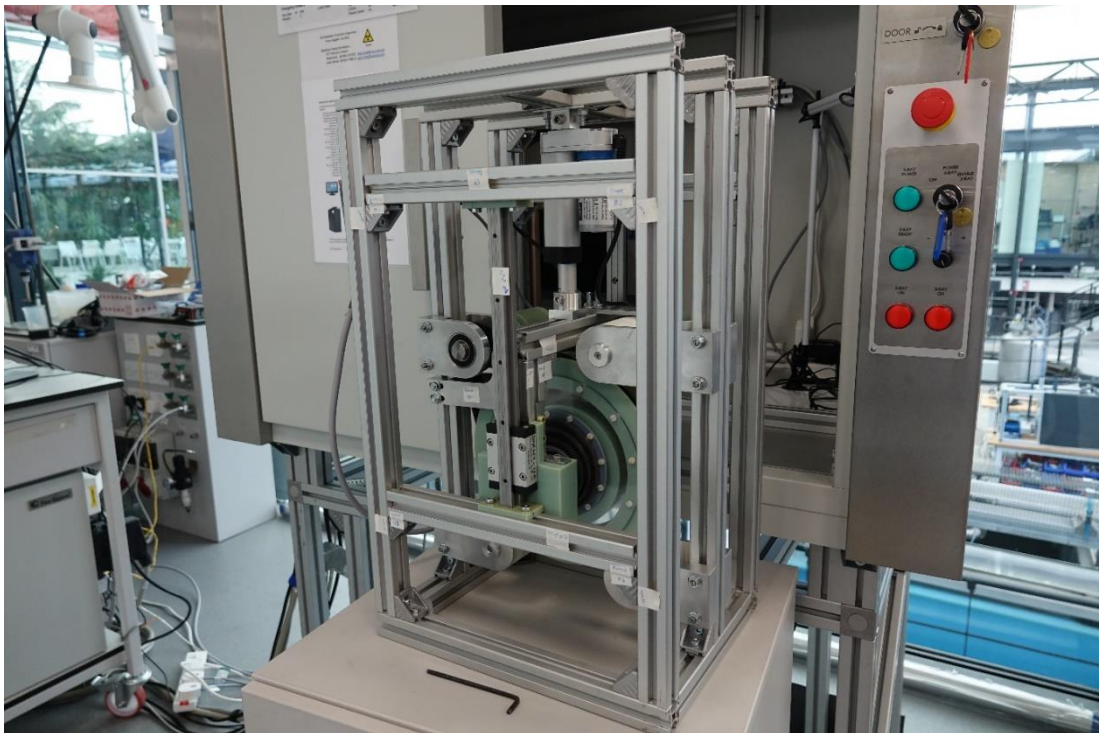

Figure 72: The fully assembled rig. This is placed inside the X-ray Chamber before operation to perform x-ray shadowgraphy during shear experiments.

4.3 X-ray Calibration

All experiments in this project were measured using a Rex Cell 1X x-ray instrument. It is equipped with a single x-ray source (20 – 80 kV, 0.5 – 7 mA, 0.4 – 0.8 mm focal point) opposite a single detector with dimensions 229.8 mm × 64.6 mm [117]. By altering the power settings of the x-ray source the resultant shadowgraphs can include or exclude certain details of the sample. Doing so allows the operator to penetrate an opaque object to observe the internal behaviour in real time. Preliminary tests using the bench top demonstration showed that the x-ray setup could visualise the flow of sand and steel pieces immersed in oil during the rotation of a Perspex chamber.

The source emits x-ray radiation that penetrates the sample. Some of this radiation is absorbed by the sample while the remaining light is transmitted to the detector. Unlike traditional UV/Vis spectrometers which give a single absorbance signal we obtain a greyscale shadowgraph. Objects appear as different grey values due to the intensity of transmitted light that arrives at the detector. The denser an object is the darker it will appear in the shadowgraph as the radiation must pass through more matter to reach the detector and the intensity is decreased significantly, fig. 73 shows and example of this.

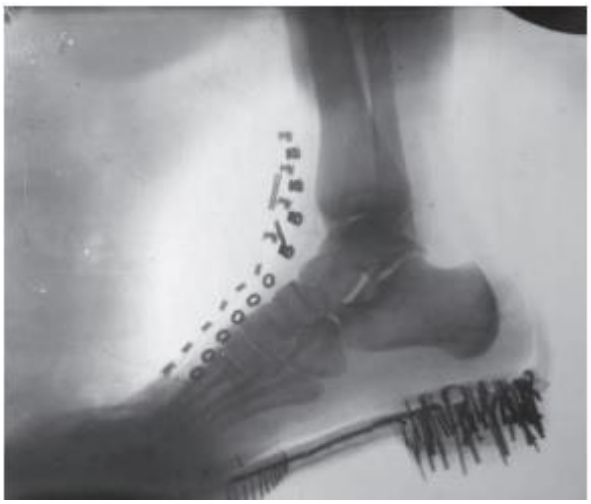

Figure 73: One of the earliest x-ray shadowgraphs produced by Nikola Tesla, obtained from [118].

Shadowgraphs are a powerful tool for detecting the internal structure of objects in a non-invasive and non-destructive manner and have an extensive history of application in the medical field for detecting broken bones or organ damage without performing invasive surgery.

The transmittance of light through an object can be calculated by the ratio of the transmitted light after it has passed through an object to the initial (incident) light emitted from the source, $T = I/I_o$ as shown

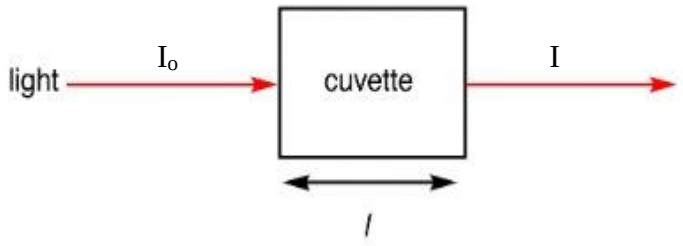

Figure 74: Diagram of incident light passing through an object. The resultant transmitted light leaves and typically shows a lower intensity [121].

We can also determine the absorbance of the fluid by using Beer's law which is commonly written as $A = \varepsilon cl$ where A is the absorbance, ε is the extinction co-efficient specific to each chemical species, c is the concentration of the species and l is the path length of the sample (typically on the scale of centimeters) [119]. In other applications such as UV/Vis spectrometry Beer's law is useful for identifying unknown chemical species or their concentration.

In this setup we use Beer's Law to obtain relative values of absorption to relate to the concentration of the kaolin. The absorbance can be calculated from the intensities of incident and transmitted light from $A = \log_{10}(I_o/I)$ or just the transmitted light using $A = -\log_{10}T$ [119].

We expected to observe that each concentration of kaolin would give a unique transmittance value. This would allow for the identification of concentration changes when shadowgraphs were taken of the rig during shear experiments. To provide evidence that this was possible a selection of kaolin clays (50, 55 and 60 wt%) were made up. These samples were put in plastic cuvettes on their sides to measure the gray value. The gray value indicates the brightness of a pixel, the higher the gray value in this case, the less dense the material the x-ray is passing through. By laying the cuvettes on their side the thickness of the samples would be similar to the thickness of the clay within the annular geometry (~ 36 mm thick).

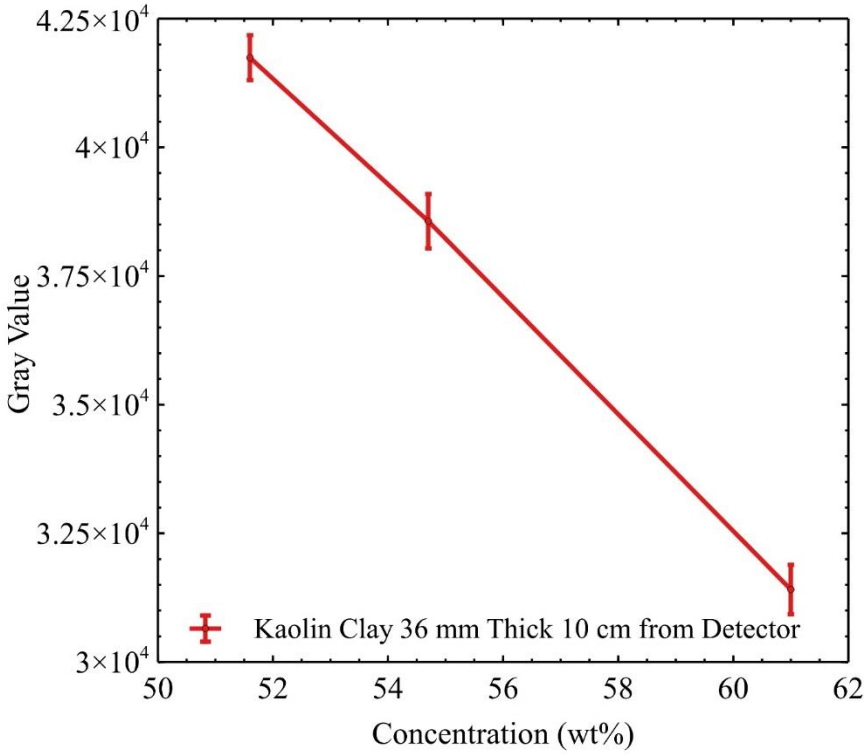

Figure 75: Gray values of three kaolin concentrations (concentration determined by drying in an oven until constant mass obtained, 51.6, 54.7 and 60.9 wt%). Gray values are displayed for each concentration. X-ray source settings 36 kV and 3.7 mA.

Fig. 75 above shows that, as predicted, it is possible to identify a kaolin concentration from its respective average grey value, we define the average gray value as the mean value obtained. We observe a high contrast between the concentrations chosen which suggests we can identify a concentration change within a sample of approximately 2 wt% during the annular shear experiments due to the uncertainty of our results. This calibration method also inspired the centrifuge experiments detailed in Chapter Five where concentration changes were used to monitor the compaction of kaolin.

4.4 Parallels with other experiments

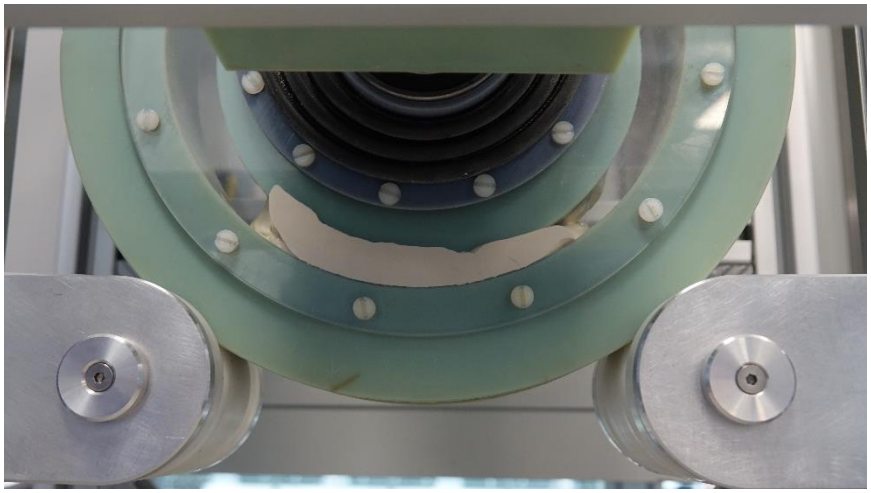

Figure 76: For preliminary experiments a small volume of kaolin was loaded between the cylinders to measure shear flows.

A 55 wt% kaolin clay was made to be sheared in the annulus of the accretion rig. In order to visualise the flow of the kaolin in this setup a mass of 0.5 mm diameter steel ball bearings was mixed into the clay during initial mixing in an attempt to distribute them relatively evenly in the bulk volume. These tracer particles appear black in the shadowgraph. We can also use the rods observed in fig. 77 to determine the angular velocity of the cylinders. This was achieved by measuring the distance the inner cylinder travelled using ImageJ to create an arc to calculate its angular velocity of 0.131 rad s^{-1}

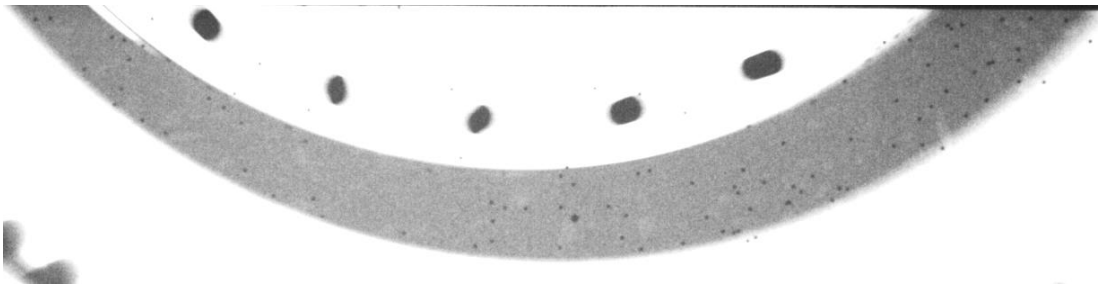

Figure 77: X-ray shadowgraph captured of the rig during operation. The inner cylinder has metal bars inserted into its structure at regular intervals to allow visualisation of its rotation. The clay is also impregnated with steel ball bearings to allow visualisation of the shear in real time. In this figure we observe the clay (grey band), steel ball bearings (black dots) and the bars used for rotation tracking (large black rectangles)

Both cylinders were fitted with strips of Perspex sandblasted with Saftigrit Brown to provide similar surface characteristics discussed in Chapter Two and Three. In the initial experiments, some similarities with the simple shear behaviour discussed

in Chapter Two were observed. The first notable similarity was that, as the cylinders rotated, there was slip at the kaolin/Perspex interface.

The slip is shown to continue with rotation as the ball bearings travel with slower angular velocity than the inner cylinder. This is consistent with the behaviour observed using similar surfaces during simple shear experiments using the rheometer. We also observe the presence of shear banding, see supplementary video 3. The bands appeared as two distinct regions of different shear rate and close to the inner rotating cylinder we see fast-moving ball bearings while the fluid and particles adjacent to the stationary outer cylinder (except for small initial movement) are motionless as the ball bearings remain still throughout. Over time we also observe that the size of this shear band diminishes as the rotation continues and towards the end only the fluid adjacent to the rotating cylinder is sheared, see figure 78.

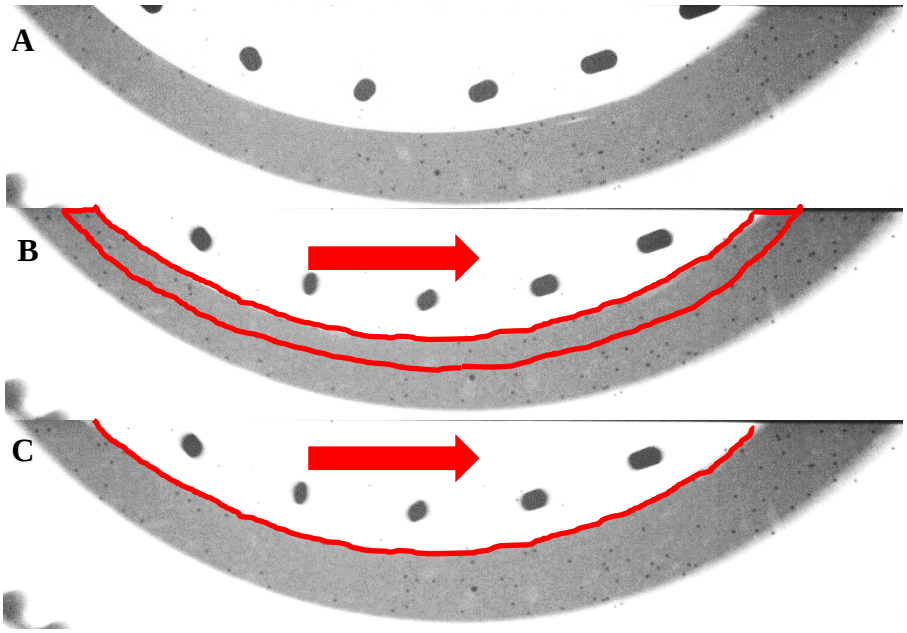

Figure 78: Images of the accretion rig in operation, regions marked in red denote the flowing regions. Image A is the initial state, image B is a mid-point in the shear and image C is close to the end of the process. The red arrow shows the direction of the shear.

Particle tracking of the steel ball bearings was attempted using the PIVlab Matlab software developed by William Thielicke and Eize J. Stamhuis [120]. PIVlab is a useful tool that allows the visualization of particle velocities and shear rates as particles travel through a medium. Upon reviewing the processed data the results appear almost random and show no clear flows. This suggests that there was a problem with our use of the software and additional work is required to clear up the shear flows. While modifying the parameters such as the contrast limited adapted histogram

equalization (CLAHE) in the image the sample showed a lot of noise in the clay itself. This proved to be difficult to remove without obscuring the ball bearings used for the tracking. In fig. 78 we also observe that there are large volumes of the clay which show very few if any tracer particles. In order for a PIV algorithm to work effectively it requires a lot of tracers so that it can better infer vectors in a medium. The small number of tracers did not give the algorithm enough information to create sufficient vector fields and so the resultant data appears random. PIVlab is a popular tool that has been used by many authors, the rig however is a first iteration prototype. Early in this short project we used the software to analyse data obtained from a bench top demonstration and it proved to be successful in tracking these flows. This may be due to the bench top setup being thinner and so there were fewer particles for the x-ray radiation to travel through to cause distortions. It is clear that there are several limitations with this prototype that need to be addressed in iterations going forward.

As previously mentioned, we observe the presence of a shear band in the kaolin as the inner cylinder rotates. Immediately at the clay/inner cylinder interface there is some slip as the ball bearings are measured as travelling at 0.131 rad s^{-1}. A shear band is established and the clay at the outer wall does not move, however this band is short

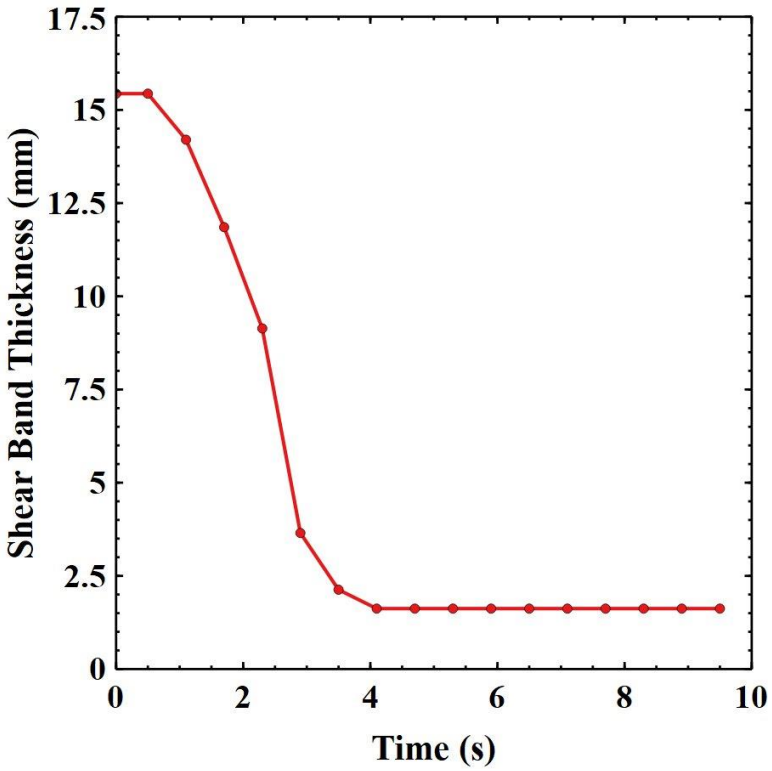

Figure 79: Graph to show the decay of the shear band width over time as the inner cylinder rotates.

lived (several seconds) and as the depth increases the speed significantly drops. At a radius from the inner cylinder of 1 mm the angular velocity halves to 0.08 rad s^{-1} and at 3.2 mm below the clay/inner cylinder interface we see that it has dropped to 0.04 rad s^{-1}. The shear band quickly shrinks over time until only the bearings close to the surface are moving, this could suggest the establishment of wall slip as the majority of the shear occurs close to the surface of the rotating cylinder, see Fig. 79.

4.5 Weaknesses and pitfalls

The annular rig was a first stage prototype at the time of usage and due to unforeseen circumstances completion of the apparatus came very late into my time at Schlumberger and so few experiments were performed with the rig. This meant that when drawbacks in the design were identified there was no time to alter the apparatus.

The setup was both large and heavy which made it difficult to move in and out of position in front of the detector. Due to the arrangement within the x-ray chamber it had to be lifted awkwardly into the chamber in front of the x-ray source which proved difficult due to its weight. When in position the rig sat on two vertical jacks that could be raised or lowered to the correct height. A disadvantage of this setup was that although to the eye, these jacks could appear level, if they were not correctly in line with each other there could result in optical effects such as the fluid appearing thicker than it is, affecting the path length, or the trajectories of tracer particles to be different in the recording. For example, in fig. 78 the markers within the inner cylinder appear stretched as they rotate. The detector sees both faces of the rods simultaneously and so they appear to stretch during the rotation.

The layout of the design also needs some improvement. The way the rig was put together meant that during loading and unloading a lot of components needed to be removed in a particular order, making it a time-consuming process to setup and maintain the equipment between experiments. The cylinders rotated using belts under high tension, when analysing the videos it was noticed that the position of the central cylinder changed between experiments. This made reproducibility of the results difficult as the gap between the cylinders was not uniform. Future iterations of the annular geometry should attempt to simplify its construction while ensuring that the relative positions of components cannot move sufficient distances

For the Annular Rig to be improved it requires several changes. It needs to be made lighter to allow the operator easier control during loading and unloading procedures. To improve the reproducibility of experiments the instrument needs a system of locking the relative positions of the cylinders. There are a lot of movable parts around the annulus, such as the buffers around it that must be set by hand, as can be seen in fig. 80. By locking some components in place, the positions of the cylinders may be more consistent, resulting in greater reproducibility.

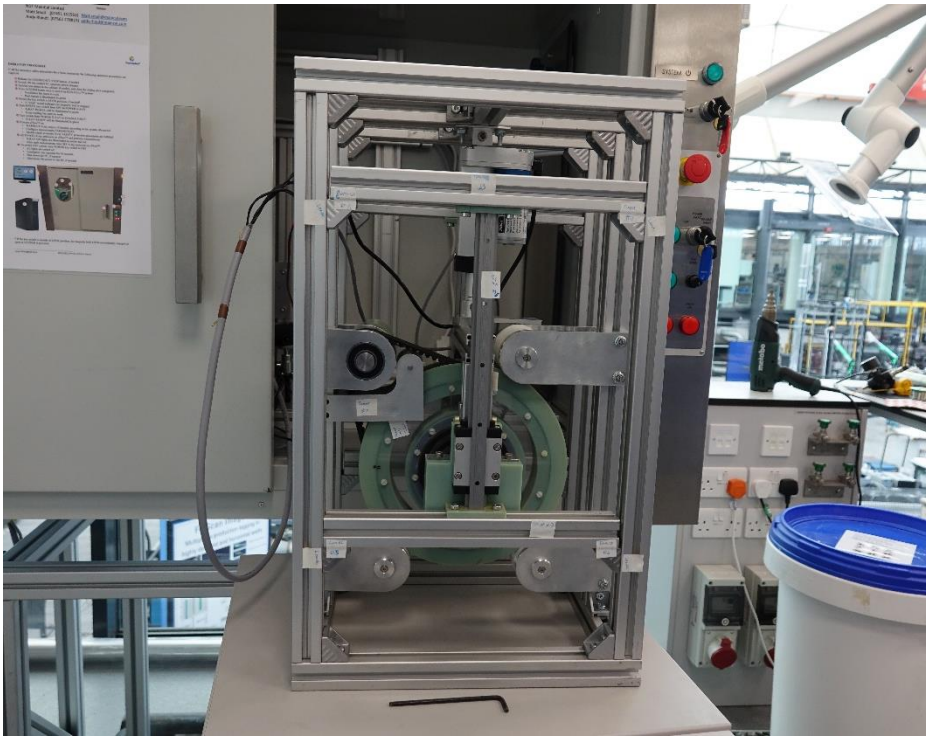

Figure 80: The rig when fully constructed, each component with a white tag on it in this image had to be removed in a particular order to allow full access to the annulus. The braces below the annulus were also removable which could also result in issues such as misalignment of the cylinders.

To improve the accuracy of the x-ray shadowgraphs the vertical jacks should also be removed. To reduce this problem the design could be adapted to allow the outer cylinder to be raised into the correct position. If the annulus can be positioned in front of the detector by an actuator the rig can be placed on the floor of the chamber. It would also allow for repositioning as the x-ray source is active and the position could be changed to remove optical effects in situ rather than deactivating the instrument before repositioning the rig by hand.

Chapter 5. Mechanical Compaction of Kaolin Clay

5.1 Motivation of Work

We observed in Chapter Two that when kaolin is compressed from the trim height to the working height that a small amount of water is extruded close to the kaolin/plate interface. We concluded this is due to a compaction process that may change the local concentration of the clay suspension. If the clay was compacted to a higher degree, i.e. a greater force was applied, this would result in a larger volume of water being pushed out to the peripheries. The resultant compaction made the clay stiffer and more difficult to shear.

In this chapter we investigated this behaviour on a larger scale and related the extrusion behaviour to a structural mechanism of particle compaction. In addition to visually measuring the compaction / effusion of interstitial liquid, we also used x-ray shadowgraphy which allows the visualisation of concentration changes at different depths in the sample to be measured after they had been centrifuged. We decided to focus on the most interesting concentration regimes studied in Chapters Two and Three where the qualitative dynamics of slip were found to change (50-60wt%).

5.2 Introduction

A container can be filled with a pile of particles, the particles will fill the space randomly until no more particles can be added. When a pile is formed there are gaps between the individual particles. These gaps are referred to as voids or pores; these are spaces that fluids like air or water can become trapped in or pass through. The void ratio, e, of a system (defined here as a granular skeleton immersed in a liquid matrix) is a dimensionless quantity that is often useful as a measure of the porosity of a granular system. It is calculated as the ratio of the volume of voids over the volume of solid,

$$e = \frac{V_v}{V_s} \ , \tag{25}$$

$$\Phi = \frac{e}{1+e} \ , \tag{26}$$

where Φ is the porosity of the system. The larger the volume of voids, the higher the porosity of the system is. Therefore, a highly porous material will allow interstitial fluids to flow through easily. Porosity can take different forms depending on the system concerned. The main types are matrix and fracture: matrices are formed by an interconnected network of pores between the individual particles while fractures are the result of cracks opening in a granular material [121]. Clays typically show a large degree of matrix porosity with a small degree of fracture porosity.

The most efficient packing of a set of particles occurs when there is only one particle species of uniform size and shape. In a monodisperse system the densest packing corresponds to a regular crystalline structure, theoretically this would result in a volume fraction, φ, ~ 0.74 for spherical particles [122]. However, this is difficult to achieve practically and a critical volume fraction of 0.64, known as random close packing is often found to be the limit [122]. The shape of the particles can play a critical role on the packings of particles. For example, the maximum volume fraction of packings of spherical particles can be reduced by roughening their surfaces and making their shapes more irregular [123]. However, this only holds true for spherical particles, there is no equivalent packing limit for particles of irregular shape.

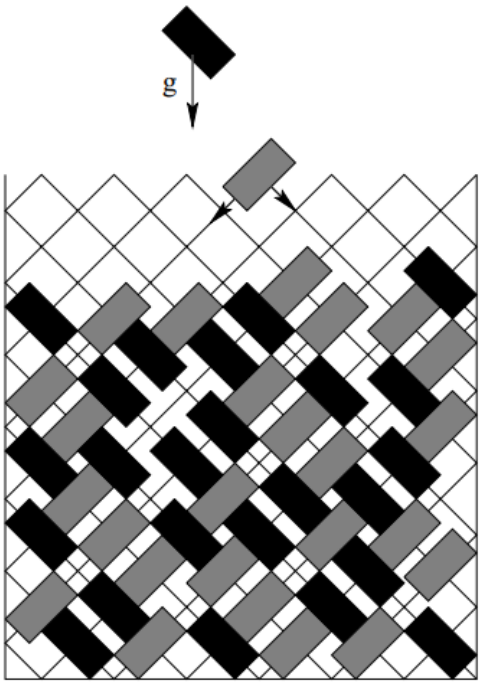

Figure 81: Schematic diagram of the tetris like model of packing [124].

Kaolin is comprised of platelets which organise themselves into a “house of cards” type structure as interparticle bonds between the charged edges and faces form, similar to figure 81 [75]. As they are non-spherical charged particles there will be some irregular packing leading to a somewhat lower volume fraction than the maximum possible for regular spheres, yet this is difficult / impossible to calculate analytically.

Clays, like many granular systems show very interesting consolidation behaviour when a force is applied. If we first consider a dry system, there may be a multitude of different states and densities. This is due to the irregular packing of particles which can increase their “effective” volume fraction. Kaolin is comprised of thin platelets. Depending on the orientation of these particles one can fit a variable number of particles into a given volume. Caglioti et al. [124] proposed a model of compaction where dry particles are introduced one by one at the top of a box and allowed to perform a random walk until they meet the floor of the container or another particle. “Vibrations” are introduced to allow movement (both up and down) with probability p_{up} of $0 < p_{up} < 0.5$ and $p_{down} = 1 - p_{up.}$ The process ends when particles can no longer move to change their orientation; they describe this model as a “tetris-like” process, see fig. 81.

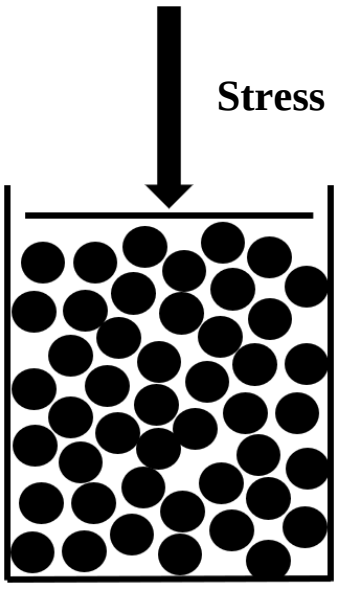

Figure 82: uniaxial compression acting on a packing of granular particles. As the stress is applied the particles will be forced to rearrange into a more closely packed system minimising the volume of empty spaces between each body.

When a dry granular packing is prepared it can be in a loose arrangement. To be useful in practical applications, such as construction, these packings often need to be made denser to improve their strength, see fig. 82. One method of doing so is by increasing the vertical stress on the packing. This process will lead to some rearrangement and compaction. As the stress is increased the particles will deform, leading to a further increase in volume fraction. At sufficiently large stresses, particles can undergo plastic deformation and break leading to more available arrangements and cause a significant compaction to occur [122].

There has been some debate concerning the mechanisms that dictate the structure and density of non-crystalline solids. Experiments have indicated that a system can become solid-like at lower volume fractions, down to the random loose packing limit of 0.55 [125]. Liber et al. showed that the dynamics play a key role in determining the final packing of particles. They found that suspensions with low solid volume fractions formed sediments that approached the random loose packing limit. When experiments were repeated with denser systems they found that "denser suspensions form denser sediments" and obtained sediments with volume fraction approaching the random close packing limit [125].

A number of studies have also reported non-linear behaviour occurring as a result of uniaxial compression [123,126,127]. When small strains are applied, a strong deviation from a linear elastic response is observed. This implies that the system hardens when small stresses are used during compaction. However, for larger deformations the compression was found to be linear elastic [126].

In addition to the compaction of the dry aggregate or particles, interactions with the fluid have an important role in the compaction process.

5.2.1 Stokes' Drag

Consider a single spherical particle immersed in a Newtonian liquid. The particle will either remain stationary or sink to the bottom depending on the balance between buoyancy and gravitational forces. If a particle sinks through a column of liquid there is a drag force that slows down the sedimentation of the particle,

$$F = 6\pi r\eta v\ , \tag{27}$$

where r is the radius of the particle, η is the viscosity of the fluid and v is the velocity of the particle. This framework is very useful and describes the behaviour of many low-density suspensions well. The two phases can be described as continuous media that flow at different average velocities [128] in a volume of fluid. The concentration of a suspension will inform us how much of a role Stokes' Law plays in the dynamics. In a dilute system there are no contacts between grains and the dynamics are equivalent to the Stokes' drag force. With no contacts being present the force is carried by the fluid and a Newtonian response is obtained. However, at higher concentrations systems are often characterised by grains that may be either in close contact or are separated by a thin lubrication layer [122]. The dynamics of a dense system are mainly governed by contact interactions between grains. However, many real-world systems exist somewhere between these two limits. The samples that we are using in this chapter are all high concentration therefore, there are many contacts between the particles.

5.2.2 Immersed Granular Media

If we mix a high concentration suspension thoroughly, we will find that the pores have been filled with water. Due to this there is an associated pore pressure within the system which can influence many processes [128]. When a stress is applied to the system there is a transfer of "effective stress". This is known as Terzaghi's Principle which states:

"When a stress is applied to a porous material, it is opposed by the fluid pressure filling the pores of the material". From Terzaghi's Principle this is determined as

$$P^p = \sigma_v - \sigma_e \,, \tag{28}$$

where σ_v is the total vertical stress i.e. the magnitude of stress that is applied to the sample. σ_e is the effective stress, this is the portion of the applied stress that is resisted by the particle structure. The difference between the total and effective stress is equal to the pore pressure of the system. Terzaghi emphasized the importance of the non-uniformity of voids with regards to the permeability of clays. He found that there was a substantial dependence of the permeability on the void ratio. He also considered that

the physical properties of the pore water would change depending on how close they were to the surface of the clay system [129].

In systems where both the fluid and grains are incompressible the density of each component, ρ_{part} and $\rho_{fluid,}$, will remain constant under compaction. The components of the system carry the force in different ways: some of the force will be carried by the contacts between the individual particles and the remaining force is carried by the interstitial fluid [122].

The flow of water through a sediment is important in many applications such as the oil and gas industry and groundwater flow. Consider two water tanks with different initial water levels, connected by a packing of a porous sand. Over time the water levels will gradually equalize as fluid flows between the two tanks. The rate of flow of the liquid depends on the size and packing of the sand particles. Darcy's Law provides a quantitative description of the flow of fluid through the packing:

$$Q = KA\frac{\Delta h}{L} \ , \tag{29}$$

here, Q is the volumetric flow rate through a porous medium. The porous medium has an associated permeability K to allow water to pass through it. The amount of water that may be passed through the medium is controlled by the cross-sectional area of the packing with length, L. Δh is the change in height of a system which helps to drive the process of fluid flow [130]. The permeability of a porous medium is a function of both its grain size and the efficiency with which it has been packed. If there is a pressure gradient, flow will occur from high to low pressure. If there is a large pressure gradient one will observe a greater rate of discharge. For a given pressure gradient, a packing comprised of large particles will allow a large volume to flow through its pores while a packing of small particles has much smaller pores and the rate of fluid flow is greatly diminished [131]. This discharge rate will also depend on the packing used [132].

Consider a water saturated system with an impermeable bottom surface, called a basement, see fig. 83.

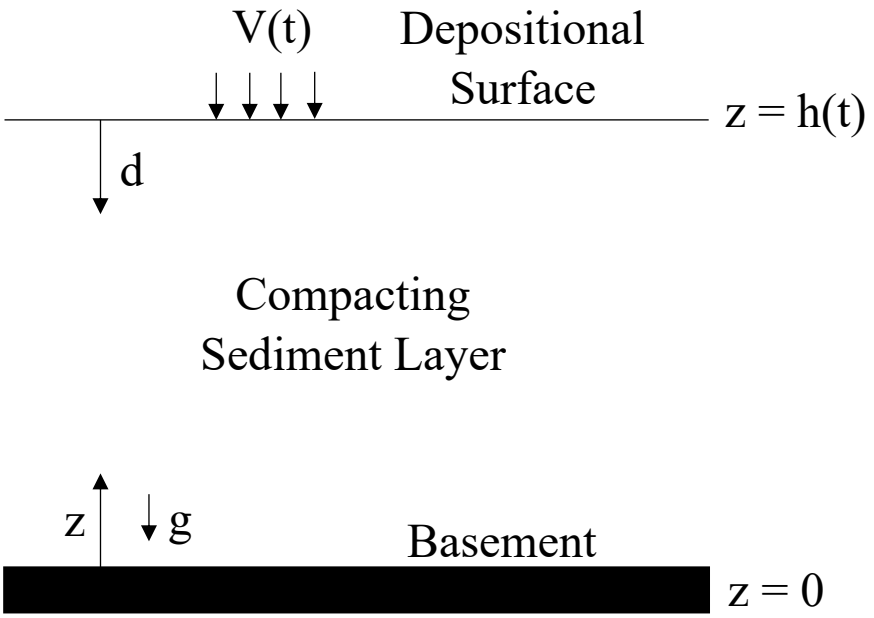

Figure 83: Model diagram of gravitational compaction. A basement is defined as z = 0 and the surface of the porous material at is z = h(t). V(t) is the rate of deposition. Gravity is denoted by g and operates in the negatve z direction. Obtained from [130].

When an external stress is applied it does not initially propagate to the granular skeleton and is carried solely by the fluid. This results in an increase in pore pressure. Liquid becomes expelled from the pores and will travel upwards towards the surface. As it does so the pore pressure reduces and part of the external force is transferred to the granular skeleton. This process will continue until the external force is removed or is carried by the granular skeleton only. During this process the pore pressure returns to levels similar to when the system is unstressed. The motion of a fluid through the granular system is however rarely spatially uniform and can be visualised [133] as capillary channels connected to the surface. Over time these channels can fluidise their surrounding regions and create localised instabilities.

5.2.3 Compaction of Kaolin

There have been several studies that have shown that particle properties can have a significant effect on the removal of water from saturated solid suspensions [134]. These properties are particle charge, size distribution, shape, concentration and hydrophobicity. Kaolin particles generally have a plate-like shape with different zeta potentials associated with the face and edge surfaces. The magnitude of the zeta potential can have a significant effect on how readily a suspension will settle out. If particles possess a large zeta potential they will disperse readily whilst particles with lower associated potentials will more easily sediment out. Kaolin often shows slow settling rates compared to other minerals such as calcite over a wide range of pHs with particularly low settling rates being observed between pHs 6 and 10. There is also some suggestion that this behaviour is due to the platelet structure of kaolin particles [134].

5.2.4 Centrifugation

One method of compacting a granular system is to use a centrifuge which has proved to be a very useful way of providing small-scale models to simulate unpredictable and destructive events such as earthquakes [135]. A centrifuge is an instrument that is typically used to separate mixtures by applying a centrifugal force by rotating samples at high speed. Under the influence of a gravitational force, mixtures will separate according to their densities with more dense materials separating out to the bottom of the sample tube [136]. During the centrifugation process there is a balance of forces acting on both the particles and interstitial liquid that govern the effectiveness of the separation. These forces include the buoyant and frictional forces acting on the particles as well as a viscous force between the particles and liquid as well as a resistance to fluid flow through the porous network. Particles will only move when the centrifugal force exceeds these forces, resulting in sedimentation at a constant rate [137]. However, in particularly dense suspensions, for compaction to occur there may be the need for cooperative movements of particles.

The Relative Centrifuge Force (RCF) of a rotor is typically expressed in xG or multiples of the gravitational force of Earth,

$$RCF = 1{,}118 \cdot R \cdot ({}^{rpm}/_{1000})^2 \,, \tag{30}$$

where R is the rotor radius in cm and rpm is the speed of the rotor in revolutions per minute. Some centrifuges only have settings for speed (rpm) rather than rcf and a conversion is required between them:

$$g = (1.118\, x\, 10^{-5}) \cdot R \cdot S^2 \,, \tag{31}$$

where g is the RCF, R is the rotor radius in cm and S is the speed of the centrifuge in rpm. The magnitude of the centrifugal force is also calculable,

$$F = m \cdot r \cdot \omega^2 \,, \tag{32}$$

where m is the mass of the sample (kg), r the radius (m) and ω is the angular velocity of the rotor (rad s^{-1}).

Speed (RPM)	G (xg)
500	46
800	118
1100	223
1500	415
2000	738

Table 3: Conversion between rpm and g force.

5.3 Method

Kaolin clays of concentration 50, 55 and 60 wt% were centrifuged at different speeds (500, 800, 1100, 1500 and 2000 rpm) for increasing periods of time (10, 30, 60, 120, 360 and 600 minutes total) using a Thermo Scientific Megafuge 16 centrifuge fitted with a swing arm rotor (rated to 5500 rpm) with an internal bucket radius of 16.5 cm, total radius 17.5 cm, see fig. 84. At t=0 mins, and after each period of rotation, the samples were photographed at three different orientations to obtain information about the volumes of water extruded and the compaction of the sediments. After the photographs were taken the samples were then immediately returned to the centrifuge for further rotation until compaction of the sediments was found to saturate (maximum of 10 hours).

Figure 84: Centrifuge fitted with the swing arm rotor, internal bucket radius is 16.5 cm, total radius 17.5 cm.

X-ray photographs of some of the samples were taken using a Rex Cell L Series x-ray chamber and camera (image capture settings of 10 fps, 100 ms exposure time, voltage 32 kV and current 2 mA) in an attempt to measure changes in the concentration of the 55 and 60 wt% clay during rotation at small time scales at 1500 rpm using a similar protocol to the other experiments described in Chapter Four. The x-ray photographs were captured in a similar setup as displayed in fig. 85

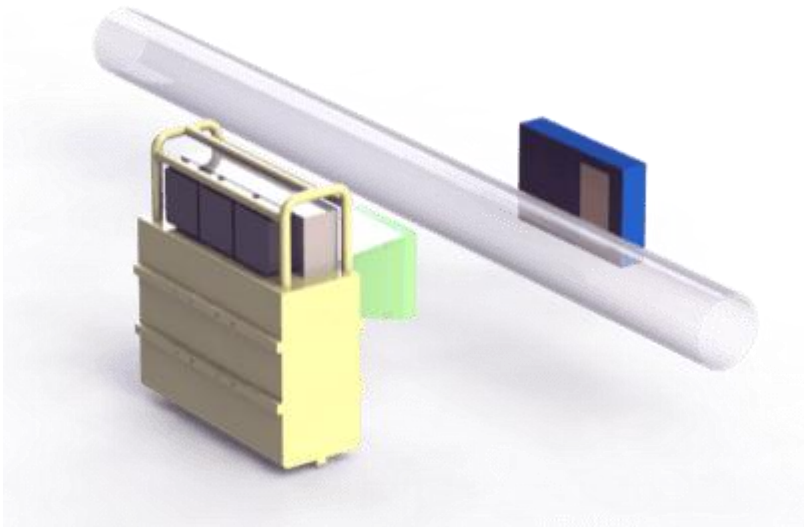

Figure 85: A diagram of the equipment inside the Rex Cell L chamber. At the front we have an x-ray source (yellow) that bombards the object of interest with radiation. X-rays that pass through the object are then captured by the detector (blue) behind it. The detector produces a shadowgraph of the information that it receives [138].

Masses of kaolin clay (50, 55 and 60 wt%) were centrifuged for extended periods of time and the volume of water extruded was measured. Images were recorded after each period of rotation to provide insight into the evolution of the separation process under high stress. The procedure shown in figure 86 was repeated to measure volumes of each sample after being centrifuged.

5.4 Results and Discussion

We recorded four images from around the circumference of the tubes. This was performed to give a more accurate picture of the volume changes in the expelled water and compacted packing.

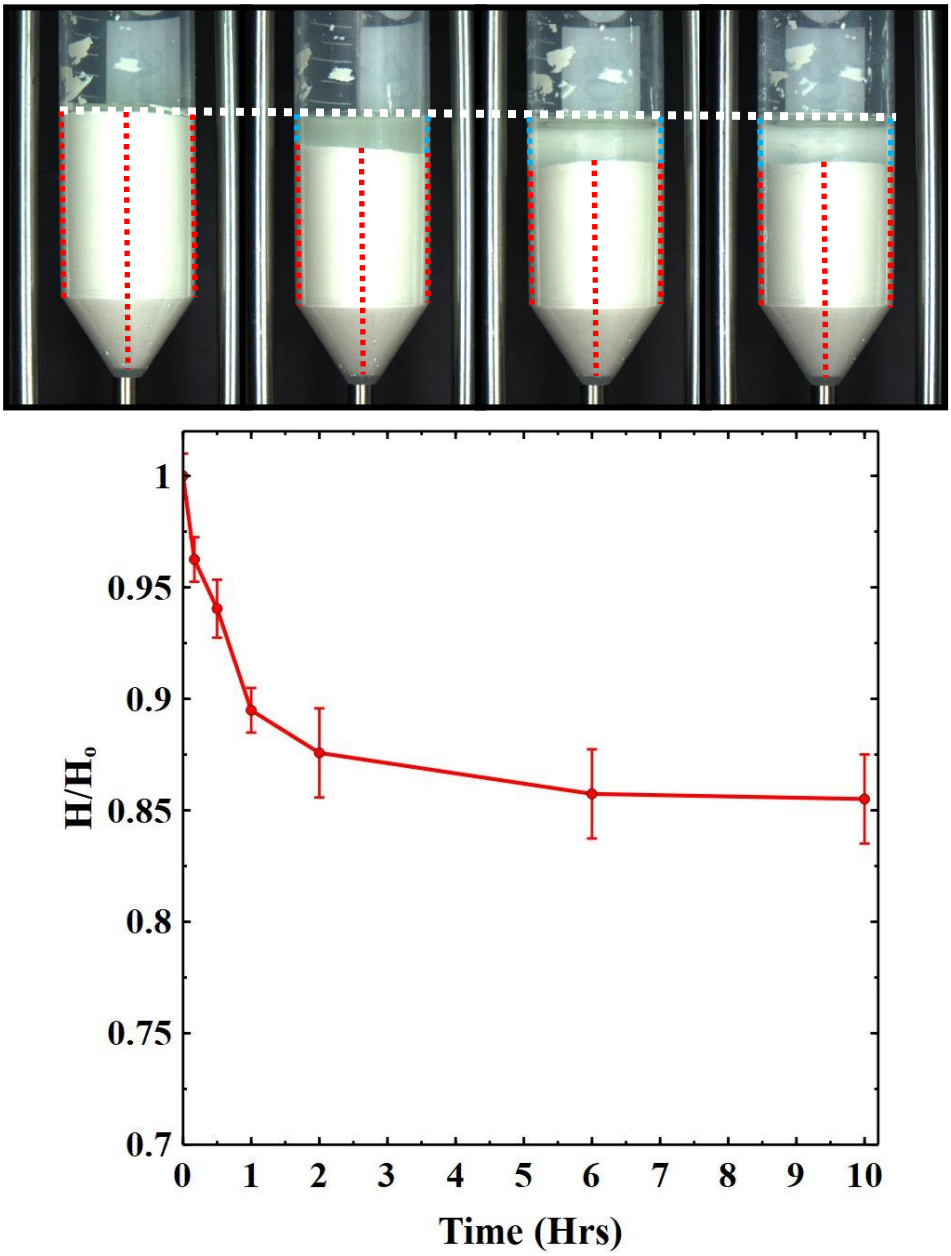

Figure 86: Top) A sample of 55 wt% kaolin centrifuged at 1100 rpm for 0, 30, 60 and 120 minutes from left to right. Samples were often found to saturate (very little additional water extruded) after centrifugation exceeding 120 minutes regardless of the applied G force. Measurements of the height of kaolin and free water were taken to determine their relative volumes: kaolin indicated in red and free water measured in blue. Bottom) In the graph we see this behaviour as the relative height decreasing rapidly in the same amount of time before levelling off after 2 hours. H/H_o is defined as the height of the clay packing divided by the initial height of the starting packing.

We observe that there is a rapid change in the height of the kaolin in the initial stages of the compaction however this quickly diminishes (after ~1hr) as the granular skeleton reaches maximum compression. Unsurprisingly two clear trends emerge from the experiments. As the concentration of the sample increases, the relative volume of water that is expelled from the kaolin decreases. We also observed that as the speed of centrifugation is increased the initial volume of water released increased.

5.4.1 The Kaolin/Water Interface

In the photographs of the centrifuged samples the water/clay interface is not flat as one might expect. The interface instead appears irregular or jagged.

Figure 87: Interface of a 55 wt% kaolin sample centrifuged at 1500 rpm for 30 minutes. Observe that across the interface there are troughs and crests present instead of a flat interface as one might expect, which is likely due to the formation of channels. In the red box we see what may be two of these channels at the tube/kaolin surface. These terminate at the top of two crests, which appears to corroborate our hypothesis.

In figure 87 we observe the presence of some slightly lighter coloured vertical lines. In chapter 4 we demonstrated that clay with a higher water content appeared lighter in colour. This suggests these lines may be thin channels of lower concentration clay which result in preferential flow of pore water to the surface. This is reminiscent of Mörz et al's work where they were able to visualise the development of vents when water was expelled through packings of sediments [139]. In their study they observe that the water creates bulges in the sediment surface as it vents through the packing. It should be noted however that they are injecting the water from the bottom rather than compressing their samples.

We observe that the channels exit the kaolin interface underneath the crests of the jagged interface. This suggests that there is a non-uniform flow of water through the sample. If it was more uniform a flatter interface would be expected. One might suspect these crests are caused by clay sticking to the surface of the sample tube but in figure 86 additional crests can be seen across the kaolin/water interface. This confirms that they are not the result of wall effects. This would imply that the water is extruded preferentially via the location of crests. Varas et al measured similar behaviour in the venting dynamics of air through a packing of granular material [136]. They observed this phenomenon to occur for small particles (150 to 250 μm), the particles in our aggregates are much smaller than this (approximately 50 μm).

5.4.2 Crack Formation?

Interestingly at high rotation speeds, 1500 and 2000 rpm, we observed that cracks began to open within the 60 wt% samples after extended periods of compaction as shown in fig. 88. During compaction particles rearrange into a configuration where they take up a smaller volume of space, it is therefore very surprising that a crack can open up. Upon further centrifugation (10 hours at 2000 rpm) the cracks are still present but have closed to some degree.

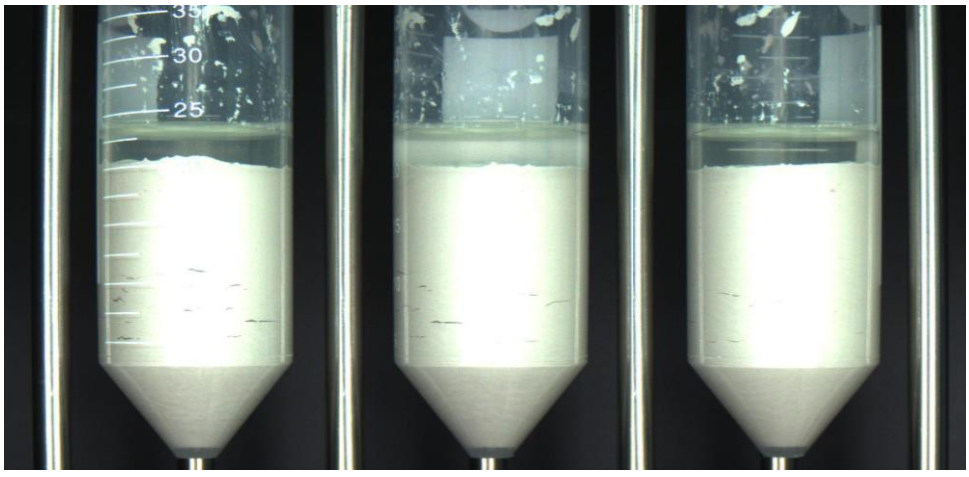

Figure 88: Sample of 60 wt% kaolin centrifuged at 2000 rpm for 6 hours, we observe "fractures" in the packing at depth. These fractures may affect the structure and volume of the resultant packing.

In the experiments discussed in section 5.4 above measurements samples were centrifuged at a set speed for a certain period of time. We then stopped the centrifuge, carefully removed each sample and photographed them. The samples were then returned to the centrifuge. This was repeated until the samples had been centrifuged for 10 hours in total. In some samples we observe cracks being formed during high G force experiments as seen in fig. 88. To check whether this process influenced the crack formation, a second set of samples was centrifuged at 1500 and 2000 rpm for 10 hours, but without interruption. These samples did not exhibit any cracks. This suggests that the cracks are a result of the acceleration and deceleration of the centrifuge to take photographs for analysis. From these experiments it is unclear how deep these cracks penetrate the bulk of the fluid. We assume that this phenomenon is the result of surface interactions with the walls of the container. It may be the case that friction with the surface slows down the downward motion of clay in the location of these cracks. In a situation where the sample is accelerated and decelerated this may cause processes such as wall slip and friction to become exaggerated resulting in large cracks opening. We have seen that channels form to allow water to travel upwards resulting in low concentration zones, this may account for the relative localisation of these cracks in the sample. Further experimentation would be required in order to confirm the mechanism behind this behaviour.

5.4.3 Quantitative measurements of Kaolin compaction

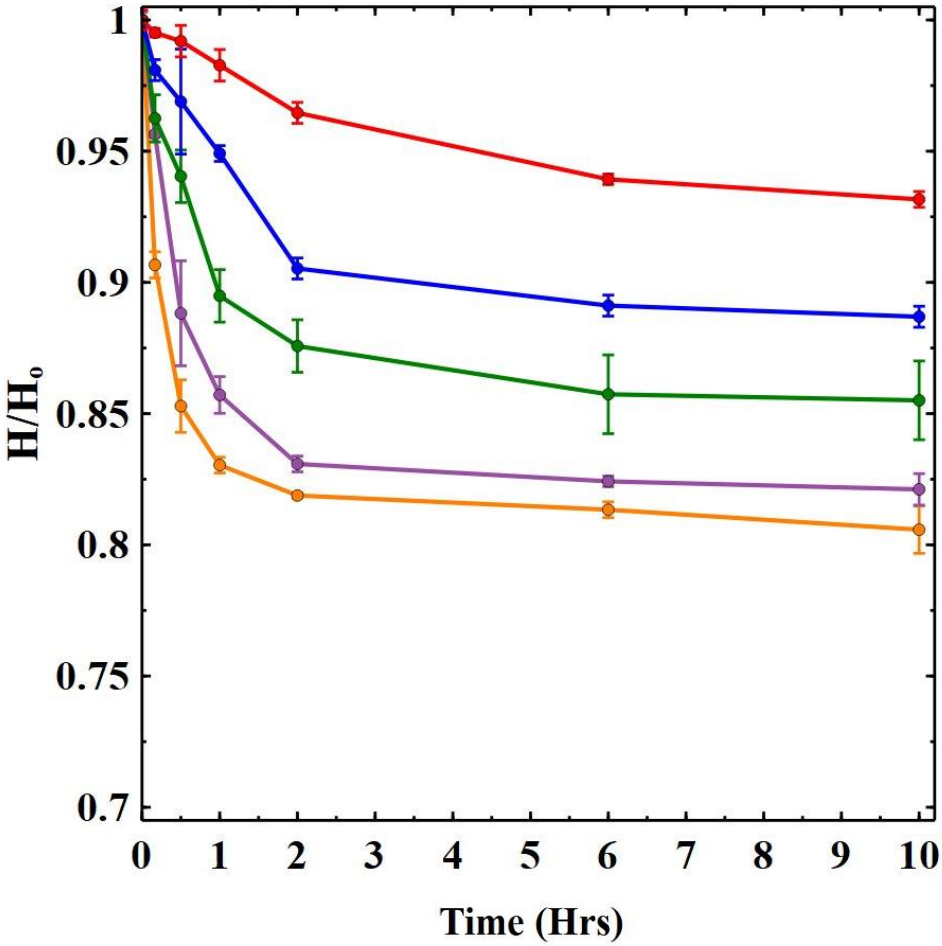

Figure 89: H/H$_o$ (defined the measured height, H, divided by the initial height H$_o$) as of the 55 wt% kaolin over the course of the experiment. Data shown is samples centrifuged at 500 (red), 800 (blue), 1100 (green), 1500 (purple) and 2000 (orange) rpm.

Samples of kaolin were centrifuged at each spin speed (500, 800, 1100, 1500, 2000 rpm) and measurements of the sample such as the average height of the clay and the height of the water layer were made from the photographed images. Using this information, we were able to determine the volumes of each separated phase. In all cases the samples undergo a period of compaction followed by a plateau in which the volume remains constant.

Figure 89 shows that the plateau value oh H/H$_o$ decreases with increasing centrifugal stress. The rate of compaction also shows a significant increase with increasing stress.

We hypothesise that this process of compaction is controlled by the changes in yield stress with density of the clays. We observe that more water is extracted from lower concentration clays which is likely due to the yield stress being more easily overcome by the centrifugal stress. As the sample compacts, the yield stress increases until it eventually equals the centrifugal stress.

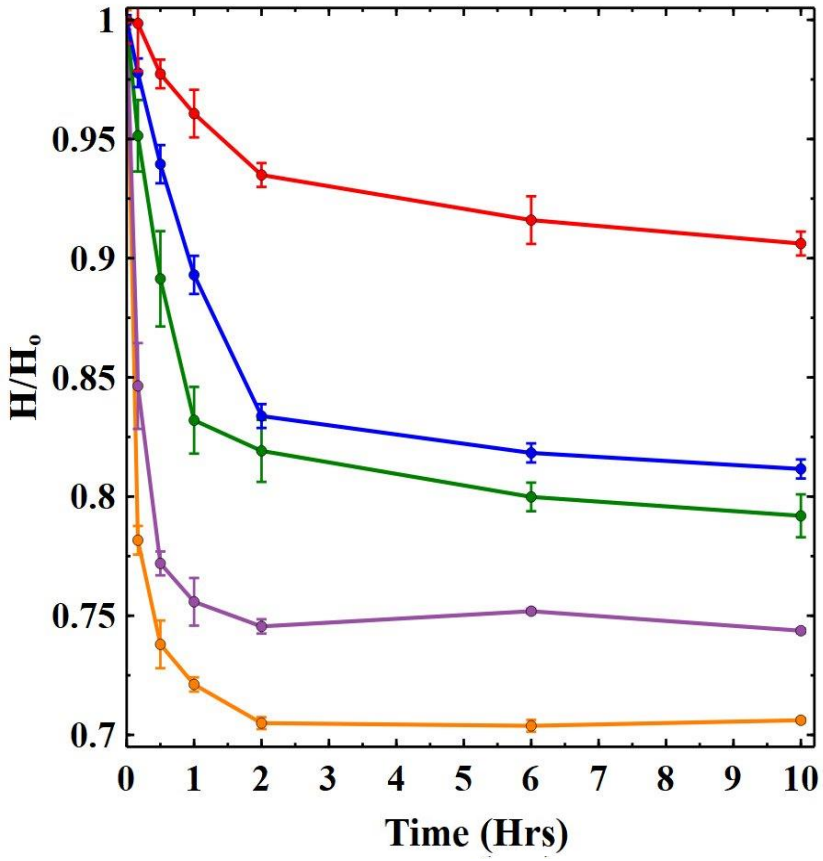

Figure 90: H/H$_o$ of the 50 wt% kaolin over the course of the experiment. Data shown is the 500 (red), 800 (blue), 1100 (green), 1500 (purple) and 2000 (orange) rpm.

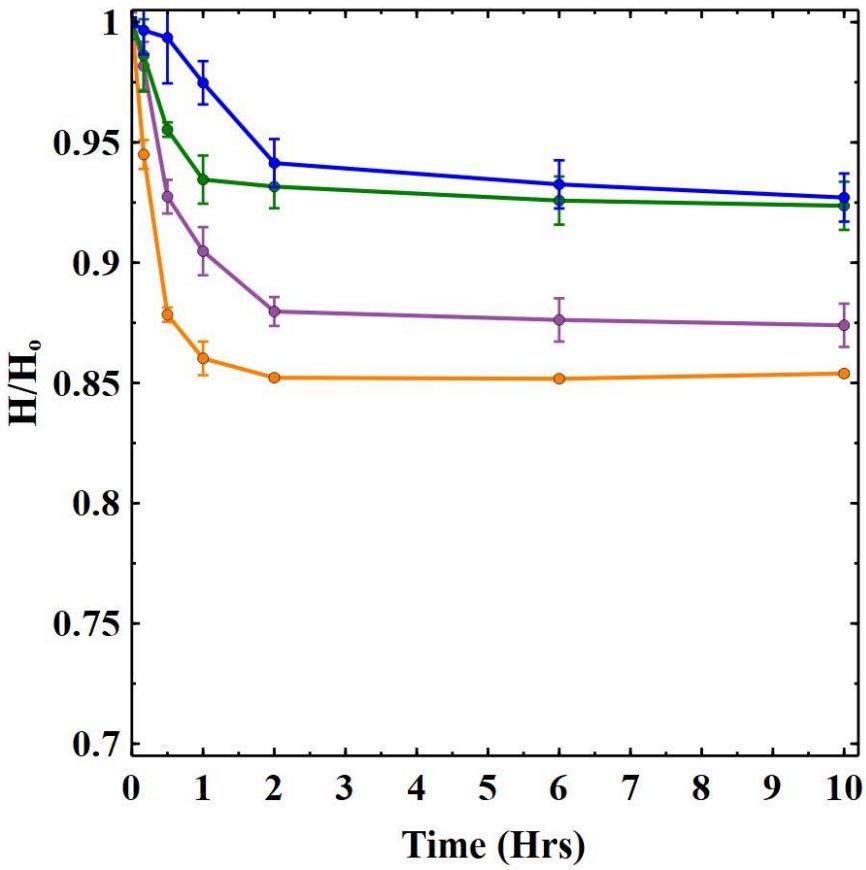

Figure 91: H/H_o of the 60 wt% kaolin over the course of the experiment. Data shown is the 500 (red), 800 (blue), 1100 (green), 1500 (purple) and 2000 (orange) rpm.

We do not include data for the 60 wt% kaolin at 500 rpm because we do not observe any significant loss of water from the packing.

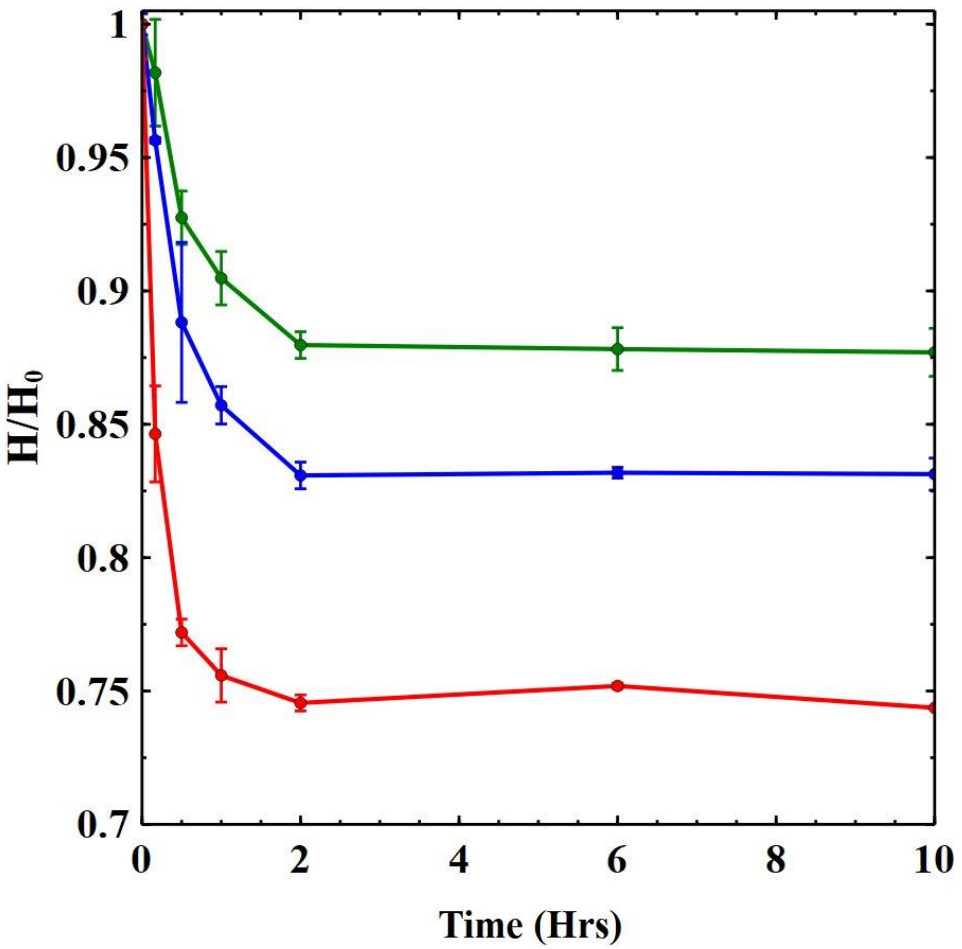

Figure 92: The change in height of the 50 (red), 55 (blue) and 60 (green) wt% kaolin samples at 1500 rpm

From fig. 92 we observe a trend that the relative height change of the packings is directly related to the initial concentration of the solids. We observe that the height change varies monotonically with spin speed and the lower concentration clays compact to a lower relative height than the high concentration clays. As the packings are compressed the solid volume fractions increase and will theoretically increase until they reach a maximum packing density. One might expect this maximum density to be the same for all samples.

We measured estimates for the 50, 55 and 60 wt% by drying known volumes (2 ml) of each sample to constant mass in a vacuum oven overnight. Using the known density of water we were able to determine the volume lost and hence estimate the volume fraction of the initial clay samples ($1\text{-vol}_{water}/\text{vol}_{initial}$). For samples of 50, 55, 60wt% we estimate that the volume fractions are 0.3716, 0.4023 and 0.4399.

5.4.4 Changes in Volume Fraction

One might expect that after some time in the centrifuge the kaolin packings will all reach a similar final volume fraction. We observe however that instead of the volume fractions reaching the same value the samples with higher initial volume fraction will compress to a greater volume fraction than the lower concentration clays. This observation is consistent with results published by Liber et al. [125]. They found that the density of the sediment varies monotonically with the initial concentration of the suspension. Their results suggest that low concentration systems tend towards the random loose packing limit (0.55) while higher concentration systems will compact to the random close packing limit (0.64) [125]. Our results in figs. 93-95 show an increasing trend as we would expect however, the observed volume fraction does not attain 0.55 in any of our samples. This is likely due to the more irregular shape of kaolin particles and aggregates. The maximum observed concentration increase is seen in the 60 wt% sample of 0.51.

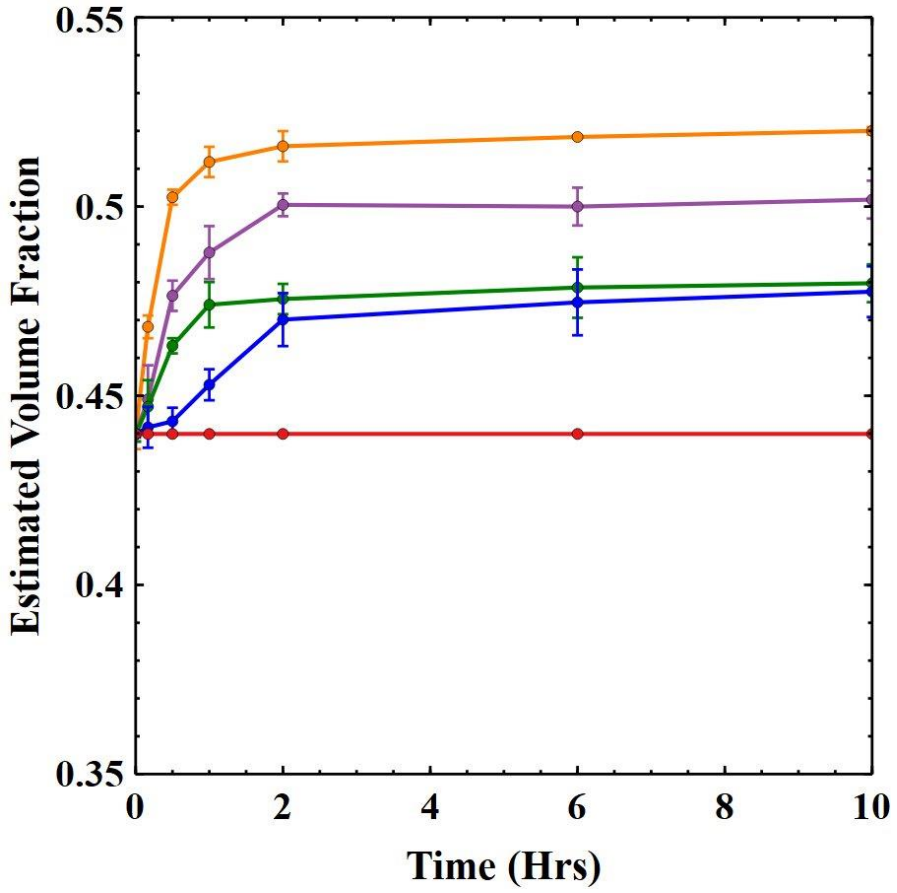

Figure 93: Evolution of the volume fraction of the 60 wt% kaolin at different rotation speeds. Displayed are the 500 (red), 800 (blue), 1100 (green), 1500 (purple) and 2000 (orange) rpm datasets.

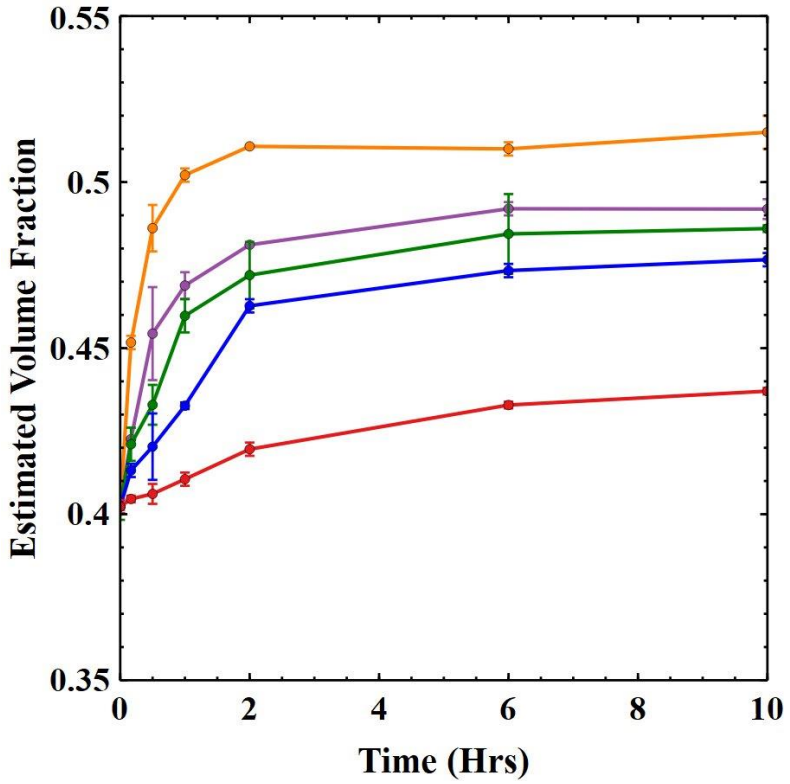

Figure 94: Evolution of the volume fraction of the 55 wt% kaolin at different rotation speeds. Displayed are the 500 (red), 800 (blue), 1100 (green), 1500 (purple) and 2000 (orange) rpm datasets.

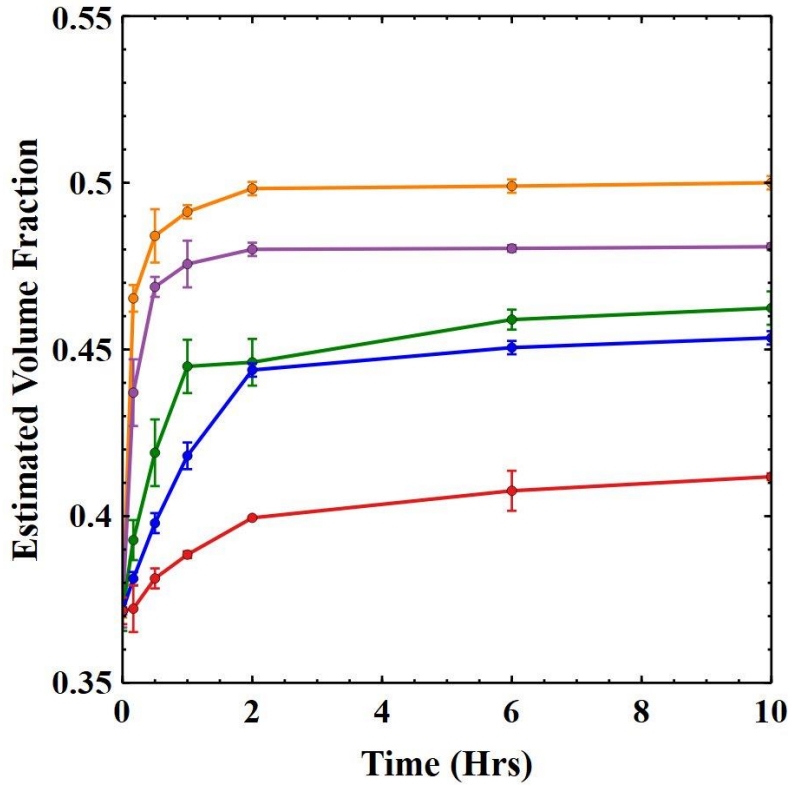

Figure 95: Evolution of the volume fraction of the 50 wt% kaolin at different rotation speeds. Displayed are the 500 (red), 800 (blue), 1100 (green), 1500 (purple) and 2000 (orange) rpm datasets.

It is clear from the above data sets that despite what may be expected by common sense, high concentration packings will compact to higher volume fraction sediments. We can show this trend more clearly by comparing the evolution of the packing concentrations of each tested sample at different spin speeds as shown in fig. 96. We observe that consistently the 60 wt% kaolin volume fraction is higher than the 50 and 55 wt% clays at each spin speed.

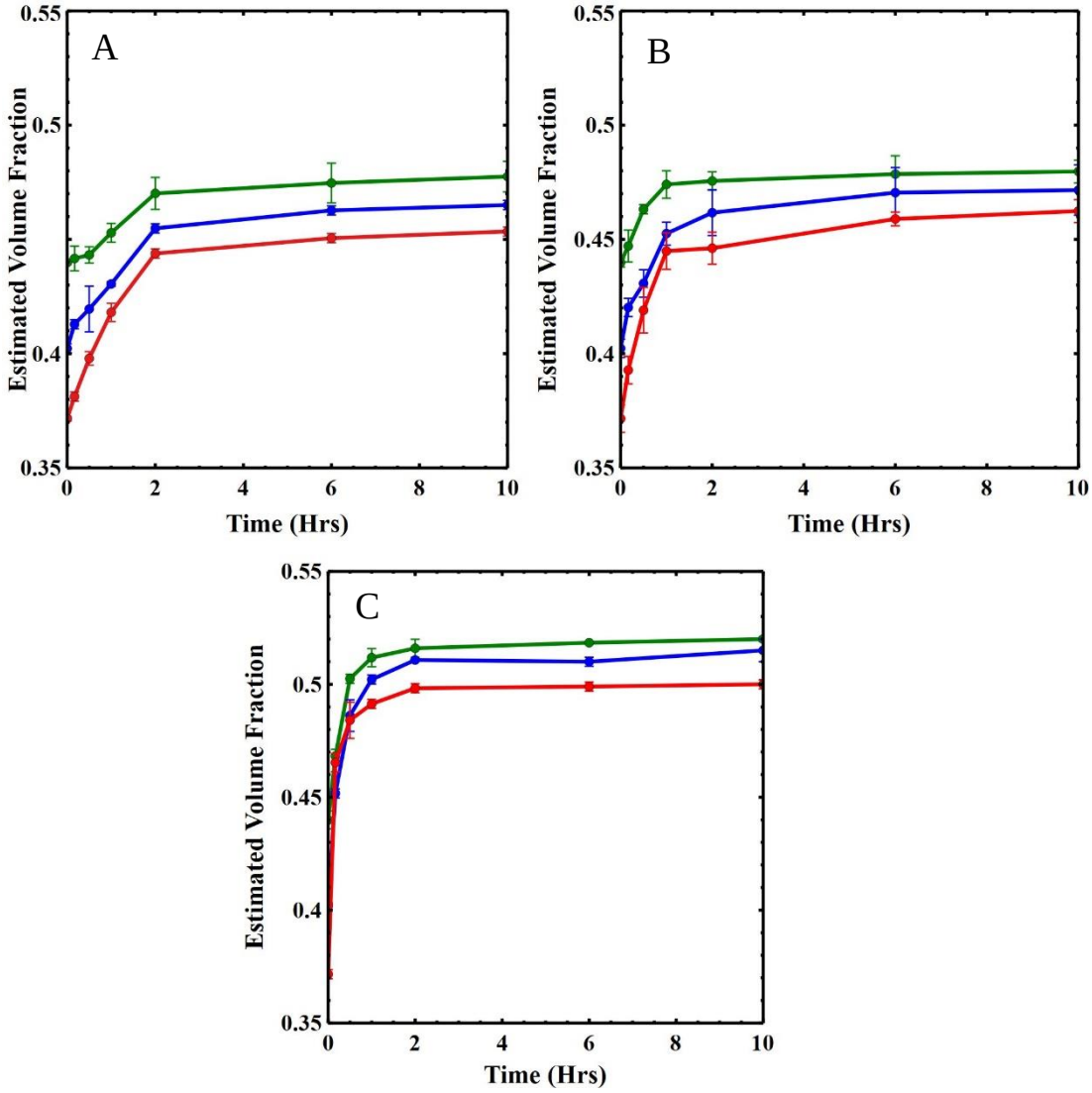

Figure 96: Comparison of the estimates of the resulting volume fraction during compaction experiments using three different speeds. Inset a is the 800 rpm samples, b the 1100 rpm samples and c the 2000 rpm samples. Displayed are the 50 (red), 55 (blue) and 60 (green) wt% kaolin samples.

Liber et al. argue that the sedimentation process is predictable from the state of the initial system. They suggest that frictional forces between the particles may play a key role though admit they are difficult to measure directly. Their results show that a system with a greater density has a more ordered arrangement of particles. Under these initial conditions it is easier for particles to "slot" into a more uniform arrangement when at high concentration. However, in a low-density system, the particles have more freedom to rotate and arrange themselves into a much less ordered network [125]. This freedom makes the resultant packing less efficient and so the density of the sediment is lower. This mechanism might account for our observations of final sediment density. In fig. 97 we present the estimated volume fractions as the corresponding weight percentage to indicate the final concentration of each initial sample.

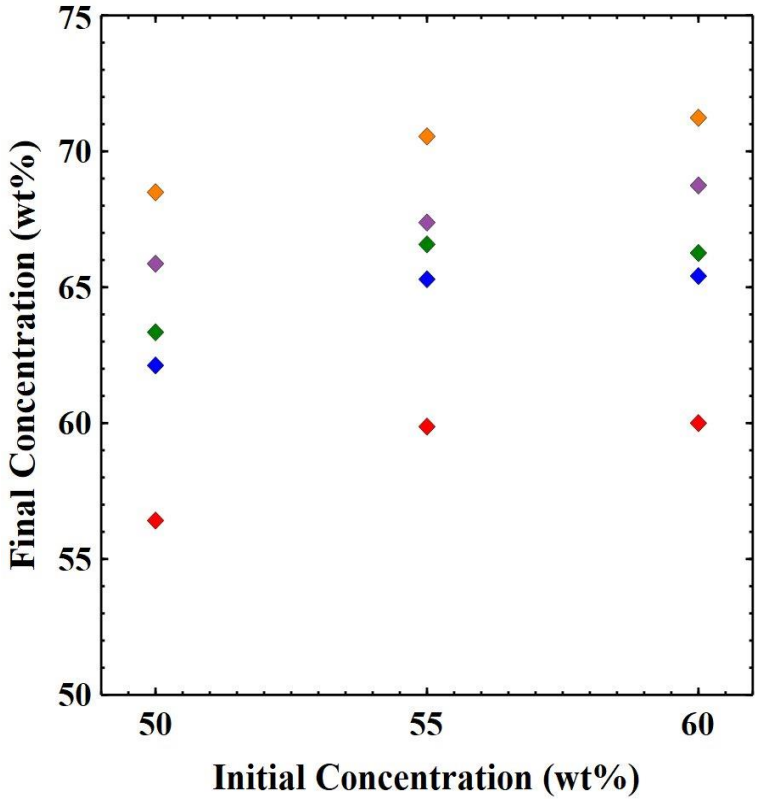

Figure 97: Graph showing the final concentration of each kaolin sample after it has reached saturation at each rotation speed. Data presented is the 500 (red), 800 (blue), 1100 (green), 1500 (purple) and 2000 rpm (orange).

It is likely that there is an upper limit of the volume fraction that can be reached for our kaolin samples. However, it is difficult to predict the value it would have due to the irregular shape of the aggregates of our particles. Additional experiments would need to be carried out to find this limit.

5.4.5 Rate of Drainage

The inspiration for this chapter came from the observation we made in Chapter Two that water was squeezed out of the kaolin during compression. Our data enable us to calculate the rates that water is extruded from the Kaolin clay in each concentration.

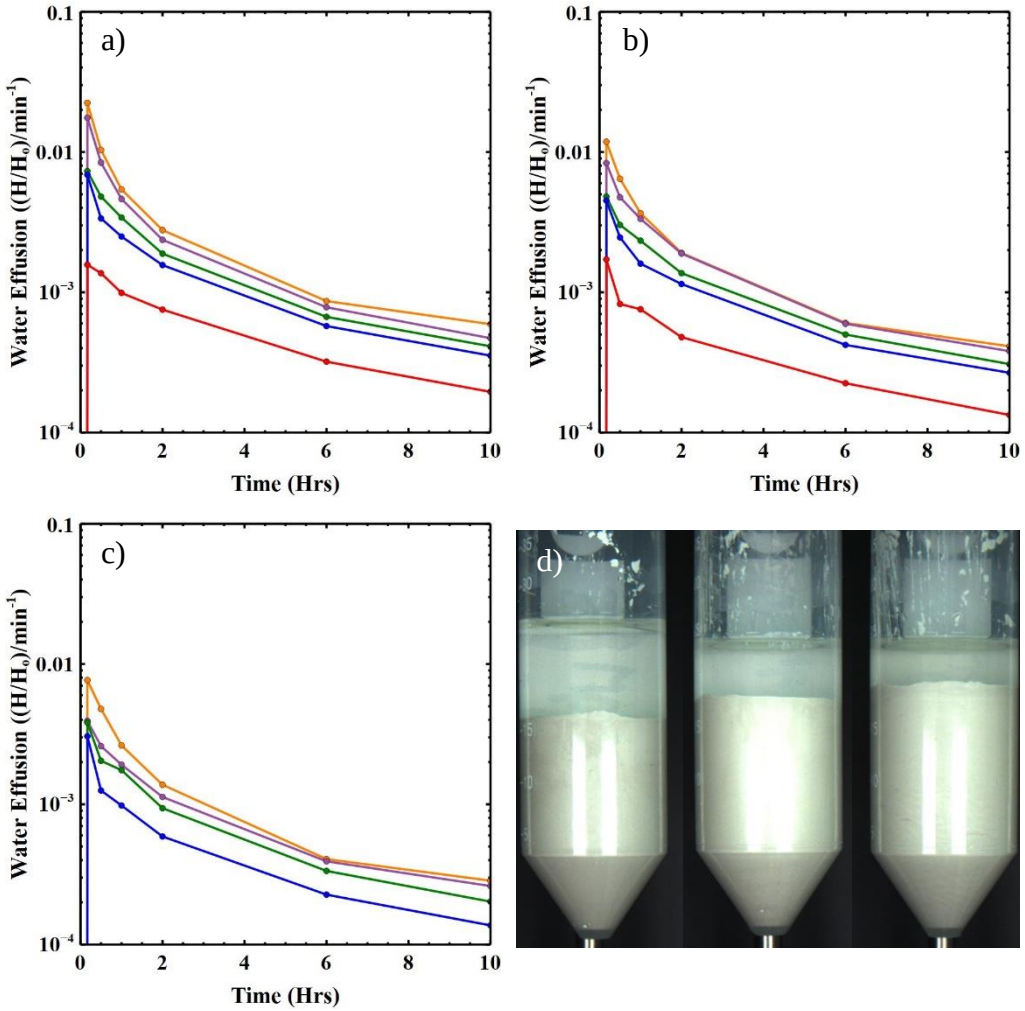

Figure 98: (a,b, and c) Graphs of the rates of compaction for the 50, 55 and 60 wt% respectively kaolin clays with measurements taken after each rotation period in the centrifuge. Data displayed in each graph is speeds 500 (red), 800 (blue), 1100 (green), 1500 (purple) and 2000 rpm (orange). Image (d) shows the large difference in the volume of water that has been extracted from each concentration (from left to right 50, 55 and 60 wt%) when centrifuged at 2000 rpm. Interestingly however, despite the high separation speed we do not always observe a flat water/clay interface.

Figure 98 shows the calculated rates for liquid being extruded from the surface of the sample determined from the relative height changes of water with time. The initially quick flow gradually reduces over time. In the 60 wt% sample at 500 rpm there is little or no water leaving the clay We suspect that this is due to the significantly

higher yield stress of this kaolin suspension being harder to overcome at these G forces. Due to the time resolution of these centrifuge experiments it is difficult to make an exact comparison with the shear observations. However, for slip to occur only a small lubricating layer is required which would therefore require only a short amount of time. Therefore, although the timescales in these experiments are much longer, the experiments may still be relevant to the processes observed during the slow compression steps in Chapter Two.

5.4.6 X-ray Shadowgraphy

Up to this point we have assumed that the clay undergoes uniform compaction. The measurements that we have undertaken so far are relatively simple and are unable to measure the variations in clay concentration in a given volume. To remedy this, we use x-rays in order to look inside the samples and record changes in solid content of the clays.

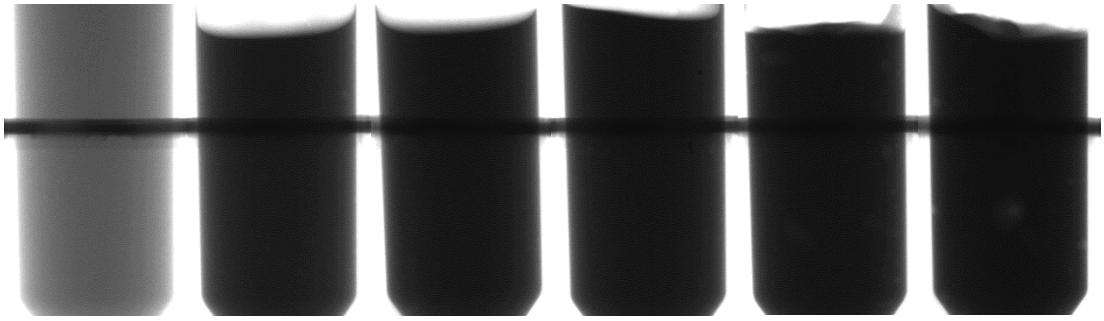

Figure 99: X-ray shadowgraphs of samples taken with the Rex Cell instrument. We observe that with a higher kaolin content the samples appear darker in the image. From left to right are a water blank, 45, 50, 55, 60 and 65 wt% kaolin.

Doing so allowed for the identification of a sample and the monitoring of any concentration changes that occur during and after a flow has been caused. Firstly, we calibrated the x-ray shadowgraph using known concentrations of kaolin. To do this, shadowgraphs of 45, 50, 55, 60 and 65 wt% clays were taken using the Rex Cell x-ray instrument.

5.4.7 Calibration of the Cell

A background image of an empty sample tube was also captured to provide a baseline for 100% transmittance. This was carried out to confirm that the x-ray source did not saturate the detector. The mean background intensity value is denoted as I_o. A water blank was also recorded and analysed so that we could identify regions of water that had been extracted after each centrifugation step more easily in the absorbance profile.

Using the shadowgraphs obtained we used the grey values to determine the absorption of the objects in each image. We observe that if a higher concentration kaolin is measured it will appear darker in the x-ray shadowgraph, the grey value is decreased and so the intensity is diminished. This is due to the greater density making it much more difficult for x-rays to pass through the structure. This will result in a greater amount of absorbance from higher concentration clays. We can use this observation to track concentration changes in a kaolin sample during or after shear is induced in the system. We took the data from the shadowgraphs to calculate the absorbance of transmitted light to generate a calibration curve for future use ($A = -\log_{10}(I_o/I)$).

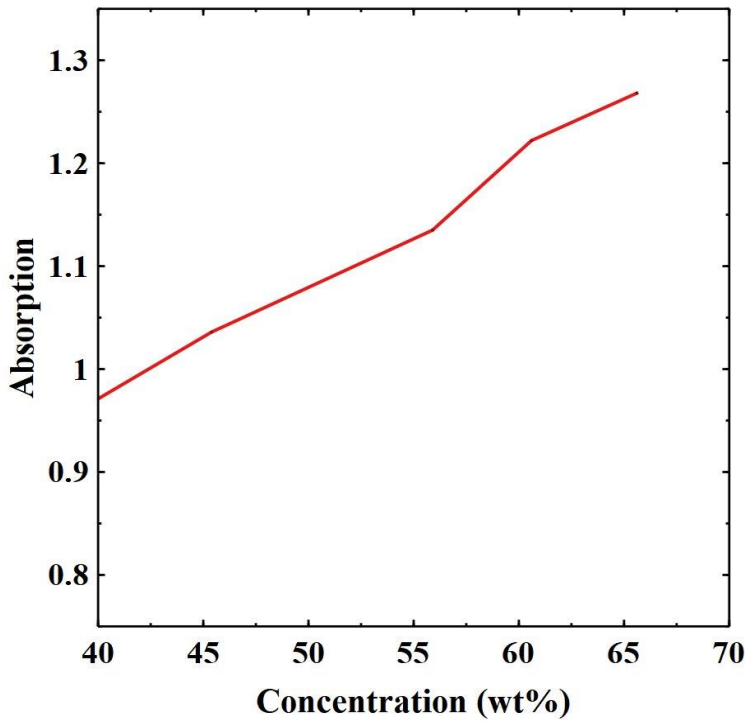

Figure 100: Calibration curve of the kaolin clay concentrations before being centrifuged. This will help to identify concentration changes in the systems. Data point for 50 wt% has been omitted as it is very similar in magnitude to the 55 wt% sample.

This calibration curve allowed us to estimate the water content of samples after they have been centrifuged. We took scans of a shadowgraph and averaged the intensity of light at points along its depth. We then compared the absorption of the sample to those of the known concentrations above in order to infer local concentration variations in the bulk. In general we do not observe air bubbles in the samples: this may be because they are absent from the samples or are too small to observe in the shadowgraphs.

5.4.8 Tracking Concentration Changes

There are several common features of the 55 and 60 wt% systems as they are centrifuged, namely that there is a developing region of low concentration close to the surface of the surface of the solid packing. We also observe in fig. 101 that at depths closer to the bottom of the sample tube there is an increase in the amount of absorption we measure, particularly in the 55 wt% sample where we see a marked increase in the absorption. The increase in absorption at depth observed in the 60 wt% is less significant, this is likely due to the higher initial yield stress associated with this concentration. It appears that the process of consolidation occurs close to the middle of the packing.

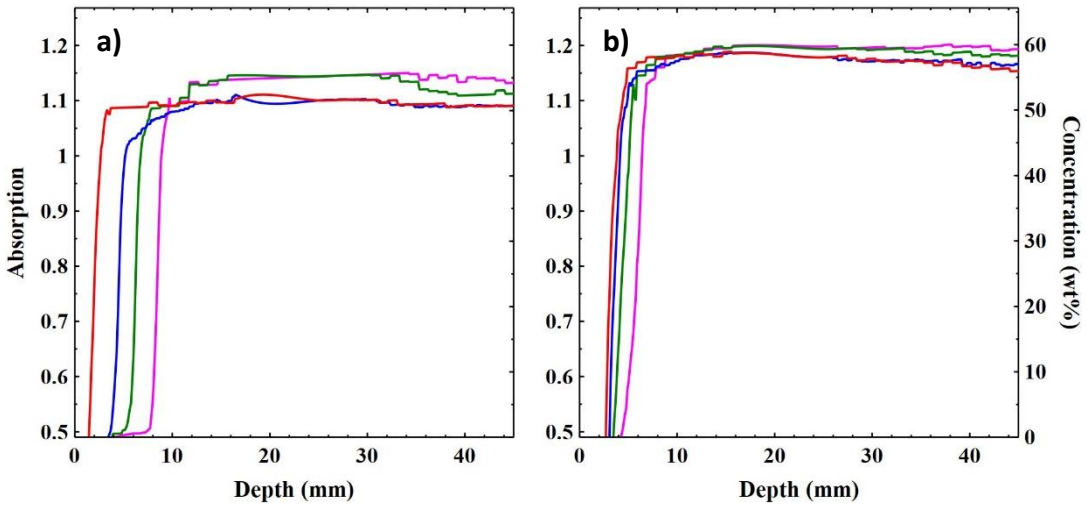

Figure 101: Absorption profiles for the 55 (left) and 60 (right) wt% samples. Data presented is for rotation times 0 (red), 10 (blue), 15 (green) and 25 (pink) minutes.

Centrifugating for 10 minutes pushes a small amount of water out to the surface and we observe a concentration decrease at the interface. We observe an absorbance of 1.02 in the 55 wt% sample suggesting a surface concentration of approximately 43 wt%. After the first rotation there also appears to be a transitory region where a concentration gradient is present that slowly increases to the initial concentration. In consecutive rotations this region appears to consolidate and is more reminiscent of a band in the sample. However, we see that after 15 minutes of rotation there is a large region that appears to be a higher concentration (approximately 57 wt%) below the surface in fig. 101(a). At this point there also appears to be a region at the bottom of the tube that is higher than the initial concentration but lower than the upper region (approximately 56 wt%). These results suggest that there is a contribution of liquid from the entire system however at this point there is a greater amount of water leaving the mid region of the clay. This is a transient behaviour and when the system is analysed after 20 minutes of rotation most of the system shares a common concentration. This behaviour is observed in both the 55 and the 60 wt% samples. However, we see this behaviour to a lesser degree in the 60 wt% kaolin, see fig. 100(b). In the 55 wt% sample we do observe some artefacts in the initial dataset close to the surface. The interface is not completely flat, this is later removed by the compression. We also should note that the datasets show a drop in the concentration close to the bottom of the tube, this is because they have a tapered bottom and so the thickness of the layer we observe decreases. This allows more light to be transmitted through the sample.

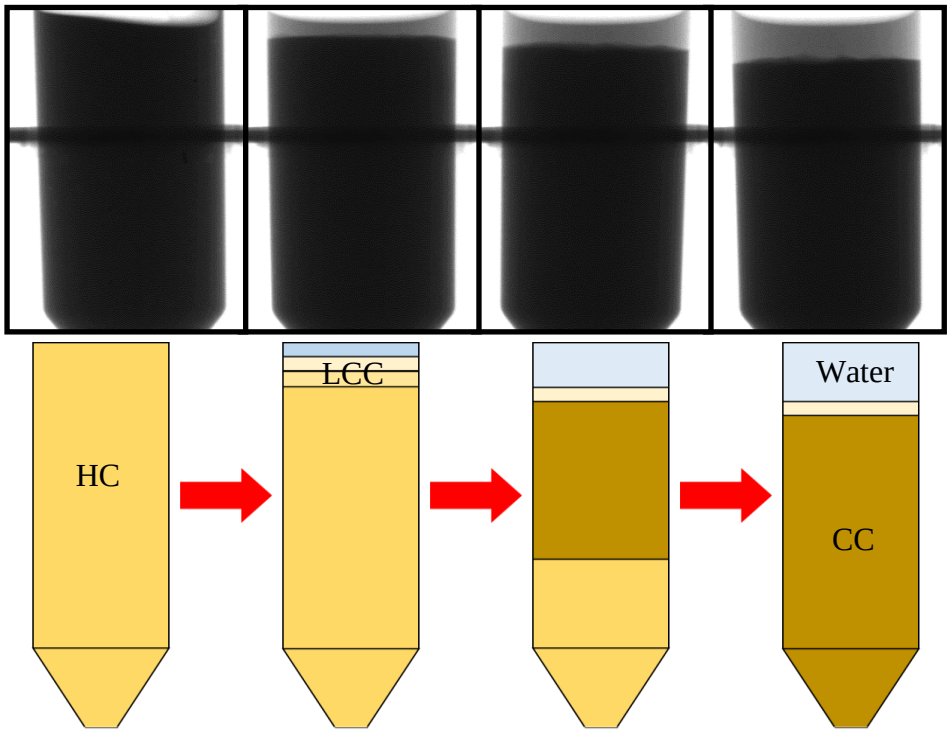

Figure 102: X-ray shadowgraph images of the 55 wt% at times 0, 10, 15 and 25 minutes after rotation at 1500 rpm (left to right). Below these images is a schematic diagram of how the dewatering occurs informed by the x-ray data presented in figure 100. Key for annotations HC – homogenous clay, LCC – Low Concentration Clay, CC – Compacted Clay.

We are unable to observe whether there are any channels in the systems in the shadowgraphs similar to those observed optically previously in the chapter. We would assume that these channels exist throughout the samples to allow for transport of water through the system and would expect to observe them in the shadowgraphs. It is likely that we cannot see these channels because of their relatively small volumes compared to the thickness of the material we are using. In future it would be useful to measure the effect of compression using thinner samples to allow for better visualisation of these channels in the shadowgraphs.

5.5 Complications and Limitations

We had plans to extend the work carried out in this chapter, particularly in the way of x-ray shadowgraphy. Unfortunately, a lot of this work was carried out during the COVID pandemic. As a result we were unable to perform additional work in collaboration with Schlumberger where the Rex-Cell instrument is situated. As a consequence, the amount of available shadowgraph data is limited covering only two concentrations using 1500 rpm rotation. We would have investigated a wider range of centrifugation speeds and time scales selected from the experiments that we were able carry out in the university lab. This information may have provided a greater amount of information to draw from when describing the processes of compaction for kaolin clays around the crossover concentration.

Due to limitations in available equipment, we were also unable to measure properties of the packings such as pressure changes which limited our ability to measure useful quantities such as changes in the porosity of the systems as they are compacted. If we had this capability, we would be able to characterise the compaction of these systems in much greater quantitative detail. If we had the opportunity to repeat this work we would consider how we could measure changes in the pressure of the system as porosity is a key value in determining many quantitative aspects of how packings compact under force. There are several ways of achieving this noted in the literature that would be pertinent to use in future studies [134, 140, 141]. We were also unable to confirm whether there was any air trapped in the systems which would be eliminated in the initial compression. This could alter the results of our experiments and affect the calculated concentration and subsequently the yield stress. Future studies should focus on this to provide more accurate information relating to the concentration change.

5.6 Conclusion

In this chapter, motivated by our previous observations in Chapter Two, we tried to understand how clay might be influenced by compressive stress. It is important to note that the timescales of compression in Chapter Three are relatively small, it is therefore likely that the most relevant period is the early stages of the experiments explored here. Stronger compressions in the slip experiments caused more water to be expelled which correlates with our findings in this chapter that higher spin speeds or applied stresses resulted in a faster rate of fluid flux from the samples. The most interesting result found in this chapter is that denser clay suspensions make denser sediments. This result was unexpected, due to these materials being yield stress fluids it was expected that they would compact to a critical concentration. It would be interesting to see whether this behaviour is still observed with even greater centrifugal stress. Although there is no defined packing limit for irregular particles intuitively there must be one. The low concentration clays show less order in these experiments resulting in the lower final concentrations. Whether this order can be exerted with greater force is yet to be seen.

Chapter 6. Extensional Rheology of Laponite Suspensions

6.1 Introduction

Industrial processing of yield stress fluids frequently results in the break-up or separation of two masses of a fluid, e.g. the detachment of a droplet during a dispensing application or two surfaces coated with a liquid being pulled apart. Whilst measurements using a shear rheometer can extract precise rheological properties, other simpler tests are often preferred by industry to characterise or provide quality control of samples [1].

One approach makes use of the detachment of a pendant droplet from a needle. Measuring the weight of the detached droplet enables an estimate of the applied forces at the neck, which when combined with visual measurements of the thinning, allows certain rheological properties such as the yield stress to be extracted [142,143]. The size of drop and hence applied stress can be modified to some degree by altering the imposed flowrate [143]. The strain-rate however varies throughout the experiment, controlled by gravity and the rheological properties.

Another approach is to use an extensional rheometer [144] which consists of two cylindrical plates, with a layer of liquid sandwiched between. As the plates are separated, the thinning and shape of the resulting break-up behaviour are monitored with either a laser micrometer or a camera to monitor the changes in sample profile. Precise equations exist to describe the thinning behaviour of some fluids in an extensional rheometer [145,146]. Often as the fluid is deformed, a stable bridge will develop between two liquid masses that wet each of the plates. This bridge then thins under the action of capillary pressure enabling the applied stress to be easily calculated from the bridge radius [147]. Extensional rheometry has been used to characterise a range of common yield stress fluids (Ketchup, Mayonnaise, Yoghurt [148]). An equation was also developed to describe the thinning of an oil-emulsion yield stress fluid, enabling measurement of its yield stress [146].

However, yield stress fluids may sometimes break-up long before the formation of such a bridge. Sometimes the yield stress of the fluid is of sufficient magnitude that surface tension induced thinning is negligible or at least confined to a very small period and region of the flow just before breakup. Recently, Zhang et al [101] were able to perform an extensional measurement using a shear rheometer with a sufficiently large plate that they could directly measure the normal forces. To achieve this, they had to use boundary conditions that created almost complete slip at the boundaries. Their measurements showed that the shear and extensional yield stress, whilst always proportional, were related by different constants depending on the type of fluid studied.

Even when no measurement of the normal stress is possible, important information about the sample properties can still sometimes be deduced from observation of the sample's break-up behaviour using extensional rheometry. For example, in several complex fluids visual observation of fluids subjected to an extensional deformation has allowed researchers to assess changes in brittleness/ductility [149, 150, 151]. Recent theoretical work has also suggested that as samples age, yielding in amorphous materials results in a change between ductile and brittle behaviour [152, 153]. These studies predict that the brittleness of a sample is related to a stress-strain curve increasingly defined by a stress overshoot measured under homogeneous shear [153]. Therefore, quantifying these changes in a simple way could provide an indication of the age of a sample.

In this study we focus on how the aging of a Laponite suspension effects the observed break-up behaviour in extension. Laponite is a clay that is commonly used as a rheology modifier [154]. It consists of disk like particles of thickness ~1 nm and lateral dimension ~25 nm. Depending on the conditions (concentration, pH, electrolyte concentration) it can form a variety of different phases including a Wigner glass, isotropic liquid and isotropic or nematic gel [155]. Laponite suspensions often exhibit a yield stress and are strongly thixotropic, with substantial changes in properties observed over the timescales of hours. However, the evolution of the sample properties has in some studies been shown to continue for many months [156].

6.2 Method

Stock suspensions of Laponite RD (ms16, Conservation Resources) were prepared by dissolution in solutions of deionised water containing 10^{-4} M NaCl. The pH of the suspension was then adjusted to pH 10 by adding 0.1M NaOH dropwise. Suspensions of 3, 3,5, 4, 4.5 wt% were prepared and then sealed in large bottles prior to use. Before each set of experiments 50ml of suspension was removed and mixed with 40 µL of blue food colouring and thoroughly mixed through mechanical agitation and sonication.

Shear and extension measurements were performed with a Malvern Kinexus Pro Shear Rheometer. The large waiting times required to observe the aging of the Laponite samples meant that experiments in air risked significant evaporation of the sample, thus compromising the results. We therefore devised a methodology that immersed the Laponite samples and rheometer plates in oil, thus eliminating sample evaporation.

For the extension measurements, the lower 10 mm diameter plate of the rheometer was mounted inside a transparent, square cross-section Perspex tube (see fig. 102). The tube was sealed at the bottom and open at the top and had a small access tube in one of the side walls which was covered with a rubber seal. The upper plate was then moved to a gap height of 5 mm and the tube was filled with Silicone oil (density 0.963 gcm^{-3}) – chosen to nearly match the density of the Laponite samples (~1.01g/cm^3). The Laponite suspension was then loaded into a luer-lock syringe and, using an 8cm long G21 hypodermic needle, injected through the rubber seal between the rheometer plates. The process of injecting the Laponite, strongly shears the sample, rejuvenating it, and is taken to be the beginning of the aging process (i.e. t_w=0). Injecting the sample, we slightly overfill the gap between the plates. To trim the sample the upper rheometer plate is equipped with a PTFE collar that can be slid downwards over the sample and onto the bottom plate, removing any excess fluid.

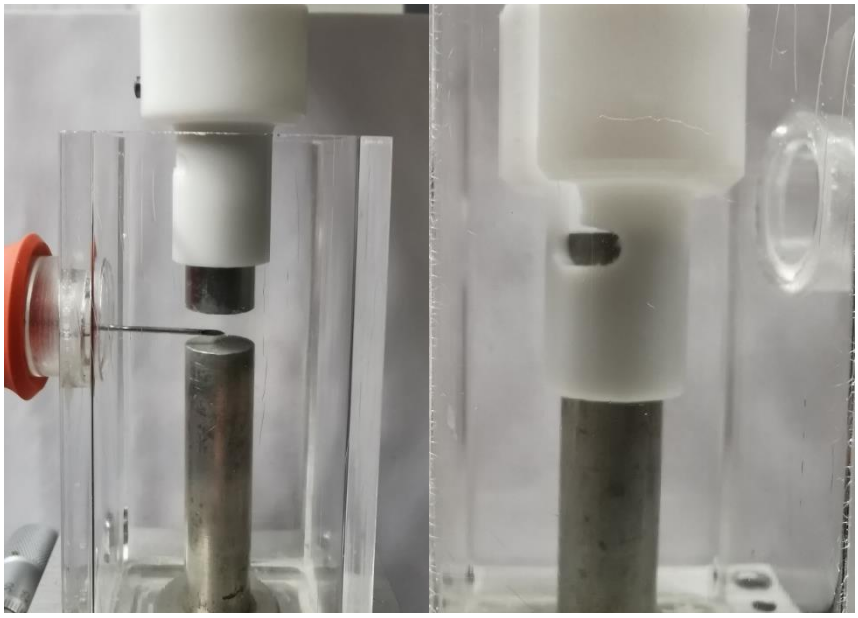

Figure 103: Photographs of the extensional geometries. In both images one can see the white PTFE collar used to trim the sample before measurements were taken. This collar is pushed over the sample to remove the excess in one motion, to generate a flat interface.

After an appropriate waiting time the upper plate is then moved upwards with a constant Hencky strain rate of 0.08 s^{-1}. The rate is fast enough that minimal aging of the sample happens over the course of the experiment [157]. Significantly higher strain-rates would result in strong viscous dissipation which we aim to minimise [17]. Whilst the normal forces acting on the upper plate are too small to measure, the experiment is filmed with a camera (Point Grey, Flea3) so that the break-up behaviour can be analysed. Automated image analysis of the plate separation, diameter of the midpoint and the contact angles was performed by subtracting two colour channels from each other to highlight the appropriate feature (plates or fluid), thresholding the image and then measuring the width of the sample at different heights. The midpoint was located as the narrowest region of the fluid. The angles were measured by extracting multiple widths at known heights in a region up to 1 mm from the bottom plate and calculating the associated gradient.

Shear measurements were performed using a conventional 50 mm cone and plate (cone angle 1°). To immerse the sample in oil, we designed a 60 mm diameter removable cylindrical ring which could be reversibly attached to the bottom plate. For these measurements the Laponite suspension was deposited on the bottom plate via the same syringe and needle as before. The upper plate was brought to the trim height and excess sample removed. No further pre-shear was applied, to as closely as possible match the conditions in the extensional experiment. The ring was attached and the gap around the rheometer plate filled with Dodecane oil – chosen for its low viscosity (1.34 mPas). After the appropriate waiting time the samples were then measured using oscillatory or continuous shear. Control experiments showed that the difference in stress measured with or without the Dodecane oil was not significant.

6.3 Results and Discussion

Figure 104 shows example images of a 3wt% Laponite suspension subjected to an extensional Hencky strain-rate ~0.08 s^{-1}. Images, left to right, illustrate the starting configuration, an intermediate position, and the sample just prior to break-up. Each row shows how the experiment is modified by waiting different amounts of time (t_w) following the loading of the sample.

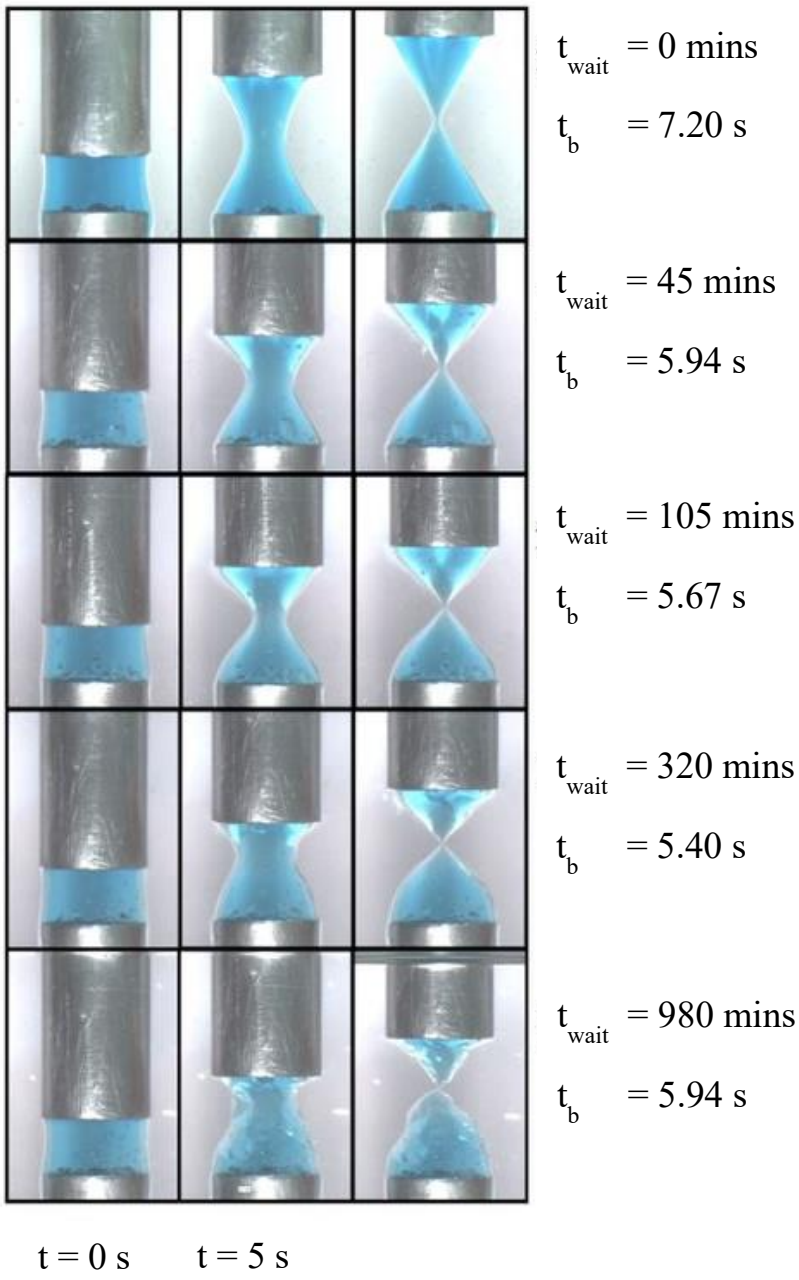

Figure 104: Extensional rheology of a 3 wt% Laponite suspension left to age for different waiting times as indicated. Each row of pictures shows the initial fluid, the final shape just prior to breakup and an intermediate point.

At t_w =0 the samples deform in such a way that the sides resemble a hyperbola, finally resulting in a conical deposit. As the samples age this gradually changes, with the sample profile necking faster in the middle, resulting in an earlier breakup behaviour.

In extensional rheology for many types of complex fluid it is common to observe a thin cylindrical region between two masses of fluid adhered to each end plate [158]. This has been used in some studies to estimate the yield stress given a knowledge of the interfacial tension [146, 158]. Whilst the sample thins in the middle, we never observe such a filament. A particularly notable feature at t_w = 980 minutes that is even more pronounced for higher concentrations, is that the breakup is no longer smooth but begins to result in fracture surfaces. We can summarise these initial qualitative observations by stating that the break-up dynamics for each concentration visually change from a more ductile behaviour, in which the sample is drawn out into a long smooth profile, to a more brittle behaviour, in which samples eventually begin to fracture [149, 150, 151]. Before returning to quantitatively study these dynamics we now characterise the behaviour of the fluid using standard shear rheology techniques.

6.3.1 Characterising the Laponite Suspensions

To characterise the sample aging we performed oscillatory shear measurements on the different concentration samples. The elastic modulus G' obtained from oscillatory shear of the 3 and 4 wt% samples at 5% strain was found to be largely independent of frequency over the range 0.02-20Hz (see supplementary figure 1). We therefore chose to perform all our oscillatory measurements at 1Hz.

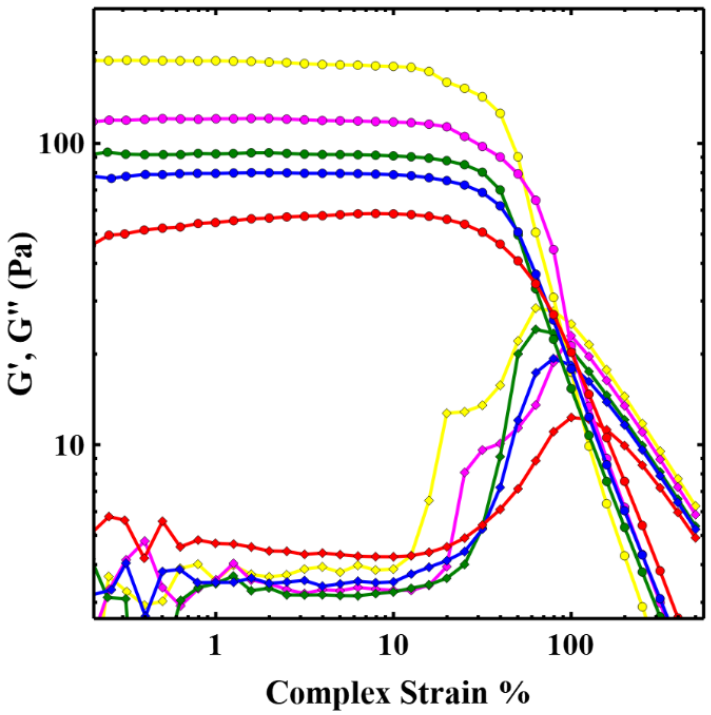

Figure 105: Strain amplitude sweeps at 1Hz for a 3wt% sample at waiting times of 0 (red), 45 (blue), 105 (green), 320 (magenta) and 980 (yellow) minutes. Measurements of G' (circles) and G" (diamonds).

Fig. 105 shows strain amplitude sweeps of the 3 wt% laponite suspension at a frequency of 1 Hz, showed that the linear-viscoelastic regime persists up to complex strains γ_{lve}~15-20% at all concentrations and aging times studied. Indeed, the maximum strain in the linear-viscoelastic regime appears to be unchanged across all our samples. This is similar to the observations of Wendt [159] who studied suspensions of another thixotropic clay, Bentonite. At strain amplitudes less than γ_{lve}, G' far exceeds G" for all concentrations, with values of tan(δ) ranging from 0.05 for t_w=0 to 0.02 for t_w=980 minutes. Consequently, G' ≈ G*. However, it should be noted that G' remains significantly greater than G" at higher strains (γ ~ 50%), although the elasticity in this region is non-linear and plastic deformations will become increasingly significant [160].

To monitor the aging of the samples we therefore measured G' as a function of waiting time (t_w), taking single measurements at 1 Hz and 5% strain amplitude at intervals of 10 minutes. We also plotted the value of G' at 5% strain, obtained from strain amplitude sweeps performed for 3, 3.5 and 4wt% at 0, 45, 105, 320 and 980 minutes. These latter measurements used a fresh sample, aged without any agitation, for each value of t_w. These latter measurements agree quantitatively with the single

measurements taken at 10 minute intervals. This indicates that the measurement protocol did not have a significant influence on the structure of the Laponite suspension.

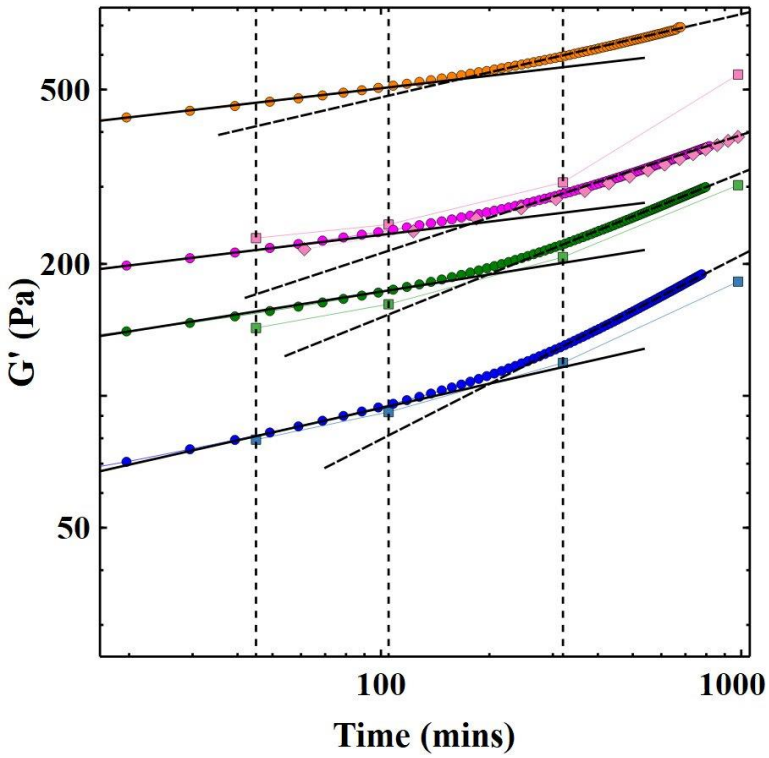

Figure 106: Aging of Laponite suspensions. The elastic modulus G' of aging samples of Laponite (3 wt% blue, 3.5 wt% green, 4 wt% magenta, 4.5 wt% orange) measured using a strain amplitude of 5% at 1 Hz every 10 minutes. The growing elastic modulus exhibits a two stage concentration-dependent power law growth. The crossover aging time between the two regimes decreases with increasing concentration. Also shown are data for 4wt% measurements collected every hour (pink diamonds), showing that the protocol did not unduly influence the Laponite structure. Measurements of G' at a strain of 5% taken from strain amplitude sweeps conducted on undisturbed samples after the indicated aging time for 3, 3.5 and 4 wt% are shown as blue, green and pink squares.

The measured values of G' for each sample exhibited a two-stage power-law dependent growth. Fig. 106 the exponents during both the initial and latter stages decrease with increasing sample concentration. A number of studies of thixotropic clays (Bentonite [159], Na-Montmorillionite [161] and Laponite [162, 163]) have observed power-law growth in the measured value of G' with waiting time. These studies however saw just a single exponent for each sample. However, all the concentrations studied here show a definite crossover between the initial growth in G'

and the later higher exponent. The crossover time decreases with sample concentration after some waiting time ~2.5-4 hours. To confirm that the crossover behaviour was not a result of the method used, we measured a 4wt% sample in the same way as before but with measurements taken at hourly rather than 10 minute intervals (pink diamonds). These measurements showed a crossover between the two exponents at a very similar aging time to the sample measured at 10 minute intervals. The fact that our measurements were performed in oil also rules out possible effects due to evaporative losses.

The existence of two exponents suggests two processes of changing relative importance at different waiting times. Under the conditions considered here (3-4.5 wt%, 10^{-4} M NaCl, pH 10), Laponite is believed to form a repulsive glass made up of small T-clusters of particles with attractive interactions (face to edge contacts) [155]. Whilst increases in G' occur due to the forming and rearrangement of the particles into more stable configurations within a glassy sample, it has also been shown in the context of silica gels that G' increases with t_w due to the stiffening of inter-particle contacts [164]. In the context of glasses of star polymers, it was found that G' can evolve with two exponents: one due to caging and one due to rearrangement of cages [165]. It is also possible for the stresses induced in a system through shear rejuvenation to modify aging [166]. The pre-shear applied to our samples, forcing the Laponite at a volumetric flow rate $\dot{Q}$ through a thin hypodermic needle of diameter d, is quite strong with a crude estimate of the shear-rate $\dot{\gamma} \sim 8\dot{Q}/\pi d^3 \approx 2000 s^{-1}$. The rejuvenation of our samples however only occurs for a short period. This differs from other studies where the Laponite is repeatedly sheared until a steady state value is achieved [159, 162]. These differences might lead to a different starting condition.

6.3.2 Yield stress and growing stress overshoot

The closest equivalent shear rheology experiment to the extensional experiments performed in this study is a constant shear-rate start up experiment. To gain some insight into our extensional measurements, we therefore measured the stress-strain curves for the different sample concentrations and at the different sample ages at a shear rate of 0.08 s^{-1} (chosen to match the Hencky strain rate). Figure 107 shows a series of measurements for 3wt% samples at waiting times of t_w=0, 45, 105, 320 and 980 mins.

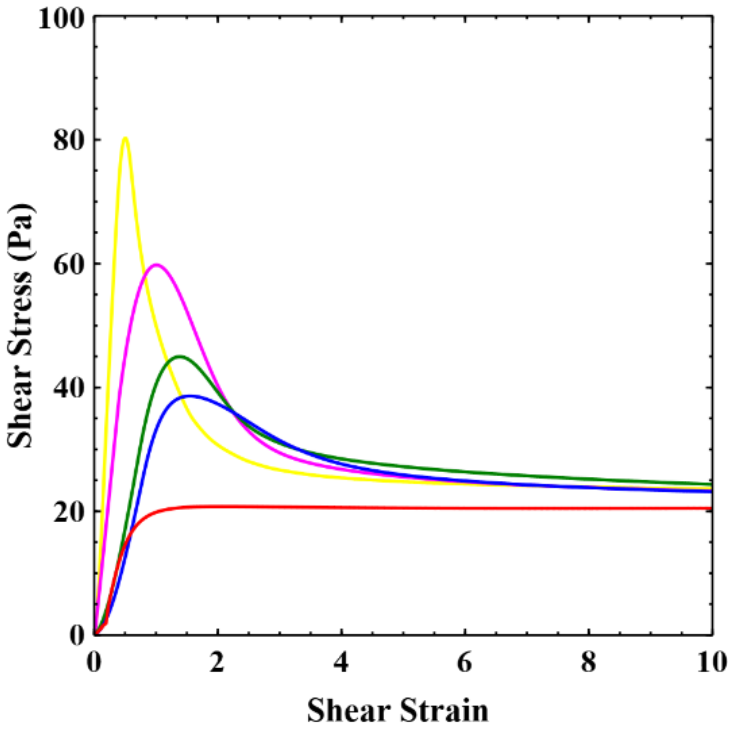

Figure 107: Shear stress versus shear strain for 3wt% Laponite samples at aging times of 0 (red), 45 (blue), 105 (green), 320 (magenta) and 980 (yellow) minutes. Samples show an increasingly large stress overshoot with a growing static yield stress. The yield strain also reduces as the sample ages.

Shear start up measurements were also performed for 3.5 and 4wt% samples at t_w=0, 45, 105 and 320 minutes. The static yield stress (σ_{static}) was defined as the maximum stress (σ_{max}) measured. The yield strain was defined as either the strain at which the stress maximum was measured or, in the case of samples with no stress overshoot (t_w=0), when the stress reached 98% of the plateau value.

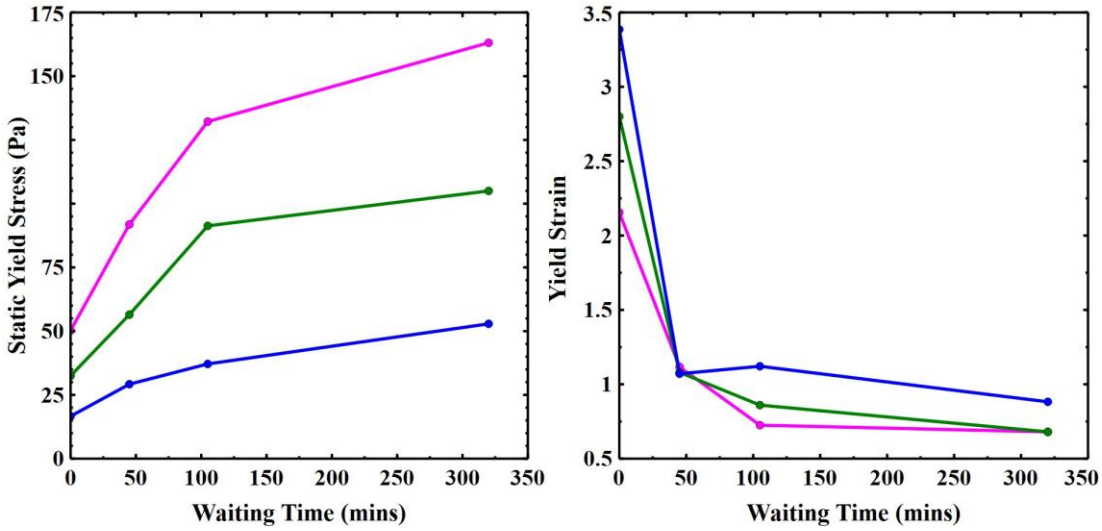

Figure 108: the static yield stress and yield strain in aging samples of Laponite. A) The static yield stress B) the yield strain (see text for definitions) of 3 (blue), 3.5 (green) and 4wt% (magenta) samples at the sample aging times shown.

Fig. 107 shows that at t_w=0 the static ($\sigma_{static} = \sigma_{max}$) and dynamic ($\sigma_{dynamic}$) yield stress are approximately equal [24]. However, as the waiting time t_w increases, the curves exhibit an increasingly pronounced stress overshoot, resulting in a large increase in the measured static yield stress. In addition, the yield strain at the stress maximum also decreases monotonically with the age of the sample. Wendt et al., studying the thixotropic clay Bentonite in simple shear, also observed an increase in the stress overshoot and a decreasing yield strain in samples allowed to age for longer [159] similar to behaviour observed in fig. 108. They concluded that aging resulted in an increasingly brittle sample. This is also consistent with recent theoretical works on amorphous systems which argue that brittle failure is preceded by a strong stress overshoot which arises as the samples are allowed to age [152, 153].

6.3.3 Assessing the role of interfacial tension in extension

A number of authors have attempted to measure the yield stress of a fluid in an extensional geometry by determining the point at which the Laplace pressure due to interfacial tension and surface curvature exceeds the yield stress of the material [146, 158]. Visually it appears that the thinning of the midpoint is controlled by the motion of the plates until very near the end of the experiment. Whilst we do not observe a long thin filament between the two end plates, it does appear that near to the point of breakup the samples undergo spontaneous thinning.

Since it was difficult to precisely determine where interfacial tension, rather than the motion of the plates, controlled the thinning of the midpoint we used our initial measurements (figure 104) to determine the gap at which breakup of the sample occurred. We then repeated these measurements, following the same stretching profile until the gap was 0.5mm less than the gap at which break-up occurred. We then moved the upper plate upwards in 50μm steps at $10\mu ms^{-1}$, taking a picture and pausing to determine if the midpoint was static. This process was repeated until the filament thinned without motion of the plates. This was repeated for 3 wt% samples at $t_w = 0$, 45, 105 and 320 mins and for 3.5 and 4 wt% at $t_w = 0$ and the radii of curvature manually measured from the image at which spontaneous thinning began. In all cases the thinning occurred once the midpoint radius was less than ~250μm.

In order to assess whether the associated Laplace pressure is consistent with the measured yield stresses we need a measure of the interfacial tension. This is sometimes simply assumed to be equal to that of the suspending liquid [1,167,168]. Although, in another study on Carbopol suspensions, this was shown to be incorrect [17]. A common method used to measure the interfacial tension is the pendant drop method [169]. This however does not work if the yield stress is too high since it relies on the gravitational induced distortion of the sample against interfacial tension. Whilst not ideal we measured the interfacial tension of a 0.5 wt% Laponite suspension suspended in oil from a blunt syringe needle. Using the opensource software OpenDrop [170] we then estimated the interfacial tension. At concentrations of 0.5 wt% Laponite, under these conditions, has no measurable yield stress and hence the measurements should reflect the interfacial tension. The interfacial tension measured was $33 \pm 2\ mNm^{-1}$ which is very similar to the interfacial tension between the water

and oil from tests we carried out (32 mNm^{-1}). Whilst it is possible that the interfacial tension might differ at the slightly higher concentrations used, it seems likely that if the interfacial tension of Laponite suspensions is markedly different to that of oil and water, this should be apparent at 0.5wt%. This suggests that, at least in the case for Laponite yield stress fluids, the interfacial tension is set by the suspending liquid.

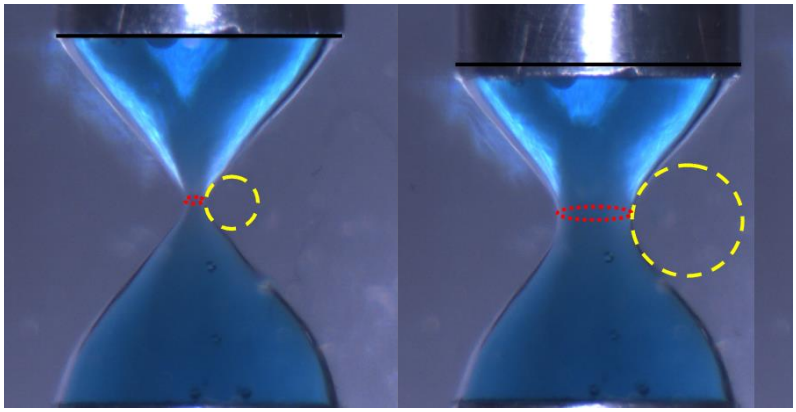

Figure 109: Left) Example image of a 3wt% Laponite suspension showing measurements of the sample prior to spontaneous thinning. Right) approximate diameter at which the Laplace pressure should equal the yield stress measured in shear. The red circle corresponds to the inner curvature R_{rz} while the yellow circle corresponds to the outer curvature $R_{r\theta}$.

Due to the geometry of our samples there are two relevant surface curvatures at the midpoint of the sample (see figure 109). To assess what role interfacial tension had on our experiments we manually measured (ImageJ) the final image before the filament began to thin spontaneously. This occurred very close to the breakup in all cases. We then calculated the critical Laplace pressure $\Delta P = \gamma\left(\frac{1}{R_{r\theta}} - \frac{1}{R_{rz}}\right)$ for 3 wt% samples at aging times t_w=0, 45, 105, 320 mins. For comparison we also measured 3.5wt% samples (t_w=0 mins) and 4wt% (t_w=0). Table 4 shows the calculated pressures for each sample and the yield stresses measured in shear.

Sample	Calculated Laplace Pressure (Pa)	Static Yield Stress (Pa)	Dynamic Yield Stress (Pa)
3 wt% t_w = 0	76 ± 9	16.6	16.1
3 wt% t_w = 45	84 ± 4	29.2	16.5
3 wt% t_w = 105	63 ± 6	37.1	16.6
3 wt% t_w = 320	158 ± 22	52.8	17.9
3.5 wt% t_w = 0	97 ± 15	32.5	31.5
4 wt% t_w = 0	183 ± 30	50.2	50.2

Table 4: Comparison of the Laplace Pressure calculated during the extensional rheology to the static and dynamic yield stresses measured in shear.

Whilst the measurements have considerable uncertainty there is a significant difference between the calculated pressures and the measured yield stresses, outside of our estimated uncertainty. Some previous authors have shown that the yield stress of a fluid can scale with Laplace pressure [146]. In theory the values of the Laplace pressure should equate to the static yield stress in extension. Studies have shown that the yield stress in extension can be larger than the yield stress measured in shear, although the measured ratio varies between different yield stress fluids, with values reported ranging from 2.5 to 6 [101]. Our measurements result in a ratio of 3±1 which is consistent with this. The geometry of the necking region is also not a perfect extensional flow and so these results should be viewed with some caution. It does appear that one can make an approximate measurement of the static yield stress using this methodology, however more measurements are needed to confirm this.

6.3.4 Thinning of the sample and sample yielding

It is clear from figure 104 that aging does have a significant effect on the breakup behaviour. To further characterise the break-up behaviour of our samples, we wrote image analysis code to measure the diameter of the narrowest point of the sample and the gap between the plates. Figure 110 shows the thinning of the midpoint of a 3wt% sample during extensional experiments.

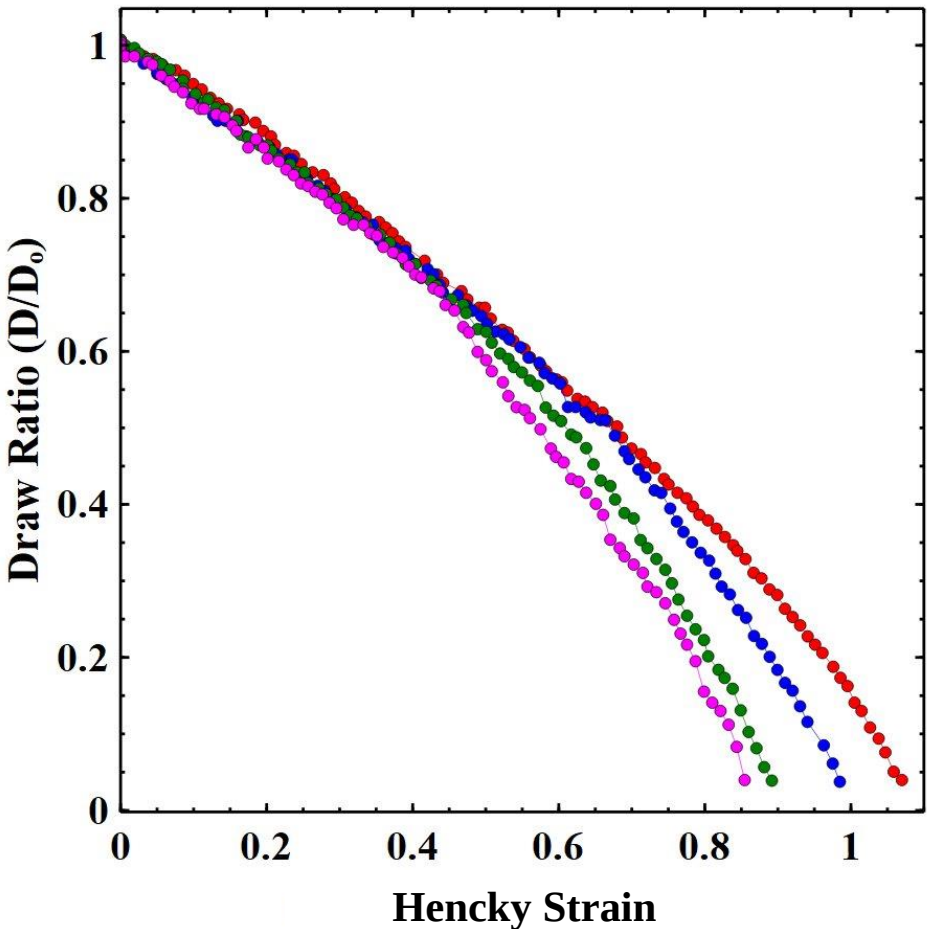

Figure 110: Thinning of the midpoint of a 3wt% sample at aging times t_w=0 (red), 45 (blue), 105 (green), 320 (magenta) minutes. D/D_o refers to the diameter (D) at the thinnest point normalised by the initial diameter (D_o).

All the samples, regardless of age, initially follow the same curve. However, each sample displays a "kink" at which the draw ratio of the sample begins to deviate significantly from that of the other samples. This "kink" appears at progressively lower values of the Hencky strain, as the sample age increases and is indicative of the sample beginning to neck more quickly at the midpoint.

Simulations of elastoplastic fluids in an extensional rheometer were recently conducted by Moschopoulos et al [171]. These predict that the thinning depends on the Bingham number σ_Y/kU^n (where k is the consistency index, n the flow index and U the velocity) provided the effect of surface tension is small. As yield stress increases, the flow results in greater necking resulting in earlier breakup, with plastic deformations more heavily concentrated in the neck.

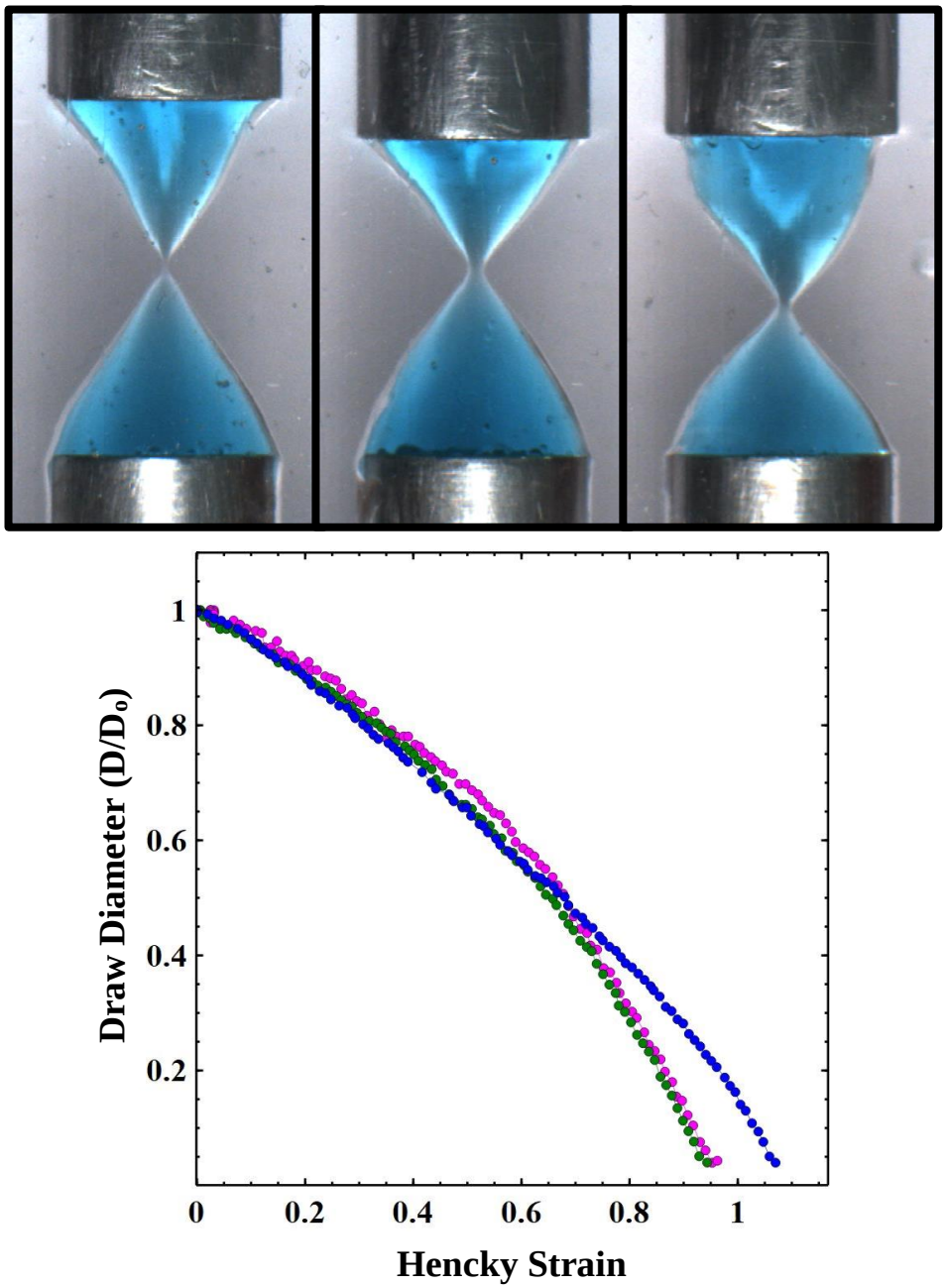

Figure 111: Extensional images of the 3, 3.5 and 4wt% samples at t_w=0 just before breakup. We also show the draw ratio obtained for these concentrations during extension.

Figure 111 shows the thinning of 3 different concentration samples at t_w=0. The yield stresses measured in simple shear vary by a factor ~ 3 between the lowest and highest concentrations. This is comparable to the change in static yield stress measured in figure 108 between the 3wt% t_w=0 and 320 minute samples. There is undoubtedly an effect on the curves due to yield stress however it appears that the onset of the kink shifts significantly more in the 3wt% aging samples. This implies that the necking is not just a function of the sample's yield stress. Precisely identifying where this kink occurs is difficult, but it is clear that this decreases monotonically with sample age. However, as we show below the same information can be measured much more easily by examining the contact angle of the base of the sample

6.3.5 Changes in Contact Angle

Extensional experiments are usually analysed through measurements of the diameter of the midpoint as above. However, we also tried to see if any information could be extracted from analysing the layer of fluid near to the bottom plate by measuring the change in angle with the vertical of the sample. Contact angle measurement software is commonly used in machine vision applications in industry and so could provide an additional way to analyse samples [172]. Using only the region of the fluid less than 1mm from the bottom plate, we measured the change in the angle made by the edge of each sample as a function of the applied Hencky strain, averaging the results of both sides. See figure 112 for example plots of a 3 wt% sample at different aging times. The longest age samples (t_w = 980mins) were not used because the rough morphology of the final samples (see figure 104) made the measurement of the subtended angles impossible. At higher concentrations and longer waiting times there was also a tendency for samples to slip, which meant that not all samples could be analysed in this way.

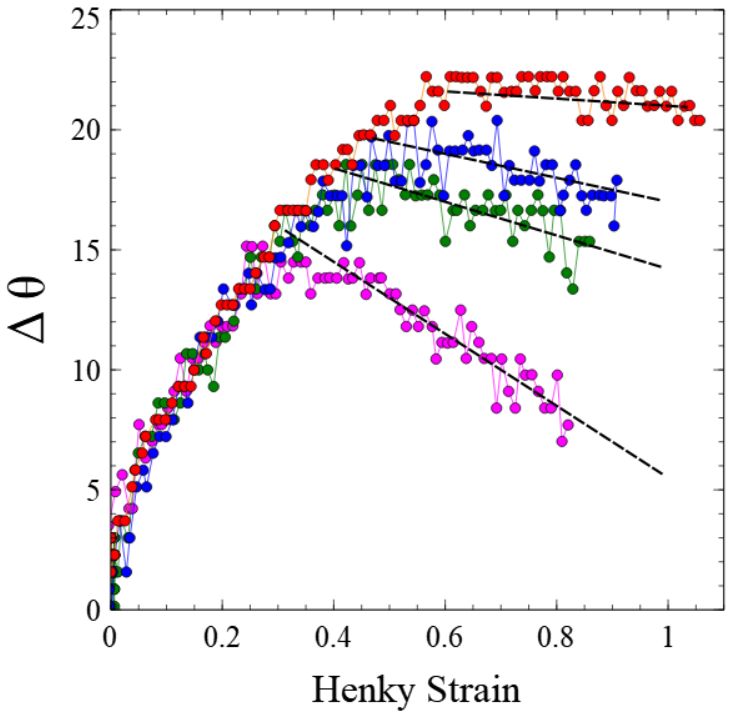

Figure 112: Change in the angle of the sample edge during an extension measurement. Data is shown for samples with aging times tw=0 (red), 45 (blue), 105 (green), 320 (magenta) mins.

In a yield stress fluid subjected to a slow extensional deformation, the initial build-up of stress in the sample results in an elasto-plastic strain. In our Laponite samples oscillatory shear measurements showed that G' >> G" at small strains. Most of the strain energy is therefore initially stored elastically. Since the tensile axial force transmitted through a sample in a quasi-static extensional experiment is the same at all heights, the local stress at two different heights is related by the cross-sectional area of the sample. The stress σ_{max} will therefore always be largest at the midpoint. At low strain-rates where viscous dissipation is minimised [17] and when the local strain is sufficient, the stress in the fluid near the midpoint is $\sigma \sim \sigma_Y$. At this stress, the fluid near the midpoint yields whilst the stress at the endplates is $\sigma \sim \sigma_Y (R_{mid}/R_0)^2$. The fluid near to the endplate, if G' >> G", however continues to behave somewhat like a strained elastic solid, with a deformation related to the local stress. This is somewhat analogous to a normal force sensor or strain-gauge: the strain in an elastic material subjected to an external stress is measured and used to infer the properties of the adjacent material applying the force. Assuming the material close to the bottom plate does not yield, if we can measure the local strain, it tells us about the forces being transmitted through the sample. The angle the edge of the sample, near to the bottom plate, makes with the vertical, assuming elastic deformation, is related to this strain in

the sample. The angle of the edge of the sample is therefore related in a complex way to the stress at the midpoint of the sample.

This argument obviously breaks down for larger strains and ignores the plastic deformations that will also occur in a yield stress fluid prior to the yield strain [160] but providing G' >> G" and the strains are sufficiently small, it provides a reasonable way of understanding the behaviour in this layer adjacent to the bottom plate. For our sample, figure 104 shows that G' >> G" for strains less than ~ 50%. We must also remember that it is the strain in the layer adjacent to the bottom plate, not the global strain that matters. Indeed, recent simulations of fluids with a large enough yield stress to ignore surface tension using a similar initial sample aspect ratio demonstrate the existence of a substantial unyielded region near to the endplates [171]. If the midpoint of the sample yields and accumulates significant strain this would increase the range of Hencky strains at which the bottom layer would satisfy this condition. The exact contribution of elastic and plastic deformation to the total depends on the local strain and shifts as this approaches the yield strain [160]. Even if plastic deformations make it hard to assess quantitatively the properties of the fluid, with an appropriate calibration between measured behaviour and known rheological properties this could still prove useful for sample characterisation.

In figure 112 we observe several features of the generated curves. Firstly, all the samples follow the same initial increase in angle. In fact, samples of different concentrations also follow the same shape. This makes sense since initially the samples are in the linear viscoelastic regime with very little plastic deformation.

Secondly, the sample angle's reach a maximum. The Hencky strain corresponding to these maxima appears to match up well with the Hencky strain at which the kink in the thinning data was observed earlier (figure 110). This supports the idea that the region of fluid near the plates allows one to infer properties associated with the stress at the sample midpoint. Whilst this information is available in both data sets, it is far easier to analyse in the angular plots. Noise in the plots of the type shown in figure 112 results in considerable uncertainty as to exactly where the rate of thinning increases. In contrast the maximum of the angle plot shows this point much more clearly.

Figure 113 shows estimates of the Hencky strain together with the associated errors at which this necking appears as a function of aging time. The decreasing value of the Hencky strain with sample age captures quantitatively the qualitative observations that the samples appear more brittle as the samples age. It also agrees with the data obtained in simple shear.

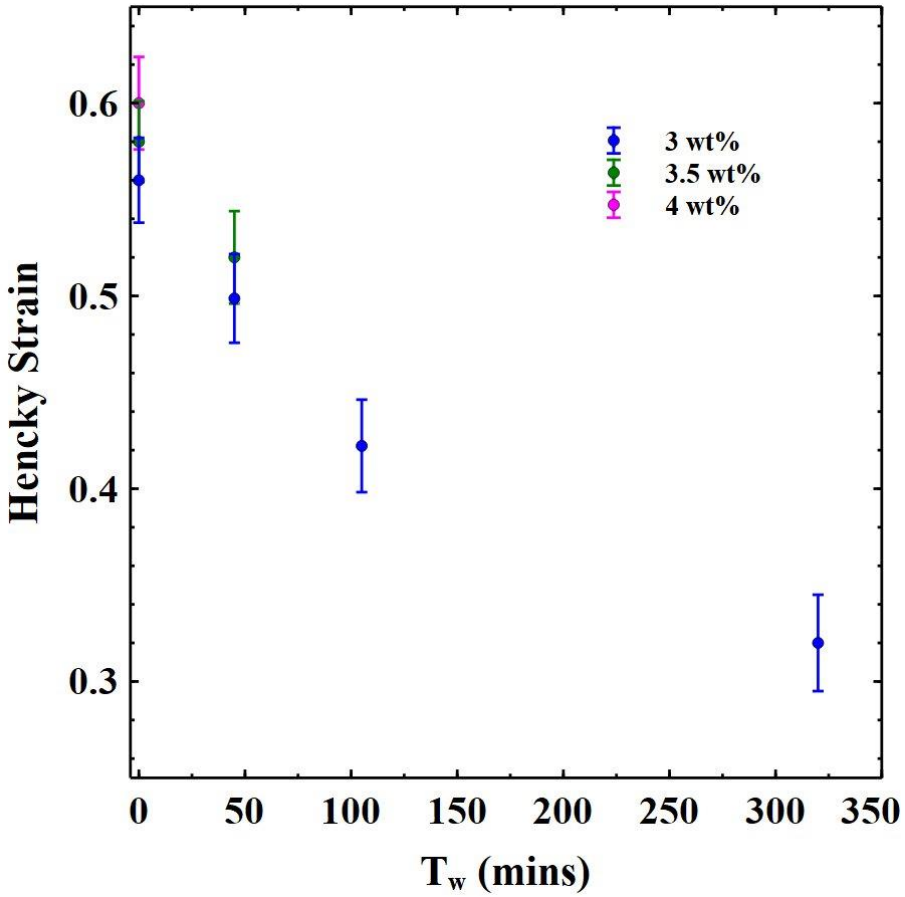

Figure 113: onset of necking for 3 (blue), 3.5 (green) and 4 (pink) wt% samples at the aging times shown.

The angle of the sample $\Delta\theta_{max}$ at which the sample begins to neck for a given sample geometry gives an indirect measure of the strain at which the sample yields. From our shear stress measurements, we measure the yield strain corresponding to the static yield stress for each concentration and aging time. At t_w=0 none of the samples display a significant stress overshoot and so we define the yield strain as the strain at which the stress reaches 98% of the plateau value. In figure 114 we plot this yield strain versus $\Delta\theta_{max}$ for all our samples. We observe a relationship which, in the limited range of samples studied, does not depend on the concentration of the material, implying that with the appropriate calibration curve it should be possible to infer the

yield strain. It should also be noted that a similar plot of yield strain versus Hencky strain does not produce the same collapse.

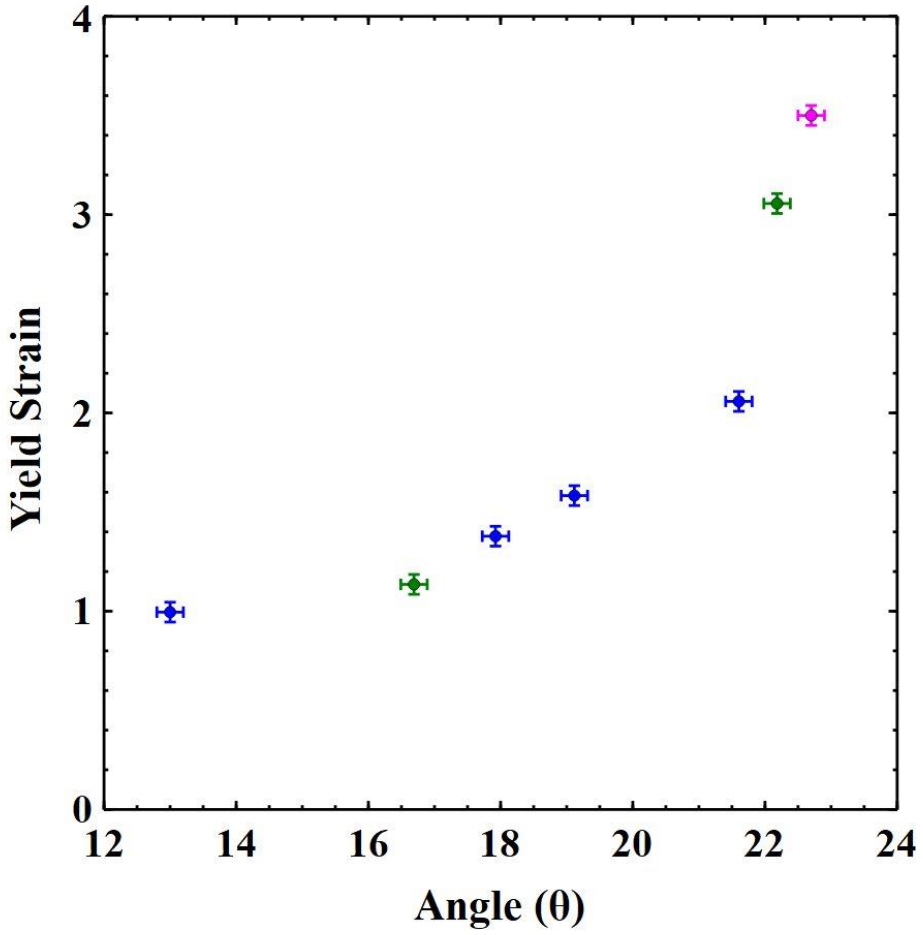

Figure 114: Graph of yield strain vs $d\theta_{max}$ for the 3 (blue), 3.5 (green) and 4 (pink) wt% samples.

The final and most difficult to interpret aspect of these curves is the subsequent reduction in $\Delta\theta$. All the plots only show data prior to sample breakup (ie whilst there is a continuous liquid bridge between the two plates). As the samples age, there is a slope of increasing magnitude to these plots. The stress applied to the region of fluid near the plates is $\sigma_0 \sim \sigma_{mid} R_{mid}^2/R_0^2$. The initial reduction in stress occurs just after the sample first begins to neck and yield. Since at this point the middle of the sample reaches a stress $\sigma_{mid} \sim \sigma_Y$ we might expect a subsequent reduction in stress σ_0 due to the thinning of the midpoint. Whilst this undoubtedly occurs at t_w=0 we observe no changes in the angle $\Delta\theta$. This presumably indicates that there is no elastic strain energy recoverable from the layer of fluid near to the end plates, that is that plastic deformations dominate. Simulations performed by Moschopoulos et al. [171] indicate

that as the yield stress/Bingham number increases, plastic deformations are increasingly localised in the neck. Since the age of our samples results in an increase in yield stress, one explanation could be that at larger aging times the increased yield stress results in less plastic deformation near the end plates and therefore some elastic strain energy can be recovered as the stress relaxes. This would be observed in the changing contact angle.

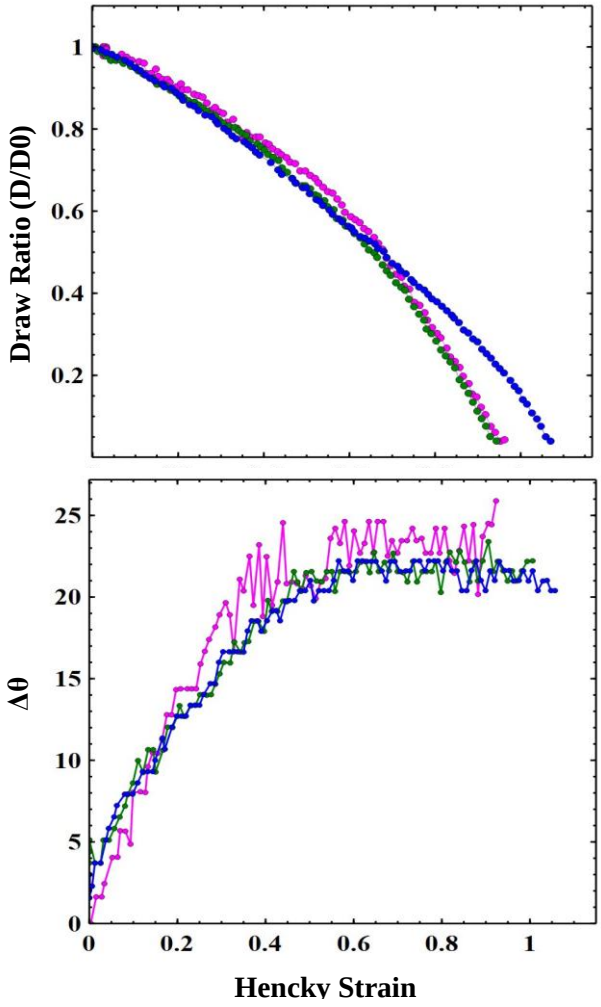

Figure 115: Comparison of the 3 (blue), 3.5 (green) and 4wt% (Magenta) Laponite concentrations at t_w=0. A) thinning of the midpoint of the sample as a function of Henky strain. B) Change in angle of the bottom region of the fluid.

To test this idea we compared different concentration samples at t_w=0. Figure 115 shows both the thinning of the midpoint (a) and the corresponding angular plots (b) for 3, 3.5 and 4wt% samples at t_w=0. The shear yield stress of these samples varies by a factor of ~3. Whilst the thinning of the midpoint shows a clear dependence on yield stress the angular plots show that once $\Delta\theta_{max}$ is reached the sample angle remains

fixed. This demonstrates that the relaxation of the contact angle is not solely related to the yield stress of the sample.

In trying to understand this behaviour we offer the following tentative explanation. N'Gouamba et al. [16], in studying the shear start up behaviour of several yield stress fluids were able to isolate the elastic and plastic contributions. We highlight two important ideas from this study:

1. If σ is much less than σ_γ then deformations are mainly elastic with some recoverable energy.
2. If σ is less than but close to σ_γ then plastic deformations dominate.

As a thought experiment we now consider two idealised cases: one fluid without (A) and one fluid with (B) a large stress overshoot.

In the early stages both the midpoint and the region near the endplates undergo largely elastic deformation. As the Henky strain increases, the amount of plastic deformation increases in both regions though always faster at the midpoint due to the higher value of stress. In sample A when the midpoint reaches the yield stress the sample begins to yield and the stress at this point remains static. The stress near the end plate slowly reduces but since it is still close to the yield stress of the fluid it continues to accumulate significant plastic deformations resulting in very little recoverable strain energy. As a result, $\Delta\theta_{max} - \Delta\theta$ is small. The more uniformly distributed plastic deformation is why these samples do not neck very much. In contrast in fluid B once the stress at the sample midpoint reaches the static yield stress (σ_Y), the stress drops to the much lower value of the dynamic yield stress. The midpoint continues to accumulate significant plastic deformation (as evidenced by enhanced necking of the sample). For the sample region near the plate this means the stress σ_0, which depends on σ_{mid}, drops to a value that is much less than σ_γ. As a result less plastic deformation occurs after the midpoint yields, and a limited amount of the elastic strain energy is gradually recovered as the stress drops further due to filament thinning. $\Delta\theta_{max} - \Delta\theta$ is therefore larger. If our interpretation is right then $\Delta\theta_{max} - \Delta\theta_{final}$ would be related to the amount of elastic vs plastic strain accumulated in the region of fluid near the bottom plate. This would also suggest that the value of $\Delta\theta_{max} - \Delta\theta_{final}$ is linked indirectly to the stress overshoot. In figure 116 we plot these two quantities which at

the very least are correlated. However, further work would be needed to confirm whether the above interpretation is correct / robust.

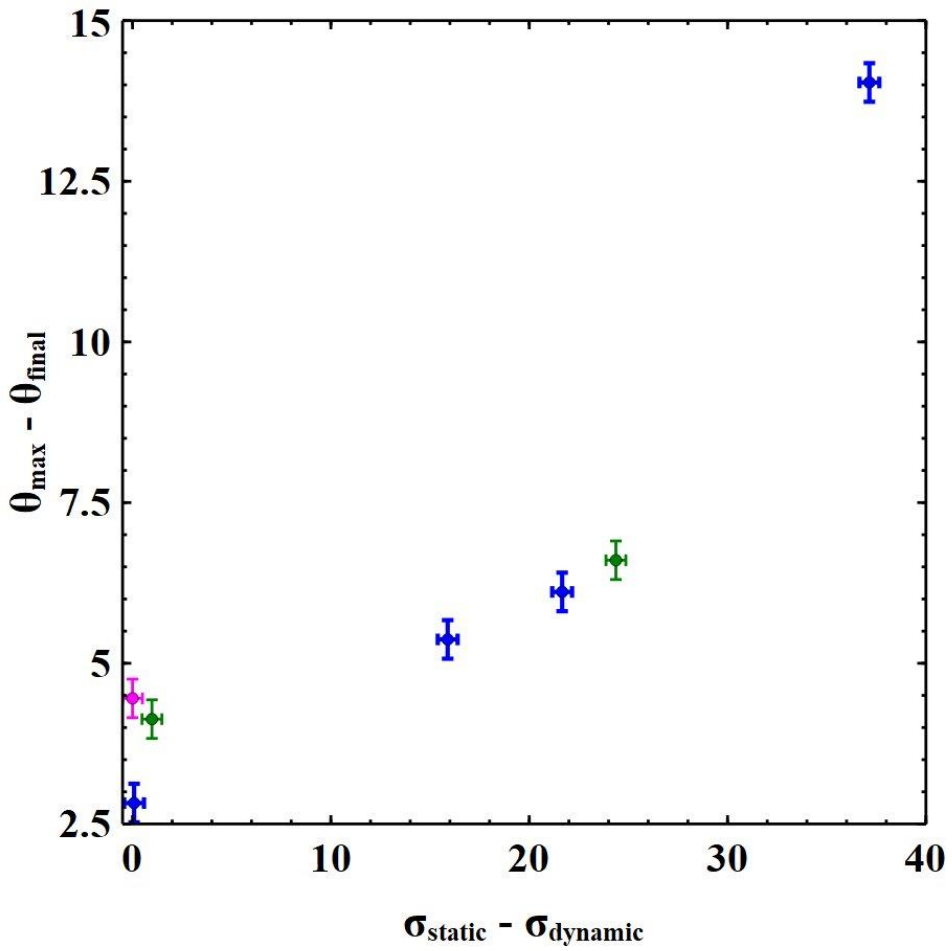

Figure 116: Figure of the maximum stress minus the dynamic yield stress against the maximum angle minus the final angle. Data presented is the 3 (blue), 3.5 (green) and 4 (pink) wt% samples.

6.4 Conclusion

Our initial observations of a simple extensional measurement at increasing aging times showed that there was an apparent change in the break-up behaviour from one that was more ductile to one that was more brittle. The rough fracture surfaces at longer waiting times made this particularly apparent. It should not be missed that this initial observation, as simple as it is, allows this important transition to be assessed without any involved rheology, something that cannot be easily done in simple shear. However, with measurements of the sample midpoint and contact angle, we have shown that some of the key rheological properties can also be quantitatively compared for different types of samples, and insight into changes in their rheology gained. Although mapping of these values to conventional rheological measurements would require some form of calibration curve this does not limit its application for process monitoring / quality control in more applied applications. Several conditions are important for this analysis to hold. Firstly, a no slip condition must hold at the sample plates. Secondly, G' must be significantly bigger than G" at reasonable strains. The Bingham number must also be large, with the effects of interfacial tension confined to a small region near the end of the measurement.

Conclusions

In this thesis we have discussed the dynamic breakup behaviour of kaolin and laponite samples. The experiments that have been presented here provide some insights into the effects of slip and thixotropy in both shear and adhesion rheology experiments as well as interesting results in compaction. Although we have not fully answered the questions behind the process of adhesion, this work provides insights into the behaviour of low concentration gels and saturated suspensions that may inform additional experiments in this field.

There have been several key findings in this work. We have shown that, in adhesion tests of saturated kaolin suspensions, the initial stages of a stretching experiment are subject to the influence of slip. Two distinct behaviours are observed for clays in the concentration range used here with a crossover. This crossover arises from a change in slip mechanism: wall-slip to shear localisation. With practical applications in mind, this chapter also shows that by manipulating the shear-history of the sample through compaction, one can influence the measured slip behaviour and peak force.

Though not explored as fully as we would have liked, monitoring local changes in concentration using x-ray shadowgraphy seems extremely promising. This technique will allow real-time measurement of how shear and extensional experiments evolve for highly concentrated samples. This application could be of interest for industries that deal with opaque, viscous fluids such as drilling or manufacturing.

Since kaolin is a yield stress fluid one might assume compaction would stop when the stress is balanced by the yield stress resulting in a unique critical density. The compaction experiments however showed that dense fluids form denser sediments than lower concentration counterparts when squeezed with the same stress. This emphasises the importance of the shear history in determining the final sample properties. In industrial settings this could result in soils that become harder to remove as previous activities drastically increase the yield stress needed to be overcome.

Experiments with laponite also provided a new method for performing quantitative comparisons of different samples. Whilst thinning of the mid-point is a common approach, we are not aware of other extensional studies on yield stress fluids

that considered the contact angle of the fluid near the plates. Our study suggested that certain material properties are more easily measured in this way, able it requiring calibration.

There are a couple of areas that would benefit from extension to this work in future studies. As part of this work a new shear apparatus was constructed with the help of our industrial partners at Schlumberger. While only a prototype, it shows the potential for dynamic use of x-ray shadowgraphy in rheological experiments. One of the major issues in studying real fluids is their opacity, which limits ones knowledge of the flow profile inside material. This technique provides high speed measurements inside flowing samples. In the context of our project it would have been interesting to further study the interaction of slip and shear banding, comparing it with the complicated shear ramp hysteresis behaviour observed in our initial experiments.

In the laponite experiments, further measurements comparing the static yield stress with the Laplace pressure would be helpful to reduce the measurement error and clarify the relationship between shear and quasi-extensional measurements. It would also be beneficial to use a wider range of sample concentrations and aging times for our experiments to provide further insight into the relationships between the contact angle measurements and conventional shear measurements. Many of our experiments with laponite have also focused on relatively short aging timescales (maximum of 5 hours). There are several examples in the literature of studies that investigate the behaviour of laponites with much longer aging times. We would also be interested to perform several longer aging experiments to demonstrate whether these trends are consistent with longer aging time.

Bibliography

[1] P. Coussot, “Rheometry of Pastes, Suspensions, and Granular Materials”, John Wiley and Sons Inc., New Jersey (2005)

[2] M. Roché, E. Myftiu, M.C. Johnston, P. Kim and H.A. Stone, Phys. Rev. Lett., **110**, 148304 (2013)

[3] M.G. Marudova-Zsivánovits, J. Food Phys., **19**, 85 – 92 (2006)

[4] G. Hulme, Geophys. J. R. astr. Soc., **39**, 2, 361 – 383 (1974)

[5] N.J. Wagner, J.F. Brady, Phys. Today, **62**, 10, 27 (2009)

[6] F. Andreola, E. Castellini, J.M.F Ferreira, S. Olhero and M. Romagnoli, App. Clay Sci., **31**, 1 56 – 64 (2006)

[7] B.M. Guy, J.A. Richards, D.J.M Hodgson, E. Blanco and W.C.K Poon, Phys. Rev. Letts., **121**, 128001 (2018)

[8] E. Brown, N.A. Forman, C.S. Orellana, H. Zhang, B.W. Maynor, D.E. Betts, J.M. DeSimone and H.M. Jaeger, Nature, **9**, 220 - 224 (2010)

[9] E.C. Bingham, “Fluidity and Plasticity”, McGraw-Hill, New York, Chapter 8, 215 – 240 (1922)

[10] I.A. Frigaard, K.G. Paso and P.R. de Souza, Rheol Acta., **56**, 259 – 282 (2017)

[11] P. Coussot, “Soft and Biological Matter: Rheophysics”, Springer, Berlin (2014)

[12] D. Bonn, M. M. Denn, L. Berthier, T. Divoux and S. Manneville, Rev. Mod. Phys., **89**, 035005 (2017)

[13] H.S. Tang and D.M. Kaylon, Rheol Acta, **43**, 80 – 88 (2004)

[14] Enseeiht, Implementation of Rheology, Fluid Mechanics, Energy and Environment Department, available at https://hmf.enseeiht.fr/travaux/beiepe/book/export/html/293 (accessed 16th August 2022)

[15] T. Divoux, D. Tamarii, C. Barentin and S. Manneville, Phys. Rev. Letts., **104**, 208301 (2010)

[16] D. Derks, A. Lindner, C. Creton, D. Bonn, J. App. Phys., **93**, 1557 (2003)

[17] Q. Barral, G. Ovarlez, X. Chateau, J. Boujlel, B. Rabideau and P. Coussot, Soft Matter, **6**, 1343 – 1351 (2010)

[18] R. Sainudiin, M. Moyers-Gonzales and T. Burghelea, Soft Matter, **11**, 5531 - 5545 (2015)

[19] T. Burghelea, M. Moyers-Gonzalez and R. Sainudiin, Soft Matter, **13**, 2024 – 2039 (2017)

[20] H.A. Barnes, J. Non-Newtonian Fluid Mech., **81**, 133–178 (1999)

[21] P.C.F Møller, A. Fall and D. Bonn, EPL, **87**, 38004 (2009)

[22] P. Moller, A. Fall, V. Chikkadi, D. Derks and D. Bonn, Phil. Trans. R. Soc A, **367**, 5139 – 5155 (2009)

[23] M. Dinkgreve, J. Paredes, M.M. Denn and D. Bonn, J. Non-Newton Fluid Mechs. **238**, 233 - 241 (2016)

[24] P.C.F Møller, J. Mewis and D. Bonn, Soft Matter, **2**, 274 – 283 (2006)

[25] T. Divoux, C. Barentin, and S Manneville, Soft Matter, **7**, 9335 – 9349 (2011)

[26] X. Zhang, E. Lorenceau, P. Basset, T. Bourouina, F. Rouyer, J. Goyon and P. Coussot, Phys. Rev. Letts., **119**, 208004 (2017)

[27] P.C.F. Møller, J. Mewis and D. Bonn, Soft Matter, **2**, 274 – 283 (2006)

[28] P. Coussot, Q.D. Nguyen, H.T. Huynh and D. Bonn, J. Rheo, **46**, 573 (2002)

[29] R.N. Zia, Annu. Rev. Fluid Mech., **50**, 371 – 405 (2018)

[30] A.N. Alexandrou, N. Constantinou and G. Georgio, J. Non-Newtonian Fluid Mech., **158**, 1, 6 – 17 (2009)

[31] D.M. Kaylon, J. Rheol, **49**, 621 (2005)

[32] G. Ovarlez, S. Rodts, X. Chateau and P. Coussot, Rheol Acta, **48**, 8, 831 – 844 (2009)

[33] W. Wolthers, M.H.G. Duits, D. van den Ende and J. Mellema, J. Rheo., **40**, 799 (1996)

[34] D. Quemada, Appl. Rheol., **18**, 5, 1 – 13 (2008)

[35] P. Coussot, Q.D. Nguyen, H.T. Huynh and D. Bonn, Phys. Rev. Letts., **88**, 175501 (2002)

[36] E. Younes, M. Himl, Z. Stary, V. Bertola and T. Burghelea, J. Non-Newtonian Fluid Mech., **281**, 104315 (2020)

[37] A. Franck, TA Instruments, AAN004 (1994)

[38] Q. Yuan, X. Lu, K.H. Khayat, D. Feys and C. Shi, Mater Struct., **50**, 112 (2017)

[39] J.M. Dealy, K.F. Wissbrun, Melt Rheology and Its Role in Plastics Processing Theory and Applications, Van Nostrand Reinhold, New York, Chapter 5 (1990)

[40] K. Hyun, S.H. Kim, K.H. Ahn, S.J. Lee, J Non-Newtonian Fluid Mech., **107**, 1, 51 – 65 (2002)

[41] H.G. Sim, K.H. Ahn and S.J. Lee, J. Non Newtonian Fluid Mech., **112**, 2, 237 - 250 (2003)

[42] A.P. Deshpande, Indian Institute of Technology, Techniques in Oscillatory Shear Rheology (2009)

[43] E.E. Bischoff White, M. Chellamuthu and J.P. Rothstein, Rheol Acta, **49**, 119 – 129 (2010)

[44] H.A. Barnes and J.O. Carnali, J. Rheo., **34**, 841 (1990)

[45] J.J McCarthy, V. Jasti, M. Marinack and C.F. Higgs, Powder Technol., **203**, 1, 70 – 77 (2010)

[46] C.W. Macosko, Rheology: Principles, Measurements and Applications, NY Weinheim Cambridge, New York (1994)

[47] D.K.P. Yue, MIT, Marine Hydrodynamics 2.20, unpublished (2005)

[48] P.A. Kelly, University of Auckland, Solid Mechanics, unpublished (2012)

[49] H. Grosser, P. Bormann, Departmento de Geofisica y Meteorologia, Madrid (2003)

[50] F.A. Morrison, Michigan Technological University, Standard Flows CM4650 (2020)

[51] J. Engmann, C. Servais and A.S. Burbidge, J. Non-Newtonian Fluid Mech, **132**, 1, 1 – 27 (2005)

[52] I. Fiebig, V. Schoeppner, Weld World, **62**, 997 – 1012 (2018)

[53] G.P Picher-Martel, A. Levy, P. Hubert, Polym. Compos., **38**, 9, 1828 – 1837 (2015)

[54] Q. Barral, G. Ovarlez, X. Chateau, J. Boujel, B. Rabideau and P. Coussot, Soft Matter, **6**, 1343 – 1351 (2010)

[55] D. Derks, A. Lindner, C. Creton and D. Bonn, J. App. Phys., **93**, 3 1557 (2003)

[56] D. Taylor, The Theory of Critical Distances: A New Perspective in Fracture Materials, Elsevier Science (2007)

[57] K. Cheong, On the Influence of the Through-Thickness Strain Gradients for Characterization of Formability and Fracture of Sheet Metal Alloys, University of Waterloo (2019)

[58] M.A. Abdulrazaq, Physics, Masters Thesis, KTH Royal Institute of Technology (2020)

[59] I.S Yasnikov, A Vinogradov and Y. Estrin, Scr. Mater., **78**, 37 – 40 (2014)

[60] H.J. Barlow, J.O. Cochran and S.M. Fielding, Phys Rev Letts, **125**, 168003 (2020)

[61] A. Furukawa and T. Hanaka, Nat. Mater, **8**, 601 – 609 (2009)

[62] D. Hoyle and S. Fielding, Phys. Rev. Letts., **114**, 15830 (2015)

[63] M. Cloitre, R.T. Bonnecaze, Rheol Acta, **56**, 283 – 305 (2017)

[64] S. Cliffe and S. Young, AADE, AADE-08-DF-HO-10, Agglomeration and Accretion of Drill Cuttings in Water-Based Fluids (2008)

[65] P. Ballesta, N. Koumakis, R. Besseling, W.C.K. Poon and G. Petekidis, Soft Matter, **9**, 3237 – 3245 (2013)

[66] B.K. Aral and D.M. Kalyon, J. Rheo., **38**, 957 (1994)

[67] J.R. Stokes, M.W. Boehm and S.K. Baier, Curr. Opin. Colloid Interface Sci., **18**, 4, 349 – 359 (2013)

[68] R.H. Ewoldt, C. Clasen, A.E. Hosoi and G.H. McKinley, Soft Matter, **3**, 634 – 643 (2007)

[69] D.D Joseph, R. Bai, K.P. Chen, Y.Y. Renardy, Ann. Rev. Fluid Mech., **29**, 65 – 90 (1997)

[70] A.A. Adeyemo, I.O. Adeoye and O.S. Bello, Appl. Water Sci., **7**, 543 – 568 (2017)

[71] P.F. Weck, E. Kim and C.F Jové-Colón, Dalton Trans., **44**, 12550 – 12560 (2015)

[72] M.S Prasad, K.J. Reid and H.H. Murray, Appl. Clay Sci., **6**, 2, 87 – 119 (1991)

[73] S. Mathur, J. Colloid Interface Sci, **256**, 1, 153 – 158 (2002)

[74] A. Perrot, D. Rangeard and A. Levigneur, Mater. Struct., **49**, 4647 – 4655 (2016)

[75] E.J The. Y.K. Leong, Y. Liu, A.B Fourie, M. Fahey, Chem Eng Sci, **64**, 17, 3817 – 3825 (2009)

[76] C.D. Muzny, B.D. Butler, H.J.M. Hanley, F. Tsvetkov and D.G. Peiffer, Mater. Lett., **28**, 4, 379 – 384 (1996)

[77] R. Perkins, R. Brace and E. Matijević, J. Colloid Interface Sci., **48**, 3, 417 – 426 (1974)

[78] B. Ruzicka and E. Zaccarelli, Soft Matter, **7**, 1268 – 1286 (2011)

[79] B. Abou, D. Bonn and J. Meunier, Phys Rev Letts, **64**, 021510 (2001)

[80] A. Knaebel, M. Bellour, J.-P. Munch, V. Viasnoff, F. Lequeux and J.L. Harden, Europhys Lett., **52**, 1, 73 – 79 (2000)

[81] B. Robertson, Engineering, Clay Accretion, University of Bristol (2017)

[82] J. Montilva, E. van Oort, R. Brahim, B. Dye, J.P. Luzardo, M. McDonald and L. Quintero, AADE, AADE-07-NTCE-21, Improved Drilling Performance in Lake Maracaibo Using a Low Salinity High Performance Water-Based Drilling Fluid (2007)

[83] M.S. Prasad, K.J. Reid and H.H. Murray, App. Clay Sci., **6**, 2, 87 – 119 (1991)

[84] B.D. Rabideau, P. Moucheront, F. Bertrand, S. Rodts, Y. Mélinge, C. Lanos and P. Coussot, J. Am. Ceram. Soc., **95**, 2, 494 – 501 (2012)

[85] G. Ovarlez, S. Rodts, X. Chateau and P. Coussot, Rheol Acta, **48**, 831 – 844 (2009)

[86] C.A. Burns, P.A. Gauglitz and R.L. Russell, U.S. Department of Energy, Shear Strength Correlations for Kaolin/Water Slurries: A Recent Comparison of Measurements with Historical Data (2010)

[87] J.John, J. Botchu and S.W. Baek, Rheology of Ethanol Based Hybrid Solid Propellant, (ISTS, Kobe-Hyogo, 2015)

[88] H.A. Barnes, J. Non-Newton. Fluid Mech., **56**, 133 – 178 (1995)

[89] P. Coussot, S. Boyer, Rheol. Acta, **34**, 534 - 543 (1995)

[90] V. Bertola, J. Phys.: Condens. Matter, **21**, 035107 (2009)

[91] W.J. Smith, C. Kusina, J.F. Joanny, A. Colin, Phys. Rev. Lett. **123**, 148002 (2019)

[92] J. Engmann, C. Servais, A.S. Burbidge, J. Non-Newton Fluid Mech. **132**, 1, 1–27 (2005)

[93] D. Derks, A. Lindner, C. Creton, D. Bonn, J. App. Phys. **93**, 1557 (2003)

[94] B. Adhikari, T. Howes, B.R. Bhandari, V. Truong, Int. J. Food Prop. **4**, 1–33 (2001)

[95] Y.O.M. Abdelhaye, M. Chaouche, H. Van Damme, Eur. Phys. J. E, **36**, 128 (2013)

[96] Y.O.M. Abdelhaye, M. Chaouche, J. Chapuis, E. Charlaix, J. Hinch, S. Roux, H. Van Damme, Eur. Phys. J. E, **35**, 45 (2012)

[97] Q. Barral, G. Ovarlez, X. Chateau, J. Boujlel, B. Rabideau, P. Coussot, Soft Matter, **6**, 1343–1351 (2010)

[98] O.A. Fadoul, P. Coussot, Fluids, **4**, 1, 53 (2019)

[99] T. Divoux, A. Shukla, B. Marsit, Y. Kaloga, I. Bischofberger, Phys. Rev. Lett, **124**, 248006 (2020)

[100] Y.O.M. Abdelhaye, M. Chaouche, H. Van Damme, Appl. Clay Sci., **42**, 1, 163 – 167 (2008)

[101] X. Zhang, O. Fadoul, E. Lorenceau, P. Coussot, Phys. Rev. Lett., **120**, 048001 (2018)

[102] N. Koumakis, G. Petekedis, Soft Matter, **7**, 2456 - 2470 (2011)

[103] M. Dinkgreve, M.M. Denn, D. Bonn, Rheol. Acta, **56**, 189 – 194 (2017)

[104] S. Jesinghausen, R. Weiffen, H. Schmid, Exp. Fluids, **57**, 153 (2016)

[105] P. Ballesta, G. Petekidis, L. Isa, W.C.K. Poon, R. Besseling, J. Rheol., **56**, 1005 (2012)

[106] S. Manneville, Rheol Acta, **47**, 301 – 318 (2008)

[107] J.R. Seth, M. Cloitre, R.T. Bonnecaze, J. Rheol. **52**, 1241 (2008)

[108] V. Bertola, F. Bertrand, H. Tabuteau, D. Bonn, P. Coussot, J. Rheol., **47**, 1211 (2003)

[109] Schlumberger, Case Study: Columbia, South America, "HydraGlyde System Relieves BHA Balling, Torque, and Stick/Slip Issues, Colombia", https://www.slb.com/resource-library/case-study/mi/hydraglyde-colombia-cs (accessed 19th August 2021)

[110] A. Kaci, R. Bouras, V.T. Phan, P.A. Andreani, M. Chaouche, H. Brossas, Cem.

Concr. Compos., **33**, 2, 218 - 224 (2011)

[111] F. Pignon, A. Magnin, J. Piau, J. Rheol. **40**, 573 (1996)

[112] L. Isa, R. Besseling, W.C.K. Poon, Phys. Rev. Lett. **98**, 198305 (2007)

[113] M. Arcinagio, C. Kuo, M. Dennin, Colloids & Surfaces A. **382**, 36 – 41 (2011)

[114] M.I. Smith, Sci. Rep. **5**, 14175 (2015)

115[116] K. Yang, W. Yu, J. Rheol. **61**, 627 (2017)

[116] B.K. Aral, D.M. Kaylon, J. Rheol. **38**, 957 (1994)

[117] Flow Capture, REX-CELL U Series Specifications, http://www.flowcapture.com/portfolio/rex-celltm-u-series/ (accessed 16th July 2020)

[118] M. Hrabak, R.S. Padovan, M. Kralik, D. Ozrectic and K. Potocki, Radiographics, **28**, 1189 – 1192 (2008)

[119] G. Wypych, Handbook of UV Degradation and Stabilization, ChemTec Publishing, Scarborough, Chapter 2, 9 – 35, Second Edition (2015)

[120] W. Thielicke, E.J. Stamhuis, J. Open Res. Softw., **2**, 1, 30 (2014)

[121] C.R. Fitts, Groundwater Science, Elsevier, Amsterdam, Second Edition, Chapter 6, 187 – 242 (2012)

[122] B. Andreotti, Y. Forterre and O. Pouliquen, Granular Media Between Fluid and Solid, Cambridge University Press, Cambridge, Chapter 7, 285 – 310 (2013)

[123] H.A. Makse, D.L. Johnson, L.M. Schwartz, Phys. Rev. Letts, **84**, 4160 (2000)

[124] E. Caglioti, V. Loreto, H.J. Herrmann and M. Nicodermi, Phys. Rev. Letts., **79**, 1575 (1997)

[125] S.R. Liber, S. Borohovich, A.V. Butenko, A.B. Schofield and E. Sloutskin, PNAS, **110**, 15, 5769 - 5773 (2013)

[126] R.C Hidalgo, C.U. Grosse, F. Kun, H.W. Reinhardt, H.J. Herrmann. Phys. Rev. Letts., **89**, 205501 (2002)

[127] T. Travers, D. Bideau, A. Gervois, J.P. Troadec and J.C. Messager, J. Phys. A: Math. Gen., **19**, 16, L1033 (1986)

[128] D.M. Audet, Geophys. J. Int., **122**, 1, 283 – 298 (1995)

[129] G. Mesri, R.E. Olson, Clays Clay Miner, 19, 1971

[130] W.G. Gray and C.T Miller, Environ. Sci. Technol., 38, 2004

[131] R. Nolen-Hoeksama, Oilfield Review, 26, 3, 2014

[132] A. Atangana, Fractional Operators With Constant and Variable Order With Application to Geo-Hydrology, 15 – 47, 2018

[133] G. Varas, V. Vidal and J.C. Géminard, Phys. Rev. E., 83, 2011

[134] L. Besra, D.K. Sengupta, S.K. Roy, Inter. J. Miner. Process., 59, 2000

[135] M. Mirshekari, M. Ghayoomi and A. Borghei, Geotech. Test. J., 2018

[136] Eppendorf Handling Solutions, Basics in Centrifugation, available at https://handling-solutions.eppendorf.com/sample-handling/centrifugation/safe-use-of-centrifuges/basics-in-centrifugation/ (accessed October 2021)

[137] Fisher Scientific, Centrifugation Theory, available at https://www.fishersci.co.uk/gb/en/scientific-products/centrifuge-guide/centrifugation-theory.html (accessed October 2021)

[138] Flow Capture, Multi-energy X-ray Imaging for Large Objects, available at https://www.flowcapture.com/?page_id=402 (accessed 16th February 2022)

[139] T. Mörz, E.A. Karlik, S. Kreiter and A. Kopf, Sediment. Geol., **196**, 1, 251 - 267 (2007)

[140] A. Tarantino and E. De Col, Géotechnique **58**, 3, 199 – 213 (2008)

[141] D. Reid, A.B. Fourie and S. Watson, "Accelerated consolidation of soft clays and mine tailings using a desktop centrifuge", 15th International Seminar on Paste and Thickening Tailings, Perth (2012)

[142] G. German and V. Bertola, Phys. Fluids, **22**, 033101 (2010)

[143] P. Coussot and F. Gaulard, Phys. Rev., **72**, 031409 (2005)

[144] G.H. McKinley and T. Sridhar, Annu. Rev. Fluid Mech., **34**, 375 - 415 (2002)

[145] S.L. Anna and G.H. McKinley, J. Rheo, **45**, 115 (2001)

[146] K. Niedzwiedz, O. Arnolds, N. Willenbacher and R. Brummer, Appl. Rheol., **19**, 41969 (2009)

[147] A.V. Bazilevskii, V.M. Entov and A.N. Rozhkov, Fluid Dyn., **46**, 613 (2011)

[148] G.H. McKinley, Department of Mechanical Engineering, MIT, (2005) 05-P-04, Visco-Elasto-Capillary Thinning and Break-Up of Complex Fluids

[149] M. Arciniaga, C. Kuo and M. Dennin, Colloid Surf., **382**, 1, 36 - 41 (2011)

[150] R.H. Temperton, M.I. Smith and J.S. Sharp, Eur. Phys. J. E., **38**, 79, 2015

[151] S. Arora, A. Shabbir, O. Hassager, C. Ligoure and L. Ramos, J. Rheo., **61**, 1267 (2017)

[152] M. Ozawa, L. Berthier, G. Biroli, A. Rosso and G. Tarjus, PNAS, **115**, 26 (2018)

[153] H.J. Barlow, J.O. Cochran, and S.M. Fielding, Phys. Rev. Letts., **125**, 168003 (2020)

[157] J.L. Dávila, M.A. d'Ávila, Carbohydr. Polym., **157,** 1 – 8 (2017)

[155] B. Ruzicka and E. Zaccarelli, Soft Matter, **7**, 1268 - 1286 (2011)

[156] H.A. Baghdadi, J. Parrella and S.R. Bhatia, Rheol Acta, **47**, 3, 349 - 357 (2008)

[157] D. Hoyle and S.M. Fielding, Phys. Rev. Letts., **114**, 158301 (2015)

[158] M.K. Tiwari and A.V. Bazilevsky, Rheol. Acta, **48**, 6, 597 - 609 (2009)

[159] E.M.S. Wendt, R.R. Fernandes, J.F. Galdino, D.E.V Andrade and A.T. Franco, J. Rheo., **65**, 1089 (2021)

[160] E. N'Gouamba, J. Goyon and P. Coussot, Phys. Rev. Fluids, **4**, 123301 (2019)

[161] M. Shoaib, N. Molaei and E.R. Bobicki, Phys. Chem. Chem. Phys., **24**, 4703 - 4714 (2022)

[162] Y.M. Joshi, G, Ranjith, K. Reddy, A.L. Kulkarni, N. Kumar and R.P. Chhabra, Proc. R. Soc., **464**, 469 – 489 (2008)

[163] A. Shaukat and A. Sharma, Rheol. Acta, **49**, 1093 - 1101 (2010)

[164] F. Bonacci, X. Chateau, E.M. Furst, J. Fusier, J. Goyon and A. Lemaître, Nat, **19**, 775 – 780 (2020)

[165] C. Christopoulou, G. Petekidis, B. Erwin, M. Cloitre and D. Vlassopoulos, Phil. Trans. R. Soc. A, **367**, 5051 – 5071 (2009)

[166] S. Mazoyer, L. Cipelletti and L. Ramos, Phys. Rev. Letts., **97**, 238301 (2006)

[167] R. Blanc, H. Van Damme, Mobile Particulate Systems, ed. E., E. Guazzelli and L. Oger, Ch. 9, Kluwer, Amsterdam (1995)

[168] Y. Yoshitake, S. Mitani, K. Sakai, and K. Takagi, Phys. Rev. E., **78**, 041405 (2008)

[169] E.Y. Arashiro and N.R. Demarquette, Mat. Res, 2, 1 (1999)

[170] E. Huang, A. Skoufis, T. Denning, J. Qi, R.R Dagastine, R. Tabor and J.D. Berry, J Open Source Software, **6**, 58, 2604 (2021)

[171] P. Moschopoulos, A. Syrakos, Y. Dimakopoulos and J. Tsamopoulos, J. Non-Newton Fluid Mech, **284**, 104371 (2020)

[172] Y. Chen, J. Tsai and Y. Hsu, Meas Sci Technol, **27**, 074010 (2016)